Radiation Damage of Superconducting Materials for Fusion Application

A thesis submitted for the degree of Doctor of Philosophy

William Iliffe

St. Catherine's College

University of Oxford

Supervisors:

Prof. Chris Grovenor   Prof. Susannah Speller

30TH SEPTEMBER 2021

Abstract

Radiation Damage of Superconducting Materials for Fusion Application

William Iliffe
St. Catherine’s College

A thesis submitted for the degree of Doctor of Philosophy
The University of Oxford
September 2021

Superconducting wires are a key enabling technology for generating electricity from fusion reactions as they can carry high current densities in high magnetic fields, allowing them to make better use of the limited space available in a tokamak and improve its power density. This thesis focused on REBCO coated conductors (CC) as, despite its documented deterioration during neutron irradiation, it is the superconductor of choice for several tokamak power plant (TTP) concepts due to reliable products with appropriate performance becoming increasingly commercially available. During their operation in TPP, REBCO CC will carrying large currents whilst being neutron irradiated, subjected to high applied fields and maintained at their operating temperature. An appraisal of the previous literature shows that experiments designed to determine REBCO’s suitability for fusion applications use various irradiation methods, but all apply it to samples maintained at room temperature. This thesis, therefore, aims to get closer to the actual operating conditions within a TPP by investigating the response of REBCO to irradiation when irradiated at its operating temperature.

After a thorough discussion of the previous literature and a description of the experimental methods used herein, this thesis presents 4 experimental chapters before summarising and drawing conclusions. The first (chapter 4) uses computer simulations to evaluate how REBCO is affected by fusion spectrum neutrons and compares that with published data of how it responds to the fission neutron spectrum. Discussion of these results includes an analysis of this comparison, determination of the expected lattice damage and impurity build-up in REBCO during its operating lifetime in a TPP, and determination of an appropriate ion and energy combination to be used as a proxy for fusion neutron irradiation. The second (chapter 5) describes an experiment to determine how the chosen ion-energy combination effects REBCO samples when they are maintained at room temperature, using magnetometry to track superconducting properties between irradiation steps. This experiment allowed distinctions between the samples to be made, and allowed one sample, Fujikura’s 2018 unenhanced GdBCO CC, to be chosen to go forward to cold irradiation experiments. The third (chapter 6) presents a description of the design process behind the Cold Irradiation Experiment (CIE)

– an apparatus capable of maintaining a REBCO CC at a set temperature below its critical temperature (T_c), performing electrical testing to determine superconducting properties and allowing the sample to be ion irradiated, although the later 2 were not done simultaneously during this work. This culminated in the successful building of the CIE which is used in the fourth experimental chapter (chapter 7) to generate data on how the temperature of a REBCO sample effects how its superconducting properties change with increasing irradiation dose. The key results of this experiment were that sample temperature does not affect how the REBCO superconducting properties deteriorate with increasing irradiation dose but does affect what happens if the samples are left to anneal at room temperature for extended periods. Although the exact cause of this change is not definitively established during this work, various hypotheses are discussed and several avenues of further work that would allow the hypotheses to be tested are presented.

Acknowledgements

During my time at Oxford, I have been fortunate to have benefitted from an enormous amount of support for which I am extremely grateful.

To my supervisors, Chris and Susie, many thanks for all the feedback you have provided and for putting in the hours reading some of the complete drivel that I must have written since arriving in 2017. My understanding always improved, and the work always ended up being much better.

To my industrial sponsors, Greg Brittles, Rod Bateman and Robert Slade at Tokamak Energy (TE), many thanks for your feedback during the many progress meetings and in the run up to conferences, for helping me out with equipment when breakages threatened to halt progress and, particularly, for letting me do my industrial placement part-time as I learnt a lot and it allowed me to keep both thesis and placement work progressing.

To my collaborators at the Surrey Ion Beam Centre, Nianhua Peng and Roger Webb, for access to equipment for the Cold Irradiation Experiments and getting the large number of separate irradiations this project required completed in good time.

To the various staff at Oxford University and the UKAEA without whose help my project would have surely floundered. Particular thanks go to Clara Barker at CfAS Materials, Amelia Coldea, Kieran McCall and Matt Bristow (now at TE) at CfAS Physics, Radka Chakalova in the cleanroom in Begbroke, Simon Clark and Simon Cassidy of the Chemistry Department's SQUID lab, Brain Eade (now retired) and Cleveland Williams in the Engineering Department's mechanical workshop, Stuart Higgs and Mike Stockford (now retired) in the Engineering Department's electronics workshop for access to equipment, Tony Wheeler in the Material's Department workshop and Mark Gilbert of the UKAEA for helping me get started with FISPACT-II and SPECTRA-PKA.

Finally, to my little family. To my daughters, Daisy and Betsy, you are my guiding stars, getting more beautiful every day and I simultaneously don't want you to grow up and can't wait to see the remarkable young women you will no doubt become. To my beautiful Katy, your support and encouragement have been such a boon but, given the arrival and your tireless nurturing of Daisy and Betsy, I think that you have achieved far more than I during our time in Oxford, for which I will always be eternally grateful.

Statement of Originality

The work reported in this thesis was carried out by the author in the Department of Materials, University of Oxford, between October 2017 and September 2021, under the supervision of Prof. C.R.M. Grovenor and Prof. S.C. Speller.

No part of this thesis has been previously submitted for a degree at this or any other university. The work of other authors has been freely drawn upon and is duly acknowledged in the text. A list of references has been given at the end of the thesis.

Some of the work described in this thesis has been published in the following journals and presented at the conferences listed below:

Publications

W.R. Iliffe et al. "In-situ measurement of the effect of radiation damage on the superconducting properties of coated conductors" *Superconducting Science and Technology, Volume 34 (2021) 09LT01*

Conferences

European Conference of Applied Superconductivity. Moscow, Russia (Virtual). September 2021. Oral Presentation – "On the effect of low temperature, in-situ ion beam irradiation on the critical current density of coated conductors" #126

United Kingdom National Ion Beam Centre User Day. Guildford, UK. September 2021. Virtual Poster – "In-situ measurements of the effect of radiation damage on the superconducting properties of coated conductors."

Cryogenic Engineering Conference and International Cryogenic Materials Conference (23rd). July 2021. Oral Presentation – "In-situ measurements of the effect of radiation damage on the superconducting properties of coated conductors." M2Or5B-04

Materials Research Society – Spring Meeting. April 2021. Virtual Poster – "Investigating the use of 2G REBCO Coated Conductors in Magnetic Confinement Fusion Devices".

Applied Superconductivity Conference. October-November 2020. Virtual Poster – "Investigating the use of 2G REBCO Coated Conductors in Fusion Devices".

United Kingdom National Ion Beam Centre User Day. Guildford, UK. July 2020. Virtual Poster – "Radiation Damage in High Temperature Superconducting Materials for Fusion applications"

European Conference of Applied Superconductivity. Moscow, Russia (Virtual). September 2019. Poster – "Ion Beam Irradiation Experiments on REBCO Coated Conductors"

List of Acronyms

Acronym	**Meaning**
^{2}D	Deuterium
^{3}T	Tritium
ABAD	Alternating Beam Assisted Deposition
AES	Auger Electron Spectroscopy
APC(s)	Artificial Pinning Centre(s)
ARC	Affordable, Reliable, Compact (name of Tokamak concept)
arc-NRT	An extension of the NRT model to account for Athermal ReCombination
BAD	Beam Assisted Deposition
BCA	Binary collision approximation
BCS	Bardeen, Cooper, Schrieffer (pertaining to their 1956 theory)
BSE	Back Scattering Electron (pertaining to imaging)
BSSCO	Bismuth strontium calcium copper oxide (pertaining to family of superconducting materials)
c276	Hastelloy Grade c276
CC(s)	Coated Conductor(s)
CfAS	Centre for Applied Superconductivity
CIE	Cold Irradiation Experiment
CIF	Central Irradiation Facility (pertaining to the Vienna TRIGA reactor)
CSD	Chemical Solution Deposition
DCCEM	David Cockayne Centre of Electron Microscopy
DDD	Discrete Dislocation Dynamics (family of irradiation simulation codes)
(TD) DFT	(Time Dependent) Density Function Theory
DI	Deionised (pertaining to purity of water)
$dpa_{(t)}$	Displacements per (target) atom
DT	Deuterium – Tritium Fusion reactions
eBAD	Electron Beam Assisted Deposition
EBSD	Electron Back Scattered Diffraction
EDTA	Ethylenediaminetetraacetic acid
EDX	Energy Dispersive X-ray
EOL	End of Life
FEM	Finite Element Method
FPY	Full Power Year
FW	First Wall (pertaining to a tokamak)

GL	Ginsburg – Landau (pertaining to their 1950 theory)
HCPB	Helium-cooled Pebble-Bed (pertaining to TPP technology)
HTS	High Temperature Superconductor ($T_c > 77$ K)
IBAD	Ion Beam Assisted Deposition
Int	Interstitial (pertaining to crystallography)
ISD	Inclined Substrate Deposition
I-V	Current – Voltage Curve
JET	Joint European Torus (name of a Tokamak experiment)
KMC	Kinetic Monte Carlo (family of irradiation simulation codes)
KP	Kinchin-Pease (pertaining to their 1955 theory)
LM	Light Microscopy (or Light Microscope, depending of context)
LSS	Lindhart, Scharff and Schiott (pertaining to their 1963 theory)
LTS	Low Temperature Superconductor ($T_c < 77$ K)
MCF	Magnetic Confinement Fusion
MCNP or MCN	Monte Carlo N-Particle (type of neutronics calculation)
MCPCB	Metal Clad Printed Circuit Board
MD	Molecular Dynamics (family of irradiation simulation codes)
mdpa	milli displacements per atom (ie. 1mdpa = 10^{-3} dpa)
MF	Matching Field (for full definition, see table 2-6)
MMC	Metropolis Monte Carlo (family of irradiation simulation codes)
MOCVD	Metal Organic Chemical Vapour Deposition
MOD	Metal Organic Deposition
MURR	Missouri University Research Reactor
ND	Normal Direction (pertaining to CC orientation, defined in figure 3.1)
NRT	Norgett, Robinson and Torrens (pertaining to their 1975 theory)
O2T	Orthorhombic to Tetragonal (pertaining to crystallography)
PALS	Positron Annihilation Lifetime Spectroscopy
PF	Poloidal Field (of a Tokamak)
PFM	Phase Field Modelling
PID	Proportional-Integral-Differential (pertaining to a standard case of control system design)
PIPS	Precision Ion Polishing System
PKA(s)	Primary Knock-on Atom(s)
PLD	Pulsed Laser Deposition
PPMS	Physical Property Measurement System

PSU	Power Supply Unit
RD	Rolling Direction (pertaining to CC orientation, defined in figure 3.1)
RE	Rare Earth Element (Yttrium, Gadolinium, Europium etc…)
RE	Rate Equation (family of irradiation simulation codes)
REBCO	Rare Earth (RE) Barium Copper Oxide (superconductor family
RaBITS	Rolling Assisted Biaxially Textured Substrate
RCE-(C)DR	Reactive Co-evaporation – (Cyclic) Deposition and Reaction
rfMS	Radio Frequency Magnetron Sputtering
rMS	Reactive Magnetron Sputtering
rpa	Replacements per atom
RRI	Robinson Research Institute (at Victoria University, Wellington)
SD	Silicon Diode Temperature Sensor
SE	Secondary Electron (pertaining to SEM imaging)
SEM	Scanning Electron Microscopy
SIBC	Surrey University Ion Beam Centre
SKA(s)	Secondary Knock-on Atom(s) (can also be tertiary (TKA), quaternary (QKA), etc…)
SNS	superconductor-normal-metal-superconductor (pertaining to type of Josephson proximity junction)
SQUID	Superconducting Quantum Interference Device
SRIM	The Stopping and Range of Ions in Matter
SS	Stainless Steel
TD	Traverse Direction (pertaining to CC orientation, defined in figure 3.1)
TDE	Threshold Displacement Energy (E_d)
TE	Tokamak Energy Ltd
TEM	Transmission Electron Microscopy (or Transmission Electron Microscope, depending on context) (pertaining to family of imaging methods)
TENDL	TALYS-adjusted Evaluated Nuclear Data Library
TF	Toroidal Field (of a Tokamak)
TFA	Trifluoroacetate
TLAG	Transient liquid assisted growth (pertaining to type of CSD)
TPP	Tokamak Power Plant
V(α)	Vacancy position labelled ‘α’ (pertaining to crystallography)
Vac	Vacancy (pertaining to crystallography)
VSM	Vibrating Sample Magnetometer (part of a PPMS)
YSZ	Yttrium Stabilised Zirconium

(Z)FC	(Zero) Field Cooled

Table of Contents

1 Introduction

This EPSRC Industrial CASE studentship, in collaboration with Tokamak Energy Ltd (TE), aims to inform the design of Tokamak Power Plants (TPP) by investigating the response to irradiation damage of commercially available rare-earth, barium copper oxide (REBCO) superconducting coated conductors (CC) by using a combination of ion irradiation at cryogenic temperatures and both in-situ and sequential superconducting property measurements. This chapter gives a more rigorous description of where this work sits in the context of the wider goal of using fusion reactions to generate electricity, before defining an overarching research question for the thesis and summarising the methods used.

1.1 Background

During the next century, three factors will bring about a seismic shift in the world's energy landscape; a rising world population, a global increase in the per-capita energy demand and the depletion of natural stocks of fossil fuels [1]. Couple this with the issues inherent with our changing climate [2] and the options for producing this energy become increasingly limited. Precisely how these factors will impact global energy use and its sources has been the subject of numerous studies (e.g. [1], [3]) but they typically conclude that fossil fuels, particularly natural gas, will make up a significant, but falling, proportion of world electricity supply in 2050 and hence there will still be work to do to decarbonise the world's electricity supply [4].

Being able to replace these natural gas plants with near-carbon-neutral alternatives as they reach their end-of-life (EOL) is therefore an attractive long-term investment opportunity. One option is to build tokamaks (Figure 1.1a): a type of magnetic confinement fusion (MCF) device that confines a plasma of deuterium (^{2}D) and tritium (^{3}T) nuclei which fuse to produce a considerable energy gain [5], [6]. To produce fusion energy economically, however, the tokamak's confining toroidal magnetic field (B_t) needs to be of the order 1-10T and operate for extended periods. For this type of application superconducting wires are likely to be chosen as they can achieve high current densities in high magnetic fields, allowing them to make better use of the limited space surrounding the plasma torus, and avoid the inherent losses in resistive electromagnets.

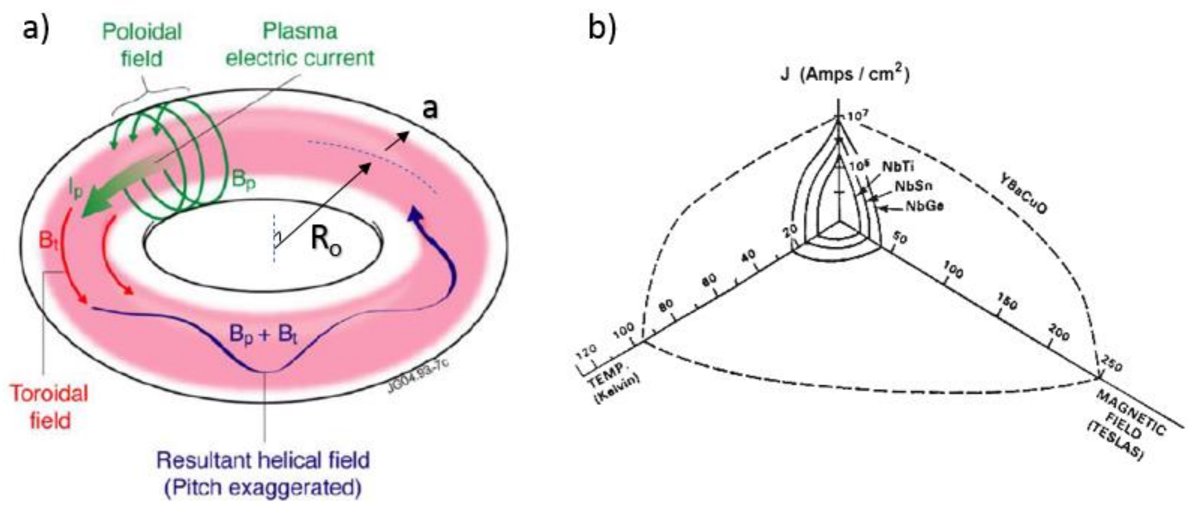

Figure 1.1: a) Schematic of a Tokamak Plasma of major radius (R_0) and minor radius (a), showing direction of toroidal magnetic field (B_t) applied by a toroidal electromagnet and the poloidal magnetic field (B_p) applied by the plasma current (I_p). Original image modified from [7]. *b) comparison of critical surface of low temperature superconductors NbTi, Nb_3Sn and NbGe with high temperature superconductor REBCO* [8].

Moving forward to an economically viable, energy producing TPP, however, is more problematic as superconducting toroidal field (TF) coils are being subjected to the neutrons emitted by the fusing plasma. Given that the critical surface of all superconductors (i.e. the boundary in temperature (T), magnetic field (B) and current density (J) space between the normal and zero resistance state – Figure 1.1b) has been shown to be affected by neutron bombardment [9], [10], the degradation of superconductors in service is now a plant lifetime limiting factor in the design of all TPPs.

1.2 Motivation for further investigating irradiation damage in REBCO CC

Like any product, the economic viability of a TPP is a function of its initial cost, plant efficiency and operating lifetime. Determining these for a TPP is a multi-stage process, the first of which is a systems code. These take a few independent variables (e.g. major radius (R_0), minor radius (a), required fusion power (P_{fus}), etc…) and define a TPP device that can achieve these goals. Depending on the code's complexity, it can optimise just the plasma physics [11] or can go further, defining a set of engineering parameters [12], [13], initial capital costs [14] and/or 3D mechanical design [15]. The plant lifetime, however, is not definable at this stage and, given the complexity of a TPP and its numerous interdependences, needs the conceptual design to be expanded before being subjected to neutronics modelling [16]. Only with this neutronics data can estimates be made about how the properties of materials in each region of the TPP will change and where and when failure modes will occur.

It has been recognised that degradation of the superconductor in the TF magnet due to neutron irradiation is a key failure mode limiting the lifetime of TPPs. This is particularly problematic at the toroidal field coil inner midplane, as this volume is subjected to the peak mechanical stress and the strongest magnetic field. It is the design of this section[1], therefore, that determines the maximum time the TPP magnet can operate at its rated field. Knowing how the supercurrent carrying capacity and stress-strain characteristics of a superconducting wire will change post-neutron irradiation, therefore, represents a significant de-risking factor in the design and cost of the coil.

In the case of REBCO, the situation is further complicated by its anisotropic unit cell and superconducting properties, and how these properties respond to the direction of an applied magnetic field [17]. Adding to this complexity is that REBCO CC manufacturers take great pains to optimise the construction and microstructure of their products for maximum supercurrent carrying capacity and mechanical properties (e.g. [18], [19]) for specific applications. These optimisations typically involve the introduction of a precisely designed defect structure in the REBCO layer, and, as neutron irradiation leads to structural changes in materials [20], exactly how these two mechanisms affect the overall supercurrent carrying capacity of the wire during irradiation is hard to predict.

Given this, experiments have been performed to characterise how the supercurrent carrying capacity of manufactured REBCO CCs is affected by irradiation damage, but no source of fusion-spectrum neutrons has been available. The proxies that have been used are fission spectrum neutrons (e.g. [21]) and irradiation with a wide variety of different ions (see Table 2-6). Both types of experiments show that current carrying capacity is strongly affected by irradiation.

1.3 Aims and Overview

One shortfall of current experiments used to predict how the critical surface of REBCO will change with neutron fluence is that they do not rigorously interrogate how different regions of neutron energy spectrum damages REBCO and so have not used that information to inform their choice of proxy irradiator. Another is that in experiments irradiating REBCO, the superconductor is at room temperature or higher (20-60 °C), whereas in fusion reactors it will be at its operating temperature (4-50 K) whilst being subjected to high fields and carrying its rated current during neutron irradiation. Addressing all these differences was not possible within the timeframe of this work, so these 2 research questions were defined.

1) How is the critical surface of REBCO CC affected by fusion spectrum neutrons, and

2) does this differ when irradiation occurs at low temperature vs room temperature?

Addressing these research questions has included the simulation of neutron damage in REBCO using a variety of different fusion-relevant spectra, and performing experiments to test how $J_c(B,T)$

---

[1] Assuming it cannot somehow be replaced

changes with irradiation damage whilst at its operating temperature of 4-50K and to compare that with data from room temperature irradiations.

The thesis is structured as follows. Lessons learnt from the published literature make up chapter 2. Aspects of the relevant experimental techniques used in this thesis are described in chapter 3. In chapter 4, the results of simulating the damage and impurity build-up in REBCO due to neutron irradiation from fission and fusion neutron spectra are presented and discussed. This is followed by a report on the results of room temperature ion irradiation of REBCO CCs in chapter 5, performed to give a baseline for latter experiments. Moving towards the irradiation of REBCO CCs at cryogenic temperatures, chapter 6 details the development of an experiment designed for this purpose. In chapter 7, the results of using the apparatus described in chapter 6 to perform in-situ low temperature irradiation and superconducting property measurements are reported. Finally, in chapter 8, all the results presented in chapters 4-7 are summarised, conclusions drawn, and suggestions made for further work.

2 Literature Review

This chapter aims to present the relevant background science and a review of the published literature surrounding TPPs, the need for superconducting magnets in fusion machines, superconductivity in rare-earth, barium copper oxide (REBCO) and the manufacture of REBCO-based coated conductors (CC), a discussion of irradiation damage, its effects and its simulation, and the documented effects of different types of irradiations on REBCO and REBCO-based CCs.

2.1 Fusion

First demonstrated in 1932 [22], nuclear fusion is when two light nuclei fuse to form other elementary particles, losing mass and releasing energy. The most promising fusion reaction for creating electricity in a tokamak is that between deuterium (^{2}D) and tritium (^{3}T) as it has a higher reactivity than other potential reactions at relatively low temperatures [5], [23]:

$$ {}_{1}^{2}D + {}_{1}^{3}T \rightarrow {}_{2}^{4}\alpha \text{ (3.5 MeV)} + {}_{0}^{1}n \text{ (14.1 MeV)} \tag{2-1} $$

The principal difficulties in generating and sustaining deuterium-tritium (DT) fusion reactions are maintaining the very high temperatures required and stably confining the energy of the reactants and emitted alpha particles in sufficient quantities for sufficient time. The temperature required is ≈120 MK at which the reactants are in a plasma state and therefore can be confined using magnetic fields. Being a plasma, the energy of the emitted alpha particles is readily absorbed, hence a DT plasma can be self-heating if it is appropriately controlled, but plasmas in general have high thermal conductance, readily losing their stored energy if it is not well confined or replaced by an external heat source. Decades of experiments have shown that tokamaks are the most efficient magnetic confinement fusion (MCF) devices, using a combination of strong toroidal and poloidal magnetic fields (TF and PF respectively, Figure 1.1a) to stably confine a plasma away from the walls of a toroidal vessel.

Since the inception of the tokamak in 1950 [24], tokamak technologies have progressed towards the conditions where the energy from the emitted alpha particles is sufficient to nearly sustain fusion reactions. This progress can be evaluated by comparison with the Lawson criterion which equates the alpha particle heating power with the rate of energy loss from the plasma [5], [25]:

$$ (p\tau_E)_{exp} = \frac{24}{E_\alpha}\frac{\langle T\rangle^2}{\langle\sigma v\rangle_{DT}}\left(\frac{Q}{Q+5}\right) \tag{2-2} $$

where p [atm] and τ_E [s] are the measured tokamak plasma pressure and energy confinement time respectively, E_α is the energy of the alpha particle emitted from fusion reactions (3.5 MeV), $\langle T\rangle$ [K] is the average plasma temperature, $\langle\sigma v\rangle_{DT}$ [barns] is the average reaction cross section for a deuterium-tritium plasma of temperature $\langle T \rangle$ accounting for the plasma particle's Maxwellian velocity distribution [26] and Q is the ratio of fusion power released by DT reactions to any external heating power required to maintain p and τ_E. Once $Q = \infty$ the plasma is said to be 'ignited' and is generating sufficient alpha particles to be self-heating. Progress towards achieving reactor relevant conditions in tokamaks is shown in Figure 2.1. Although $Q = \infty$ is an ideal goal for a fusion power reactor, $Q > 15 - 100$ is the typical requirement of most TPP concepts [14], [27]–[29].

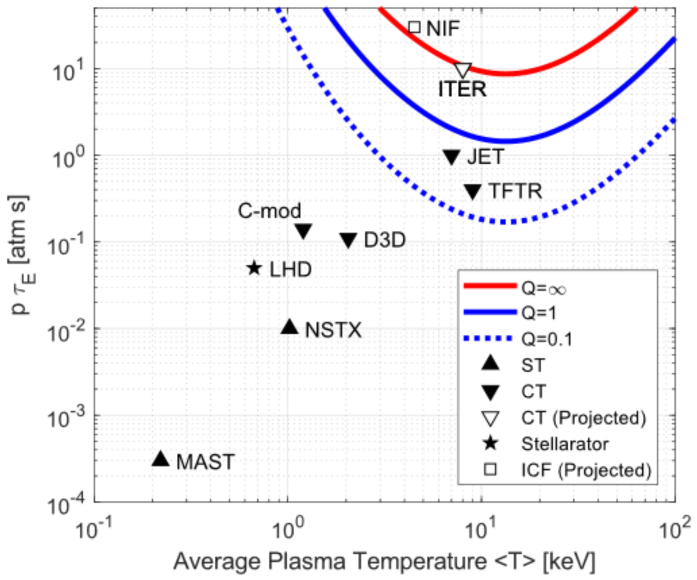

Figure 2.1: Achieved performance of several fusion devices with respect to the ignition criterion in the ($p\tau_E$,T) plane. The expected performances of ITER and NIF are included. Acronyms in the legend are ST: Spherical Tokamak; CT: Conventional Tokamak; ICF: Inertial Confinement Fusion. Reproduced using data from [30].

2.1.1 Towards a Tokamak Power Plant

Making the step from current devices to TPPs is the subject of continued debate (e.g. [31]–[33]). The focus of the optimistic part of this debate are the issues of whether the development of a fusion reactor can be somehow accelerated with respect to the European Roadmap to Fusion energy [7] and how to make TPPs smaller and cheaper to build. The basis for this debate can be illustrated using the following expression from Petty et al. [34]:

$$(p\tau_E)_{exp} \propto B_t^3 a^{2.5} \tag{2-3}$$

where B_t [T] and a [m] are defined in Figure 1.1a. Based on equation 2-3, increasing either B_t or a can lead to better plasma performance. Experiments have shown that p must be limited for a given B_t to avoid destructive loss of the plasma, but this limit can be significantly raised by reducing the aspect ratio (A) [29]. Table 2-1 summarizes 4 devices that are billed as next step devices after the Joint European Torus (JET). The ITER & DEMO tokamaks aim to achieve TPP relevant conditions by increasing both size and magnetic field [35] whilst the ARC reactor aims to achieve a similar goal by increasing the operating field without a size increase [27], which requires the use of superconducting materials to generate very high fields. Although not a TPP, Tokamak Energy's (TE) ST135 concept aims to achieve modest fusion power gains in a smaller device using the benefits of low aspect ratio and high field superconductors (HTS) [11]. There are several material classes with high upper critical fields, as discussed below, often loosely described as high temperature superconductors (HTS).

Table 2-1: Comparison of 4 proposed future devices with JET. Symbols: R_0 – Major radius; a – Minor Radius; A – aspect ratio; B_t: Toroidal Field strength at R_0; Q_{fus}: Fusion Power gain; P_{fus}: Fusion Power produced. LTS/HTS: low/high temperature superconductors.

Tokamak	**JET** [36]	**ITER** [36]	**DEMO** [37]	**ARC** [27]	**ST135** [38], [39]
R_0 [m]	2.96	6.2	9.1	3.3	1.35
a [m]	1.25	2	2.9	1.13	0.75
A	2.4	3.1	3.1	3	1.8
B_T [T] at R_0	3.45	5.3	5.7	9.2	3.7
Q_{fus}	0.55*	10	10	15	5
P_{fus} [MW]	Na	500	≈2000	525	180
TF coil material	Copper	LTS	LTS/HTS	HTS	HTS
***: Achieved**					

2.1.2 Fusion Neutrons to Toroidal Field Magnets

It has been recognised that degradation of the superconductor in the TF magnet due to neutron irradiation is a key failure mode limiting the lifetime of TPPs [40]. The DT fusion reaction emits neutrons at 14.1MeV but, due to the relative movement of plasma particles and second order effects, the distribution of neutron energies is in the range 11-19MeV [41]. The combined spectra escape the plasma in all directions to interact with the tokamak, travelling through various components before they reach the TF coil. Typically, these include the plasma facing components, neutron shielding materials and the wall of the plasma vacuum vessel.

Subject to a sufficiently detailed design being created for a TPP concept, calculating the neutron flux to the TF coil requires the use of Monte Carlo N-particle (MCNP) code [42]. Depending on the TPPs chosen layout, these calculations often find two problematic areas for the TF coil: 1) in the plasma-side superconducting layer of the central column magnet at the tokamak's vertical midplane as this volume is typically closest to the plasma and 2) in the coil volumes adjacent to a divertor as these regions tend to be less well shielded. The results of an MCNP calculation for the EuroFusion DEMO TPP are shown in Figure 2.2 [16] which illustrates which TF coil volume is subject to the highest neutron flux depends on the layout of the tokamak's poloidal magnets (Figure 2.2a) and the breeder blanket technology used. Of these regions, the performance of the toroidal inner midplane of the coil (marked 11, Figure 2.2) tends to be most limiting as it also is subjected to the largest mechanical stresses and the strongest magnetic field. Therefore, it is the design of this section[2] that determines the working life of the TPP TF magnet. The neutron spectrum at the inner midplane of the TF coil has been calculated for several TPPs [39], [43], [44] and is discussed more in chapter 4.

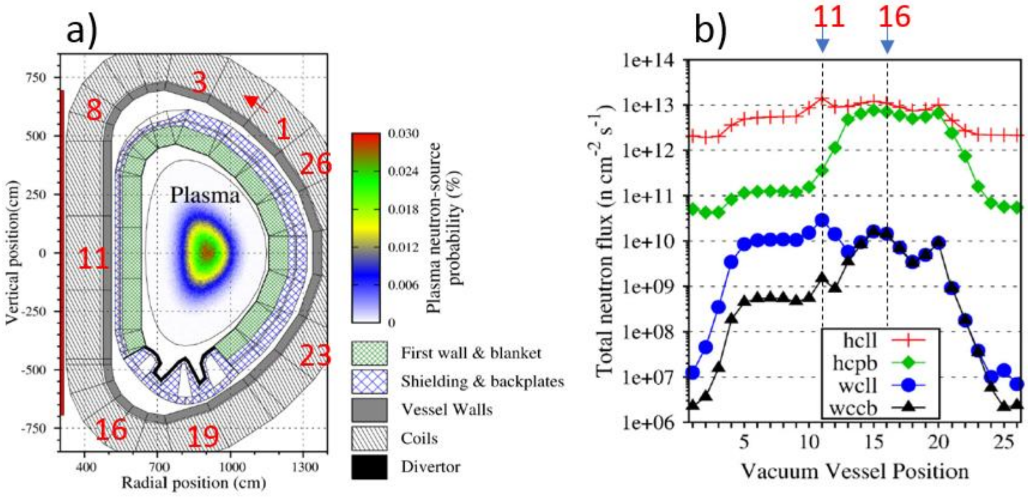

Figure 2.2: 2D poloidal slice through the neutronics model of the conceptual design for the DEMO TPP (version: 2015/16), showing the layout of key components and the likely location of the neutron source, peaked at R_0. Right: Total flux predicted for the vacuum vessel wall of the four different concepts (hcll: helium-cooled, liquid LiPb blanket; hcpb: helium-cooled, Li+Be pebble blanket; wcll: water-cooled, liquid LiPb blanket; wccb: water-cooled, Li+Be ceramic breeder blanket). The numbering of each vacuum vessel cell given in the plot (right) refers to the numbers in the schematic of the model (left, in red). Positions 11 (adjacent to inner midplane TF coil) and 16 (peak neutron flux through divertor region) are highlighted. Modified from Gilbert et al. [16].

2.2 Superconductivity in REBCO

1986 and 1987 were exciting years for research into superconductivity. At the start of this period, the empirical search for new superconducting materials was at the forefront of superconductivity research [45] with Nb_3Ge holding the record of $T_{c0} \approx 23$ K [46]. By the end, however, the work of Bednorz and Miller [45], Chu et al. [47], Wu et al. [48] and Hinks et al. [49] culminated in the demonstration of superconductivity in the cuprate superconductor $Yba_2Cu_3O_{\delta\approx6.9\text{-}7}$ (YBCO) with $T_{c0} \approx$ 93 K [49] and B_{c2}(0 K)≈80-180 T [48], [50]. This was particularly astonishing as YBCO was a ceramic, prepared using 3 non-superconducting oxides [51] (Y_2O_3, BaO, CuO_2) and its discovery started researchers investigating superconductivity in other complex compounds. Notable complex compounds found to exhibit superconductivity at relatively high temperature and field included the rare-earth free cuprate $Bi_2Sr_2Ca_2Cu_3O_x$ (BSSCO-2223) with T_{c0}=105K [52] and B_{c2}(0 K)≈200 T [50], MgB_2 with $T_{c0} \approx$39 K [53] with B_{c2}(0 K) > 30 T[3] [54] and, more recently, iron-based superconductors such as Fe(Se,Te) which, despite having $T_{c0} \approx$15 K, has B_{c2}(0 K) ≈ 50 T [55]. Of these, several companies have enjoyed success producing wires from REBCO (see Table 2-4 and Figure 2.12), hence

---

[2] Assuming it cannot somehow be replaced

[3] if appropriately doped and prepared as a thin film

it is the material of choice for several future TPP concepts (e.g. ARC [27] and TE's STE1 [56]) and the subject of this thesis.

In this section, the phenomenon of superconductivity is described in general as it applies to REBCO superconductors. This is followed by a description of the microstructure and superconducting properties of REBCO materials and what these methods have revealed about the use of REBCO in superconducting wires.

2.2.1 Superconductivity in general

2.2.1.1 Phenomenon

The term 'Superconductivity' was coined to describe the state exhibited by various metallic elements when their resistivity effectively dropped to zero and they became perfectly diamagnetic below a critical temperature (T_c) (Figure 2.3a&b) [57], [58]:

$$\boldsymbol{M} = \chi \boldsymbol{H}_{\boldsymbol{app}} \qquad \text{where} \qquad \chi = \begin{cases} \approx 10^{-5} & T > T_c \\ -1 & T < T_c \end{cases} \tag{2-4}$$

Where **M** [A/m] is the magnetisation per unit volume, χ the susceptibility and $\boldsymbol{H}_{\boldsymbol{app}}$ [A/m] the applied magnetising field. This occurs because, below T_c, screening currents are spontaneously set up that encircle the superconducting volume, diverting magnetic flux around its boundary. For a given T $(< T_c)$, this effect was found to persist until a critical 'maximum' field ($B_c = \mu_0 H_c$ where B is the applied magnetic field) is exceeded [59], occurring whether the sample was first cooled, then the field applied or vice versa [60], [61] and was accompanied by a step change in the specific heat (Figure 2.3c), implying that superconductivity in a material represented a shift to a more favourable thermodynamic energy state [62].

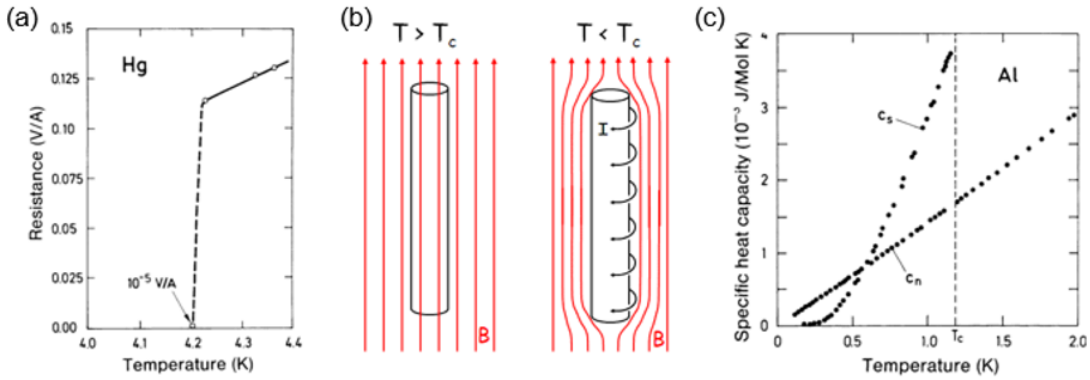

Figure 2.3: Superconducting Phenomenon. (a) Results of Onnes et al.'s 1911 experiment during his cooling of mercury (Hg) with liquid helium [58]. *At ≈ 4.2 K, the resistance of mercury dropped to a very low value. (b) Illustration of the Meissner-Ochsenfeld Effect. Flux can penetrate a sample above T_c but below T_c the sample transitions to a superconducting state and screening currents are generated in the material leading to the complete expulsion of the applied field, characteristic of type I superconductivity. (c) Results of Phillips et al. showing a step change in specific heat capacity with temperature of aluminium when in the superconducting state (c_s) compared to its normal state (c_n). The normal state experiment was performed at low magnetic field to supress the superconducting transition. Reproduced from* [57], [61]–[63].

Several attempts to theoretically describe the phenomenon of superconductivity from first principles have been documented, with notable works including those of the London brothers [64], Ginzburg and Landau (GL) in 1950 [65] and Abrikosov in 1952 [66], [67]. These were brought together by Bardeen, Cooper and Schrieffer (BCS) in 1956 with a quantum mechanical description of superconductivity, identifying that it was caused by the correlation of pairs of electrons[4] via lattice-phonon interactions [68]. In these works, two important decay lengths associated with superconductivity were defined: the penetration depth (λ_L [m]) and the intrinsic coherence length (ξ_0 [m]). The penetration depth related to how the external magnetic field exponentially decays to zero with distance inside a superconducting volume. The coherence length relates to how the density of Cooper pairs[5] rises to its equilibrium level with distance into a superconducting volume. The ratio of these length scales ($\kappa = \lambda/\xi$) determines whether minimising (type I, $\kappa < 1/\sqrt{2}$, Figure 2.4a) or maximising (type II, $\kappa > 1/\sqrt{2}$, Figure 2.4d) the area of the normal-to-superconductor boundary within the sample is thermodynamically favourable [69]. λ_L and ξ_0 both vary with temperature with the same dependence – $\sqrt{T_c/(T_c - T)}$ – hence κ is independent of T [65]. The consequences of varying κ are shown in Figure 2.4b&e where either all magnetic flux is expelled from the material (type I) or as many phase boundaries as possible are created. These take the form of cylinders of normal state material of diameter ≈2ξ and lie parallel to an applied field along which flux can flow (fluxons). The number of these normal regions is determined by the requirement that each carries a single quantum of flux ($\Phi_0 = 2.07\text{x}10^{-15}$ Wb) [70]. The typical magnetisation behaviours for type I and II superconductors are shown in Figure 2.4c&f. Type I superconductors only have a thermodynamic critical field where $\chi = -1$ for $0 < B < B_c$ but type II materials have both lower and upper critical fields (B_{c1}, B_{c2}). Ginzburg and Landau showed that [61]:

$$B_c = \frac{\Phi_0}{2\sqrt{2}\pi\lambda\xi} \qquad B_{c1} = \frac{B_c \ln\kappa}{\kappa\sqrt{2}} \qquad B_{c2} = \sqrt{2}\kappa B_c = \frac{\Phi_0}{2\pi\xi^2} \tag{2-5}$$

These definitions give rise to a theoretical maximum achievable supercurrent for the superconductor, defined as when its Cooper pairs naturally decouple due to an abundance of available kinetic energy, known as the GL depairing current density (J_d [A/m^2]) [71]:

$$J_d = \frac{\Phi_0}{3\sqrt{3}\pi\mu_0\lambda^2\xi} \tag{2-6}$$

The arrangement of fluxons in a pristine type II superconductor varies with B. Below B_{c1} no flux penetrates the superconductor (Meissner state, Figure 2.5). As B increases above $B_{c1}(T)$, fluxons start to enter the superconductor from the external surfaces (the mixed state, Figure 2.5). Each

---

[4] Known colloquially as Cooper pairs

[5] Also known as the superconducting order parameter

fluxon is encircled with screening currents and these interact to repel each other, resulting in the fluxons arranging into a hexagonal lattice[6] with nearest neighbour spacing [72]:

$$d = \left[2\,\Phi_0/\sqrt{3}B\right]^{\frac{1}{2}} \tag{2-7}$$

As $B \rightarrow B_{c2}$, $d \rightarrow 2\xi$ and leads to the superconducting state breaking down [61].

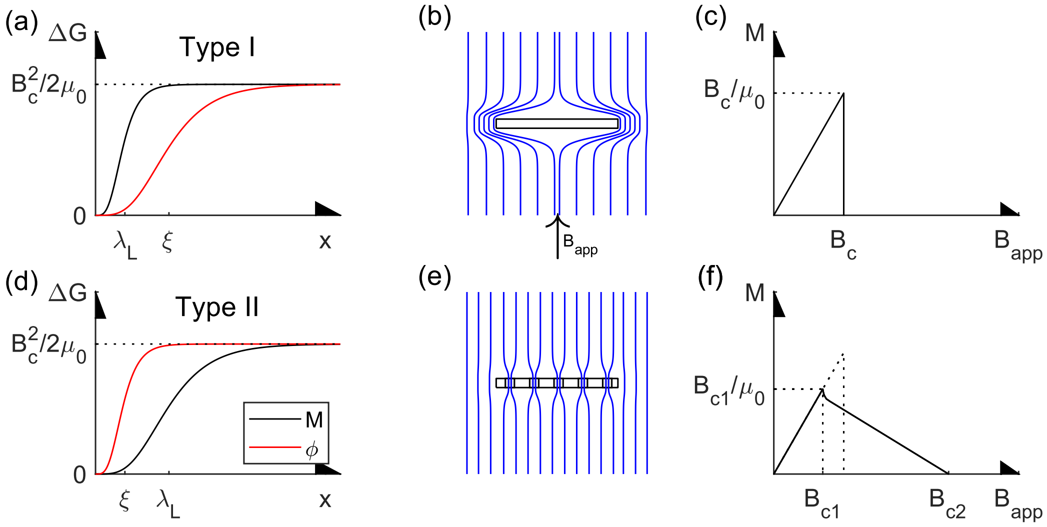

Figure 2.4: An illustration of the difference between type I (a, b, c) and type II (d, e, f) superconductivity. (a, d) the change in Gibbs free energy of due to the magnetisation 'M' and the order parameter (ϕ) with distance from a normal-superconducting material interface (x). (b, e) The effect of an applied field (B_{app}) on a superconductor showing volumes of superconducting (white) and normal (grey) state material. (c, f) the effect of varying B_{app} in each type of superconductor.

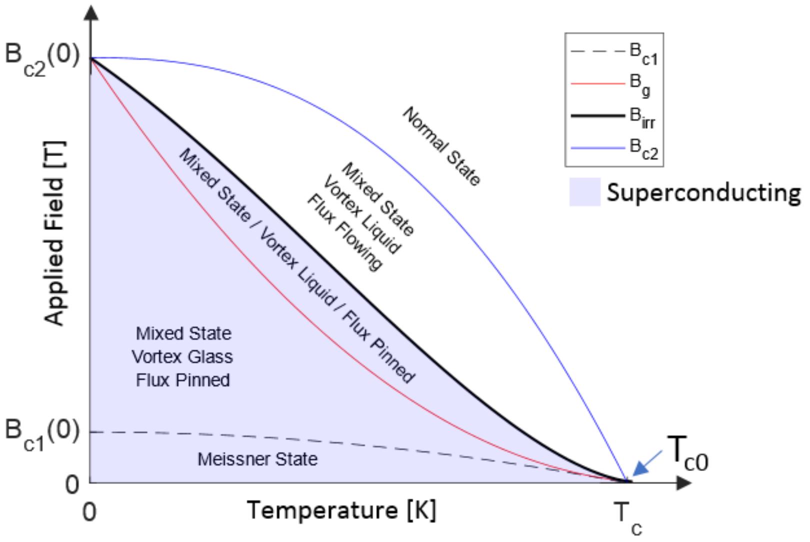

Figure 2.5: Superconducting phase diagram for a hard superconductor carrying zero current. Reproduced with reference to [73]–[76].

---

[6] Known as an Abrikosov lattice

2.2.1.2 Flux Pinning

In the previous section, the mixed state of a pristine superconductor is described, however, real superconductors, like all materials contain defects. The presence of defects in superconductors has 2 effects: firstly, it modifies the effective penetration depth ($\lambda_L \rightarrow \lambda$) and the extrinsic coherence length ($\xi_0 \rightarrow \xi$) by reducing the mean free path of electron scattering (l_e [m]) within the superconductor volume. The decay lengths of these new 'dirty' superconductors in the limit $l_e \ll \xi_0$, are [61], [77], [78]:

$$\lambda = \lambda_L\sqrt{\left(\frac{\xi_0}{l_e}\right)} \qquad \text{and} \qquad \xi = \sqrt{\xi_0 l_e} \tag{2-8}$$

Hence, decreasing l_e by adding defects significantly raises λ and lowers ξ leading to a more effective (higher κ) type II superconductor. Secondly, it results in fluxons not following straight line paths parallel to the applied field. This is because defects in superconductors either have poorer properties than the pristine material (i.e. lower κ) or they cannot support a superconducting state at all [72], [79]. As such, it becomes thermodynamically favourable for fluxons to flow through these defective regions of the material as this maximises the superconducting volume. The thermodynamic energy well this creates therefore forms an energy barrier preventing the movement of fluxons, resulting in them being pinned in place [80] with the restoring 'pinning' force proportional to the depth of the energy well.

The practically important consequence of flux pinning manifests when a current is applied. In defect free superconductors, fluxons would move due to the Lorentz force created by the interaction between each fluxon and the applied current. This force leads to fluxon movement and the generation of an electric field opposing the flow of applied current. With fluxons pinned, however, the superconductor can carry a supercurrent up to a maximum current density (J_c) limited by the depth of the energy well pinning defects in place. Once the supercurrent increases above this maximum, however, fluxons will start to move and, although the superconductor is still in a superconducting state from a thermodynamic point-of-view, a flux flow resistance can be measured which increases with current. This has led many to accept a criterion defining the current at which a superconductor effectively becomes non-superconducting [81], [82]. A commonly used criterion is that $J = J_c$ when the flux flow resistance has an effective critical electric field (E_c) = 1 µV/cm [83]–[85], as this leads to a reasonably small amount of power dissipation in the superconducting material. As such, the location of a superconductor's critical surface – $J_c(B,T)$ – now depends not only on the quality of the pristine superconducting material but also the number density, size and type of pinning defects it contains relative to the distance between fluxons introduced by the applied field ($\propto B$), the distance they can be displaced due to thermal fluctuations ($\propto T$) and/or the

Lorentz forces acting to unpin them due to current flowing in the superconductor ($\propto J$). For practical superconductors, all of which are type II, the defect size and spacing with respect to the ξ value is particularly important. Line, surface and volume defects with reduced superconducting properties with 1, 2 or 3 dimensions > ξ can lead to 1-, 2- and 3-dimensional pinning and can exert relatively strong pinning forces on fluxons. Point defects are defined as having all dimensions $< \xi$ and are weaker pinning centres but their proximity to each other can allow them to act collectively to effectively pin fluxons [80].

Finally, the rigidity of a pinned fluxon lattice means that, when $\boldsymbol{H_{app}}$ changes to a new value, the sample is not initially in its equilibrium state. The new equilibrium distribution of fluxons takes time to establish with their movement velocity determined by the available thermal energy and the pinning landscape. The change in $\boldsymbol{H_{app}}$ also leads to the induction of supercurrents in the superconductor proportional to the rate of change of $\boldsymbol{H_{app}}$. As the fluxon lattice relaxes towards its equilibrium state, the moving fluxons interact with the induced supercurrent, generating a flux flow resistance. This process is known as flux creep [86] or flux jumps [87] depending on whether it occurs over long or short time scales respectively, and is characterised by drop in the magnitude of the induced supercurrent.

2.2.1.3 Intergranular Weak Links

So far the discussion has considered uniform or single crystalline superconductors, but it has been shown that the presence of grain boundaries can lead to significant reductions in achievable J_c [88]. This is particularly true for superconductors with a short coherence length, such as REBCO, as this means that even the smallest imperfections in the crystal impede the flow of supercurrent [71].

The size limiting mechanism for these imperfections is described by the proximity Josephson effect [89]. This effect is due to paired electrons in superconducting materials remaining coupled across a barrier material (N, Figure 2.6a) due to quantum mechanical tunnelling. The density of supercurrent carrying electrons was found to decrease exponentially, with length scale $\approx$ ξ, inside the barrier material. Therefore, if the width of the barrier between superconducting materials is sufficiently thin (ie $L \leq \xi$, Figure 2.6b), the supercurrent can cross the normal barrier without dissipation [90]. If the normal region is too wide, the superconducting current flow is suppressed, and the junction is known as a weak link.

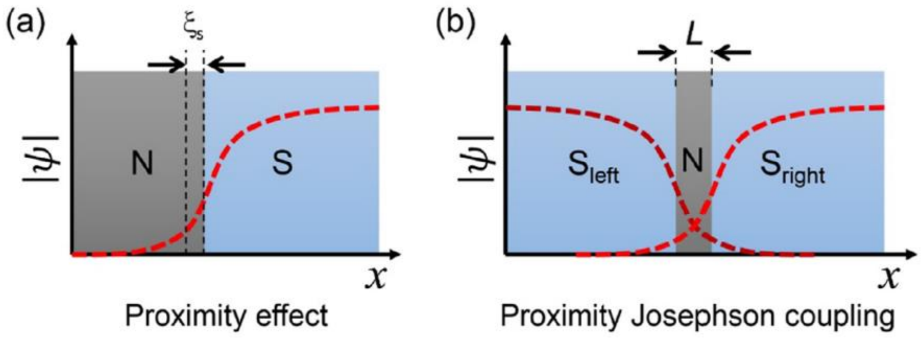

Figure 2.6: a) The superconducting order parameter $|\Psi|$ of a superconductor (S) penetrating a distance (x) into the normal metal (N) with a length scale of the superconducting coherence length, ξ_s. (b) Order parameters from two superconducting materials separated by normal materials (e.g. a grain boundary) overlap, producing a proximity Josephson coupling [90].

This type of proximity junction, known as a superconductor-normal-metal-superconductor (SNS) junction, is present at grain boundaries in polycrystalline samples of superconductors like REBCO with small ξ. Much of the drive in creating practical HTS devices has, therefore, been in trying to harness this effect for practical electronic or sensing purposes (e.g. [91]), or eliminate or reduce the density of wide (i.e. $L \geq \xi$) grain boundaries for high current applications. This is typically achieved in HTS bulks using top-seeded growth processes to produce samples that are dense monocrystals that are free of cracks and voids (e.g. [92]). In HTS wires, grain boundaries that are not weak linked can be achieved by aligning the grains to within a few degrees (<3°) throughout a thin film. This type of processing – known as texturing – can be produced by the deposition of the superconducting material on a substrate specifically chosen to promote epitaxial grain growth (e.g. [93]) and is commonly used in the manufacturing of modern REBCO CCs, expanded on in section 2.2.2.4.

2.2.2 REBCO Properties

In this section, REBCO's structure is introduced, followed by a discussion of its unit cell, its crystallinity, the effects of doping and its diffusion properties. This leads on to a description of how these findings have influenced the manufacturing of commercial REBCO coated conductors (CC) and their resulting superconducting properties.

2.2.2.1 Unit Cell

All cuprate superconductors have a structure consisting of alternating conduction and binding layers. The conduction layer consists of 2 planes of CuO_2 molecules, held together in REBCO by the rare-earth element, and it is the electrons released by these copper ions that conduct current when $T>T_c$ and form cooper pairs to conduct supercurrents when $T<T_c$. The binding layers that link the conduction layers in REBCO take the form BaO-CuO-BaO, giving REBCO its triple perovskite unit cell (Figure 2.7a). In the structure of high T_c REBCO, the binding layer copper (Cu^{2+}) and its bonded

oxygens form in a chain parallel to REBCO's b-axis direction and are therefore known as chain sites whilst the conduction layer copper (Cu^{3+}) and its bonded oxygens are known as plane sites [61], [71].

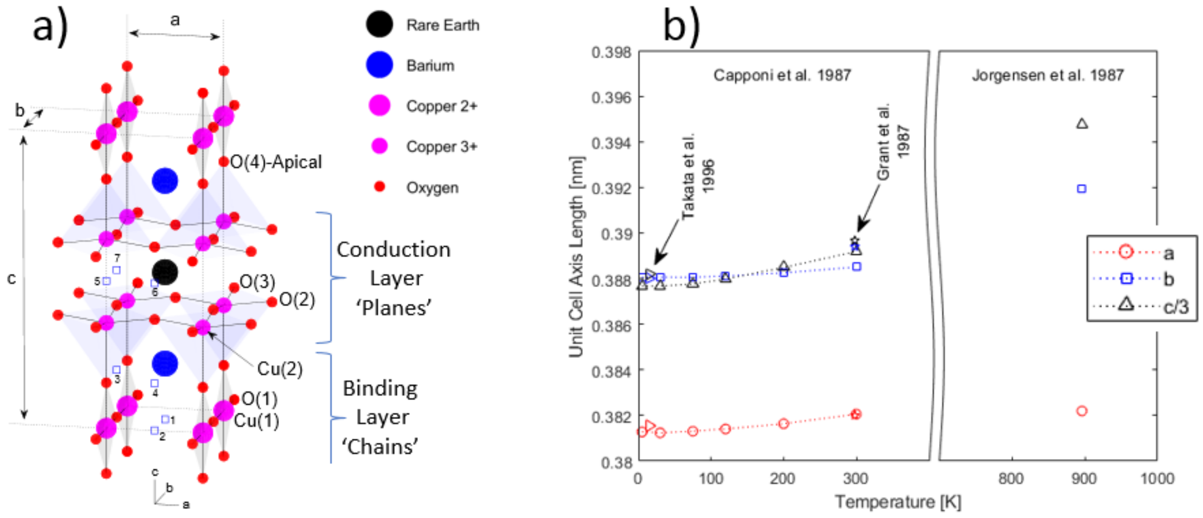

Figure 2.7: a) REBCO unit cell showing the Conduction layer (plane sites) – Cu(2) & O(2,3) – and the Binding layer (chain site) – Cu(1) & O(1) atoms. The unit cell is symmetric in the (a,b)-plane about the central rare-earth element. Each coloured sphere represents a different atom types (see the key, top right). a, b & c dimensions refer the unit cell dimensions (shown in figure b) and Table 2-2). Each labelled atom is at a unique unit cell positions. Each of the numbered '□' denotes an available vacancy site. Reproduced with data from [94]*; b) How YBCO unit cell dimensions (y-axis) varies with temperature (x-axis), using data from* [94]–[97], [49].

Extensive studies of the $YBa_2Cu_3O_\delta$ (YBCO) unit cell were performed by Capponi et al. [95], Jorgensen et al. [98] and Cava et al. [99] correlating neutron powder diffraction (NPD) and x-ray diffraction (XRD) data at varying temperatures with superconducting property measurements. These confirmed that the unit cell of the high T_c YBCO phase is orthorhombic with $\delta \rightarrow 7$ (Figure 2.8a) and that the lattice parameters vary with temperature [94], [97]–[101] (Figure 2.7b). Precise determination of the atom locations inside the unit cell showed that, with $\delta = 7$, YBCO has ordered one-dimensional Cu(1)-O(1) chains running parallel to the b-axis, and that as δ decreases to 6.4 the oxygen sites between Cu(1) sites along the a-axis begin to empty, eventually leading to $T_c \rightarrow 0$ K (Figure 2.8a). This has been shown to correlate with the decreasing summed bond strengths of Cu(2) with its neighbouring oxygens (Figure 2.8b), and implies that significant charge transfer is occurring through the apical oxygen site O(4) between the CuO chains – which act as charge reservoirs – and the CuO_2 planes where the supercurrent carrying electron pairs reside. The CuO_2 planes are charge deficient (also known as hole doped) [98] as δ increases above 6.4. The mechanism of hole doping in the CuO_2 planes has been recognised as an important parameter determining T_c in all cuprate superconductors [102], with T_c of YBCO reaching a maximum when the hole doping is equivalent to ≈0.16 holes per Cu(2) ion, equivalent to $\delta \approx 6.93$ [71].

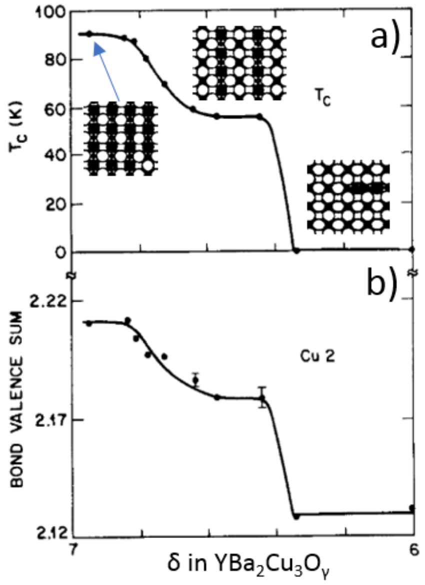

Figure 2.8: Comparison of T_c (a) and bond valence sum around the plane copper (b) as a function of oxygen stoichiometry 'δ' [99]. *insets: YBCO Cu-O chain structure for varying δ from* [103].

2.2.2.2 Effects of Crystallinity

Regardless of δ, slow cooling is required to produce REBCO with high T_c. This was shown by Schuller et al. who used high temperature XRD to show that $YBa_2Cu_3O_y$ has two stable, cuboid microstructures: the non-superconducting tetragonal phase above 750 °C and the superconducting orthorhombic phase $YBa_2Cu_3O_7$ below 700 °C. To form $YBa_2Cu_3O_7$, slow cooling is required as rapid cooling leads to the tetragonal phase being quenched-in [104]. A consequence of this slow cooling and its subsequent orthorhombicity is that REBCO single crystals (and each grain in a polycrystalline sample) contain a multitude of (110) twin boundaries, formed to relieve stress build up during the transition from the high temperature tetragonal to lower temperature orthorhombic structure [105] with a near 90° inter-grain angle [106] (Figure 2.9a). Comparing twinned with un-twinned REBCO has shown that, whilst twinning has little effect on T_{c0} and the irreversibility line (B_{irr}, Figure 2.5), removing twin boundaries decreases the current carrying capacity of a REBCO single crystal as twin boundaries act as effective 2D flux pinning sites when the field is parallel to the c-axis [107].

As a result of the triple perovskite unit cell, REBCO has anisotropic superconducting properties with two principal directions; parallel and perpendicular to the (a, b) plane. This anisotropy can be primarily characterised through measurement of λ and ξ, whose values are typically reported at 0 K given their dependence on temperature:

- $\lambda_{ab}(0) \approx 130 - 150$ nm [108], [109]
- $\lambda_c(0) \approx 450 - 700$ nm [108], [110], [109]
- $\xi_{ab}(0) \approx 1.4 - 2$ nm [111], [112], [113], [114]
- $\xi_c(0) \approx 0.2 - 0.4$ nm [112], [113], [115], [114]

The small ξ_{ab} and ξ_c values make REBCO a high κ superconductor but lead to several practical issues. Firstly, as the spacing between each pair of CuO_2 planes (Figure 2.7a, 0.834nm) is $> \xi_c$, each plane is effectively an isolated superconducting layer, being only weakly coupled through the Josephson proximity effect to the layers on either side [61]. As a result, supercurrent flow perpendicular to the (a, b) plane is reduced, with $J_{c\parallel(a,b)} \cong 30 - 100 \times J_{c\parallel c}$ [116]–[118] and therefore all practical CCs have their REBCO layer orientated so that supercurrent can flow as much as possible along the (a, b) plane (i.e. $J_c \equiv J_c^{ab}$).

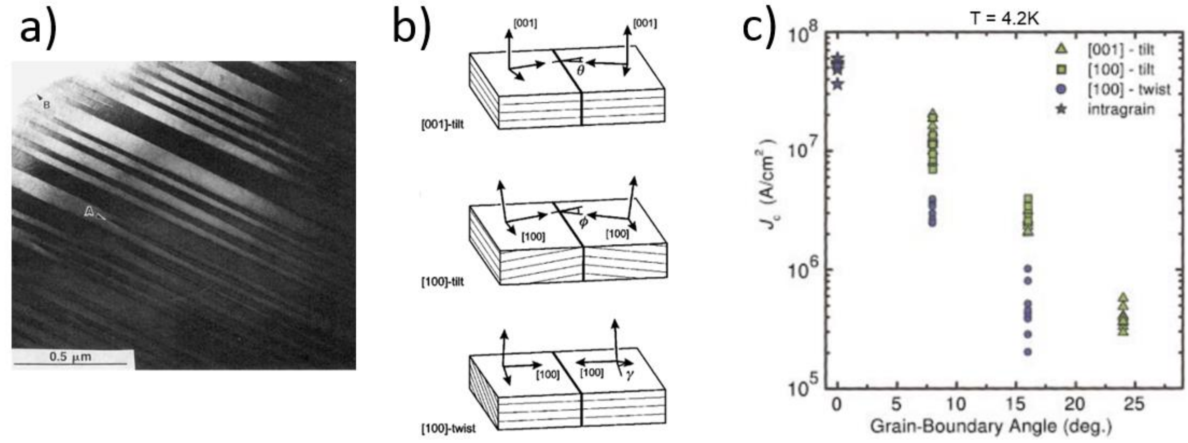

Figure 2.9: a) twin structure of a GdBCO thin foil observed along [001] axis. A: included lenticular twin and B: absence of twins at foil's thin edge. Reproduced from [119]. *b) Schematic diagram showing the crystallography of a [001]-tilt boundary (top), a [100]-tilt boundary (middle), and a [100]- twist boundary (bottom) in REBCO* [120]. *c) How the critical current density at 4.2K of REBCO films (y-axis) with the different types of small-angle grain boundary misorientation decreases exponentially with increase misorientation angle (x-axis)* [120].

Secondly, the small ξ_{ab} value effects how supercurrents flow across non-superconducting regions such as grain boundaries. Supercurrent carrying electron pairs can only efficiently traverse normal state volumes via the Josephson proximity effect if their total width is $\lesssim \xi_{ab}$ [121], and grain boundary widths in REBCO are of the order of ξ_{ab} [91]. Dimos et al. and Hilgenkamp et al. showed that the achievable J_c of a polycrystalline REBCO films decreases exponentially with grain angle misalignment up to 25° [120] (Figure 2.9b&c) whilst Halbritter shows it also decreases exponentially with grain boundary width with a decay constant of ≈ 7nm [122].

2.2.2.3 REBCO doping

Given that bond lengths and unit cell parameters have such a strong effect on the superconducting properties of YBCO, related compounds with different compositions have been extensively investigated. These compositional changes tend to involve substituting one or more of the elements in YBCO fully or partially for another in a similar position on the periodic table. These experiments found that replacing the copper or barium only harmed the superconducting properties [123]–[132]. Substitution of the rare earth (RE) has been extensively studied due to its effect on the cost vs performance of superconducting wires. One particularly thorough study on 13 optimised REBCO thin films was performed by Zhang et al. [133]. The results are shown in Figure 2.10 and in general agreement with previous studies [134]. Zhang et al. suggest that the optimum combination of RE elements for enhancing current carrying capacity depend on their operating temperature. These advantageous RE choices were Y or (Gd,Yb) for operation at 20K and various combinations of Eu, Y, Gd and Sm for 77K [91]. A review of the prices of raw material powders [135], [136] would suggest that Y or a (Sm, Y) mixture were popular choices at both high and low temperatures but, in practice Y, Gd, (Y, Gd) and, more recently, Eu, are commonly used to make REBCO CCs due to the high T_c values shown in Figure 2.10 [137]–[140]. The rest of this literature review therefore focuses on CCs using optimally doped REBCO containing either Y, Gd, Eu or combinations thereof. The properties of these 3 types of REBCO used throughout this work are shown in Table 2-2 and Table 2-3.

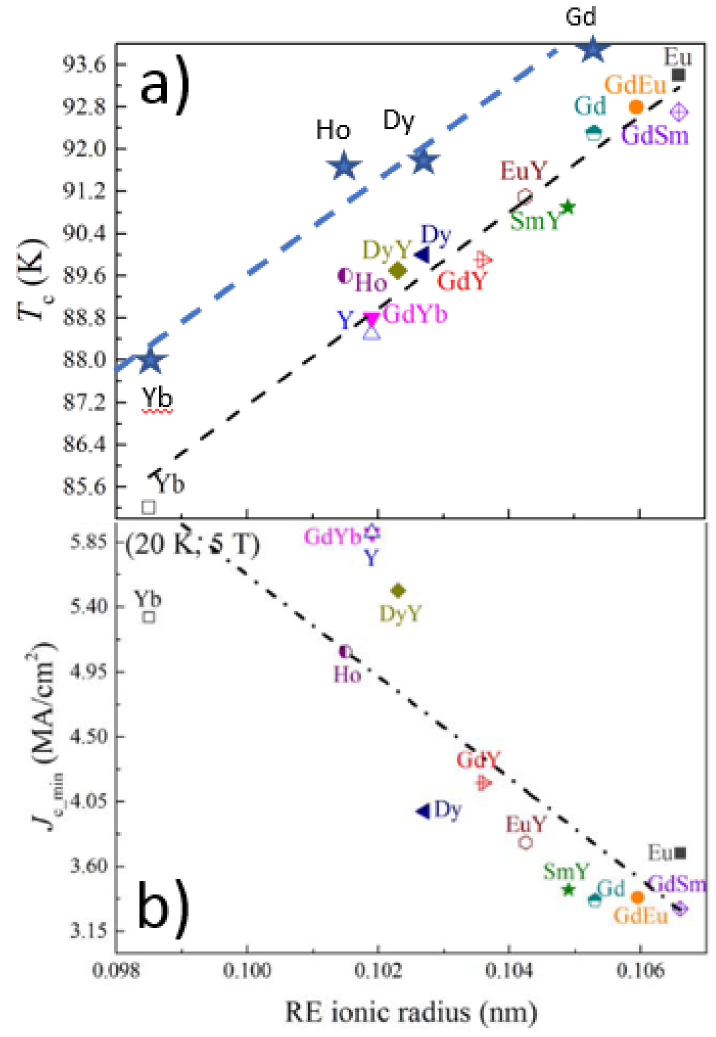

Figure 2.10: T_c (a) and J_c(20K, 5T) (b) versus average RE ionic radius (x-axis) for several textured REBCO films deposited on a MgO-buffered Hastelloy substrate by metal-organic chemical vapour deposition (MOCVD). Starred values are for polycrystalline samples. Reproduced with data from [133], [134].

Table 2-2: List of pristine REBCO Unit Cell dimensions (a, b, c), unit cell volume (V), REBCO number density (n_{REBCO}), molar mass (M) and mass density (ρ_{REBCO}) recorded at Room Temperature.

REBCO	**a [Å]**	**b [Å]**	**c [Å]**	**V [Å^3]**	**n_{REBCO} [10^{22} at/cm^3]**	**M [g/mol]**	**ρ_{REBCO} [g/cm^3]**
YBCO [51], [141]	3.8230	3.8857	11.680	173.5	7.493	666.19	6.376
GdBCO [51], [141]	3.8416	3.8984	11.707	175.3	7.416	734.54	6.958
EuBCO [142]	3.8440	3.9040	11.709	175.8	7.395	729.25	6.888

Table 2-3: Weight and Atomic Percentages of each atomic species in REBCO with δ=7.

%wt	**YBCO**	**GdBCO**	**EuBCO**	**%at**	**REBCO**
RE	13.34	21.52	20.84		7.69
Ba	41.22	37.34	37.66		15.38
Cu	28.62	25.92	26.14		23.08
O	16.81	15.23	15.36		53.85

2.2.2.4 Diffusion of oxygen in REBCO

As discussed above, ensuring that REBCO is fully oxygenated ($\delta \rightarrow 7$) is an important step in producing REBCO with a high T_c. This is typically achieved using a dedicated oxygenation step. Examples include the 3h anneal at 300 °C used by Eley et al. to reoxygenate there sample after irradiation [143] although higher temperatures are often used when manufacturing commercial coated conductors (see section 2.2.2.5). In this section, the diffusion of oxygen through the REBCO lattice is discussed.

Several authors have published work studying diffusion of oxygen in REBCO, which were succinctly reviewed by Vazquez-Navarro [144]. The main points of interest from this review were:

- that microstructural features such as porosity, grain size, twin density, grain orientation, sample surface area, impurity content and initial oxygen distribution can affect diffusion in REBCO.
- that the measured diffusion rate was orders of magnitude slower in the c-axis direction than in the (a, b) plane [145]. The likely cause was modelled by Ronay and Nordlander, suggesting that oxygen movement along the path V(2)-V(1)-V(2) (Figure 2.7b) had a near zero activation energy even at low temperatures whereas oxygen movement parallel to the c-axis required jumps like that from V(1)-V(3) which each had an activation energy of ≈ 1.7eV [146].
- that oxygen diffusion along grain boundaries was significantly faster than bulk diffusion through grains and that this difference is exacerbated if the sample is porous [147].
- that, in the temperature range 300-800 °C, most authors found that the dependence of the diffusion co-efficient on temperature follows the Arrhenius equation ($D =$

$D_0 \exp\{-E_a/kT\}$) without deviation, implying that the oxygen stoichiometry does not impact the rate of oxygen diffusion.

- that the lowest temperature studied up to 1998 was 300 °C, likely due to experiment time constraints. At this temperature, the measured diffusion co-efficient varied between 10^{-8} - 10^{-12} cm^2/s [103], [145], [148], declining rapidly with temperature with an activation energy (E_a) of the order of 1eV.

2.2.2.5 REBCO Coated Conductors

Given that REBCO is a brittle ceramic and has anisotropic superconducting properties, methods to economically manufacture high performance CCs are the subject of continual research by several companies. They are all aiming to produce dense, biaxially textured and chemically stable films of REBCO of the order of a micrometre thick with good stoichiometry and grain alignment controlled over long lengths. Some manufacturers also include controlled concentrations of precipitates uniformly dispersed through the REBCO to act as artificial flux pinning centres (APCs).

To achieve a stable superconducting layer with good grain alignment, REBCO is deposited as a thin film on a compatible textured substrate, assembled either on a nickel alloy [149] or stainless steel [137] base. These materials are chosen as they have low magnetic susceptibility [150], comparable thermal expansion to REBCO [51] and, given the response of a thin film of a brittle ceramic to applied strain [151], have a high Young's modulus [152], [153]. Before texturing, the substrate is often treated with layers of Alumina (Al_2O_3), Yttria (Y_2O_3) or Ceria (CeO_2)[7] to prevent cation and oxygen diffusion between substrate and superconductor, and to provide a pristine surface for the adhesion of the texturing layers [154], [155]. Texturing is achieved using one of two methods; on an untextured substrate by adding several buffer layers which build up to a textured surface (Figure 2.11a), or by inducing texture in the metal substrate itself and then adding fewer buffer layers (Figure 2.11b). The former can be achieved using Beam Assisted Deposition (BAD) whose subtypes include electron, ion or alternating (eBAD, IBAD or ABAD respectively) to build-up textured layers of MgO [156], [157] or yttria-stabilized-zirconia[8] (YSZ) [158] on the treated substrate [159]. The latter is achieved using a deformation texturing and recrystallisation process known as Rolling Assisted Biaxially Textured Substrate (RaBITs) [160]. Other compounds often included as buffer layers are $SrTiO_3$ [161], $LaAlO_3$ and $LaMnO_3$ as they have a compatible unit cell size and structure [51], allowing good alignment of the REBCO [100] or [110] direction with the substrate's cubic [100] or [110] directions [162], [163]. Finally, further layers are deposited – typically $SrTiO_3$, $LaMnO_3$ or CeO_2 - on

---

[7] Only used in conjunction with a YSZ over-layer [376].

[8] YSZ also can serve as a nickel and oxygen diffusion barrier [377]

the textured substrate as their dielectric properties, lattice constants and chemistry ensure a stable, chemically inert interface layer of low induced strain with the superconductor [159]. Both processes have been shown to achieve adequate REBCO layer texturing over tape lengths > 100m in both single sided [159], [160] and double-sided configurations [164]. Some manufacturers who use evaporative deposition methods to deposit buffer layers, however, also choose to offset the REBCO c-axis by rotating it up to $50°$ about the tape's longitudinal axis – known as Inclined Substrate Deposition (ISD) – as it has manufacturing speed benefits and can improve REBCO layer quality, especially if film thickness is > 2 µm [165].

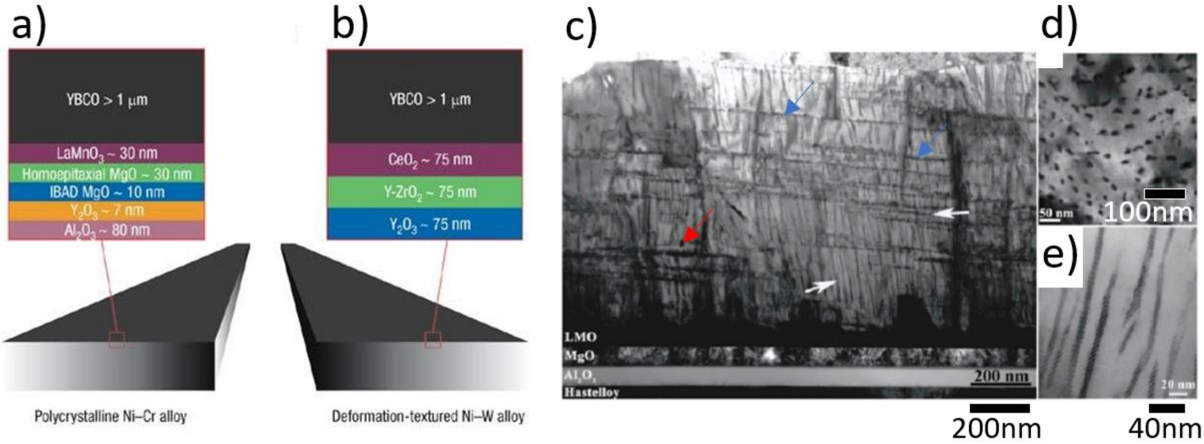

Figure 2.11: Coated Conductor architectures of (a) a polycrystalline Ni-alloy, coated used IBAD with layers to apply a texture to a YBCO layer laid down by MOCVD or PLD and (b) a Ni-alloy substrate with associated buffer layers, textured by the RABITs process and then the YBCO layer laid down using MOD-TFA [166]. *c) Transmission Electric Microscopy (TEM) bright field images of the microstructure of SuperPower CC from 2010. Image viewed along [100] direction showing buffer layers at the bottom and the resulting REBCO microstructure on top. Image shows that the first 1µm of the REBCO layer includes features such as nanorods (white arrows), small RE_2O_3 precipitates forming in line arrays on the (a, b) plane (red arrow) and stacking faults (blue arrows). d) same sample as c) but viewed along [001] direction. Black dots show where nanorods meet the exposed surface indicating their rough lateral dimensions (20-40nm) and spatial separation (≈50nm), both much larger than $\xi_{ab}(0)$. e) a magnified image of the nanorods viewed along [100] direction showing that there lateral dimensions and spatial separation and roughly consistent along the entire length of the nanorod.*

On to this textured substrate, the REBCO layer is deposited. The literature describes at least three common methods, listed in order of decreasing concentration of REBCO delivered to the substrate during manufacturing (also known as supersaturation):

- Pulsed Laser Deposition (PLD): PLD uses a bulk REBCO precursor of the required stoichiometry held ≈10 cm from the substrate. Its surface is then pulsed with a laser which sputters REBCO droplets from the surface, creating a plume that impinges on the substrate, leading to REBCO deposition [167]. The advantages of PLD are that its simple and versatile whilst providing a highly concentrated source of REBCO to the substrate leading to fine columnar grains [19]. PLD's disadvantages, however, are that it is slow, with deposition rates much above 3nm/s leading to reduced superconducting performance. This slow rate is often compensated for by passing a CC through the reaction chamber several times [168], [169].

- Reactive Co-evaporation – (Cyclic) Deposition and Reaction (RCE-(C)DR). Elemental Rare-Earth, barium and copper sources are pulse evaporated with an electron beam and feedback controlled to ensure the resultant plumes mix with the correct stoichiometry (≈1RE : 2Ba : 3Cu) before depositing on a heated substrate. This precursor then passes to a hot, oxygen rich atmosphere where oxidisation occurs, stabilising the REBCO layer [170]. To contrast this to PLD, the source of REBCO in RCE-CDR is not as concentrated, leading to a larger grain size [19].
- Chemical Solution Deposition (CSD): CSD-based methods have been investigated for REBCO production due to the high cost of PLD and RCE-(C)DR [171]. In one such technique, known as Metal Organic Deposition (MOD), a textured substrate is passed through a chemical bath that contains a REBCO precursor which is pyrolyzed and then converted to a REBCO film [172]. This process has been further developed to improve layer deposition rate by using a vaporised precursor to transport REBCO to the substrate, known as Metal Organic Chemical Vapor Deposition (MOCVD), which uses ultra violet irradiation to stably produce thicker REBCO layers [173]. More recently, transient liquid assisted growth (TLAG-CSD) methods have been developed to increase deposition rates up to 100nm/s without sacrificing properties [174], [175]. Like RCE-CDR, the source of REBCO using this process is less concentrated than that for PLD, resulting in a larger grain size [19].

Although these methods can all successfully deposit REBCO on a textured substrate, the resulting REBCO layer has diminished oxygen content and can be amorphous if the substrate was not heated during REBCO deposition. REBCO deposition is therefore typically performed at temperatures > 600-850 °C as it has been shown that in this temperature range REBCO can undergo an amorphous-to-crystalline transition without melting to its tetragonal phase [176]. Post hot deposition, epitaxially textured stoichiometric REBCO with an orthorhombic structure can be formed if the layer is held in an oxygen rich atmosphere and then slowly cooled through REBCO's orthorhombic-to-tetragonal (O2T) transition temperature (670 °C [94], [176]). Given that oxygen diffusion in REBCO is anisotropic and that most CCs align their c-axis with the tape normal direction, this key oxygenation step can be manufacturing rate limiting as it needs high temperatures for extended periods.

Once the superconducting layer is laid down, it needs protection from the environment as, although REBCO is stable when thermally cycled (±80°C) in vacuum [177], it is unstable in the presence of water[9] [178], [179] and will decompose upon heating above 400°C [180] to a material with no superconducting phase [99]. REBCO is also highly resistive once in its normal state, leading to issues caused during uncontrolled losses of its superconducting properties (quenching) [181]. Finishing of the wire therefore typically includes the deposition of a protective matrix of silver or gold [182] to stabilise the superconductor and protect it from the environment, and a copper layer to provide a surface of high electrical and thermal conductivity to protect the superconductor from heat spikes during soldering and provide some quench protection [183]. The result is known as a coated conductor (CC) and details of how several commercially available CCs are made is summarised in Table 2-4. For more information, the reader is directed to a recent review of REBCO CC manufacturing [19].

Table 2-4: Summary of HTS CC manufacturers, their chosen substrate and buffer laying topology and the REBCO deposition technologies utilised. Base table taken from Tsuchiya et al. [184] *and supplemented with information from the references given. Acronyms used here but not introduced elsewhere include bi: biaxially textured, rMS: reactive magnetron sputtering and rfMS: radio frequency magnetron sputtering.*

Manufacturer	Substrate	Buffers	Technology
AMSC [185]	Ni-5%wt W^t	Y_2O_3 / YSZ / CeO_2	RaBITS / MOD
Bruker [137], [186]	Stainless Steel	bi-YSZ / CeO_2	ABAD / PLD
Fujikura [140]	Hastelloy c276	Al_2O_3 / Y_2O_3 / IBAD-MgO / CeO_2	IBAD / PLD
SST [187]	Hastelloy c276	Al_2O_3 / Y_2O_3 / IBAD-MgO / $LaMnO_3$ / CeO_2	IBAD / PLD
Theva [188]	Hastelloy $c276^t$	ISD-MgO / MgO	RABiTS / ISD / eBAD
SuNAM [189]	Hastelloy c276	Al_2O_3 / Y_2O_3 / IBAD-MgO / MgO / $LaMnO_3$	IBAD / RCE-DR
SuperPower [154]	Hastelloy c276	Al_2O_3 / Y_2O_3 / IBAD-MgO / MgO / $LaMnO_3$	IBAD / rMS / MOCVD
STI [170]	Hastelloy c276	Y_2O_3 / IBAD-MgO / MgO	IBAD / RCE-CDR
SuperOx [190]	Hastelloy $c276^t$	Al_2O_3 / $LaMnO_3$ / IBAD-MgO / $LaMnO_3$ / CeO_2	RaBITS / rfMS / PLD
t: textured substrate used			

2.2.2.6 Properties of Commercial REBCO Coated Conductors

Due to the increasing availability of commercially available REBCO CCs, several authors have undertaken work designed to help users determine which CCs are most suitable for their application.

---

[9] Resulting in significant surface damage after only 10-15 minutes exposure [315]

One good example is the work of Strickland et al. from the Robinson Research Institute (RRI) whose REBCO CC properties database is universally available (Figure 2.12) [17], [83], [84].

This data has been used to illustrate the main properties of REBCO CCs. These include that REBCO CCs follow the theoretical predictions of Nelson et al. and Blatter et al. [191], [192] that vortex pinning in REBCO leads to the exponential decay of $J_c(T)$ proportional to T at constant field for weak pins (e.g. point defects) and proportional to T^2 for strong pins (e.g. defects with 1, 2 or 3 dimensions $\gg \xi_{ab}$):

$$J_c^{wk}(T) = J_c^{wk}(0)\exp\left\{-\frac{T}{T_0}\right\} \tag{2-9}$$

$$J_c^{str}(T) = J_c^{str}(0)\exp\left\{-3\left(\frac{T}{T^+}\right)^2\right\} \tag{2-10}$$

where $J_c^{wk}(0)$ and $J_c^{str}(0)$ (both [A/m^2]) are the contributions of weak and strong pinning centres to J_c at 0 K in the absence of creep respectively, and T_0 and T^+(both [K]) are the characteristic temperatures associated with the pinning energies of the weak and strong pinning centres respectively. This is illustrated in Figure 2.12a where sections of the data for each CC could be fit with straight lines to calculate $J_c^{str}(0)$ and T^+ for equation 2-10. Departures from this dependence illustrate the added contribution of weak pinning sites at the low temperature end increasing J_c and the presence of flux flow at the high temperature end [193] decreasing J_c.

The anisotropy of the REBCO unit cell and its effects on the critical current per cm width of tape (I_c/w), used as it is a REBCO layer thickness independent measure of a CCs properties, as a function of field direction (θ) are illustrated in Figure 2.12b. This anisotropy manifests as a significant increase in current carrying capacity when the field is aligned with the (a, b) plane (θ = 90°). This peak being offset from 90° (i.e. the CC rolling direction) indicates that the REBCO layer is inclined relative to the substrate (e.g. THEVA CC). This anisotropy is typically quantified using the mass anisotropy factor (γ_m) using the procedure of Civale et al. [194]. This relies on the Blatter scaling approach [195] which asserts that, if pinning is only due to random defects:

$$J_c(B,\theta) = J_c(\tilde{B}) \qquad \text{where} \qquad \tilde{B} = B[\cos^2\theta + \gamma_m^{-2}\sin^2\theta]^{1/2} \tag{2-11}$$

The procedure requires that $J_c(B,\theta)$ at constant T for various applied fields be adjusted with equation 2-11 using a constant γ_m. An appropriate γ_m has been determined when all the data collapses onto one single smooth decreasing curve. With γ_m determined, typically 5-7 for REBCO [196], the contribution of random, or isotropic, defects to the total J_c in a CC as a function of θ can be determined, with the remainder constituting the anisotropic portion.

Figure 2.12c shows another typical property of REBCO CCs where at constant temperature and fields close to zero, $J_c \propto B_{app}^0$, known as the plateau region. Numerous experiments on REBCO bicrystals, reviewed by Hilgenkamp et al. [120], showed that, at low field, J_c is limited by the weak links between grains. This dependency changes as field increases and often there is a range of B where $J_c \propto B_{app}^{-\alpha}$ with constant α, known as the power law region. Theoretical work by Ovchininiko, Vinokur and van der Beek et al. [197]–[199] predicted that $0.5 < \alpha < 0.625$ when pinning is due to nanoparticles (3D). An investigation of changes to α due to oxygen ion irradiation by Eley et al. [143] suggested when $\alpha < 0.5$, pinning is due to smaller isotropic defects. The data in Figure 2.12c suggests that the size of the plateau region decreases with increasing temperature, becoming non-existent at 77K, and that α is often not constant in the power law region.

Given these typical properties, there has been a concerted drive to improve the cost metrics of REBCO CCs which has spawned several reviews of the materials challenges (e.g. [152], [166]). These reviews show that there is still room to improve the superconducting properties of REBCO CCs, but these improvements are dependent on the specific application [193], [200]. Using equations 2-9, 2-10 and 2-11, which combinations of anisotropic (1 or 2D defects) or isotropic (0 or 3D defects) and weak or strong pinning centres dominate at different (B, T) for REBCO thin films can be determined. The results for a CC studied by Puig et al. [200] are shown in Figure 2.13, overlaid with 3 different zones defined to be of optimum $(B,\ T)$ for different applications [201]. The resulting optimum pinning landscape for each zone is shown in Figure 2.14, with anisotropic pinning by 1 and 2D defects dominating for superconducting cables (yellow zone), a mixed landscape for mid-T and mid-B applications (red zone) and 3D or 0D defects dominating for fusion applications (black zone), depending on the intended operating temperature.

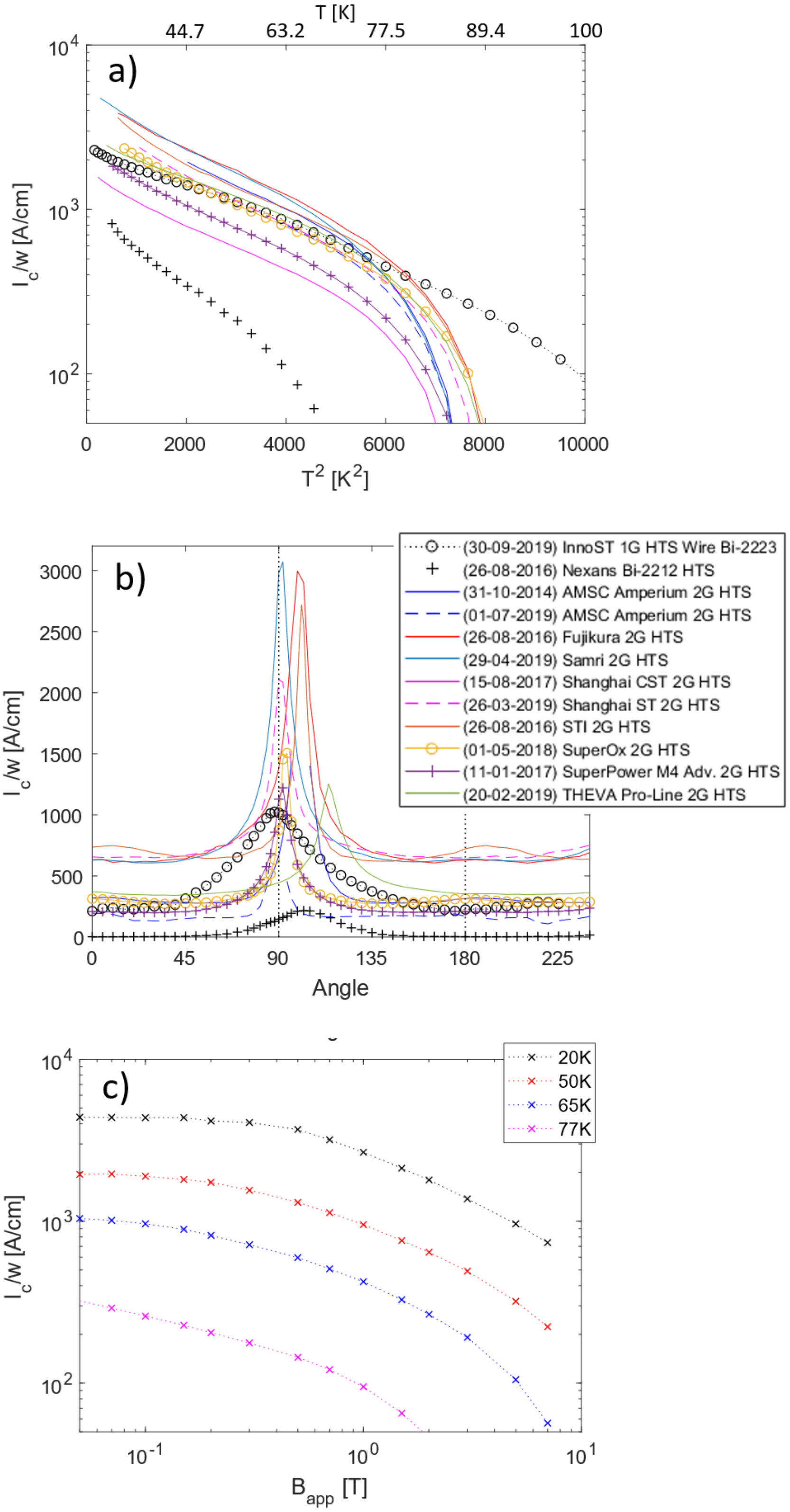

Figure 2.12: a&b) Data for commercial superconductors tested by the Robinson Research Institute and published in their database. a) I_c/w versus T^2 at self-field; b) I_c/w at (25K, 7T) versus the angle of field application. Angles 0° and 90° corresponds to the direction normal and parallel to the CC surface. c) I_c/w versus applied field parallel to REBCO c-axis between 20-77 K for the Samri sample measured by the RRI. All data from [17], [83], [84].

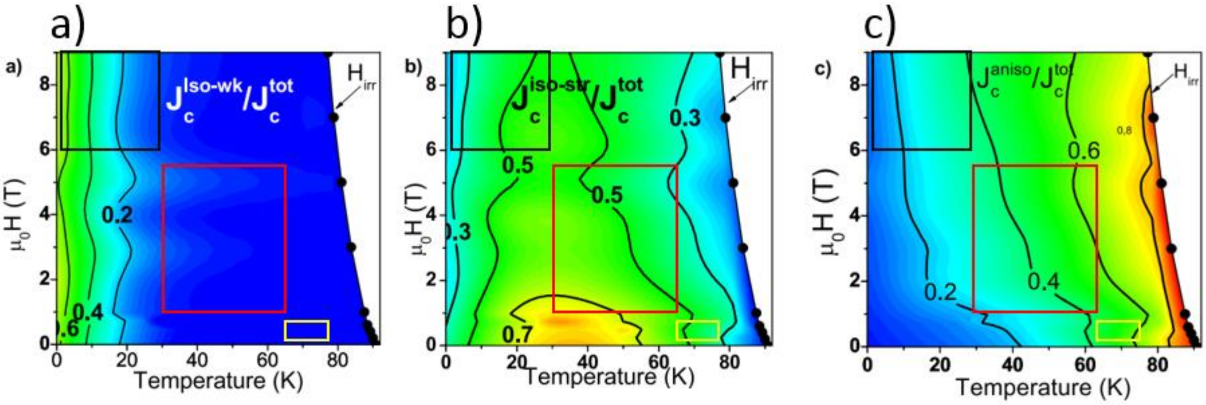

Figure 2.13: Pinning phase diagrams corresponding to (a) J_c^{iso-wk}/J_c^{tot} ratio, (b) $J_c^{iso-str}/J_c^{tot}$ ratio and (c) J_c^{aniso}/J_c^{tot} ratio as a function of temperature (x-axis) and applied field (y-axis) for a standard TFA–YBCO film. Numbers indicate the relative weight. $H_{irr}(T)$: irreversibility line [200]. *Black, red, and yellow boxes illustrate zones of (B, T) of interest for fusion, motor/generators and power cables respectively* [201].

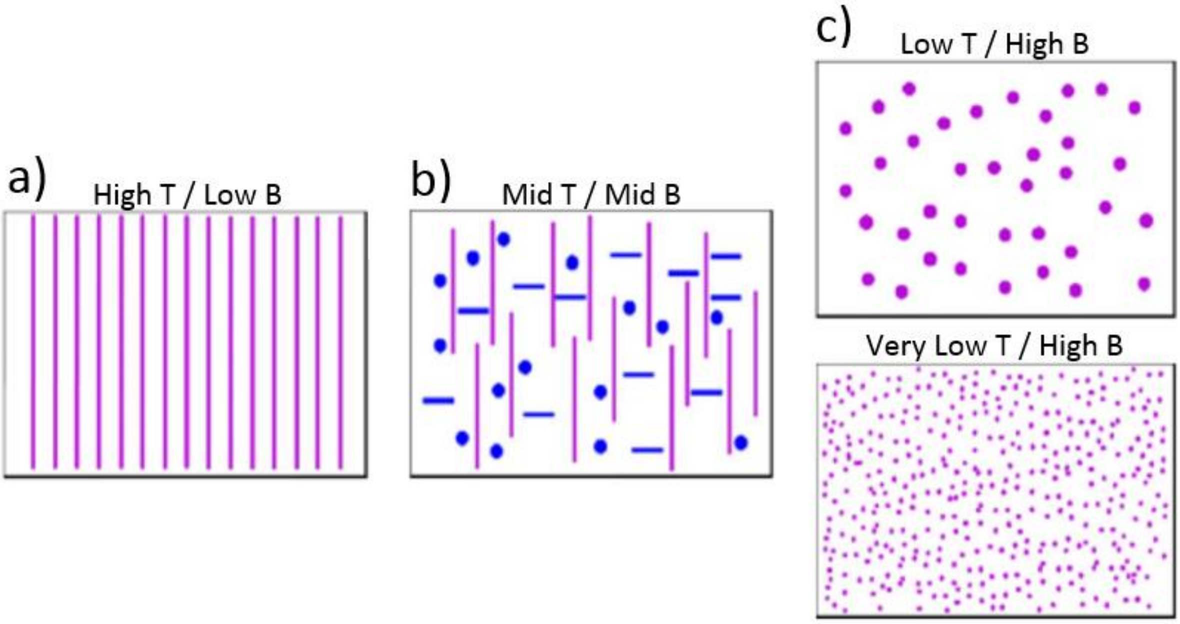

Figure 2.14: schematics for the optimal microstructures for flux pinning for the temperature/field region shown in figure 2-13. a) High T / Low B: columnar APC microstructures, b): Mid T / Mid B with a mixed microstructure; c: Low T / high B: random isotropic spherical defect microstructures. The size of these defects reduces from 3D (e.g. nanoparticles) to 0D (e.g. vacancies) defects as the temperature is lowered [201].

2.3 Effects of Irradiation Damage

Energetic particle bombardment, be it from neutrons, ions, electrons or gamma rays, affects the macroscopic properties of materials by generating additional defects and permanently displacing lattice atoms from their original positions [202]. Neutrons, having no charge, interact over relatively short distances, primarily with the materials lattice nuclei in 'hard-sphere' type collisions. The result of these collisions can vary widely from relatively benign elastic collisions, imparting only energy to the target lattice, to splitting the lattice nuclei into fragments (i.e. fission). The probability of each of the myriad of possible interactions with a particular target material, known as a reaction's cross section (σ_{ij}), varies with the neutron velocity [203] and can be determined experimentally or calculated from computer simulations (e.g. TALYS [204]).

Ions and electrons, however, have a finite charge. They therefore interact over relatively long distances with both the lattice nuclei and their associated electronic structure via the Coulomb force. Which of these interactions dominates depends on their energy with fast ions initially being slowed by electronic interactions (electronic stopping regime), but as the particle slows the dominant interaction will be with the lattice nuclei (nuclear stopping regime) [205].

Both charged particles and neutron interactions generate primary knock-on atoms (PKA, Figure 2.15a). Those PKAs that have sufficient energy travel through the lattice generating further knock-ons (Figure 2.15b) and, if sufficiently concentrated (i.e. if the mean distance between displacements is of the order the interatomic spacing), these knock-ons lead to collision cascades. These expand to absorb the energy of the PKA, causing localised melting and extensive atomic mixing before energy dissipation allows the lattice to relax back towards a stable arrangement. This relaxation, known as self-annealing, is not perfect and several lattice defects remain, such as vacancies (Vac) and interstitials (Int) [206] (Figure 2.15c). These remaining defects are mobile so can diffuse through the lattice, resulting in either further defect annihilation (i.e. Vac+Int) or defect clustering (i.e. Vac+Vac or Int+Int) (Figure 2.15d).

The cumulative effects of the repeated initiation of PKAs and subsequent defect diffusion are the creation of vacancy clusters (voids), changes in the material composition (by transmutation), phase changes and the increased number of dislocations due to the condensation of point defects into intrinsic or extrinsic loops (Figure 2.15e&f). Over longer time scales, these result in changes to the properties of the material as shown in Figure 2.16a.

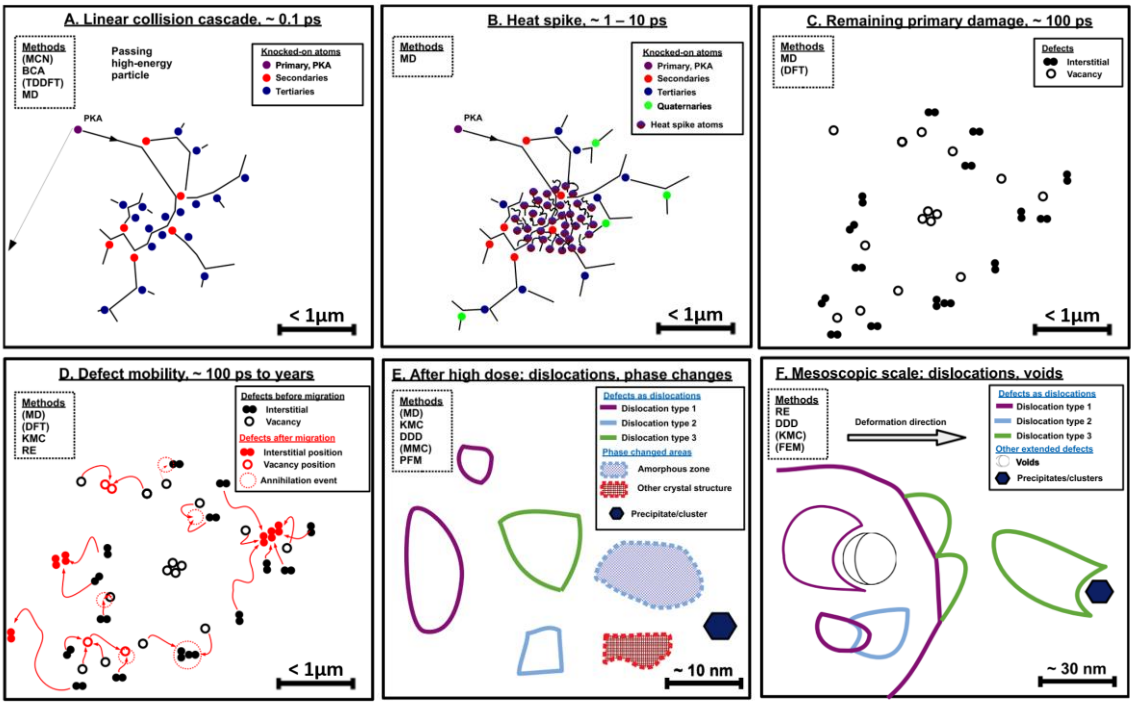

Figure 2.15: Schematic description of the time scales and physical processes occurring during irradiation of bulk materials. Frames A-C indicate a single primary damage process due to a high energy particle (neutron, ion or electron), D: the ensuing defect mobility and E-F: what may happen when multiple primary damage events overlap. The dashed boxes indicate which simulation methods are relevant to model which time scale. Abbreviations are MCN: Monte Carlo neutronics calculations, MMC: Metropolis Monte Carlo, MD: Molecular Dynamics, BCA: Binary Collision Approximation, KMC: Kinetic Monte Carlo, DDD: Discrete Dislocation Dynamics (DDD), DFT: Density Functional Theory, TDDFT: Time-Dependent DFT, RE: Rate equations, FEM: Finite Element Method, PFM: Phase field modelling. When the method is in parenthesis, this indicates that the method can describe only some aspects of the problem. Length scales added are appropriate for oxygen PKAs due to collisions with 14MeV neutrons in REBCO. Modified from [207].

2.3.1 Theoretical Treatments

Early analytical attempts to quantify the effects of irradiation damage focussed on determining the number of atoms displaced to new locations per primary collision (N_d). This work, started by Kinchin and Pease (KP) [208], was expanded upon by Lindhart, Scharff and Schiott (LSS) [209] and by Norgett, Robinson and Torrens (NRT) [210] who showed that the KP model overestimated N_d by ≈ 20%. This NRT-dpa model has been extensively used in the literature since its development to calculate N_d due to a PKA with damage energy (T_d) [202]:

$$N_d(T_d) = \begin{cases} 0 & T_d < E_d \\ 1 & E_d < T_d < 2.5E_d \\ \frac{0.8T_d}{2E_d} & 2.5E_d < T_d < \infty \end{cases} \tag{2-12}$$

where E_d is the minimum energy required to create a stable defect from a recoiling atom[10]. T_d is related to the PKA energy (E_{pka}) by using LSS theory to account for the fraction of E_{pka} lost to lattice atom ionisation during the collision [209], [211], [212]:

---

[10] E_d is also known as the threshold displacement energy (TDE)

$$T_d = \gamma_D E_{pka} \tag{2-13}$$

where γ_D is the damage efficiency calculated using LSS theory [211]. One of the key advantages of the NRT-dpa model is that it is simple to apply. One disadvantage is that it has been shown to inaccurately quantify real damage, overestimating the number of displaced lattice atoms[11] by a factor of ≈3 at high T_d and underestimating the number of atomic replacements[12] by a factor of ≈30 [202]. Both these measures of irradiation damage (displaced and replaced atoms) tend to be normalised to the target atom density as this has been shown to be strongly correlated with changes in material properties [206] (dpa and rpa respectively).

One model proposed to improve the accuracy of the NRT model has been to consider athermal recombination of lattice atoms following a collision (arc-NRT) [202]. This model does, however, require calibration with reference to Molecular Dynamics simulations, and therefore the NRT model is still widely used given that, despite its known inaccuracies, it mimics the trend in damage production for varying T_d [213].

2.3.2 Simulation

Even though defect cascades occur over time scales of ≈100ps, defect mobility and its subsequent effects occur over much longer time scales. This means that the study of irradiation damaged materials will always be a multiscale problem, requiring the use of multiple simulation techniques. Figure 2.16 gives a summary of the several physical phenomena caused by irradiation, and the types of computer simulations used to study them. These include density functional theory (DFT), neutronics calculations, calculations that use the binary collision approximation (BCA), molecular dynamics (MD), kinetic monte carlo simulations (KMC), discrete dislocation dynamics (DDD), rate equation modelling (REM) and finite element modelling (FEM). As their concurrent use is normally prohibitively expensive in terms of computation time, they tend to be used sequentially or individually. In the interests of brevity, only simulation techniques used in the literature to examine REBCO and those used during this work will be introduced. The reader is referred to the review of Nordlund [207] for more information on KMC, DDD and FEM.

At the nanoscale, DFT tends to be used to determine a material's electronic structure and ground state energy by solving a Schrodinger-like equation over a 3D array of unit cells known as a supercell [214]. This makes it ideal for calculating the formation energy and nanoscale mobility of defects such as vacancies, interstitials, anti-site defects etc… (e.g. [215]) which can then be compared with experiment (e.g. [216]) and/or used as input for larger scale atomistic simulations (e.g. [20]). Given

---

[11] I.e. those atoms that end up in distant interstitial or vacancy sites

[12] I.e. those atoms that end up in different perfect lattice sites from their original position

the complexity of DFT calculations, supercell size tends to be limited to ≈35^3 atoms, even given recent advances in the field [217].

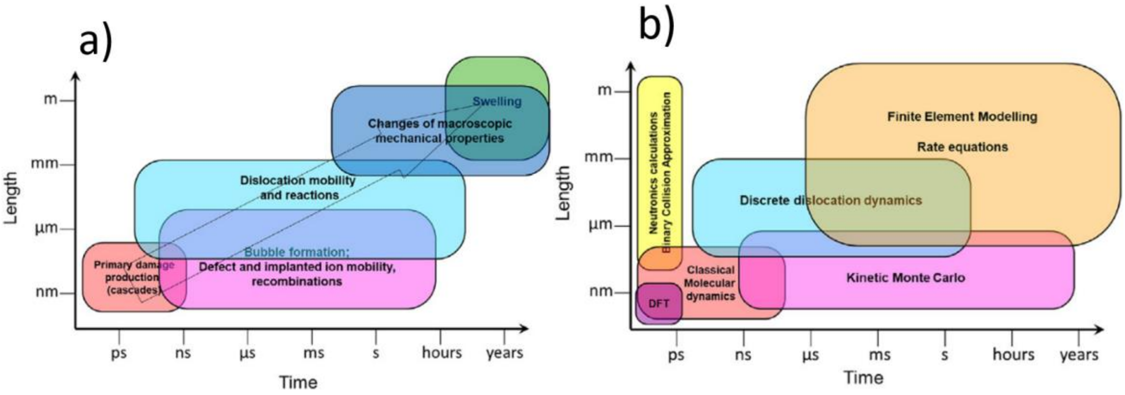

(a) Physical phenomena

(b) Simulation techniques

Figure 2.16: Multiple time (x-axis) and length (y-axis) scales of the a) physical phenomena and the b) multiscale modelling techniques used to study them. Reproduced from [20].

Beyond this, MD can be used up to a limit of ≈215^3 atoms [218]. MD can handle larger systems as each atom (or ion) is considered as a point particle of finite size and charge, with its interatomic interactions governed by a potential function ($V(r)$). $V(r)$ is used to calculate the force balance on each atom allowing their trajectory to be determined in time steps of the order of the lattice phonon frequency (≈1ps). The choice of potential function depends on the system being simulated and its complexity, but the goal is to construct a suitable function that, once calibrated, can mimic known characteristics of the material (e.g. [219]). With the correct potential established, studies of the effects of irradiation damage can begin with PKAs generated by giving a lattice atom additional energy. Repeating this for different PKA energies and directions allows statistics about the dpa, rpa and second order effects (e.g. dislocation loop formation [220]) to be generated and compared with experiments [221].

Given the spatial limitations of MD, the maximum PKA energy is limited by the supercell size needed to accommodate a cascade, therefore studying the damage caused by higher energy PKAs requires further simplification of the model. One such simplification is to simulate only the motion and interactions of particles with sufficient energy ($> E_d$) and assuming that their binary collisions are isolated [206], [211]. This approach can be used to study both neutron-target atom interactions (neutronics) and the reaction chain caused by an energetic knock-on (BCA). The former uses reaction probability tables derived from nuclear data files[13] and Monte Carlo methods to follow the

---

[13] Examples (and current versions) include the evaluated nuclear data file (ENDF) version 8.0 ([378], [379]), the joint evaluated fusion and fission file (JEFF) version 3.32 [380], the Japanese Evaluated Nuclear Data Library (JENDL) version 4 [381] and the TALYS-based evaluated nuclear data library (TENDL) 2019 version ([317], [318]).

stochastic motion of a neutron as it traverses a material (e.g. MCNP [222]). By repeating this procedure for many neutrons (typically > 10^6), statistics about the penetration and energy change of neutrons traversing a medium can be determined. These neutron spectra (e.g. Figure 4.1) can then be used to estimate PKA energy and concentration as a function of position (e.g. SPECTRA-PKA [212], section 3.5.2) and nuclear transmutation rates (e.g. FISPACT-II [223], [224], section 3.5.1).

The subsequent PKA damage can be studied using one of two methods using the BCA approximation. The first is to solve the equations of motion for a PKA as it traverses a fixed crystalline lattice, restricting the exchange of energy to that between it and the nearest lattice atoms (e.g. MARLOWE [225]). The energy and momentum vectors imparted on each lattice atom are then summed and stored until $E_{pka} \approx E_d$. At this point, all lattice atoms with sufficient energy become secondary knock-on atoms (SKA) and their paths, as well as those for subsequent knock-ons, are determined using similar means. The simulation ends when all knock-on atoms have energy $\leq E_d$, at which point statistics about the dpa and rpa due to the resulting atomic movements can be determined [226]. The second method (e.g. the SRIM code [227] for ions, expanded upon in section 3.5.3 and CASINO for electrons [228], [229]) further simplifies the BCA model by making the maximum impact parameter a function of the target density, and by determining the results of interatomic interactions by using Monte Carlo methods in conjunction with the analytic solution to the 2 particle collision model [227]. The former removes the need to define the position of every atom before every calculation, although this makes the target amorphous. Both simplifications make the model more computationally efficient as small angle collisions are neglected, greatly reducing the number of collisions analysed [230].

Due to their efficiency and availability, both crystalline and amorphous BCA methods have been used extensively in the literature [20]. This is despite it being shown that BCA codes need to be calibrated, either with experiment [231] or MD (e.g. [232]), to mimic the known characteristics of a system. Reported reasons for this include the overestimation of the electronic stopping power in high Z elements [231] and incorrectly accounting for conditions during the heat spike section of a cascade [210].

2.4 Irradiation Experiments involving REBCO

In this section, experiments investigating how the microstructure and superconducting properties of REBCO are affected by irradiation with electrons, neutrons and fast ions are discussed.

2.4.1 Electron Irradiation

Electron irradiation is typically used in conjunction with MD [233]–[235] and high-resolution imaging [119], [236] to induce point defects in a material (e.g. [237]) and/or determine a material’s TDE values. This is because relativistic electrons can penetrate >1µm into any material [238] and the maximum energy that can be imparted on the PKA (E_{pka}^{max}) is relatively low [216] due to the electron's low mass. Thus, by monitoring material properties for varying electron beam energy, the energy that causes an effect on REBCO superconducting properties can be determined and, using other investigation methods, linked to the TDE of a particular atomic species. REBCO has several TDE values given its anisotropic structure (Figure 2.7a), three cation species and copper's multiple charged states. Figure 2.17a shows E_{pka}^{max} as a function of electron beam energy and shows that electron irradiation predominantly excites the oxygen atoms in REBCO, but since REBCO has 4 different oxygen sites this means that, as the beam energy increases, point defects are eventually generated at whichever site has the lowest TDE.

Early electron irradiation experiments on YBCO aimed at investigating the twin structure of orthorhombic YBCO powders using high-resolution TEM imaging. One such experiment using 120 keV electrons was performed by Mitchell et al. and Smith et al. [119], [236], aiming to observe REBCO's twin structure at LN_2 temperatures, found that the twinned structure was gradually lost during observations (Figure 2.17c) but re-established with the twin boundaries in different places if the beam was removed for a short time (Figure 2.17d). Both authors attributed this to an orthorhombic-to-tetragonal (O2T) transition excited by fast electrons preferentially knocking chain site oxygen atoms from their lattice sites, which relaxed back to their original positions once that source of energy was removed, suggesting that $E_d^{O2T} < 18\text{eV}$. Other common reasons for a O2T transition in REBCO include deoxygenation (i.e. $\delta: 7 \rightarrow 6$) by direct collision or by sample heating above 400°C. Given that the electron beam power is low, this suggests that the oxygens are not lost from the sample, only that they are continuously mobilised between the O(1) site to either the V(1) or V(2) positions.

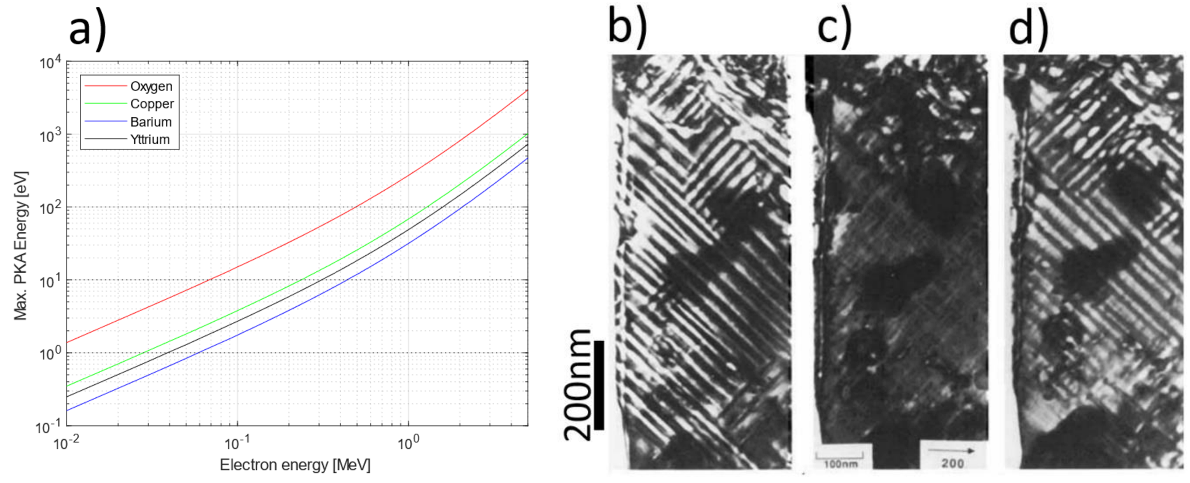

Figure 2.17: (a) $E_{pka,max}$ *(y-axis) vs Electron Energy in MeV (x-axis); b-d) YBCO particle observed in TEM with 120 keV electrons along [001] axis b) initial observation, c) after ≈20 minutes of direct viewing and d) after beam removed for ≈10 minutes and then reobserved. Shows that REBCO particle's twin structure is lost during observation but reasserts itself once the beam is removed. Reproduced from* [119], [236].

As neither Mitchell nor Smith directly measured their sample's superconducting properties, whether the O2T transition was truly reversible could not be conclusively determined. In addition, results of MD simulations by Kirsanov et al. [233] and Cui et al. [234], [235] showed that O(1,4) required as little as 1.5eV[14] and O(2,3) as little as 9eV extra energy to jump to an adjacent vacant position, suggesting that 120keV electrons had sufficient energy to displace all the oxygen species in YBCO. Experiments using lower electron irradiation energies were therefore required to deconvolve the effects of O(1,4) and O(2,3) displacements. These included the work of Seo et al. who showed that 20keV electron irradiation in untwinned non-stoichiometric YBCO crystals only redistributed O(1) atoms within the crystal, but did not affect the overall oxygen content [239]. This was confirmed by Tolpygo et al. [240], [241] who studied the effect of 20-120 keV electron irradiation on the resistance of stoichiometric and non-stoichiometric 50nm thick YBCO films. They found that 20keV electrons affected the normal state resistivity of stoichiometric YBCO but had no effect on the T_c (Figure 2.18a, inset). The same was found at 40 keV, but with a small effect on T_c (Figure 2.18a), whilst 80 keV irradiation affected the normal state resistivity and significantly decreased T_c (Figure 2.18b). For non-stoichiometric samples, 40 keV was sufficient to decrease T_c. The changes in the properties of YBCO were attributed to disruption of the CuO chain's conductivity due to the redistribution of O(1) atoms, which in turn decreases the hole doping on the CuO_2 plane. The evaluated E_d values for the plane and chain oxygens were 8.4eV and 2.8eV respectively.

Experiments on oxygen mobility in YBCO single crystals at 83 K, however, suggest that $E_d^{\Delta T_c}$ is much higher, with Basu et al. [216] showing that 100 keV electrons do not have sufficient energy to affect

---

[14] depending on incident particle direction

an O2T transition in YBCO single crystal, whilst 150 keV do, implying that $15 < E_d^{O2T} < 18$ eV. Also, Legris et al. used calculated electron-atom displacement cross sections to model the rate of change of T_c in a YBCO single crystal due to electron irradiation at 20 K for a wide range of energies [242]. This implied that both copper and oxygen displacements influenced T_c, with the model fitting their experimental data when $E_d^{\Delta T_c}(O) \approx 10$eV and $E_d^{\Delta T_c}(Cu) \approx 15$eV.

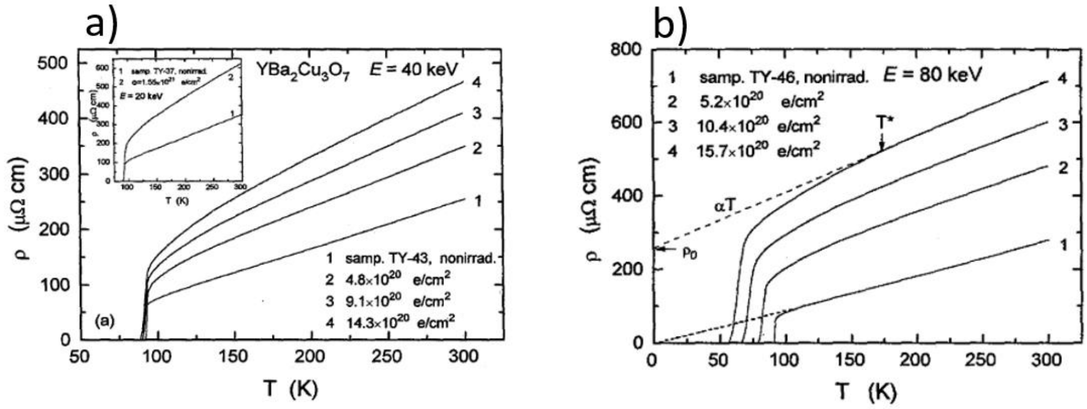

Figure 2.18: Effect on REBCO resistivity (y-axis) as a function of temperature (x-axis) of increasing fluence of (a) 40 keV, (a, inset) 20 keV and (b) 80keV electron irradiation on a 50nm thick film of stoichiometric YBCO on a LaAlO$_3$ substrate. Reproduced from [240].

Assuming that $E_d^{\Delta T_c} \approx E_d^{O2T}$ and considering that all the irradiation experiments were performed on unprotected samples in vacuum, it can be postulated that the smaller $E_d^{\Delta T_c}$ of Tolpygo's thin films is due to the smaller distance PKAs needed to travel to reach a sample boundary compared to Basu and Legris et al.'s single crystals, and hence the PKAs require more energy to overcome the surface binding energy (1.7eV [243]). In turn, this suggests that the appropriate choice of E_d depends on whether the REBCO CC sample is enclosed or has its REBCO layer exposed.

Finally on the subject of TDE calculations, recent work studying REBCO using a MD model calibrated using DFT to mimic various known material constants by Murphy et al. and Grey [244], [245] calculated the TDE for all REBCO species shown in Table 2-5. Although these are of a similar order to those determined from experiments, they are based on simulation data and, given the variability of the experimentally determined TDEs, are therefore only used as a guide going forward.

Table 2-5: REBCO TDEs in eV calculated by Grey [245]. *For the atomic species, refer to Figure 2.7a.*

Crystallographic Direction	**[100]**	**[110]**	**[010]**	**[011]**	**[001]**	**[101]**
Y	**33.3**	**33.3**	**33.3**	41.6	50.8	41.6
Ba	78.5	**4.45**	30.1	30.1	51.4	51.4
Cu (1)	10.0	13.9	10.0	**6.67**	23.8	**6.67**
Cu (2)	**10.0**	36.3	29.7	13.9	29.7	**10.0**
O (1)	**9.10**	17.4	13.0	15.1	15.1	19.9
O (2)	**13.0**	25.4	25.4	67.3	**13.0**	15.1
O (3)	15.1	17.4	**13.0**	17.4	**13.0**	25.4
O (4)	15.1	15.1	17.4	22.6	38.3	**2.5**

2.4.2 Neutron Irradiation

One of the first experiments to test the response of REBCO to neutron irradiation was by Umezaea et al. [10] using the Intense Pulse Neutron Source at Argonne National Laboratory. To avoid the added complexity of accounting for grain boundary effects, rectangular single crystalline samples of YBCO were used. They were irradiated up to 8x10^{17} n/cm^2 at < 30°C and the results confirmed that J_c was affected by neutron irradiation.

Work to assess the response of bulk and thin film YBCO to neutron damage and discover methods of improving its performance for various applications were continued on many fronts. These included the works of Cost et al. [246], Lee et al. [247] and Sickafus et al. [248] who used the Los Alamos National Laboratory's Omega West reactor to test bulk polycrystalline YBCO at fluences up to 3x10^{18} n/cm^2. Sauerzopf et al. [249], [250], working with Vienna's TRIGA reactor [43], used neutrons to assess how flux pinning is affected by different defect sizes and structures in single crystalline YBCO. Also, Vlcek et al. [251], [252] and Frischerz et al. [253] investigated the contribution of point defects to flux pinning in YBCO by comparing samples irradiated using the Missouri University Research Reactor (MURR) before and after subsequent annealing. The results were summarised by Kirk et al. [254], who reported that fast neutron irradiation led to "small amorphous volumes formed by defect cascades" and that fluences of 10^{17}-10^{18} n/cm^2 improved the superconducting properties of YBCO. Above this fluence, the density of the irradiation induced defects (size > ξ_{ab}) leads to YBCO taking on a 'cellular microstructure' with undamaged cells of YBCO being separated by amorphous material with no superconducting properties.

Commercial REBCO coated conductors were first tested in 2008 by Fuger et al. [255], [256]. A CC sample was irradiated in the Vienna TRIGA reactor up to 10^{18} n/cm^2 at temperatures <60°C and transport current tested after various fluences. One of the key results is shown in Figure 2.19a, showing that neutron irradiation improves J_c at high field parallel to the c-axis but not at low field nor when the field is parallel to the (a, b)-plane. After an upgrade to the Vienna TRIGA reactor [257], this work was expanded to fluences of 3.9x10^{18} n/cm^2 by Eisterer et al. [258], Prokopec et al. [40] and Fischer et al. [21]. The key part of this expansion was to use CCs with different manufacturing processes (from AMSC, SuperPower and SuNAM) and with and without nanoparticle APC inclusion to optimise the microstructure for flux pinning. Their results showed that the low-temperature, high-field J_c improved in CCs without APCs, compared to the initial J_c, when irradiated with fast neutrons, whereas optimised CCs showed relatively little improvement with irradiation before degrading (Figure 2.19b). This allowed Fischer et al. to intermate that the improvement in REBCO superconducting properties with B||c is a function of the combined defect density of inherent defects, dopant nanoparticles and irradiation induced defects [21]. From a practical point of view, however, it was still the case that the improvement of self-field J_c and reduced α of optimised CCs meant they had a larger high field J_c than unoptimized CCs after irradiation, even though the decline in their high field properties below their initial values began at a lower fast neutron fluence (Figure 2.19c). This suggested that whatever processing changes were made to optimise the microstructure of the SuperPower sample, they were advantageous from the perspective of achieving high field J_c after exposure to fission neutron irradiation. Supplementing this work, a positron annihilation spectroscopy (PALS) analysis of the REBCO samples irradiated in the TRIGA reactor by Chudy et al. [259] implied that the dominant defect type before and after neutron irradiation were Ba-monovacancies and Cu-O bi-vacancies respectively.

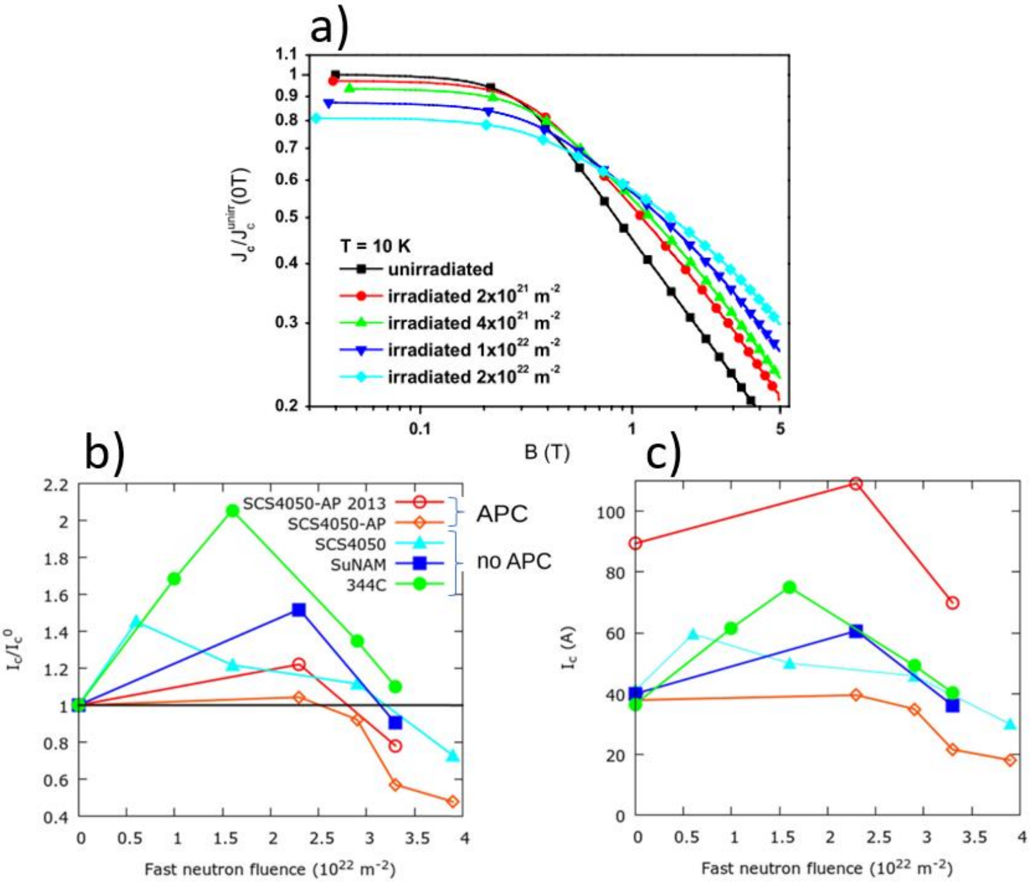

Figure 2.19: a) Change a YBCO CC's J_c, normalised to its pre-irradiation value at ≈0 T (y-axis) versus applied field (x-axis) in response to an increasing fluence of fission spectrum neutrons from the Vienna TRIGA CIF, reproduced from [255]. *b-c) Change in the I_c (c) and I_c normalised to its pre-irradiation value (b) of five REBCO CC samples, with and without artificially enhanced pinning (APCs), in response to an increasing fluence of fission spectrum neutrons from the Vienna TRIGA CIF, reproduced from* [21].

2.4.3 Ion Irradiation

Creating lattice damage in materials with fast ions instead of neutrons is useful because damage can be inflicted at rates ≈10^4 times higher that of a fission reactor, with near-zero sample activation, at low cost and with significantly better control of experimental conditions [260]. As such, there have been many more studies on ion irradiation of REBCO than neutron irradiation. Their goals, however, were the same; to investigate how defect formation in REBCO affects its J_c at varying temperatures and fields, and to correlate these with microstructural changes. Although initial experiments were at relatively low energy (E_i <1MeV) [261], [262], most experiments up to 2011 were in the 10MeV-10GeV energy range, and used multiply charged, heavy ions to create columnar defects of amorphous material [254]. Post-2011, a wide variety of beam energies were used with the aim of either investigating whether low energy ion irradiation should be included as a manufacturing step for commercial CCs (e.g. [263]) or to investigate pinning in REBCO. A summary of experiments since 2008 is shown in Table 2-6. Unless otherwise stated, all irradiation discussed below were performed at room temperature.

High energy ions (E_i >10MeV) traversing a material undergo multiple Coulombic interactions. In this electronic stopping regime, each interaction results in the creation of a sphere of amorphous material surrounding the impact site [264]. A sufficient number of them will result in REBCO adapting the 'cellular microstructure' described above for neutrons [254]. For example, Roas et al. showed that 2×10^{15} 25MeV O^+ ions/cm^2 were sufficient to destroy the superconducting properties of an 8µm thick epitaxial YBCO film [265].

At very high energies (E_i >100MeV), ion irradiation results in columnar defects of amorphous material orientated parallel to the direction of ion bombardment being formed prior to complete amorphization [266]. In his 1994 review of damage induced by fast ions in oxides, Toulemonde et al. [264] showed that the appearance of these columnar defects is dependent on the electronic interaction damage cross section (σ_e). As σ_e increases with E_i, raising the incident beam energy results in the mean distance between spherical defects decreasing until they overlap, leading to the formation of continuous columnar defects. Amorphous columnar defects effect the REBCO lattice by inducing a stress field around them that relaxes by reordering of the oxygen atoms in the Cu-O planes, resulting in local switches in the (a, b) plane directions [254] which have a characteristic lobed bow-tie shape when examined using TEM (Figure 2.20c). Toulemonde et al. and Isobe et al. found that columnar defects in YBCO had radius (R_e) of the order of 0.1-5nm depending on the irradiating ion, increasing with ion mass and energy [264], [267] and that when R_e>3.1nm these 1D defects could positively affect the sample T_c. This agreed with findings of Civale et al. who also showed that fast-ion irradiation induces columnar defects that make effective 1D pinning centres when they reported that the superconducting properties of a YBCO slab were significantly improved when B_{app} is parallel to the columns (Figure 2.21a) [268]. This improvement was also reported in thin films, as illustrated by Suvorova et al., who showed that the concentration of all elements dropped by over 40% within these tracks compared to the bulk density using TEM and EDX [269] (Figure 2.21b).

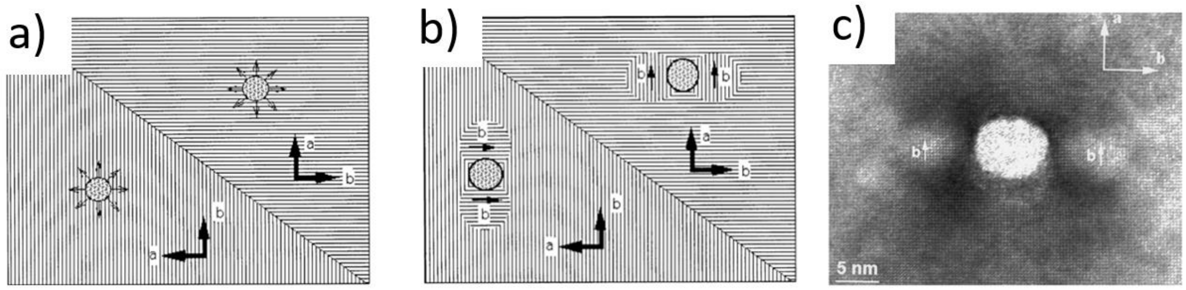

Figure 2.20: Cu-O plane oxygen reordering due to columnar defects. Once a columnar defect forms it results in a stress field on the surrounding lattice (a). This stress field relaxes by a swapping of the a- and b-axis directions (b). (c) This reordering as seen as by TEM. Reproduced from several figures in [254].

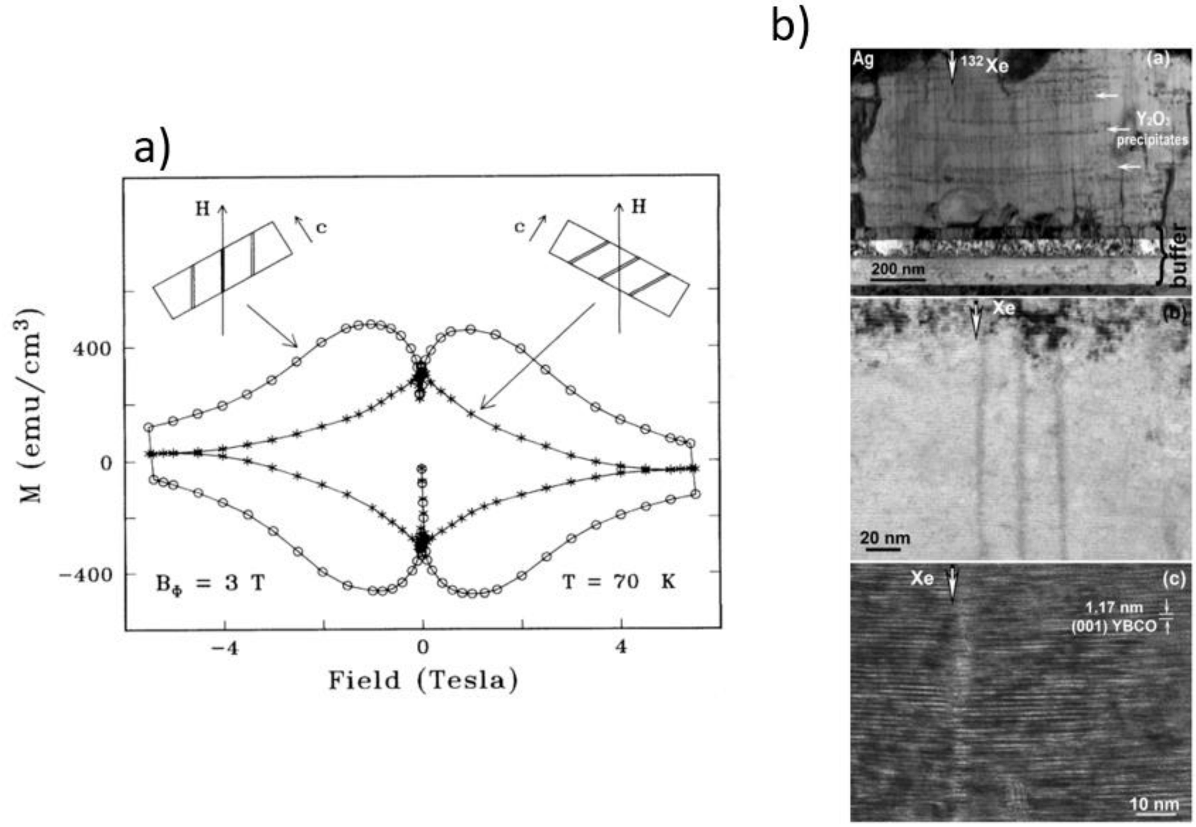

Figure 2.21: a) Magnetisation measurement (y-axis) versus applied field (x-axis) at 70 K of a REBCO slab geometry irradiated to a columnar defect density equivalent to a matching field of 3 T 30° to the c-axis. 'o' corresponds to measurements when H_{app} is parallel to the columnar defects and '' to when H_{app} is at 60° to the columnar defects. Reproduced from* [268] *(b) Continuous (and near continuous) tracks produced by 167 MeV Xe ions. The magnification of TEM images increases from top to bottom; black-and-white arrows point forward at ion tracks, and simple white arrows show rows of yttria precipitates (top). The orientation of the cross section is close to [100] YBCO, and the direction of Xe ions is parallel to the [001] axis. Reproduced from* [269].

Given the reported improvements in J_c and the challenges in controlling the size, shape and alignment of APCs when applied using synthesis techniques, ion beam irradiation is being actively considered as a cost effective technique of improving the performance of CCs at high field [263]. This cost effectiveness requires a reduction in beam energy to levels already used in industry [270] thus refocused investigations of ion-target interactions in REBCO to the nuclear stopping regime, despite Gapud et al. showing that REBCO's superconducting properties are more sensitive to ions stopped by electronic interactions [271]. In 2012, Matsui et al. showed that 10^{11} 3 MeV Au^{2+} ions/cm^2 could be used to improve J_c(77K) of a MOD CC at all angles of B_{app} (Figure 2.22a&b) [263]. TEM examination of these samples showed the appearance of Moire spots – spherical regions of amorphous material with diameter < 5nm – due to irradiation (white arrows, Figure 2.22c). Another striking consequence of this irradiation was that it led to a large improvement in J_c(77K, B||c), resulting in it eclipsing J_c (77K, B||ab) – the complete opposite of pristine REBCO. A follow up study in 2015 using a more uniform damage profile through the sample thickness exceeded the maximum improvements at 77 K of the 2012 study (Figure 2.23a) [272]. Besides the improvement in J_c, Matsui et al. showed that the highest J_c available to the CC with B_{app} >1T was not with B‖c or B‖(a,b), but at an intermediate angle (μ_0H$\|\theta_{max}$, Figure 2.23a, inset) and that the fluence leading to peak improvement in J_c(77K) and μ_0H$\|\theta_{max} = 5T$ coincided with the fluence when J_c at self-field initially decreased (Figure 2.23b) [272]. These findings agreed with later studies by Rupich et al. [273], Leroux et al. [274] and Kihlstrom et al. [275] who showed that ion beam irradiation using single ions, or combinations of ions, could be used to improve the perform of AMSC CCs at low temperature and high field. The gold irradiated sample generated by Rupich et al. [273] was the subject of a follow-up study by Zhang et al., who used TEM and EELS to conclude that the change in the AMSC CCs superconducting properties was due to the generation of “highly oxygen deficient amorphous nanoclusters and randomly distributed point defects” during irradiation [18].

The annealing behaviour of REBCO post ion irradiation has also been of interest to researchers as it has been shown that it can reverse the effects of irradiation damage. The earliest example of this was reported by Xiong et al. [262] who showed that warming a sample irradiated with protons to 7.8x10^{16} H$^+$/cm^2 at 4.2 K back to room temperature was sufficient to partially recover a superconducting current pathway in a sample that had previously had none (Figure 2.24a). A similar recovering of T_c, plus a reversion of an enhanced J_c back to pre-irradiation levels, was achieved in a YBCO crystal by Vlcek et al. [251] using annealing at 300 ^{o}C for 24 hours after proton irradiation and by Vichery et al. [276] after significant irradiation damage at 20 K before annealing at 100 K.

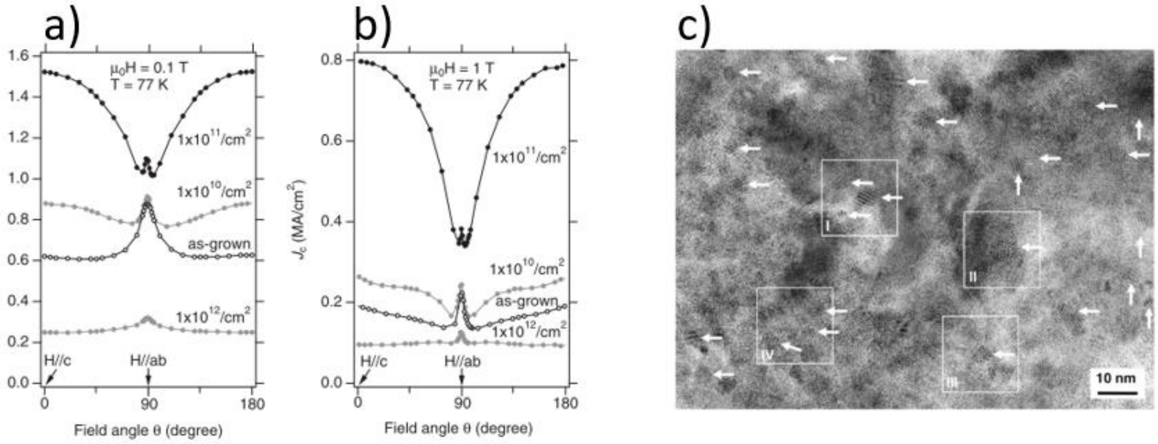

Figure 2.22: a & b) Dependence of MOD CC’s critical current (y-axis) on the direction of an applied of applied field (x-axis) relative to the REBCO unit cell c-axis direction (a): 0.1 T and (b): 1 T at 77 K before and after irradiation with 3 MeV Au^{2+} ions to 10^{10}, 10^{11} and 10^{12} [i/cm2]. Reproduced from [263]*; c) Lower magnification micrograph of a 3 MeV Au^{2+} irradiated YBCO film view along [001] showing Moire spots indicated with white arrows. Reproduced from* [263].

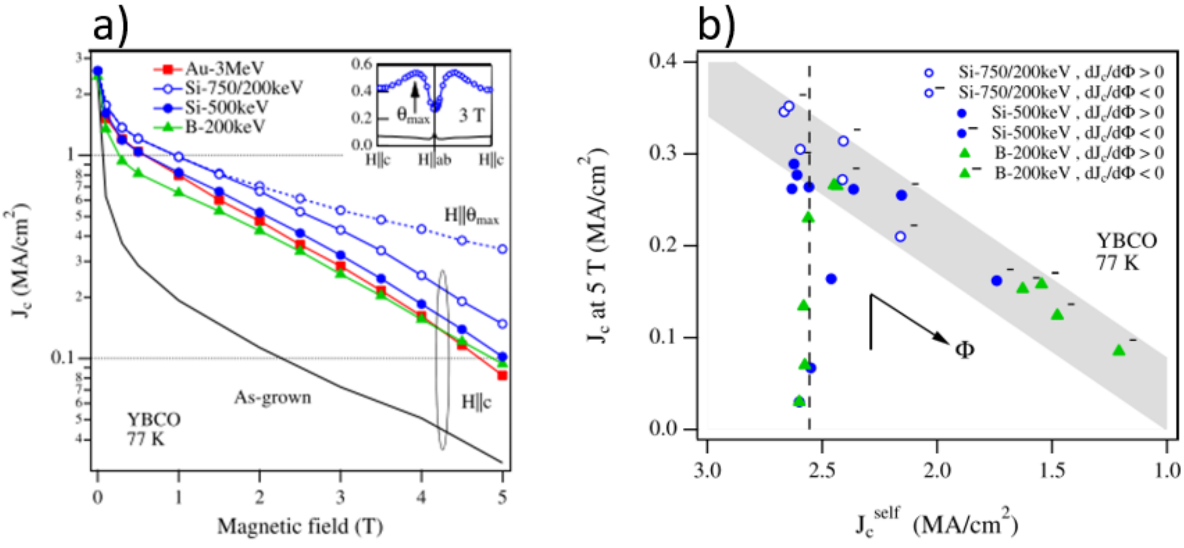

Figure 2.23: (a) Dependence of MOD CC critical current (y-axis) on applied field parallel to the c-axis (x-axis) at 77 K before and after ion beam irradiation (see legend) up to 2x10^{10} [i/cm^2]. Legend describes the irradiating ion(s) and ion energy(ies) (eg. Au-3MeV = gold at 3MeV). Beam damage leads to a more significant J_c improvement at high field. Inset: shows angular dependence of J_c at 3 T and 77 K and implies a peak J_c at an intermediate angle. Reproduced from [272]. *(b) Dose dependence of J_c at 77 K and at (5 T, H||ϑmax) in irradiated YBCO films against J_c(self-field). Legend as figure (a). Minus signs denote data decreasing with dose whilst points without a minus denote data where J_c is increasing with dose. Dashed line and grey shading are a guide for eyes. Reproduced from* [272].

More recently, Eley et al. [143] studied the annealing behaviour for varying annealing temperature of AMSC CC samples that had previously been subjected to 6 MeV oxygen irradiation to 5x10^{13} /cm^2 (Figure 2.24b). Post-irradiation, J_c(5 K, 5 T) showed an 160% improvement on pre-irradiation levels, an improvement which was slowly eroded down to 25% as the annealing temperature was raised to 600 °C and the sample started to deoxygenate (region V, Figure 2.24b). T_c also recovered with low temperature annealing; a result attributed to the rearrangement of interstitial oxygens. Given its non-linear nature, the progression in the change in T_c and J_c(5 K, 5 T) was attributed to 4 distinct regions (Figure 2.24b). The decreases in J_c were attributed to Frenkel pair rearrangement, first in the oxygen lattice at low annealing temperature (II), then in the copper lattice at higher temperature (IV). The slight increase in J_c in region III was attributed to decreased sample anisotropy.

One final piece of literature worth examining was that of Sorbom, who used 1.2 MeV protons to irradiate YBCO CCs at 80 K, 323 K and 423 K up to ≈ 0.003 dpa and then assess their different responses using transport current measurement and MD simulation. The results suggested that samples irradiated at low temperature had an increased resistance to proton irradiation, with the dominant cause attributed to a lower diffusion rate in cold samples (determined by MD), leading to less diffusion of irradiation induced defects to grain boundaries once they had been created [277]. Given the subject of this thesis, discussion of the accuracy of this conclusion will be directly assessed. Its discussion is therefore left to chapter 7.

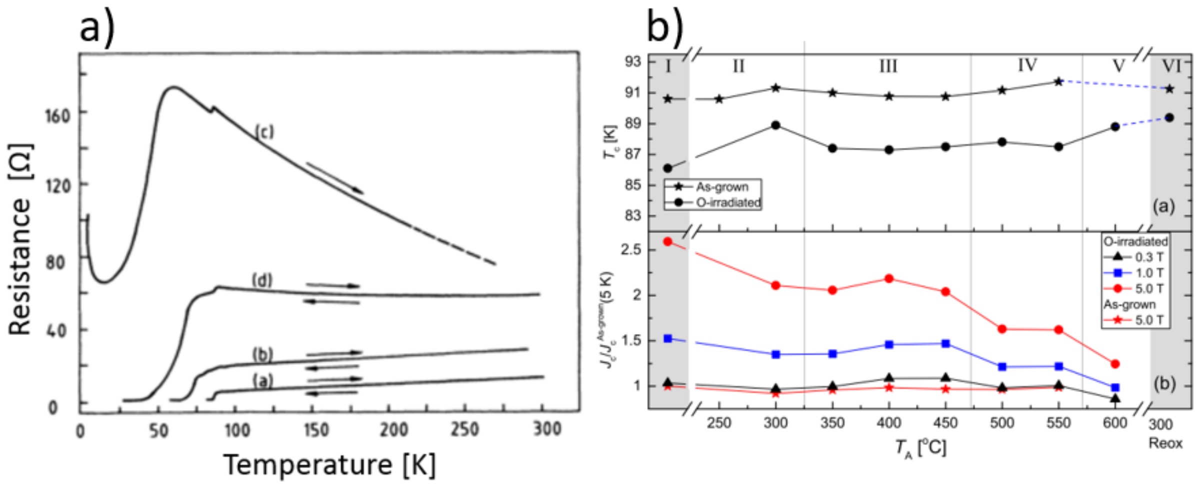

Figure 2.24: a) Resistance (y-axis) vs Temperature (x-axis) measured for p^+ irradiation of a REBCO thin film at 4.2 K. Legend: (a) before irradiation, (b) 4.3x10^{16} and (c & d) 7.8x10^{16} [H^+/cm^2]. (a) & (b) show reversible behaviour but irradiation to 7.8x10^{16} [H^+/cm^2] leads to complete loss of superconductivity (c) that is recovered and becomes reversible on subsequent cooling to 4.2K (d). Reproduced from [262]*; Figure b) Evolution of the T_c (top y-axis) and J_c(5K, 0.3/1/5 T) normalized to the as grown value for the unirradiated sample (bottom y-axis) with increasing annealing temperature (x-axis) before (stars) and after (circles, squares & triangles) samples were 6MeV O^{3+} irradiated to 5x10^{13}/cm^2. Reproduced from* [143]*.]*

2.5 Summary

Given the cost involved in commercialising electricity produced from fusion reactions, reducing the tokamak size by using REBCO CCs to increase B_t is a viable method of reducing these costs. That said, it has been shown that REBCO's superconducting properties are inherently linked to its microstructure and the defects it contains. Given that irradiation in any form modifies a material's microstructure, it has also been shown that both ion and neutron irradiation can modify the pinning landscape in REBCO by creating both isotropic (0 or 3D) and anisotropic (1 or 2D) defects. These defects can either form directly or by diffusion and subsequent clustering and, depending on several factors including defect density and REBCO grain size, can either enhance or diminish the supercurrent carrying capacity. The rate of diffusion of defects through REBCO has been shown to be highly temperature dependent, and recent work by Sorbom [277] suggests that temperature does affect how REBCO responds to ion irradiation. Sorbom also suggests in-situ ion irradiation, I_c determination and annealing studies of REBCO CCs as subjects of further work.

Table 2-6: Summary of Ion Irradiation Experiments on REBCO Thin Films and Coated Conductors published since 2008

Author [Reference]	**Year**	**Sample**	**Ion**	**Energy [MeV]**	**Max. Fluence** [i/cm^2]**
Isobe [267]	2008	DyBCO-MgO-c276	Au Ni	320 200	MF: 1T MF: 5T
Greene [278]	2009	*YBCO CC (SuperPower) *YBCO CC (AMSC)	H$^+$	142	3.4x10^{17}
Matsui [263]	2012	YBCO-CeO$_2$-SrTiO$_3$	Au	3	10^{12}
Matsui [279]	2014	YBCO-SrTiO$_3$ YBCO-B-c276	Au	3	MF: 10T
Jia [280]	2013	Au(3µm)-YBCO (ASMC)	H$^+$	4	8x10^{16}
Leonard [281], [282]	2013	*(Y,Gd)BCO +Zr *(Dy,Y)BCO *GdBCO	Ni Au	5 25	10^{12} 10^{12}
Matsui [272]	2015	YBCO-CeO$_2$-SrTiO$_3$	Si Si B	0.5 0.75 & 0.2 0.2	5x10^{12} 5x10^{12} (7:3) 2.25x10^{13}
Leroux [274]	2015	Ag(1µm) – YBCO CC (ASMC)	O	3.5	3.4x10^{13}
Gapud [271]	2015	*GdBCO (SuperPower) *(Y,Gd)BCO +Zr (SuperPower) *(Dy,Y)BCO (AMSC)	Au Ni	25 5	10^{12} 5.5x10^{11}
Haberkorn [283], [284]	2015	Ag(0.6µm) – GdBCO	H$^+$	3	6x10$^{`16}$
Rupich [273]	2016	Ag(1µm) – (Dy,Y)BCO CC (ASMC)	Au	18	2x10^{12}
Eley [143]	2017	Ag(1µm)-YBCO-B-Ni5%W (AMSC)	O	6	5x10^{13}
Haberkorn [285]	2017	Ag(0.6µm)-GdBCO (SuNAM)	O	6	4x10^{14}
Sorbom [277]	2017	Ag(2µm)-YBCO-B-c276	H$^+$	1.2	5x10^{16}
Suvorova [269]	2019	Ag(2µm)-YBCO-B-c276 (SuperPower)	Xe	46 77 167	5x10^{11} 5x10^{11} 1x10^{11}
Haberkorn [286]	2019	GdBCO-LaMnO$_3$-MgO	H$^+$	3	2x10^{16}
Zhang [18]	2020	Ag(1µm) – (Dy,Y)BCO CC (ASMC)	Au	18	3x10^{11}
Choi [287]	2020	Ag(3µm)-SmBCO-B-c276	H$^+$	30	10^{16}
Antonov [288]	2020	YBCO(0.2µm)-LaAlO$_3$	O	0.1	4.3x10^{13}
Kihlstrom [275]	2020	Ag(0.8µm) – (Dy,Y)BCO CC (ASMC)	Au/H$^+$ H$^+$	250 & 4 4	4x10^{17} 3x10^{17}

* Tapes Irradiated as delivered (supplier provided unless omitted by author)

** Matching Field (MF) criterion requires sample superconducting properties to be measured before irradiation at zero field and matching field. Irradiation then continues until zero field properties post irradiation match matching field properties, pre irradiation.

B – Buffer layers

3 Experimental Methods

In this chapter, a description of the available samples and the tools used during the data collection stage of this thesis is presented. This begins with a description of the samples made available to me for this project. The methods and tools used to measure superconducting properties are then presented, followed by a description of the microscopy tools used. The chapter is concluded with a summary of the irradiation damage simulation techniques employed and how ion irradiation damage was applied to my samples.

3.1 Samples

Seven different REBCO CC samples were collected from the several of the manufacturers listed in Table 2-4 in a form that allowed them to be used for this work. These are shown in Table 3-1 and include 6 samples with c276 Hastelloy substrates and 1 – from Bruker – with a stainless-steel (SS) substrate. The material properties of c276 and SS used below are taken from Lu et al. [150] and Xia et al. [289] respectively. The buffer layers in these CC are as shown in Table 2-4, with their properties taken from the CRC Handbook of Chemistry and Physics [290]. All samples have the c-axis of their REBCO layer parallel to the CC's normal direction and have REBCO layer thicknesses varying from 1-3.6 µm. 4 samples have been artificially doped to improve their pinning landscape whereas 3 have not. Of the 4 enhanced samples, the 2 from SuperPower are zirconium doped with the aim of producing more 3D pinning sites [291]. The SST EuBCO sample was doped with barium zirconate, and therefore should contain some nanorod-like structures parallel to the REBCO c-axis [187]. The Bruker sample is so-called 'double-disordered' thus should contain both RE$_2$O$_3$ nanoparticles and nanorods parallel to the REBCO c-axis [292].

Table 3-1: Samples Available for this work

Manufacturer	**Designation**	**Year**	**Rare Earth**	**REBCO Layer thickness [µm]**	**Substrate material / thickness [µm]**	**Protective Layers**	**Artificial Pinning**
Bruker [137], [292]	Br18	2018	Y	2.0	SS / 100	Ag	Double-disordered*
STI [170]	STI17	2017	Gd	3.6	c276 / 60	Ag & Cu	None
Fujikura [140], [293]	Fu18	2018	Gd	2.0	c276 / 50	Ag & Cu	None
SST [187]	Sh19_Gd	2019	Gd	1.8	c276 / 50	Ag	None
	Sh19_Eu	2019	Eu	2.4	c276 / 50	Ag & Cu	BaHfO$_3$
SuperPower ** [154]	SP11	2011	40% Gd 60% Y	1.0	c276 / 50	Ag & Cu	7.5% Zr
	SP17	2016	50% Gd 50% Y	1.2	c276 / 50	Ag & Cu	7.5% Zr

*: Double-disordered CCs are made by both varying the ratio of the feedstocks used to make the YBCO layer, thus varying its stoichiometry and introducing barium zirconate (BZO) precipitates. **: Details provided directly from the manufacturer.

3.2 Measuring Superconductivity

Determining the location of the critical surface – $J_c(B, T)$ – of REBCO samples can be achieved using two methods.

3.2.1 Transport Current Measurements

In this method, a REBCO sample of uniform cross section is controlled at a set temperature and subjected to an applied field before a varying current (I_{sc}) is applied. The resultant voltage (V_{sc}) along a set length of the sample is then measured and I_c is determined by fitting the power law expression to the resultant *I-V* curve:

$$V_{sc} = E_c L (I_{sc}/I_c)^n \tag{3-1}$$

where L is the length of the sample with the smallest uniform cross section or distance between voltage taps (whichever is shorter), $I_c = J_c wt$ is the critical current, n is the power law exponent extracted from the *I-V* curve (typically n=10-40 [84]), w and t are the superconducting layer width and thickness respectively, and E_c = 1µV/cm is the critical electric field along the superconductor used to define I_c. T_{c0} can also be determined by applying a constant J_c to the sample and monitoring the resistivity whilst changing the temperature through T_{c0}. These are the methods used in the Cold Irradiation Experiment (CIE) described in chapters 6 & 7.

3.2.2 Magnetometry Measurements

In this method, a sample of known dimensions is subjected to a changing magnetic field to induce circulating irreversible supercurrents ($\boldsymbol{J_{irr}}$) within the superconducting volume. This leads to an effective irreversible magnetisation in the sample (M_{irr}) that can be measured:

$$M_{irr} = \frac{1}{2V} \iiint_V (\boldsymbol{r} \times \boldsymbol{J_{irr}})\, dV \tag{3-2}$$

By monitoring how the sample M_{irr} varies over time for changing (B, T), various of its properties can be determined. For example, T_{c0} can be determined by zero field cooling (ZFC) a sample, applying a field and then monitoring the magnetic moment as the temperature increased through T_c. This type of experiment is known as an m-T sweep. Fields of ≈2-5mT are used to determine T_{c0} but higher fields are used to determine $B_{irr}(T)$ (e.g. [294]).

$J_c(B, T)$ can be determined by ZFC the sample to a set temperature and then monitoring the moment whilst varying the applied magnetic field up to some maximum value at a constant rate ($dB_{app}/dt = \dot{B}$). Due to the inductive nature of the supercurrents, when the superconductor is fully saturated with flux[15], the difference in $M_{irr}(B,T)$ – ΔM_{irr} – between the measured magnetisation when $\dot{B}$ is

---

[15] Often referred to in the literature as the sample being in a critical state

positive (M_+) and negative (M_-) can be used to calculate $J_c(B_{app}, T)$ using Bean's model for a cylindrical sample [295], [296]:

$$J_c(B_{app}, T) = \frac{3}{2R}\Delta M_{irr}(B_{app}, T) \qquad \text{where} \qquad \Delta M_{irr}\left(B_{app}, T\right) = M_+ - M_- \tag{3-3}$$

This expression[16] is widely used in the literature due to their simplicity, despite more rigorous treatments existing (e.g. Yamasaki [297] and Maratari [298]) that relax many of Bean's original assumptions [295] ($n \to \infty, J = J_c$ everywhere if $E \neq 0, J = 0$ when $E = 0, J \upuparrows E$) but require significantly longer experiments. A further extension of Bean's model, developed by Wiesenger and coworkers [295], [296], [299], is to consider whether the circulating currents in a sample act to impart a self-generated field of sufficient magnitude to affect its properties. These self-fields act to modify the field felt by the sample, are generated in a direction antiparallel to $\dot{B}$, are highly dependent on sample size and shape and can significantly affect the sample properties, particularly at low field.

Finally, the definition of E_c for magnetisation measurements is complicated by the electric field not being equal at all locations in the sample. This was studied by Brandt et al. who showed for a cylindrical sample that [300]:

$$E(r) = -\frac{\dot{B}r}{2}\hat{\phi} \tag{3-4}$$

where $0 < r < R$, R is the sample radius and $\hat{\phi}$ is the rotational unit vector in the cylindrical co-ordinate system. Given that the supercurrent circulating at larger values of the radius contribute most to the generation of ΔM_{irr} (Figure 3.2c), it is assumed that $E_c \approx E(R)$ for this work. This type of experiment is known as an m-H loop.

In this thesis, a vibrating sample magnetometer (VSM) system in conjunction with a Quantum Design (QD) Physical Property Measurement System (PPMS) was used. In these devices, a sample (assumed to be point-like) is vibrated with known frequency and amplitude within a gradiometer. The gradiometer is connected in series with counter rotation coils above and below the gradiometer to remove signals from background magnetic fields. The alternating current generated in the gradiometer is converted to an alternating voltage by a Superconducting Quantum Interference Device (SQUID). The voltage measurement can be converted to a measured magnetic moment using a calibration based on the measurements taken for a sample of known magnetic moment ($m = MV$). QD provide a cylindrical palladium reference sample of ϕ2.8mm x 3.8mm with a known susceptibility of 5.25×10^{-6} emu/g/Oe for this purpose. Various factors need to be accounted for to

---

[16] and its equivalent for rectangular samples

calculate the true sample moment from the measured moment. These include differences in the shape between the sample being measured and the reference sample, axial and radial alignment with respect to pick-up coils, accounting for background and accounting for sample movement in the holder. The PPMS system used can apply magnetic fields parallel to the gradiometer cylindrical axis of $\pm$12T with a field uniformity of better than 0.01% and a maximum sweep rate ($\dot{B}$) of 5mT/s [17]. With respect to temperature, it can sweep between 1.8 K to 300 K, and the standard error in the measured moment is $6\text{x}10^{-7}$ emu + $3\text{x}10^{-7}$ emu/T [301].

These methods and equipment are exclusively used in the room temperature irradiation experiments described in chapter 5, where the specific experimental details are given.

3.3 Electron Microscopy

Electron microscopy techniques can be used to directly image a material, and facilities were made available to me for this work by the David Cockayne centre for Electron Microscopy (DCCEM). In these devices, electrons are accelerated towards a sample at between 10-300keV (E_{beam}), giving them a de Broglie wavelength ($\lambda_{db} = h/\sqrt{2meV}$) of 2-12pm. If the sample is thin (<200nm), many of the electrons are transmitted through the sample and the resultant images can be captured using a CCD camera. This is known as Transmission Electron Microscopy (TEM) and has a typical image resolution of 0.1-0.2nm [302], [303], allowing individual atoms to be distinguished. If the sample is thick (>10µm), each electron can either be elastically scattered back towards the sample surface or it can transfer part of its energy to one of the surface atoms. The latter process leads to either electrons being ejected from target atoms (secondary electrons) or by generating transitions of atomic electrons from higher energy levels to vacant lower levels, emitting either an X-ray or outer-shell (Auger) electron, both of which have energies characteristic of the atom. By detecting the intensity and/or energy of any of these four signals – backscattered electrons ($E \approx E_{beam}$), secondary electrons (low E), Auger electrons or emitted X-rays – as the electron beam is scanned over the surface, the topography and chemistry of the sample can be studied. Each signal has their unique use; secondary electrons allow high resolution imaging of the surface (SE images), back scattered electrons can be used to determine changes in the average atomic mass across the sample surface (BSE images) and can generate crystallographic information about the sample from analysis of variations in angular intensity of the backscattered electrons (EBSD) whilst determining the energy of the emitted Auger electrons (AES) or X-rays (EDX) can be used to determine spatial variations in composition over the sample surface for low Z and mid-to-high Z materials respectively [303], [304].

---

[17] Limited by equipment owner. 3mT/s to $\pm$16T.

Two scanning electron microscopes (SEM), both made by Carl Zeiss Ltd, were use during this work, referred to hereafter as the EVO and the MERLIN. The EVO was the DCCEM entry level SEM. It has a tungsten tip electron source and can be used for basic imaging purposes, EDX and EBSD with a resolution of up to 10 nm at E_{beam} = 15keV. The MERLIN is a step up from the EVO and is equipped with a field emission electron gun to increase the achievable image resolution up to ≈1nm at E_{beam} = 15keV. Although not fitted with an EBSD detector, it is equipped with EDX and backscattered electron detectors as well as conventional SEM and high efficiency InLens SE detectors to increase resolution and allowing Z contrast between different materials. It also has a plasma cleaning system to allow sample cleaning on the fly, and a charge compensation system to reduce the image blur on insulating samples [305].

3.4 Sample Manipulation

Commercial REBCO CCs typically consist of a REBCO layer deposited on a substrate which is then enveloped in stabilising and protective layers of silver and copper, as described in chapter 2. In this section, techniques used to modify REBCO CCs so that their REBCO layer thickness could be determined and their REBCO layer could exposed and manipulated to allow further experimentation are described.

3.4.1 Cross Sectioning

Cross sectioning of CC samples was achieved using the procedure shown in Figure 3.1. First a ϕ3 mm diameter disk sample was punched from the central axis of each CC. This was then assembled slightly off the centre line (Figure 3.1, ℄) onto an appropriate blade and polished in a Precision Ion Polishing System (PIPS) using 6keV argon ions until the REBCO layer was exposed and sufficient of the overhanging disk sample was removed to allow the REBCO layer to be viewed in a direction parallel to the REBCO layer’s (a, b) plane using an SEM. An example of SE images produced using this method are shown in Figure 3.1.

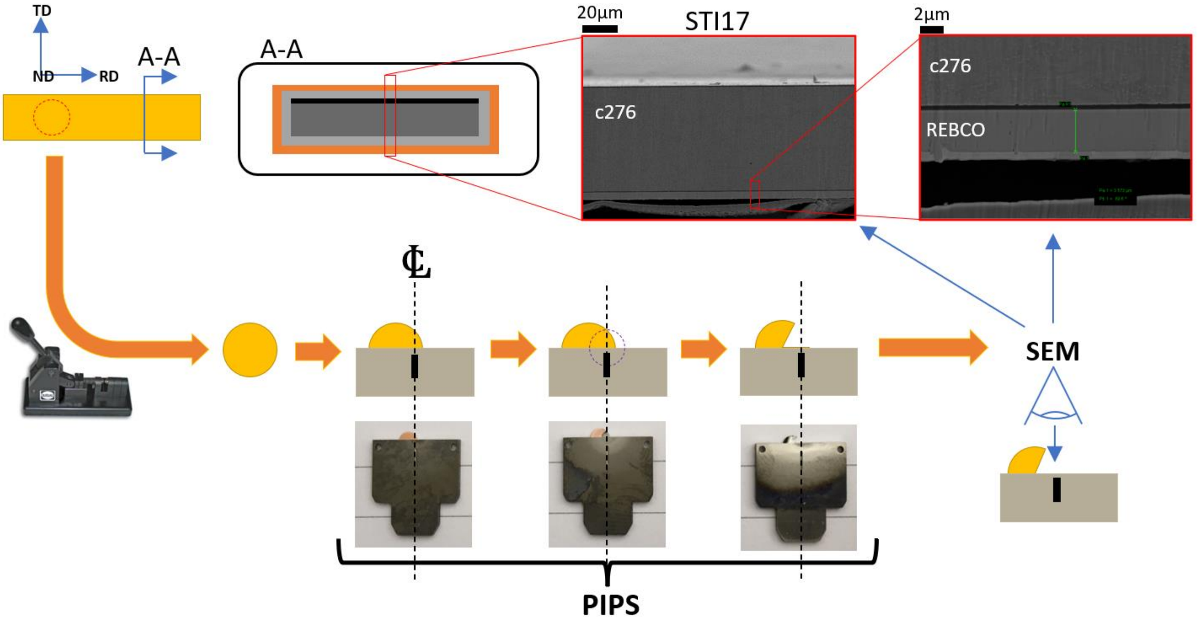

Figure 3.1: Process used to cross section a REBCO CC using the PIPS, as described in the text. Rolling direction (RD), transverse direction (TD) and normal direction (ND) of the CC is indicated in at the top left. A-A: Schematic cross-section of a REBCO CC with protective layers in place. SEM images at top right are an overview (left) of the STI sample cross section and a close-up on the REBCO and buffer layers (right). The bottom set of figures illustrates the process of exposing the CC's cross section: a φ3mm disk is punched from a CC and then mounted to PIPS blade slightly off centre. 6keV argon ions are then used to remove volumes of the CC until the REBCO layer is exposed and sufficient of the overhanging disk sample is removed to allow the REBCO layer to be viewed in a direction parallel to the REBCO layer's (a, b) plane using an SEM.

3.4.2 Exposing a coated conductor's REBCO Layer

As commercial CCs are produced with stabilising and protective layers of silver and copper as described in chapter 2, experimenting on them required that the REBCO layer first be exposed. In the literature, this is typically achieved using wet etching to remove the layers of silver and copper. Although a great many solutions can be used to dissolve these metals (see [306] for an extensive review), successful etching of these layers without damaging the underlying REBCO or substrate has been achieved during this work using the following process [307]:

1. An Iron (III) chloride solution etch (60g $FeCl_3$: 100ml DI-H_2O) was used to remove the copper layer. This reacts with the copper to form $CuCl_2$, which is soluble in water. Once all copper is removed, this then also reacts with the silver layer, leaving a surface layer of AgCl which is insoluble in water.
2. Etch in a 1:1 mixture of 30% aqueous solutions of H_2O_2 and NH_4OH. The NH_4OH dissolves the AgCl layer and the H_2O_2 reacts with the silver to create AgOH which is soluble in NH_4OH solution.

If the stabilising copper layer is not present, the process is simplified to just step 2. The effects of etching CC to expose the REBCO layer of ϕ3mm disk samples, like those used in chapter 5, and of storing exposed REBCO in dry air were evaluated using magnetometry measurements (section

3.2.2). These results (Figure 3.2a&b) show that the etching process results in an insignificant change to T_c but reduces the measured moment during m-H loops in the punched disk samples by 12-14% at all fields. The former result implies that the REBCO that remains is pristine and, given this result and that the punching action is most likely to damage REBCO volumes at higher radius, the latter result implies that punching exposed samples damages more of the outer radii of REBCO than unexposed samples. Given that the outer radii of the REBCO layer contributes a proportionately larger fraction of the total M_{irr} than inner radii (equation 3-2), the fraction of lost sample diameter that would lead to this drop in sample moment was analysed. The cumulative fraction of M_{irr}, calculated assuming Bean's assumptions, with increasing radius as a function of radius is plotted in Figure 3.2c with regions marked representing volumes which each contribute 10% of the total M_{irr}. This analysis showed that losing 12-14% of the total M_{irr} would require a reduction in the sample diameter by 4.1-4.9%, equivalent to ≈ 125-145 µm for a ϕ3mm disk sample. The implications of this source of error, along with others, for magnetometry measurements are discussed further in chapter 5.

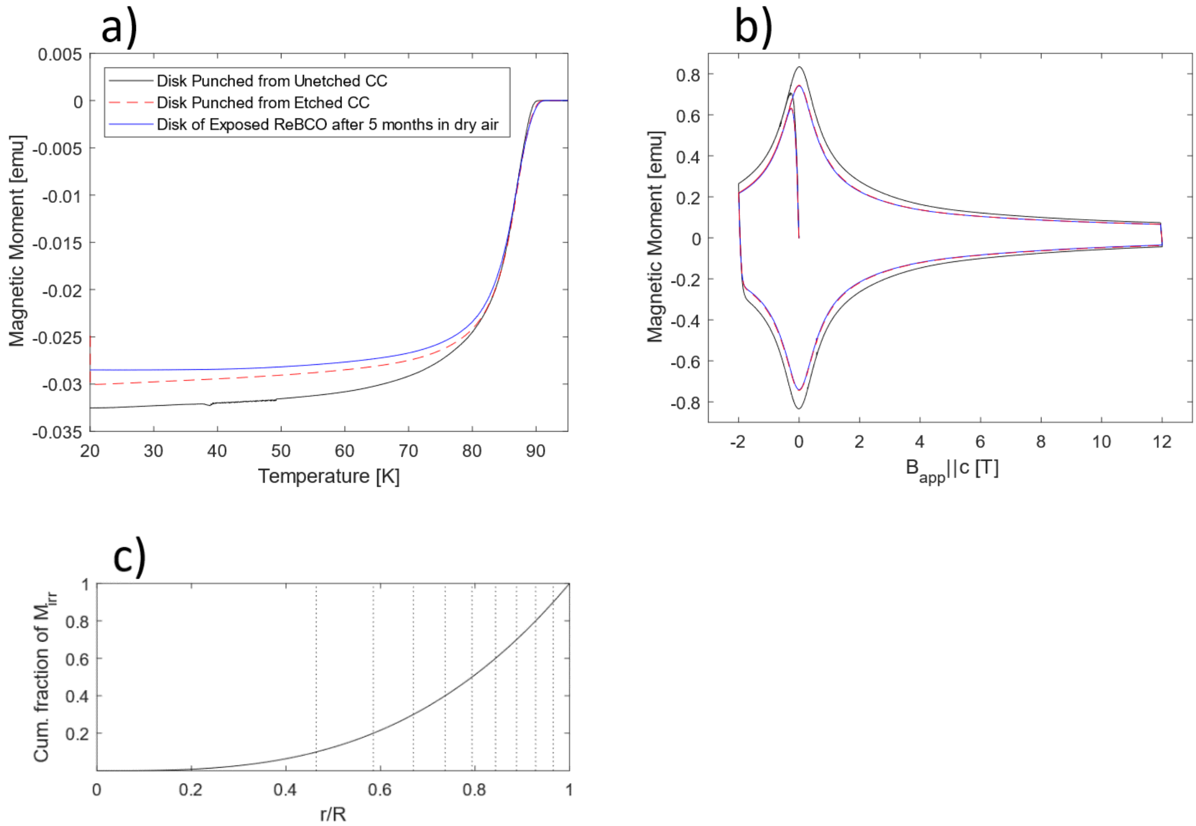

Figure 3.2: Comparison of a) m-T sweep and b) m-H loop measured sample moment comparing the effects of punching a φ3mm disk sample from unetched SP11 CC, a SP11 CC with the REBCO layer exposed by wet etching and the same etched SP11 CC after it had been stored in dry air for 5 months; c) cumulative fraction of the total magnetic moment due to induced supercurrents in a cylindrical sample of REBCO. Each section demarked denotes a radii region that generates 10% of the total sample moment.

Once exposed, the REBCO layer may need to be further manipulated. For example, many transport current testing rigs have a maximum current rating (e.g. [83]). If the current carrying capacity of the

CC is larger than this, J_c cannot be determined. In this case, a combination of photolithography (expanded on in section 6.2.1.5 [308], [309]) and wet etching can be used to pattern smaller features into the REBCO layer, reducing its width and therefore its cross-sectional area. Although not available for this work, success has also been reported when patterning REBCO with laser micromachining [310] (e.g. Terzieva et al. [311]).

This process of patterning REBCO using photolithography and wet etching has been extensively investigated in the context of developing passive and active electronic components [312]. Wet etchants that have been successfully used to etch REBCO without excessive undercutting or damage to substrate layers are several 0.1M di- and tri-carboxylic acid solutions (EDTA, Sucinic, Citric, Adipic, Oxalic, Malonic, Tartaric acids [161], [312], [313]), phosphoric acid ([309], [314]**)** and 1% nitric acid solution. The etch rates of these 3 groups were <10nm/s, <120nm/s (Figure 3.3a) and up to 200nm/s respectively. It has also been shown that treating the resultant REBCO surface with a 0.5% solution of bromine in methanol has the effect of repairing surface damage [315]. In this work, 0.7M H_3PO_4 solution was used based on the advice of a colleague experienced with the process which gave a good optimum between REBCO etching rate (Figure 3.3a) and not excessively undercutting the photomask.

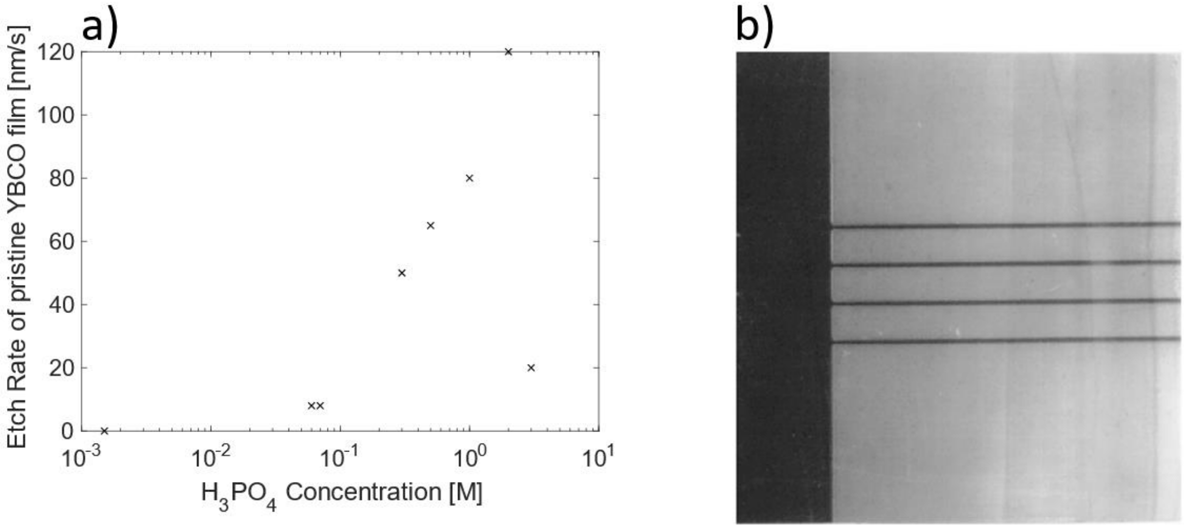

Figure 3.3: a) Pristine YBCO HTS film etch rate (y-axis) versu H_3PO_4 etchant concentration x(-axis); b) A patterned HTS film with linewidth of 5 µm made using a combination of photolithography and H_3PO_4 etching. Both reproduced from figures and data in [309].

3.5 Irradiation Simulation Tools

In this section, the tools used to simulate irradiation damage during this work, first alluded to in chapter 2, are described. These methods were used during the work described in chapter 4.

3.5.1 FISPACT-II

The FISPACT-II code allows the effects of nuclear transmutation and radioactive decay in a material subject to irradiation by a given neutron spectrum to be simulated over time [223]. Its many uses include assessing the compositional changes in different materials subject to similar irradiation conditions (Figure 3.4a) [316], calculating the expected levels of radioactivity of nuclear reactor components during their working life and the expected time required for them to become low level nuclear waste (Figure 3.4b) [44]. It achieves this by solving the following rate equation:

$$\frac{dN_i}{dt} = \sum_j \left(\lambda_{ij} + \phi_n(t)\sigma_{ij}\right)N_j \tag{3-5}$$

where N_i and N_j are the number densities of nuclides i and j respectively, λ_{ij} and σ_{ij} are the decay constant and reaction cross section of nuclide j producing nuclide i and $\phi_n(t)$ is the neutron projectile flux. The only exception is where i and j are the same nuclide when λ_{ij} and σ_{ij} are the total decay constant and total reaction cross section of nuclide j thus accounting for the depletion of said nuclide. The values of λ_{ij} and σ_{ij} used can be taken from any of the several datafiles (e.g. TENDL [317], [318]) introduced in chapter 2.

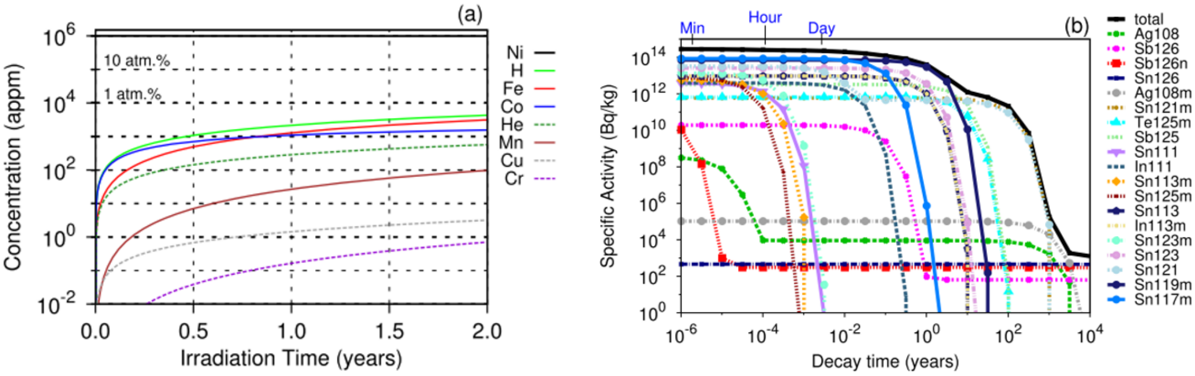

Figure 3.4: a) Elemental Transmutation response of pure nickel subjected to irradiation in the first wall of the EuroFusion DEMO. Shows concentration of the impurity (y-axis) versus the irradiation time (x-axis); b) Specify activity (y-axis) of elemental Tin (Sn) with increasing time (x-axis) after removal from EuroFusion DEMO's first wall following irradiation for 2 years at full power. Both reproduced from [223].

3.5.2 SPECTRA-PKA

As discussed in section 2.3, the rate at which neutron irradiation leads to a particular nuclear reaction (r_{ij}) is governed by its reaction cross section (σ_{ij}). Given that each neutron-target atom interaction is unique, the probability that a neutron-atom collision undergoing a particular reaction will lead to a PKA of a particular energy is also unique. Thus, SPECTRA-PKA uses σ_{ij} and each reaction's calculated outcome probability (P_{ij}), both processed using the GROUPR module of the NJOY code [319] from the TENDL nuclear datafile [318], to calculate the cross section of a neutron with energy E_n colliding with a target atom, initiating the reaction $i \rightarrow j$ and producing a daughter

PKA with an energy E_{pka}. This calculation is complicated by nuclear data and neutron spectra being presented as histograms containing several energy bins – typically 709 between 10^{-5} eV and 1 GeV [224] – hence if the neutron has an energy in bin ‘n’ and the recoiling PKA has energy in bin ‘k’:

$$\sigma_{kn}^{ij} = \sigma_{ij} P_{ij}(E_{PKA}^{k}, E_n) \tag{3-6}$$

where σ_{kn}^{ij} [barns] is the recoil cross-section matrix for reaction $i \rightarrow j$. Figure 3.5a shows an example of a σ_{kn}^{ij} spectrum for the ^{56}Fe(n, elastic)^{56}Fe reaction channel. This demonstrates that each neutron gives rise to a spectrum of PKAs of different energies due to each reaction channel, of which there are hundreds specified in the TENDL datafile [224]. SPECTRA-PKA works by using σ_{kn}^{ij} to calculate the number and energy of the PKAs of each species due to neutrons of a given spectra colliding with each target atom species and then summing them over a chosen neutron spectrum, weighted by their atomic fraction of the target material to reflect its composition (w_i), to get the volumetric PKA rate spectra for all the PKA species mobilised ($p\dot{k}a_k$ [pka/s/cm^3]):

$$p\dot{k}a_k^{ij} = \sum_n w_i \sigma_{kn}^{ij} \phi_n \qquad \text{and} \qquad p\dot{k}a_k = \sum_i \sum_j p\dot{k}a_k^{ij} \tag{3-7}$$

where an example PKA rate spectrum is shown in Figure 3.5b. SPECTRA-PKA then goes on to calculate the damage energy (T_d) of each PKA species using LSS theory (equation 2-13) [211] and uses that to determine the damage level of each reaction channel using the NRT-dpa model (equation 2-12). In this way, the effects of a given neutron spectra on each target species and reaction channel can be distinguished, allowing the dominant damage vectors to be identified.

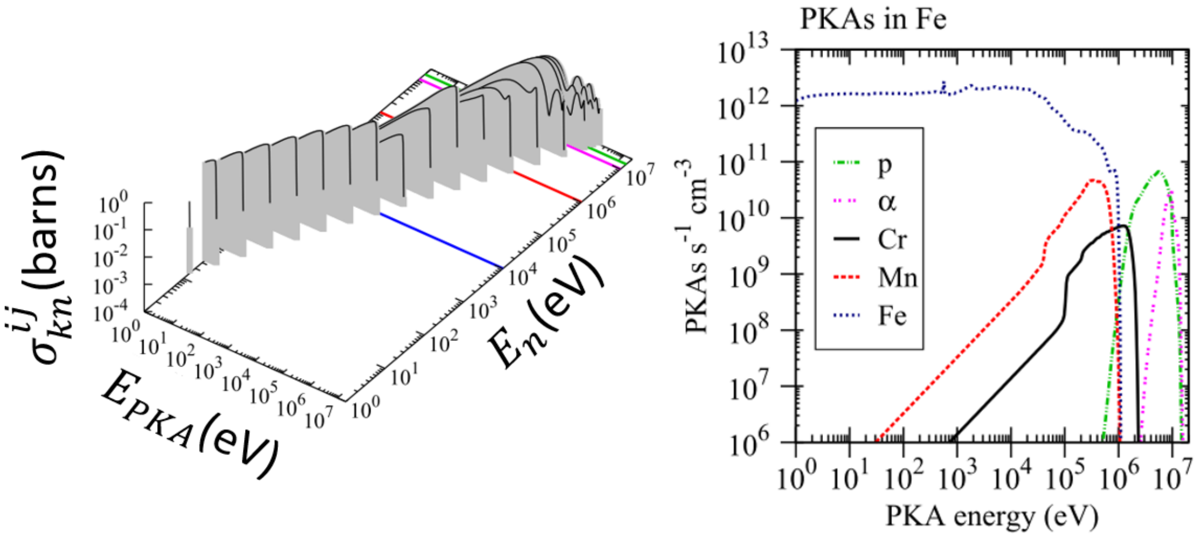

Figure 3.5: a) Example recoil cross-section matrix (z-axis) for the elastic scattering of neutrons on ^{56}Fe of a neutron at energy E_n (x-axis) resulting in a ^{56}Fe ion recoiling at E_{PKA} (y-axis). Both E_n and E_{PKA} are in units of eV. b) resultant PKA spectrum (PKA energy (x-axis) versus volumetric pka rate (y-axis)) for all reactions producing protons (p), alpha particles (α), chromium (Cr), manganese (Mn) and iron (Fe) excited in a natural iron target irradiated with EuroFusion DEMO first wall neutrons. Reproduced from [320].

3.5.3 SRIM

The SRIM code [321] uses Monte-Carlo methods [322] to simulate the processes by which energetic ions lose their energy in matter, with the aim of evaluating how ion irradiation leads to lattice damage, energy deposition and ion implantation within a target material. SRIM achieves this by calculating the outcome of both the discrete nuclear collisions and the continuous action of the material's electron clouds, which are assumed to act independently, on a projectile ion. SRIM's computational efficiency relies on the assumption that the interactions that lead to relatively large (>1°) deflections in the ion's path are rare and therefore most interactions are assumed to have a negligible impact on the ion trajectory, unless they are compounded over many small interactions. The code therefore makes the simplification that the energetic ion traverses a length L_{FFP}, calculated based on inserting a random number into a probability function governing the likelihood of a collision taking place at some point, without deviating. At L_{FFP} the ion is considered to have collided with a target atom and energy loss calculations are undertaken. For the ionic interactions with the target's electron cloud, the energy loss is calculated based on the work of Oen and Robinson [323], with this energy loss spread through the material evenly along L_{FFP}. For the nuclear interaction, the aforementioned probability function allows the impact parameter[18] of the collision to be calculated based on L_{FFP}, the target density and another random number. The impact parameter is then used to calculate the proportion of the ion energy that was transferred to the target atom and the subsequent deflection angles of both ion and target atoms to be calculated based on the solution to the general orbit equation [206] of Bierseck and Haggmark [230], modified for SRIM to use the universal screened Coulomb potential function by Ziegler et al. [227]. This process continues until the incident ion energy is less than the lowest TDE of the target and repeats for several energetic ions (typically $>10^5$) until there is sufficient data about the varying outcomes of each ion for statistics about the ion implantation and energy deposition to be calculated as a function of depth into the material. SRIM allows 2 options for determining lattice damage; either the number of displacements generated by each lattice atom excited by the main projectile ion is calculated using the NRT-dpa model (quick SRIM) or the trajectory of each excited lattice atom, and all the subsequently excited atoms, are tracked in the same manner as the main projectile ion until the energy of all of them has dropped below the target lowest TDE (full cascade SRIM).

Although accessible and easy to use [321], whether SRIM's lattice damage estimates are comparable with those calculated in other ways is the subject of continued debate [231], [324]. For example, in monoatomic targets, both full cascade and quick SRIM calculations have been shown to

---

[18] The close distance the 2 colliding particles would get it they had not otherwise interacted.

overestimate the number of lattice displacements caused by high energy ions when compared with MD simulation, and by a larger margin that the simple NRT-dpa model overestimation [324]. It has also been reported that the electronic stopping power used by SRIM overestimates the stopping of high Z projectiles, leading to measurable differences in implanted ion profiles predicted by SRIM and measured during experiments [231] (Figure 3.6). Despite these inaccuracies, the use of full cascade SRIM to predict the ion irradiation response of multi-elemental targets is recommended only as long as the critical data about how the SRIM calculation has been performed is provided [231], [324]. For all the SRIM calculations in this work, the TDEs used were based on those published in MacFarlane et al. [319], as these were also used by the FISPACT-II code. Only full cascade SRIM was used for REBCO targets, high Z projectile ions are avoided and the lattice binding and surface binding energies were both set to 0 eV as advised by Stoller et al. [324].

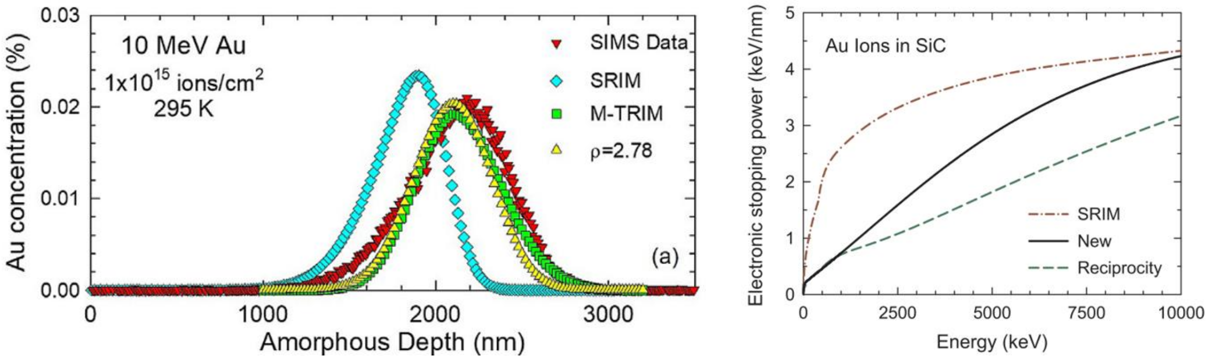

Figure 3.6: a) full cascade SRIM (cyan), M-TRIM (green) and SRIM predictions using a reduced density (yellow, ρ=2.78 g/cm^3 (ρ_{SiC}=3.21 g/cm^3)) and Secondary-Ion Mass Spectroscopy (SIMS) results (red) for irradiation of SiC with 10 MeV gold ions at 295 K to 10^{15} ions/cm^2; b) comparison of electronic stopping powers (y-axis) versus projectile energy (x-axis) for gold ions into SiC used in SRIM with those experimentally derived by Jin et al. [325]. *Reproduced from* [231].

3.6 Ion Irradiation

Ion irradiation of the samples described in this work was performed at the Ion Beam Centre at Surrey University (SIBC) using their high energy implanter shown in Figure 3.7. This beam was capable of accelerating ions up to 2 MeV (❶) and delivering a beam current of up to 10mA. On their way from the accelerator, ion beams are focused (❸) and then ions of the correct charge and mass are selected using a selector magnet (❷). These ions are than focused again before being sent through a rastering magnet (❹) that scans the beam over an area containing 4 Faraday cups (❼) encircling a hole (❻) to allow the beam through to the sample stage (❽) (Figure 3.7a). The 2 MeV beamline end station consists of 2 parts, the stationary part that supports the sample and forms part of the vacuum vessel (❽) and the sample mounting stage that can be actuated to allow any of the 12 positions to be put in the path of the beam (Figure 7.3b). Experiment specific aspects of the use of these facilities are left to the appropriate chapter.

Whilst in electron microscopy, beam rastering is used to create an image over an area of a sample, beam rastering at the SIBC is used to create an area over which the beam current density, averaged over a rastering cycle, is constant and uniform over a relatively large area. At the SIBC, the rastering magnet is several metres from the sample stage so ions can be assumed to be moving perpendicular to the sample stage surface when they impact it. Under this assumption, the beam current (I_b [A]), current density (J_b [A/cm^2]) and the resulting fluence (Φ [#/cm^2]) to the sample stage are related by the following expressions:

$$J_b = \frac{I_b}{X\,Y} \qquad \text{and} \qquad \Phi = \frac{J_b}{e\,Z}t \tag{3-8}$$

where X and Y (both [cm]) are the horizontal and vertical dimensions of the scanning area of the beam at the sample stage respectively, 'e' [C] is the electronic charge, 'Z' is the ionisation state of the beam ions and 't' [s] is the length of time the sample is exposed to beam ions. At the SIBC, I_b and the rastering properties of the beam are set up so that all 4 Faraday cups[19] (Figure 3.7a, ❼) read an equal current, indicating that the beam going through the hole and impacting the sample stage has a uniform rastering-cycled-averaged J_b. Φ is measured at the SIBC using charge collection at the sample stage and on the Faraday cups, allowing dose to be delivered to the sample with an error of $\pm$1% [326].

The damage (ν) and ion implantation (k) metrics calculated with full cascade SRIM, supplied to the user in units of vacancies Å^{-1} ion^{-1} and impurity ions cm^{-3} per ion fluence respectively (Φ), are related to the $dpa(x)$ and beam ion concentration ($appm(x)$ or atomic parts per million target atoms) with depth into the sample parallel to the beam path (x) by the following expressions:

$$dpa(x) = 10^8\,\frac{\nu(x)}{n_T}\,\Phi \qquad \text{and} \qquad appm(x) = 10^6\,\frac{k(x)}{n_T}\,\Phi \tag{3-9}$$

where n_T [#/cm^3] is the target material's number density [327]. By combining SRIM calculations and the SIBC's control over their beamline's character, it allowed me to deliver a carefully chosen fluence of energetic ions to a sample's surface and thus control the rate of sample damage and/or ion implantation.

---

[19] All with a 0.6cm^2 collection area.

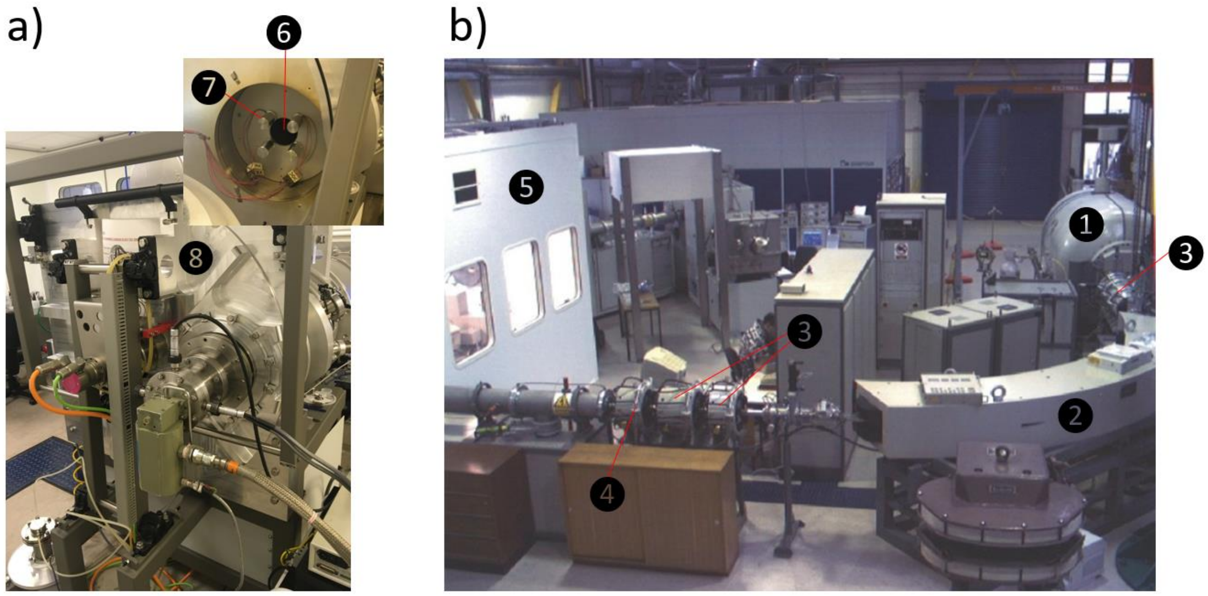

Figure 3.7: The layout of the SIBC's 2 MeV beamline. a) the beam line end station in the clean room. Inset: the hole allowing the beam access to the samples surrounded by 4 Faraday cups; b) overview of the beamline outside the clean room. Labels – 1: the accelerator, 2: beam ion charge and mass selector magnet; 3: beam focusing magnets; 4: rastering magnet; 5: the cleanroom; 6: hole allowing beam access to sample stage; 7: faraday cups and 8:sample stage. For more details, see figure 7.3.

4 Simulation of Neutron Damage in REBCO

As shown in chapter 2, experiments involving the irradiation of REBCO have been carried out using several sources (fission, heavy and light ions) to assess changes in superconducting properties, with and without performance enhancers such as artificial pinning centres, and to do more in-depth microstructural characterisation. Given that this thesis aims to investigate REBCO's response to fusion neutrons, this chapter aims to use the analytical tools SPECTRA-PKA and FISPACT-II to assess the damage accumulation in REBCO due to irradiation by neutrons from a variety of fusion and fission sources, with the aim of identifying key similarities and differences between them in terms of lattice damage and impurity build-up. The results are used to examine the effectiveness of using fission neutrons as a proxy for fusion neutrons and, using SRIM, to justify the choice of a particular ion and energy combination as a proxy for neutron irradiation in REBCO going forward.

4.1 Experiment Set-Up

4.1.1 Neutron Spectra

As discussed in section 2.1, there are a wide variety of tokamak designs being conceptualised, each of which has advantages in terms of performance, size, chosen technology utilised and cost (Table 2-1). Despite all these considerations, all have the same issues: the TF coils must be designed to maintain a rated field near-continuously and must also be cost effective. Therefore, the design problem becomes one of optimising TF coil performance and size against the device's rated fusion power output. A major engineering decision will be how much neutron shielding to place between the TF magnet winding and the fusion plasma, as any size increase to accommodate additional shielding has been shown to increase the cost of a tokamak dramatically [12], [14]. It is therefore important to evaluate REBCO's response to fusion spectrum neutrons across the entirety of potential neutron fluxes from completely unshielded (1-10MW/m^2), through to thinly shielded and thickly shielded neutron spectra. This analysis is also important to inform the choice of which ion would be a good proxy for neutron irradiation going forward to chapters 5-7. Given that this evaluation can only be done effectively if spectra of sufficient quality are available, 4 fusion neutron spectra were chosen for this work:

- The unshielded and thinly shielded spectra were taken from the first wall (FW) and inboard toroidal field coil (TF) of Tokamak Energy's ST135 concept [39]. Spectra were calculated using MCNP and taken from voxels on the tokamak's inner midplane on the outer extremity of the centre column (FW) and the TF coil housing (TF).
- Another unshielded spectrum and a thickly shielded spectrum were taken from the FW and inboard TF coil of the 2015/6 design of the EUROFusion DEMO tokamak [44]. As this design

has several variants, the variant containing the helium-cooled Pebble-Bed (HCPB) tritium breeder blanket was used. Both TF and FW spectra taken from the outboard extremity of the appropriate voxels on the tokamak's inner midplane.

To supplement these fusion spectra, and given recent results on the superconducting performance of coated conductors published after fission neutron spectra irradiation in the TRIGA Central irradiation facility (CIF), the TRIGA CIF spectrum was also used [43]. Each neutron spectra, and its associated normalised spectra, are shown in Figure 4.1, with relevant statistics about each spectrum shown in Table 4-1. These show that, due to DT reactions, all fusion spectra have a pronounced peak at $E_n \approx$ 10-20MeV. They also have a relatively high proportion of neutrons with $E_n \approx$ 0.1-1MeV, especially with thick shielding. The TRIGA CIF spectrum, by contrast, has its peak at 1MeV and relatively few neutrons with E_n >5MeV.

Table 4-1: Neutron Spectra Statistics

Neutron Source	Power [MW_a/m^2]	Total Neutron Flux [$n/cm^2/s$]	Time to reach 4.5 mdpa* [s]	Average neutron energy, E_n [keV]	Fraction of fast neutrons (E_n>0.1MeV) [%]
ST135 FW	4.55	7.53×10^{14}	≈ 5,400 (90m)	3,777	79.3
ST135 TF	0.039	3.15×10^{13}	≈ 279,000 (77.5h)	777	50.1
DEMO FW	2.36	6.60×10^{14}	≈ 9,900 (165m)	2,230	53.9
DEMO TF	$\approx 10^{-7}$	2.28×10^{8}	$\approx 6.3 \times 10^{10}$ (1996y)	258	33.5
TRIGA CIF	0.02	2.06×10^{13}	≈ 526,500 (146h)	607	36.6
*: for YBCO					

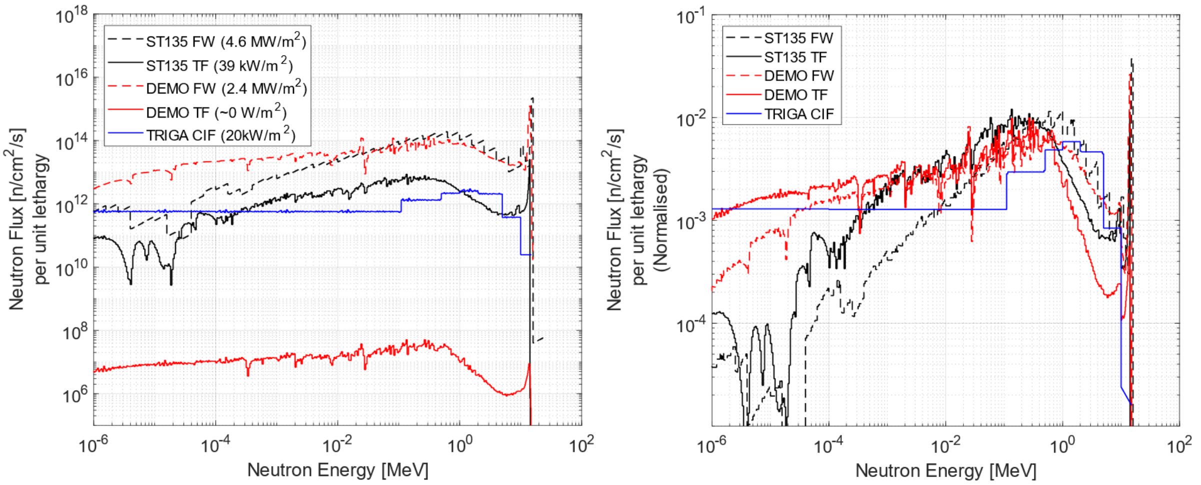

Figure 4.1: a) Neutron spectra (neutron flux per unit lethargy (y-axis) versus neutron energy (x-axis) histogram) used during this work are from Tokamak's Energy's ST135 concept (ST135) [39], *EU DEMO 2015/16 Concept* [328] *and the Vienna TRIGA reactors Central Irradiation Facility* [43]. *Fusion spectra were calculated using MCNP* [42] *and taken from the calculation volumes on the tokamak's inner midplane at the first wall (FW) and the most outboard volume of the toroidal field magnet (TF). b) Spectra from a) normalised with respect to the total fluence.*

4.1.2 Code Inputs

4.1.2.1 SPECTRA-PKA

The SPECTRA-PKA code (section 3.5.2) uses published nuclear data to calculate the spectra of recoils generated in a target material by neutrons of a particular energy of each target species and due to each nuclear reaction. Based on these recoil spectra, the lattice displacements due to each recoil is calculated and then summed over all recoils from the neutron spectrum, allowing the total displacement rate per unit volume in the target material to be calculated. SPECTRA-PKA was set up to analyse YBCO, GdBCO and EuBCO using the material properties in Table 2-3. The relative atomic fractions of each species were set by assuming that each atomic component of REBCO consisted of its naturally occurring isotopes. Data for this, the isotope atomic mass and the mass of the daughter isotope resulting from (n, γ) reactions were taken from the IAEA's live chart of nuclides and references therein [329]. Although REBCO has a complex unit cell containing multiple species in different charge states, each of which has an TDE dependent on the approach direction of the PKA (Table 2-5) [245], SPECTRA-PKA only allows a single value to be input as the material's TDE which is used for all target species. Based on the literature discussed in section 2.4, $E_d = 25$ eV was used for all species with the proviso that adjustments can easily be made as the number of displacements is linearly dependent on E_d[20]. All other SPECTRA-PKA inputs were set to the default values, with 1 exception. ".do_tdam." was set to true so that, for each knock-on, the energy lost to electron interactions was accounted for using LSS theory (equation 2-13) and that this diminished energy was used to determine NRT-dpa (equation 2-12). To allow the resulting damage spectra to have roughly integer values, the damage rate was expressed in displacements-per-target-atom (dpa_t) per year for which the REBCO is irradiated by the source at full power, also known as a full-power-year (FPY). An example input file is shown in appendix A.

4.1.2.2 FISPACT-II

The FISPACT-II code (section 3.5.1) models the time dependent inventory of a target material being subjected to neutron irradiation [223]. Each FISPACT-II calculation was set up using the REBCO material data taken from Table 2-3 and so that calculation specific COLLAPX and ARRAYX files were generated. These files were generated using the nuclear reaction cross sections taken from the TENDL 2017 datafile[21] [318], the nuclear decay data from the 2012 data file and the fission yield data from the GEFY61 data file, all of which are provided with the FISPACT-II software [223], [224]. For each irradiation condition, the neutron bombardment was considered continuous up to an applied

---

[20] Given the roughly linear relationship between T_d and displacements per impact, the conversion factor is $25/E_{d,new}$, hence if $E_{d,new} = 1$eV, conversion factor is 25, if $E_{d,new} = 40$eV, the conversion factor is 0.625.

[21] TENDL 2019 was yet not available.

neutron damage of 10^{-1} dpa. This was achieved using the damage rate calculated by the SPECTRA-PKA code to set appropriate time intervals. An example set of input files is shown in appendix A.

4.2 Results

Given the number of graphs generated, only a relevant subset is presented here. For a complete set of SPECTRA-PKA dpa rate versus recoil energy histograms and FISPACT-II impurity build-up trajectories for the 5 spectra and 3 variants of REBCO, please refer to appendix A.

4.2.1 Lattice Damage

The dpa rate spectra showing the damage rate of the 5 neutron spectra on YBCO are shown in Figure 4.2. These results imply that damage rates can be as high as 26.3 dpa/FPY for unshielded YBCO subject to fusion neutrons, dropping to 0.51 dpa/FPY for thinly shielded YBCO (ST135 TF) and further to 2.2×10^{-6} dpa/FPY for thickly shielded YBCO. TRIGA CIF neutron spectrum irradiation leads to a total dpa rate of 0.27 dpa/FPY for YBCO. A summary of the measured dpa rate for each REBCO variant is shown in Table 4-2.

Table 4-2: Total volumetric PKA production and dpa rates calculated for each fusion neutron spectrum for each type of REBCO.

	Power [MW_a/m^2]	**PKA flux [10^{12} PKA/s/cm^3]**			**Total dpa rate [dpa/FPY]**		
		YBCO	GdBCO	EuBCO	YBCO	GdBCO	EuBCO
ST135 FW	4.55	241	246	239	26.3	25.8	25.6
DEMO FW	2.36	229	245	235	14.9	14.6	14.5
ST135 TF	0.04	11.7	12.3	11.7	0.51	0.49	0.49
DEMO TF	10^{-7}	8.6×10^{-5}	9.4×10^{-5}	8.9×10^{-5}	2.2×10^{-6}	2.1×10^{-6}	2.1×10^{-6}
TRIGA CIF	0.02	8.1	13.0	8.3	0.27	0.26	0.26

Examination of all these dpa rate spectra (Figure 4.2) shows that, despite its low mass, its relative abundance makes oxygen PKAs the most prolific recoil atom, generating > 45% of all lattice damage across all spectra. For the fusion spectra considered, oxygen PKAs become proportionally more prolific as shielding thickness increases as even a small amount of shielding significantly lowers the damage due to transmutation products and lowers the proportion of damage due to barium and copper by ≈5% and due to the rare earth by ≈3% (summarised in Table 4-3). The oxygen recoil energy corresponding to the peak (or peaks) in the dpa rate spectra change with neutron source. For unshielded YBCO, there are two peaks in the oxygen recoil energy spectrum of roughly the same magnitude at ≈70 keV and ≈205 keV. This changes to a single peak at ≈70keV for thinly and thickly shielded YBCO and to a single peak at ≈205keV for TRIGA CIF neutrons.

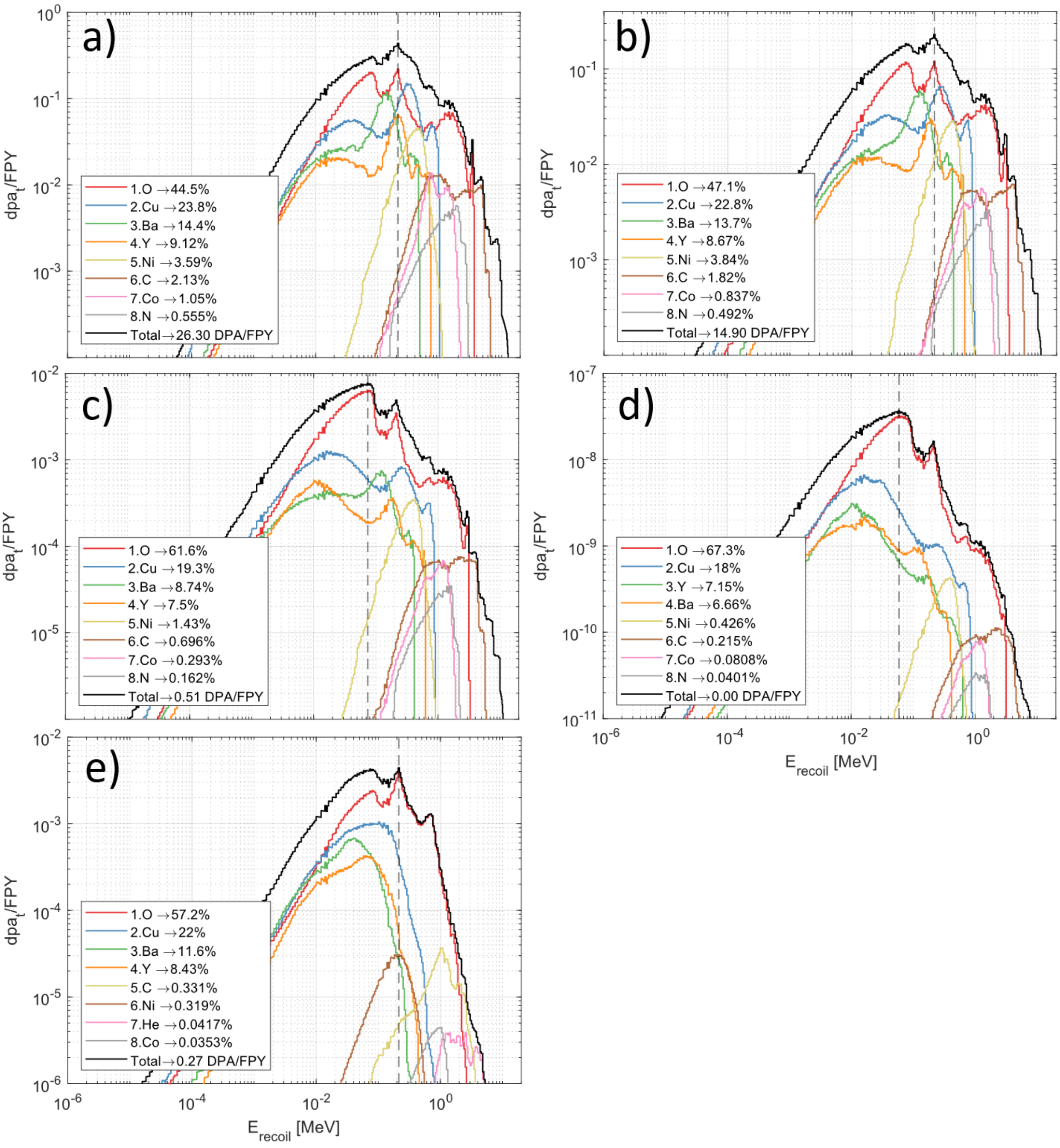

Figure 4.2: dpa$_t$ rate spectra (dpa$_t$ rate (y-axis) versus recoil energy (E$_{recoil}$, x-axis) histogram) for YBCO for different fusion neutron spectra: a) ST135 at the first wall on the tokamak inner midplane, b) DEMO at the first wall on the tokamak inner midplane, c) ST135 at the toroidal field coil on the tokamak inner midplane, d) DEMO at the toroidal field coil on the tokamak inner midplane and in e) TRIGA CIF.

The effect of each neutron spectrum on GdBCO and EuBCO was also examined using SPECTRA-PKA, leading to similar total damage rates (Table 4-2). The effect of rare-earth element on the total dpa rate for each fusion spectra is illustrated in Figure *4.3*, showing that it does not vary significantly for Y, Gd and Eu, especially for the recoil energies that are more prolific.

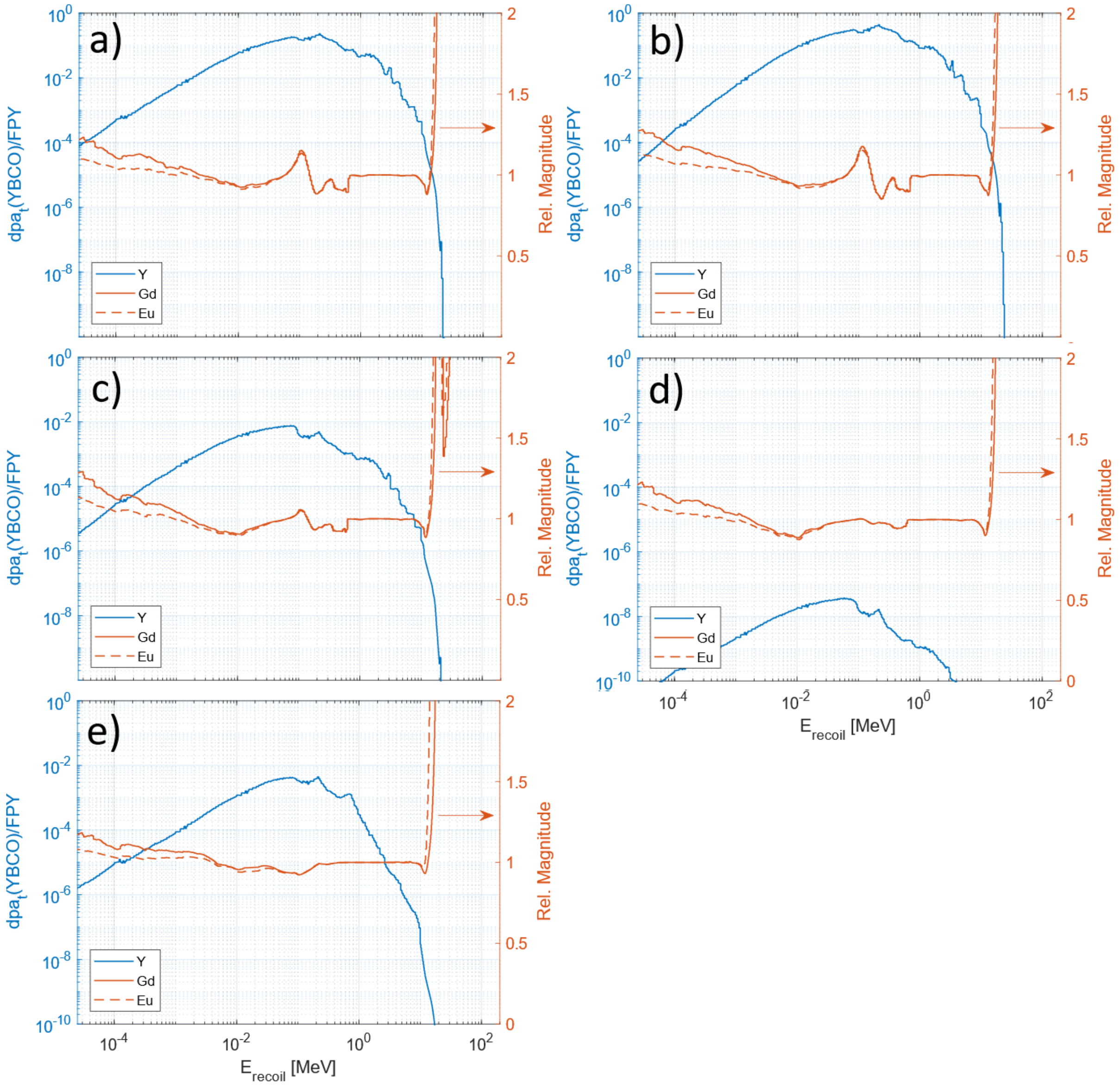

Figure 4.3: Comparing how the rare-earth used effects the dpa$_t$ rate spectra for the fusion neutron spectra. In each graph, the x-axis is the PKA recoil energy (E$_{recoil}$), the left hand y-axis is the total dpa$_t$ rate histogram for YBCO, repeated from Figure 4.2, and the right hand axis is the relative dpa$_t$ rate for each recoil energy in GdBCO and EuBCO compared to that of YBCO. The neutron spectra for each graph are a) ST135 at the first wall on the tokamak inner midplane, b) DEMO at the first wall on the tokamak inner midplane, c) ST135 at the toroidal field coil on the tokamak inner midplane, d) DEMO at the toroidal field coil on the tokamak inner midplane and in e) TRIGA CIF.

Table 4-3: Fraction of the contribution of each self-ion and the transmutation products (ie Rest) to Total dpa for REBCO due to different neutron spectra.

	Power [MW_a/m^2]	REBCO	Contribution of Each Knock-Ons [% total dpa]				
			O	Cu	Ba	RE	Rest
ST135 FW	4.55	YBCO	44.5	23.8	14.4	9.12	8.18
		GdBCO	45.5	24.4	14.7	7.44	7.96
		EuBCO	45.8	24.5	14.8	6.86	8.04
DEMO FW	2.36	YBCO	47.1	22.8	13.7	8.67	7.73
		GdBCO	48.1	23.3	14.0	7.10	7.50
		EuBCO	48.4	23.4	14.1	6.53	7.57
ST135 TF	0.04	YBCO	61.6	19.3	8.74	7.50	2.86
		GdBCO	63.5	19.9	9.00	4.81	2.79
		EuBCO	63.9	20.0	9.06	4.18	2.86
DEMO TF	10^{-7}	YBCO	67.3	18.0	7.15	6.66	0.89
		GdBCO	69.7	18.6	6.89	3.90	0.91
		EuBCO	70.2	18.8	6.94	3.20	0.86
TRIGA CIF	0.02	YBCO	57.2	22.0	11.6	8.43	0.77
		GdBCO	59.2	22.7	12.0	5.25	0.85
		EuBCO	59.6	22.9	12.1	4.60	0.80

4.2.2 Transmutations

The build-up of transmutation products due to irradiation with the 5 neutron spectra was simulated using FISPACT-II and the results are shown in Figure 4.4. The new impurity concentrations at 4.5×10^{-3} dpa[22] and the 2 most prolific contributors for each neutron spectrum are summarised in Table 4-4. This shows that, on average, impurity concentrations of the order of 1-100appm should be expected due to neutron irradiation.

The results show that for the FW spectra the abundance of ≈14MeV neutrons leads to plentiful (x, p) and (x, α) type transmutation reactions, although the resulting proton and helium concentrations are roughly similar to other impurity species. For the TF spectra, however, the decreasing fraction of 14MeV neutrons leads to copper transmutation into nickel and zinc becoming the significant contributor to the impurity build-up in REBCO. Nickel is formed during any copper transmutation reaction that emits a hydrogen isotope, typical of neutron-copper collisions of $E_n > 8$ MeV [330], and zinc forms when unstable isotopes of copper form following neutron absorption (n, γ) reactions, which predominate when neutron energies are low [330].

---

[22] The reason for this choice of dpa is expanded upon in section 4.3.1.1.

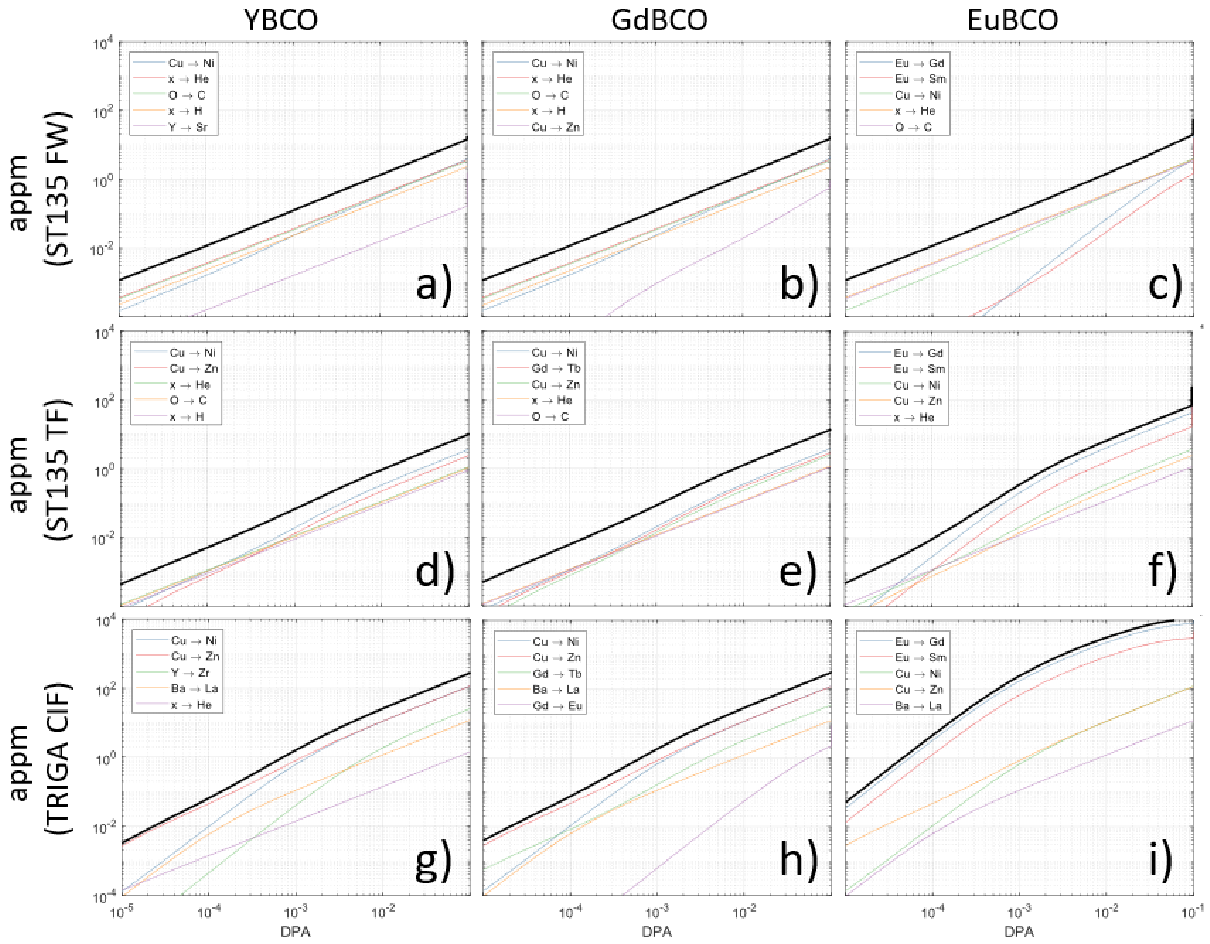

Figure 4.4: Impurity build-up in REBCO due to neutron irradiation as a function of lattice damage measured in dpa for YBCO (a, d, g), GdBCO (b, e, h) and EuBCO (c, f, i) due to ST135 at the first wall (a, b, c), ST135 at the toroidal field coil (d, e, f) and TRIGA CIF (g, h, i) neutron spectra. In the legend, 'x' represents all the reactions that lead to the transmutation product.

Another significant impurity in REBCO due to neutron irradiation is the product of transmutation reactions involving multiple (n, γ) reactions of REBCO's rare-earth, followed by the product's beta decay. This reaction leads to zirconium build-up in YBCO and terbium build-up in GdBCO, with the latter becoming a significant impurity as damage levels increase. In EuBCO this reaction chain leads to gadolinium becoming the dominant impurity at a damage level approaching 10^{-2} dpa, with the resultant impurity levels in EuBCO being far higher than for YBCO and GdBCO. The prevalence of these impurities, especially in EuBCO, is exacerbated in low fluence neutron spectra dominated by low energy neutrons as their concentration is bolstered by the increased prevalence of (n, γ) reactions, due to europium's relatively high (n, γ) cross-section compared to yttrium and gadolinium [331], and there being sufficient time for a significant fraction of each unstable Gd or Eu isotope to beta decay, even those with a long half-life ($T_{1/2}$).

FISPACT-II simulation of REBCO undergoing TRIGA CIF neutron irradiation shows a >10-fold increase in impurity concentration for all REBCO variants than that calculated for DEMO TF, the fusion spectra with the lowest flux and longest irradiation time (Table 4-4). This is most likely due to the higher fraction of low energy neutrons in the TRIGA CIF spectra compared to the fusion spectra.

Table 4-4: Impurity concentration in atomic parts per million (appm) in YBCO, GdBCO and EuBCO due to 5 different neutron spectra at 4.5x10^{-3} dpa (brackets show top 2 impurities and their fraction of the total concentration).

	YBCO [appm]	**GdBCO [appm]**	**EuBCO [appm]**
ST135 FW	**0.52** (27.6% He, 25.6% C)	**0.52** (27.9% He, 25.9% C)	**0.54** (27.3% He, 25.4% C)
DEMO FW	**0.50** (24.1% He, 23.1% Ni)	**0.53** (23.0% He, 22.1% Ni)	**0.76** (24.9% Gd, 16.3% He)
ST135 TF	**0.34** (34.8% Ni, 23.1% Zn)	**0.45** (27.4% Ni, 23.0% Tb)	**2.32** (61.4% Gd, 23.8% Sm)
DEMO TF	**0.78** (41.9% Ni, 40.3% Zn)	**1.74** (46.4% Tb, 19.7% Ni)	**159.6** (51.2% Gd, 48.4% Sm)
TRIGA CIF	**9.26** (45.2% Zn, 43.3% Ni)	**10.3** (42.2% Zn, 40.5% Ni)	**1294** (71.5% Gd, 27.8% Sm)

4.3 Discussion

4.3.1 Neutron Irradiation

In this section, the SPECTRA-PKA and FISPACT-II results are discussed in relation to the work of Fischer et al. using Vienna TRIGA CIF neutrons. The aim is to determine appropriate lattice damage levels for proxy irradiation experiments and discuss the use of TRIGA CIF neutrons as a proxy for fusion neutrons.

4.3.1.1 Response of Fischer et al. samples to TRIGA neutrons

In their 2018 paper, Fischer et al. [21] reported on an extensive study of the effect of TRIGA CIF fission spectrum neutrons on several commercially available YBCO- and GdBCO-based CC samples (Figure 2.19b&c). Their results showed that the I_c value at (30 K, 15 T) of the highest I_c sample peaked at 2x10^{18} n_f/cm^2, returning to roughly its original value at < 4x10^{18} n_f/cm^2, where n_f is the number of fast neutrons (defined by Fischer et al. as a neutron with energy > 0.1 MeV). The SPECTRA-PKA analysis of TRIGA CIF described above implies that YBCO and GdBCO receive ≈0.2715 and 0.2623 dpa/FPY respectively. Assuming that TRIGA CIF irradiation to 4x10^{18} n_f/cm^2 is applied continuously, this fluence would be reached in 147h22m, meaning their YBCO samples accumulated lattice damage equivalent to ≈4.56x10^{-3} dpa (or 4.56 mdpa) and ≈9 appm of impurities and their GdBCO samples accumulated lattice damage equivalent to ≈4.40 mdpa and ≈10 appm of impurities over the course of the experiment. This implies that for any future experiment involving the measurement of irradiation induced changes to the superconducting properties of REBCO, a lattice damage level and impurity concentration of the order of 4.5mdpa and 10appm respectively will likely cover the range over which even the best performing REBCO sample's critical current at low temperature, high field (parallel to the REBCO c-axis) improves to a peak and then decreases to a value below its initial value, assuming that the coated conductors irradiated and tested by Fischer et al. are a representative sample of all REBCO coated conductors.

Of these two mechanisms, dpa and impurity additions, it can be reasoned that lattice damage will dominate changes in the superconducting performance as it disproportionately contributes to the number of disrupted REBCO unit cells. To illustrate this, consider that at 4.5 mdpa, ≈1 in every 17 units cells contains a displaced atom and thus would have diminished superconducting properties, assuming the worst case that all displacements are isolated. In contrast, an impurity concentration of 10 appm implies that ≈ 1 in every 100,000-unit cells contains an atom that was not part of the original ensemble, meaning that impurity build-up leads to orders of magnitude lower numbers of disrupted unit cells compared to the number caused by lattice damage.

Assuming that lattice damage is dominant, the large range of neutron powers examined and the roughly linear dependence of damage rate on total neutron flux regardless of neutron source [206] (Figure 4.5a), neutron spectra capable of damaging REBCO up to 4.5 mdpa over 1 and 10 years can be determined by adjusting the total flux of both TF spectra. The results imply (Figure 4.5b) that adding shielding to reduce the flux of ST135 TF spectrum neutrons by a factor of 0.0088 or removing shielding to allow the flux of DEMO TF spectrum neutrons to increase by a factor of 2045 has the effect that the REBCO CC in the TF coil would be able to operate at the rated I_c for 1 year, with further reductions in neutron flux capable of dramatically increasing the operating life of the TF coil.

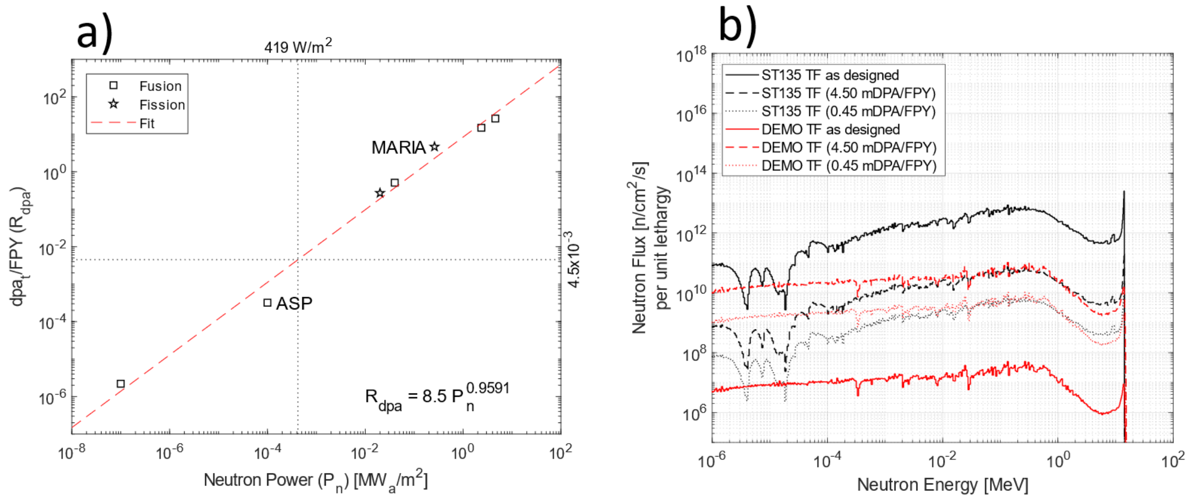

Figure 4.5: a) Log plot of neutron power (x-axis) vs dpa_t rate (y-axis), showing that the neutron dpa_t rate is roughly linearly dependent on neutron power, regardless of the neutron source. Addition points refer to the irradiation volumes offered to experimenters by the CCFE in the MARIA fission reactor [332] *and the DT neutron generator 'ASP' at Aldermaston* [333]*. b) Original ST135 TF and DEMO TF neutron spectra and their target spectra adjusted to achieve a total lattice damage of 4.5mdpa over 1 or 10 years.*

4.3.1.2 TRIGA Spectrum neutrons as a Proxy for Fusion Spectra

As Fischer et al. [21] used TRIGA CIF spectrum neutrons as a proxy for fusion spectra neutrons, in this section the differences in the dpa rate spectra are examined. Due to the power variation in considered neutron spectra, the dpa rate spectra were normalised to dpa per transiting neutron to assess differences due to each neutron spectrum's profile. The dpa per neutron spectra for oxygen, copper and barium PKAs are shown in Figure 4.6 and show that the unshielded fusion spectra produce peaks in the oxygen, copper and barium dpa spectra at recoil energies of ≈205, ≈275 and ≈210 keV respectively. These peaks are subsequently reduced in magnitude as shielding thickness increases, leading to dpa creation by oxygen, copper and barium PKAs being dominated by recoils of energy 65-70, 15-20 and 10-15 keV respectively. Moving to the TRIGA CIF spectra, for barium and copper PKAs the shape of the dpa spectra curve is different, with only a single peak at ≈ 100 keV for both PKAs. That said, TRIGA CIF's dpa spectra for oxygen is similar to that for fusion neutrons, although with the difference that the large dpa spectrum peak is at ≈205 keV, like the FW spectra, rather than at 65-70 keV, like the TF spectra.

These results imply that the number of displacements due to TRIGA CIF irradiation, per neutron, are due to oxygen, copper and barium PKAs with, on average, higher energy than their fusion TF spectra counterparts. As no literature could be found that studies the effect of different PKA energies in REBCO, the generalised results of differing PKA energy into α-iron by Sahi and Kim [334] and Terentyev et al. [335] using MD simulations will be used as a comparison. These showed that increasing PKA energy increases both the number and spatial spread of the resultant Frenkel pairs. This increased spread was shown to increase the fractions of the total interstitials that cluster together and the total vacancies that cluster together, approaching 50-60% and 25% of the totals respectively at a PKA energy of 30keV. Assuming that a similar mechanism results due to PKAs in REBCO, this increased clustering implies that each separate volume of damaged material (characterised by a diminished or zero T_c) will, on average, contain more defects and therefore be larger for the TRIGA CIF neutrons, that their TF spectrum counterparts. This increased size implies that TRIGA CIF neutron irradiation is more likely to produce a higher proportion of 3D defects (i.e. damaged volumes with 3 dimensions > ξ_{ab}) than 0D defects (see Figure 2.14). Although both types of defect are pinning centres in REBCO, 3D defects have been shown to more effectively increase the performance of REBCO CCs at high field and across a wider range of temperatures whereas 0D defects are relatively weak pinning centres, only enhancing pinning at temperatures ≤ 20K [193]. In this instance, however, the faster creation of 3D defects per unit damage by TRIGA CIF neutrons may also represent a faster rate of decrease in the superconducting volume, given that 3D defects are typically non-superconducting and are large enough not to support Josephson weak links whilst OD defects can, given they have all dimensions < ξ_{ab}. It could therefore be argued that, for unenhanced REBCO operating at T>20K, fusion TF spectrum neutrons may lead to changes in the J_c(high field) values that peak at a lower level of enhancement but the damage level of the peak enhancement and the damage level where J_c returns to $J_c(0)$ is at higher dpa, meaning the Fischer et al. results using TRIGA CIF neutrons would signify an under estimate of the true resilience of CCs subject to fusion spectra neutrons. For T < 20K, however, the improvement-and-decline profile for unenhanced REBCO could be different, given the contribution of 0D defect to the pinning landscape, and will depend on the precise operating temperature, the relative strength of the pinning enhancement due to 0D vs 3D defects and the number densities of 0D to 3D defects. Given these competing factors, investigating this is recommended for further work given that it would inform the designers of TF coils utilising REBCO CCs about whether operating at T < 20K would lead to a disproportionately more resilient TF coil.

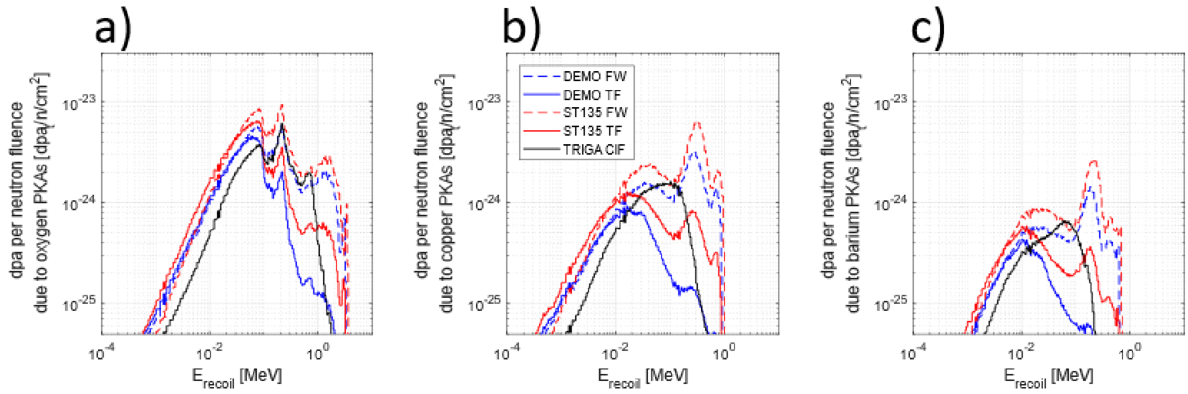

Figure 4.6: Comparing a) oxygen, b) copper and c) barium PKA induced dpa_t per neutron (y-axis) histograms with respect the Recoil energy (x-axis, E_{recoil}) for YBCO subject to neutron irradiation (these graphs are also representative of GdBCO and EuBCO).

4.3.2 Effect of Transmutations

Despite the lower concentration of unit cells disrupted by impurity build-up compared to lattice damage, the effect of certain impurities should be examined to assess whether they can disproportionately affect REBCO's superconducting properties. In this section, the effect of copper and rare-earth transmutations is examined.

4.3.2.1 Copper Transmutation

The FISPACT-II results above show that copper transmutation into zinc and nickel takes place in REBCO. Experiments examining the substitution of copper in REBCO for other elements, including zinc and nickel, have been performed by Yang et al. [126]. These showed that zinc substitution on the copper site in YBCO has a more marked effect on T_c than the other elements considered (Fe, Co, Ni, Figure 4.7) as zinc only substitutes into the copper plane sites. Nickel was found to substitute into both copper plane and chain sites with a ratio of ≈1:1. Yang et al.’s work was expanded upon by Singhal et al. [127] who determined that, even though zinc inclusion leads to oxygen stoichiometry changes and local lattice distortion, it was zinc’s magnetic ordering that played the dominant role in suppressing T_c. That said, based on Figure 4.7, the T_c drops ≈20K when x_{Zn}=0.01, equivalent to a zinc impurity concentration of ≈ 2300appm. Given the highest predicted zinc concentration from the FISPACT-II analysis was 4.5appm at 4.5mdpa, it unlikely that Zn and, by a similar argument, Ni accumulation would lead to a significant loss of bulk sample properties.

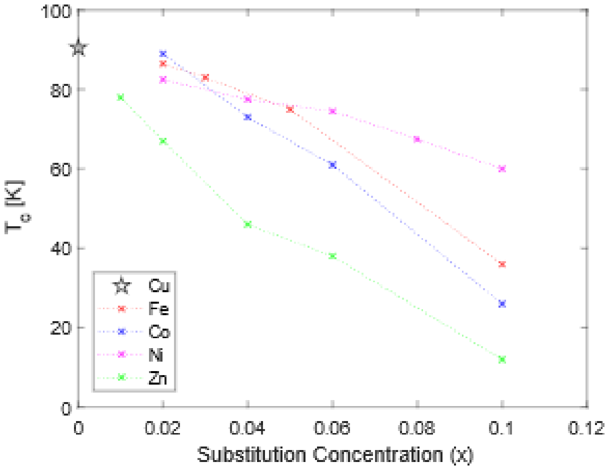

Figure 4.7: T_c decline in the T_c (y-axis) of $YBa_2(Cu_{1-x}M_x)_3O_{7-d}$ samples with increasing M concentration (‘x’, x-axis) where M = Co, Zn, Ni or Fe. Reproduced using data from Yang et al. [126].

4.3.2.2 Rare-Earth elements transmutation

Figure 4.4 and Table 4-4 show that rare-earth transmutation is a significant impurity vector for EuBCO, especially when it is combined with the time scales associated with relatively low flux fusion neutron spectra, such as DEMO TF, or the TRIGA CIF fission spectra.

The effect of europium transmutation in EuBCO is complicated by 2 factors. Firstly, that the stable transmutation products (Gd & Sm) are also rare-earth elements which can combine with Ba, Cu and O to form superconducting compounds in the REBCO family. Secondly, the nuclear reaction leading to transmutation will also transfer energy to the transmutation product which would likely remove it from its original unit cell position. The transmutation products will, therefore, either form a stable interstitial in another unit cell, fill a rare-earth vacancy site in another unit cell or fill the rare-earth vacancy just created in original unit cell (direct replacement), with the prevalence of each outcome dependent on the recoil energy of the product of the (n, γ) reaction and the diffusion rate of each subsequent transmutation product. Given that (n, γ) reactions are predominated by low energy neutrons, direct replacement is a likely outcome but which of these processes will dominant should be investigated further, given that the diffusion co-efficient of rare-earths in REBCO has only been studied at high temperatures [103], [336] and not at room temperature or lower. One potential experiment (outside the scope of this work) could be to use the TRIGA CIF to irradiate pristine EuBCO and GdBCO CCs, preferably prepared without artificial pinning centres, whilst monitoring their superconducting properties. If their response to TRIGA CIF neutrons is affected by impurity accumulation, this may show up as differences in the character of their changing superconducting properties.

4.3.3 Using Ion Sources as a Proxy for Neutrons

Due to the difficulties associated with neutron irradiating samples discussed in section 2.4.3, monoenergetic fast ion irradiation is a common technique used to simulate neutron damage. Ion irradiation has several advantages but requires that a systematic approach be adopted to account for the difference in the damage mechanisms from the 2 kinds of projectiles [260]. An example for the ferritic-martensitic alloy HT9 is shown in Figure 4.8 where dual beam ion irradiation is used to achieve the required impurity accumulation with helium ions and the required damage level with iron ions, as verified by SRIM [206], [227]. The result was that a small fraction of the sample, between 500-700nm below the sample surface, contained helium at the required concentration, low levels of impurity build-up due to the irradiating iron ions and relatively low variation in calculated lattice damage over the volume of interest. This meant that, once the sample had been irradiated, it might be expected to have similar damage and equivalent post-irradiation properties to a sample recently removed from a nuclear test reactor [260]. No work of this kind of complexity to match ion irradiation conditions as a proxy for neutron damage has been reported for REBCO materials.

To take some steps in this direction, the above results show that impurity build-up in REBCO samples subject to fusion TF spectra neutrons gain ≈1 appm of impurities and, assuming the TRIGA CIF limit, receive ≈4.5 mdpa of lattice damage, mostly due to oxygen PKAs of 50-250 keV (Table 4-5), before their superconducting properties at low temperature and high field fall below their initial values.

The example of Was et al. [260] indicates the following requirements for an ion irradiation experiment emulating neutron irradiation:

1) Use self-ions, where possible.
2) For the bombarding ion used to create lattice damage, ensure as-small-as-possible variation in the damage level and as-low-as-possible ion implantation concentration per bombarding ion over the volume of interest.

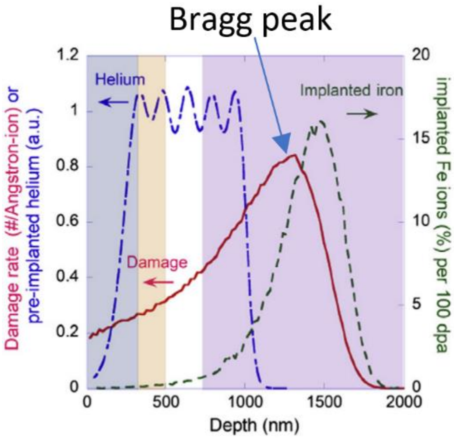

Figure 4.8: Example of alloy HT9 being ion irradiated to emulate damage due to neutron irradiation. The sample is first irradiated with 5 MeV iron ions leading to a lattice damage (red curve) and iron ion implantation (green dashed curve) then helium ion irradiated at various energies to implant helium (blue dot-dashed curve). Selection of the region for analysis (white) was determined to exclude volumes in too close proximity of the surface (blue), with an overabundance of implanted interstitial iron ions (purple) and to minimize the damage variation with depth (orange). Reproduced from [260].

3) For the bombarding ion used to create the required impurity concentration, the opposite is true; the ion energy needs to be minimised to avoid lattice damage but still sufficient to push impurity ions to the desired location.

Given the thicknesses of the CCs available (Table 3-1), these requirements indicate that oxygen is the ideal choice of irradiating ion. The oxygen ion energy required to ensure a uniform damage profile and low implantation volume was assessed using SRIM[23]. The resulting damage and impurity levels are shown in Figure 4.9. First assessed (Figure 4.9a&b) were the ideal oxygen energies (50-250keV) taken from the SPECTRA-PKA calculation. Though ideal PKA energies, an ion irradiation experiment using these energies would all lead to a large variation in damage level through the sample thickness unless the sample was <50nm thick. As this is not an in-situ TEM sample, this precluded the use of these low energies for my experiments.

Second assessed was oxygen ion bombardment in stages up to the highest available energy (5 MeV from the Dalton Cumbrian Facility [337], Figure 4.9c, d). This showed that using 5MeV O would allow the sample thickness to be increased to ≈1 µm, roughly the thickness of the thinnest REBCO layer available.

Finally, the decision was made to use helium ions as, being a noble gas, it would avoid any additional chemistry effecting the results and, being a lower mass ion, would penetrate the available CC samples at < 5MeV whilst still predominantly exciting PKAs from the oxygen ions in the REBCO sample. Figure 4.9e, f shows the SRIM analysis associated with assessing helium's damage level and

---

[23] *REBCO material inputs were taken from Table 2-3* and required SRIM inputs are described in section 3.5.3.

implantation characteristics. Helium ion energies of 150-780keV were assessed as these projectile energies, on average, result in oxygen PKAs with 50-250keV of energy, as per equation 2-13. These calculations showed that 2 MeV helium ions are sufficiently energetic and low Z to traverse even the thickest available CC sample (3.6 µm), resulting in ion implantation of <1 appm at all points in the REBCO layer of the sample whilst still damaging the REBCO at a reasonable rate (≈0.1-0.3mdpa per 10^{14} beam ions/cm^2) and with a uniform depth profile.

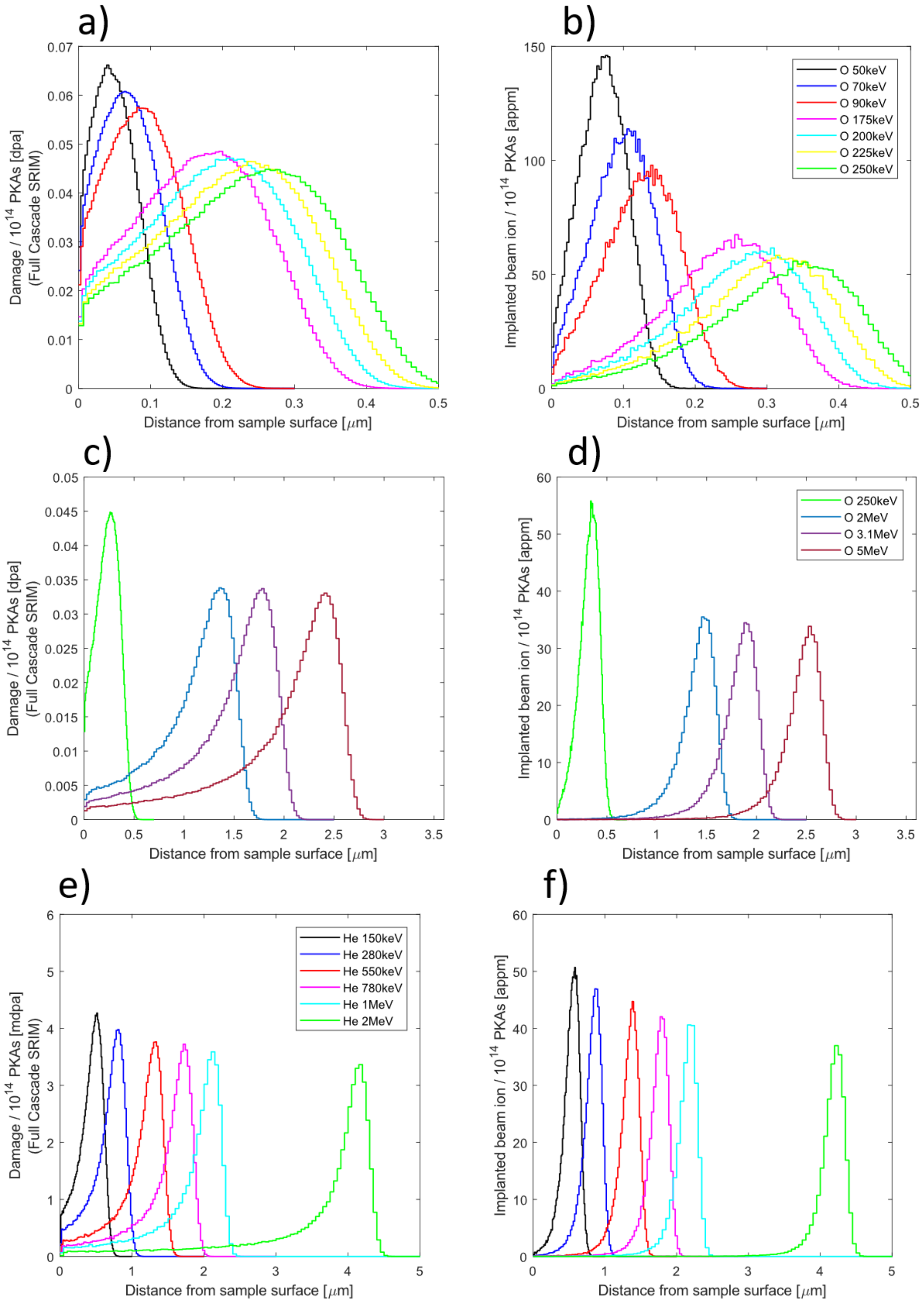

Figure 4.9: SRIM calculations associated with ion-energy combinations considered as proxies for fusion neutron spectra irradiation. Figure show the damage (y-axis - a, c, e) and implantation (y-axis - b, d, f) versus depth from the sample surface (x-axis) for the low energy oxygen (a, b), high energy oxygen (c, d) and helium ions (e, f).

Table 4-5: Reactions that contribute to Total dpa for YBCO (these numbers are also representative of GdBCO and EuBCO)

		Element (10%) *		**Reaction** **	
		Name	Energy [keV]	Fraction of Total	Details
ST135 FW	YBCO GdBCO EuBCO	O	57.5-91.2 182-219	41.2% 42.2% 42.4%	$^{16}O(n,n)^{16}O$
DEMO FW	YBCO GdBCO EuBCO	O	57.5-91.2 191-229	43.8% 44.7% 45.0%	$^{16}O(n,n)^{16}O$
ST135 TF	YBCO GdBCO EuBCO	O	57.5-87.1	60.2% 62.1% 62.5%	$^{16}O(n,n)^{16}O$
DEMO TF	YBCO GdBCO EuBCO	O	50.1-75.9	66.8% 69.2% 69.7%	$^{16}O(n,n)^{16}O$
TRIGA CIF	YBCO GdBCO EuBCO	O	174-251	56.8% 58.8% 59.2%	$^{16}O(n,n)^{16}O$

*: This is the single element that leads to ≈10% of the total damage rate over the smallest recoil energy range(s).

** Fraction of total displacements from single most prolific reaction.

4.4 Conclusions

In this section, the analytical tools FISPACT-II and SPECTRA-PKA have been used to assess how YBCO, GdBCO and EuBCO respond to fusion and TRIGA spectrum neutrons. The results show that ≈4.5 mdpa of lattice damage and 10appm of impurities built-up during Fischer et al.'s experiments irradiating YBCO and GdBCO in the TRIGA CIF and that this was sufficient to degrade the low temperature, high field superconducting properties of their best performing sample below its original value, despite those properties improving at intermediate doses.

Lattice damage was reasoned to be the dominant contributing factor effecting the superconducting properties, surpassing impurity build up by a significant margin. Going forward to cold irradiation experiments, therefore, the effect of impurity build-up should be minimised.

The results also showed that, up to a damage level of 4.5mdpa from all fusion sources, oxygen PKAs of 50-250keV undergoing elastic collisions were the most damaging PKA species, with the oxygen energy causing most damage shifting from ≈205keV to ≈70keV as the shielding thickness increased. For the TF spectra, elastic collisions involving O PKAs contributed > 60% of the total dpa.

Finally, when performing ion irradiation on REBCO designed to mimic the effects of fusion and fission neutron irradiation, the ideal ion-energy combination (O, 50-250keV) would require samples to be <50nm thick. This means that, based on the geometry of the available CCs (Table 3-1), I chose helium ions at 2MeV for my irradiation experiments.

5 Irradiation of Room Temperature Coated Conductors

In chapter 4 it was determined that, given the available samples (Table 3-1), 2 MeV helium ions can be used to emulate neutron irradiation of CC. Based on the work Fischer et al. [21], fission neutron fluences equivalent to ≈ 4.5 mdpa should be sufficient to decrease the low temperature, high field J_c of all CC samples.

In this chapter, all available samples (Table 3-1) were irradiated sequentially with 2 MeV helium ions at room temperature to test their response to radiation damage with the primary goal of establishing a room temperature baseline before going on to cold irradiation experiments. This was carried out by initially testing the superconducting properties of pristine REBCO using the magnetisation method discussed in chapter 3 and then repeated steps of irradiating disks with 2 MeV helium ions and retesting. Aspects of the experimental design are described before the results are presented and their implications discussed. This chapter is closer to a report on the data collected from these samples rather than a completed study. As the focus of this project shifted to the cold irradiation experiments aimed at assessing REBCO CCs for fusion applications, the main goal of this chapter became to decide which CC to use during the cold irradiation experiments. There are several suggestions for further work that could be undertaken to round off the work in this chapter (section 8.1), specifically to correlate the performance of different tapes under irradiation to their starting microstructure.

5.1 Experimental Set-up

5.1.1 Sample Preparation and Irradiation Plate Design

Samples for this experiment consisted of ϕ3mm disks of REBCO punched from CCs after exposure of the REBCO layer using a combination of $FeCl_3$ solution and $NH_4OH:H_2O_2$ solution etches, as described in chapter 3 (Figure 5.1a). Figure 5.1b shows how the CC changes appearance due to each step of the process. The surface of the CC becomes a silvery-grey colour following a successful $FeCl_3$ solution etch, typically taking 10-12mins. Adding $NH_4OH:H_2O_2$ solution then turned the CC surface brilliant white (likely AgOH) before revealing the shiny black surface of REBCO, typically within 1 minute. Once the REBCO surface of the sample had been revealed, the surface was dried, cleaned with acetone and isopropanol and dried again. A TEM punch [338] was then used to punch ϕ3mm disks from the exposed section of the CC (❼). Disks were punched from a position as close as possible to the centre line of the CC and with the REBCO layer facing the punch (Figure 5.1a&b). The final stage of the process was to assemble samples onto a ϕ10cm silicon wafer irradiation plate, provided by the SIBC, using double sided carbon tape (Figure 5.1c). Care was taken to assemble them as far apart as possible but within a ϕ5cm diameter about the centre of the irradiation plate to ensure all samples were irradiated to the same fluence by the rastering beam at SIBC.

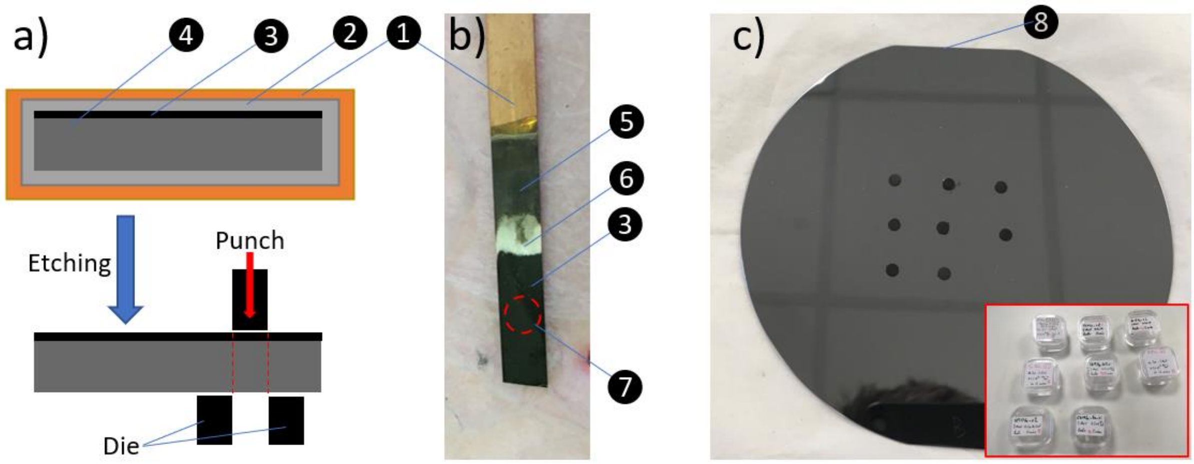

Figure 5.1: Sample Preparation Process. a) schematic of REBCO CC cross section and what results after etching (not to scale). b) Etching example of a CC showing the progression of the stages. c) Irradiation plate with 8 samples attached using double sided carbon tape. Inset: Sample containers arranged in the same way as the samples are on the plate allowed me to keep track of which sample was which. Label included: 1: CC's copper envelope; 2: CC's silver protection layer; 3: REBCO layer; 4: Substrate; 5: Appearance of CC after $FeCl_3$ etch; 6: Appearance of CC after H_2O_2:NH_4OH etch for insufficient time; 7: Approximate area removed from CC with the TEM punch for PPMS testing and irradiation; 8: φ10 cm Silicon Wafer Irradiation plate.

$J_c(B, T, \dot{B})$ is derived from the magnetic moment and size of the samples measured using the VSM insert in a PPMS system using Bean's model for cylindrical samples. Given that for equation 3-3, $J_c \propto (RV)^{-1} \propto R^{-3}t^{-1}$ a study on 3 types of CC (SP11, SP17 and STI17) was performed to assess the radius and thickness of the REBCO layer in the disk samples using light microscopy (LM) and SEM imaging of cross sections. The thickness of the superconducting layer (t) was studied using the PIPS cross sectioning method described in chapter 3 and example SEM images are shown in Figure 5.2c, its inset and Figure 5.2d. In each case, superconducting layer thickness varied within 0.1 µm of the thickness data provided by the manufacturer and this level of error was used going forward. The REBCO layer radius was studied using a combination of calliper measurements, LM and SEM imaging. Measurement with callipers and LM showed that each disk had $\phi 3^{+0.00}_{-0.01}$mm (for example, Figure 5.2a). Given that preliminary magnetometry results for etched versus unetched samples described in chapter 3 showed that punching after the sample was etched could lead to decrease in sample radius of 4.1-4.9%, equivalent to up to ≈ 145 µm for ϕ3mm samples, the state of the outer radius of an STI17 REBCO layer was assessed in cross section as this sample had the thinnest layers of protection compared to the other available CC. The resulting SE images (Figure 5.2b&d) show that, although the REBCO layer is mostly undamaged, the volume within 20 µm of the edge of the disk had been deformed by the punching process and contained cracks that would presumably prevent circulation of currents within that zone. This 20 µm wide zone is smaller than the ≈ 145 µm wide zone expected but is likely due to the differences in construction of the CC with the STI17 CC having a relatively thick substrate and thin protective layers whilst the SP11 CC discussed in chapter 3 had a thin substrate with significantly thicker protective copper layers (2 x 20 µm each side of the CC). Given these results and that this study was not exhaustive, the disk diameter is assumed to be $\phi 3^{+0.000}_{-0.145}$mm going forward.

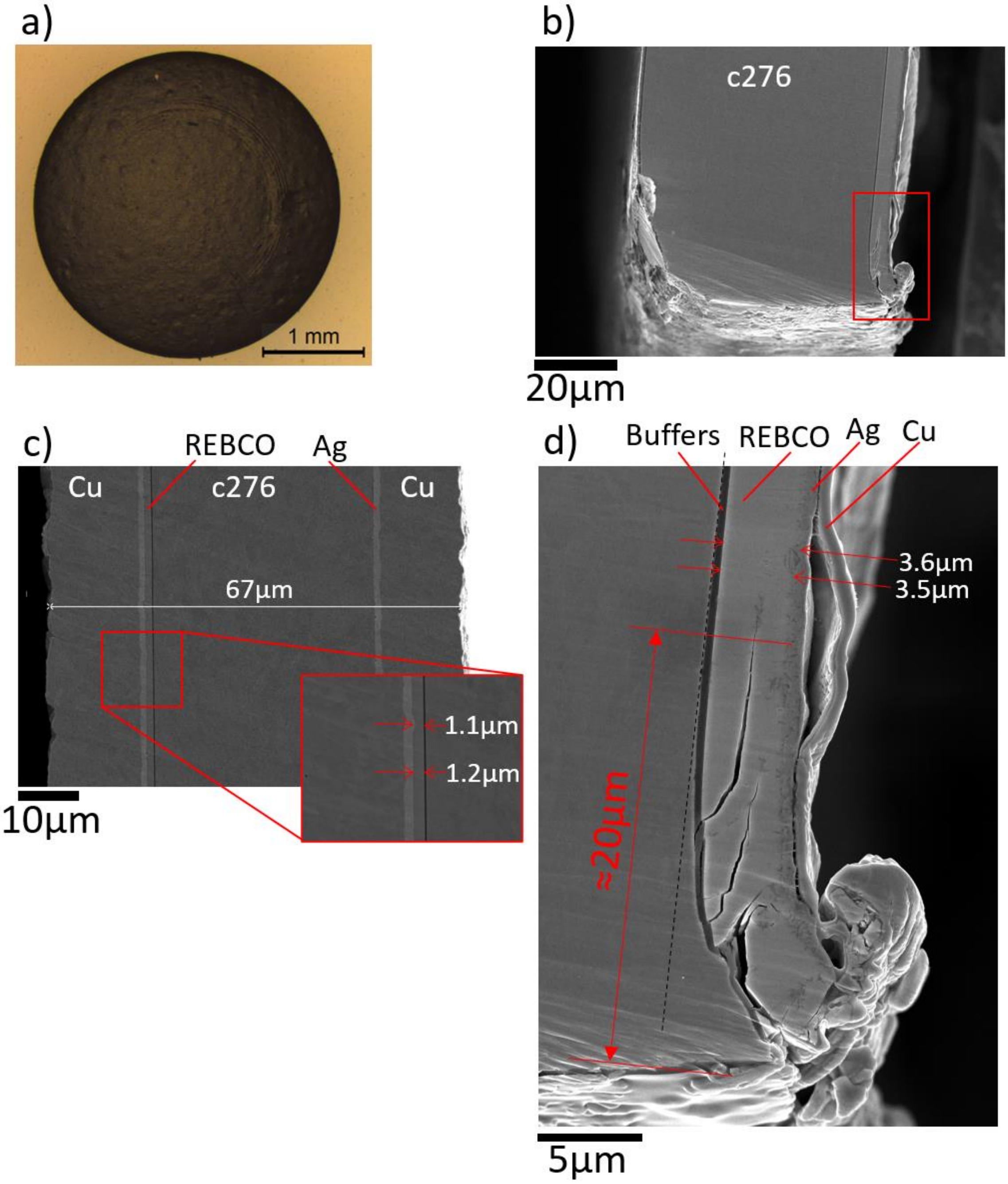

Figure 5.2: a) Bruker 2018 Sample after etching and TEM punching, resulting in a φ3mm disk of exposed superconductors, ready for irradiation experiments. The superconducting layer appeared undamaged; b&d) unetched φ3 mm disk punched from STI17 CC, cross sectioned in the PIPS. Over a large proportion of the disk, the superconducting layer appears undamaged but closer inspection of area near disk's edge (d) shows signs that superconductor near edge has been deformed and contains cracks; c) unetched SP17 sample cross sectioned in PIPs showing areas where thickness of superconducting layer deviates from mean (1.2 µm).

5.1.2 Superconducting Property Measurement

5.1.2.1 Data Acquisition

Determining the superconducting properties of the disk samples was achieved using the Vibrating Sample Magnetometer (VSM) module in a Quantum Design (QD) Physical Property Measurement System (PPMS), as described in chapter 3. Samples were installed in the PPMS-VSM small bore brass sample holder (Figure 5.3a) using 2 quartz blocks and kapton tape to secure them firmly. The sample was then vibrated within the pickup coils at an amplitude of 2 mm and the resulting signal was used to determine the sample's magnetic moment by comparing it to that of the palladium reference sample, provided by QD.

So that the data collected accurately represents the actual magnetic moment of the sample, differences between the measurements from my samples and the reference sample were accounted for. These included applying a 0.9892 compensation factor to account for the differences in sample shape, ensuring the sample was properly axially centred before all measurements, adding a 0.2% error in the measured moment due to inaccuracies in the sample's radial position, ensuring the sample was rigidly held in the sample holder and accounting for the background magnetic moment. Although these sources of error were accounted for during the data processing phase, when calculating J_c, they are all small compared to the error in the sample diameter discussed in section 5.1.1.

As all available CC samples have their REBCO c-axis aligned with the ND of the CC, the aim was to align B_{app} parallel to the gradiometer's cylindrical axis. Based on the Robinson Research Institute data [17], [83], [84] for similar samples (Figure 2.12b, 180°) I concluded that the effect of misalignment for all available CCs (except for the Br18 sample as a Bruker CC is not currently part of RRI's dataset) is small. This misalignment was therefore deemed to have an insignificant error compared to other sources.

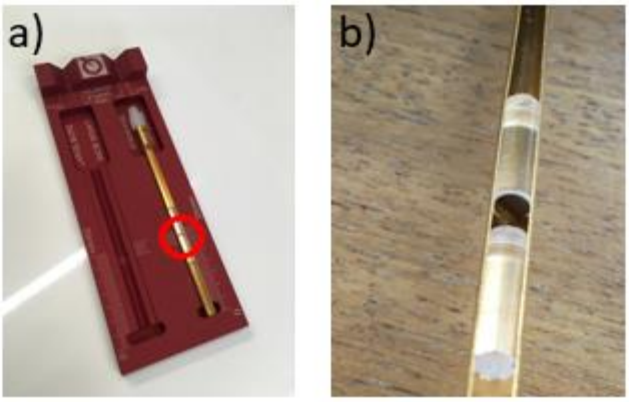

Figure 5.3: Sample mounting within the PPMS VSM. a) small bore holder with sample assembled in correct position before Kapton tape added. b) view of sample before quartz cylinders are closed around it showing that sample sits off centre from the axis holder, leading to a systematic error in the measured moment.

5.1.2.2 T_{c0} and $B_{irr}(T)$ measurement

The critical field at zero field and current (T_{c0}) was determined from moment-temperature (m-T) data taken by sweeping the temperature from 20 to 100 K in a constant measurement field of 5 mT (50 Oe) applied parallel to the REBCO c-axis. The sample was initially zero field cooled (ZFC) to 20 K and held for 5 minutes before the measurement field was applied. After a further 5 minutes to allow any relaxation of the sample moment to take place, the sample was axially centred within the VSM gradiometer. The sample moment was then measured using the VSM whilst the temperature was raised at 2 K/min up to 100 K.

Processing of the data to obtain values for T_c required the subtraction of the background magnetic moment. CCs are made up of many different materials besides the superconducting layer. All of these materials exhibit some combination of diamagnetic (Cu, Ag, MgO, Al_2O_3 [290], [339], [340]), paramagnetic (Y_2O_3, Ce_2O_3 [290], REBCO with $T>T_c$) and/or, to a lesser extent, soft ferromagnetic properties (substrates c276 Hastelloy [150] and iron dust contamination on the sample [341]). Given that the substrate makes up > 90% of each sample by volume, the magnetic response of the substrate is likely to dominate at temperatures above T_c. At constant magnetic field, any soft ferromagnetic component of the sample moment is expected to be roughly constant within the temperature range 20-100 K, hence the substrate's magnetic moment should vary in line with Curie's Law with an additional ferromagnetic component ($m_0 + C/T$). This behaviour manifests in the m-T data (Figure 5.4) where the substrate (dotted lines in a & b) makes up the bulk of the measured magnetic moment at $T>T_c$ for both unetched (a) and etched (b) samples. This allows the background moment to be estimated by fitting a curve with the character $m_0 + C/T$ to the portion of the curve above T_c. The magnetic response of the REBCO layer can then be calculated by subtracting this background moment from the measured magnetic moment.

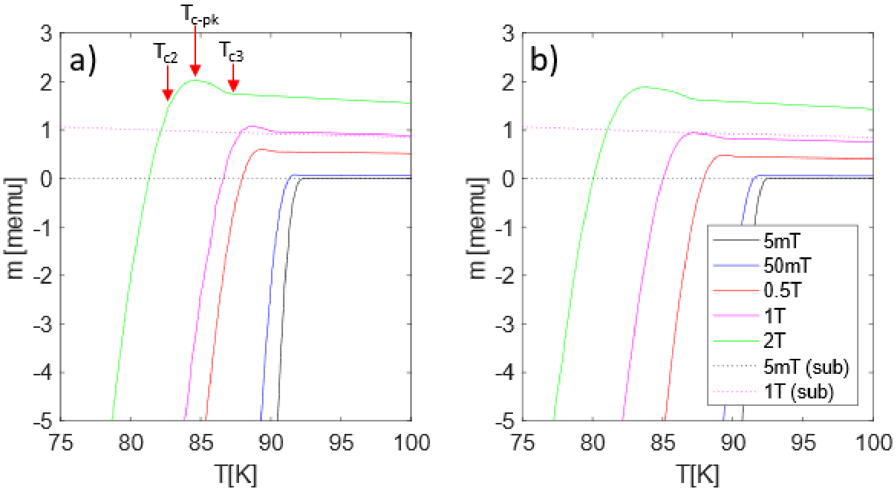

Figure 5.4: Moment vs Temperature data at 75-100 K measured in the PPMS using a temperature rise of 2 K/min for disk samples punched from Fujikura 2018 CC after ZFC and then subject to $B_{app}||c$ = 0.005, 0.05, 0.5, 1 and 2T. Sample were punched from a) unetched and b) etched CC. Dotted lines denote the responses of samples consisting of the substrate only for 5mT and 1T. Also shown in a) on the 2T m-T sweep are the options for defining T_c when a superconducting sample exhibits a small paramagnetic response near its critical temperature, as presented by Das et al. [342]*. These are T_{c2} - the highest temperature at which the sample moment falls below its apparent background level, $T_{c\text{-}pk}$ – the temperature at which the paramagnetic response of the sample is greatest and T_{c3} – the temperature at which the sample moment significantly deviates from its background moment, whether positive or negative.*

Another noticeable inclusion to the m-T behaviour of CC samples shown in Figure 5.4 is that, as T decreases through T_c, there is a paramagnetic increase in the measured moment above the background level before it falls sharply due to the increased diamagnetism of the superconducting layer. Data from Figure 5.4 shows that this feature is not present in the substrate-only samples in which the REBCO layer has been removed but is present whether the metal overlayers have been etched off (Figure 5.4b) or not (Figure 5.4a), implying it is a response of the superconducting layer. Figure 5.4 indicates that the size of this peak increases with field, and its high temperature onset decreases with increasing field, similar to that for $B_{irr}(T)$ and $B_{c2}(T)$. This suggests that it is coupled to the superconducting transition of the sample. The origin of such a paramagnetic peak for cuprate superconductor samples is typically only observed in field cooled samples. This was discussed by Braunisch et al. [343] and Reidling et al. [344] who both consider it a result of flowing supercurrents. Although their precise nature, and their unexpected appearance here given these samples are ZFC, are worth investigating, this was considered beyond the scope of this project. In light of their appearance, however, a definition of T_c is still required. For this, the example of Das et al. [342] is used and the options they present (T_{c2}, $T_{c\text{-}pk}$ and T_{c3}) are shown in Figure 5.4a. Of these options, T_{c3} is used for this work as Das et al. found that this critical temperature coincided with the departure of their sample's ac susceptibility from zero [342], which itself indicates a transition to a superconducting state.

For this work, T_c is therefore defined as the point at which the sample magnetisation departs significantly from the "$m_0 + C/T$" curve fitted to the section of the m-T sweep when the sample is in its normal state, whether this departure is diamagnetic or paramagnetic. The transition width at T_c (ΔT_c, Figure 5.5) is defined as the difference between the onset and offset temperature of the transition. The onset temperature is the temperature of the intersection points of the fit of the "$m_0 + C/T$" to the normal state section of the curve (blue dashed) and the straight-line tangent of the m-T data through the temperature where dM/dT is maximum (red dotted). The offset temperature is defined as where the red dotted line intersects the sample magnetisation at 20 K as, at low field, the sample was assumed to be in its Meissner state with constant χ (see Figure 5.5). For B_{app} > 50 mT, dM/dT ≠0 at 20 K, hence only T_c is defined.

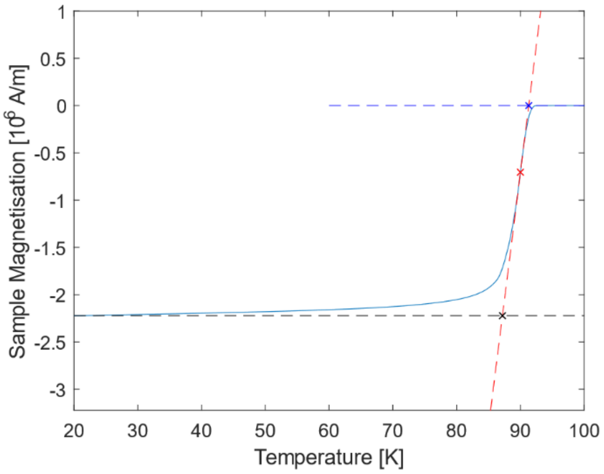

Figure 5.5: ΔT_c at 5 mT is defined as between the temperatures at the intersection points of, at the high temperature end, a fit of the Curie-Weiss law to the normal state section of the curve (blue dashed) and the straight line at a gradient max(dM/dT) through T_c (red dashed) and, at the low temperature end, where the straight line at a gradient max(dM/dT) through T_c is equal to the magnetisation at 20 K.

5.1.2.3 $J_c(B, T, \dot{B})$ and $B_{irr}(T)$ measurement

These quantities were determined by cooling the sample to the temperature of interest and sweeping the field at a constant rate of $\dot{B}$=5 mT/s. Using Brandt's definition [300] (equation 3-4), this is equivalent to a maximum electric field within the sample $(E(R)) = 0.0375$ µV/cm. A typical experiment (shown in Figure 5.6a) entailed a 5-sector sweep:

1) 0 → -2 T
2) -2 T → 0
3) 0 → 12 T
4) 12 T → 0 T
5) 0 T → -2 T

Sector 1 was used to ensure the REBCO sample is fully saturated with fluxons going forward. Sectors 3 & 4 allowed the magnetisation of the sample with increasing (M_+) and decreasing (M_-) field to be determine respectively, as required by Bean's Model (equation 3-3). To extract ΔM_{irr}, 3 independent sources of the magnetisation each disk sample need to be considered. These include the background contributions from the substrate's dia-, para- and ferromagnetism (M_{back}), the reversible component associated with the equilibrium arrangement of fluxons within the superconductor (M_{rev}) and the irreversible component due to circulating supercurrents driven by the changing field (M_{irr}). As the M_{back} and M_{rev} are functions of B only, whereas M_{irr} is function of ($B, \dot{\mathrm{B}}$), when $\dot{\mathrm{B}}$ is constant:

$$M_{back} + M_{rev} = (M_{+}(B) + M_{-}(B))/2 \tag{5-1}$$

$$\Delta M_{irr} = (M_{+}(B) - M_{-}(B))/2 \tag{5-2}$$

which can be used to calculate $J_c(B_{app})$ (Figure 5.6a inset) using equation 3-3. Sectors 3 and 4 allowed the determination of $\mathrm{B}_{irr}(T)$, defined for this work as the lowest field where $J_c(B_{app}, T) <$ 5x10^7 A/m^2, equivalent to a $\Delta M_{irr} <$ 5x10^4 A/m.

5.1.2.4 Self-field Correction

As shown in Figure 2.12c, REBCO J_c at low field is roughly constant (i.e. $J_c \propto B_{app}^0$). The width of this plateau region is a decreasing function of temperature, reaching as high as 0.2 T at 4.2 K (Figure 5.6a inset). As such, this would allow the J_c degrading effects of field generated by induced supercurrents in the sample (B_{sf}) to be neglected if $J_c(B_{sf}) \approx J_c(B = 0)$. This effect is least likely to be negligible at low temperature and field where J_c is high but data from a typical experiment showed that the $J_c(B_{app})$ dependence still shows a plateau region at low field and 4.2 K (Figure 5.6a inset), implying that self-fields are negligible. I have attributed this to several factors: 1) the small sample thickness (t); 2) that the fraction of the sample that generates the bulk of the sample moment is weighted towards higher radii and 3) that these higher weighted regions are not subjected to large fields even at high current densities. This is shown graphically in Figure 3.2c and Figure 5.6b&c where Figure 3.2c shows that the volumes of the sample at higher radii generate a higher proportion of the total sample moment[24]. Figure 5.6b shows that the self-field generated parallel to $\dot{\mathrm{B}}$ in an idealised sample where $J_c \neq J_c(\mathrm{r})$ is highest in sample volumes which contribute a relatively low fraction to the total magnetic moment. Figure 5.6c shows that $B_{sf} \| \dot{\mathrm{B}}$ is a function of sample thickness therefore the weighted effect of self-field on the sample moment should be assessed in the worst-case, where J=30 MA/cm^2 and t=3.6 µm. Performing this analysis revealed that the weighted average self-field produced in the sample is <|0.2| T. Given this, self-fields have been ignored going forward ($B_{app} \cong B$).

---

[24] calculated using Bean's Assumptions and equation 3-2

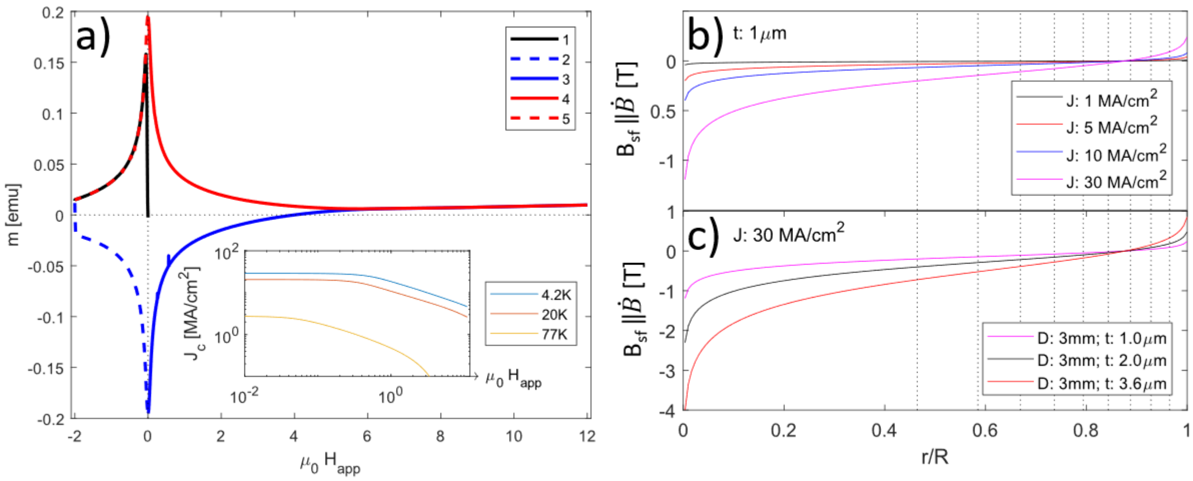

Figure 5.6: a) FJK un-exposed mH sweep at 77 K, inset: $J_c(B_{app})$ calculated using Bean's equation for a cylindrical superconductor at 4.2 K, 20 K and 77 K. b) self-field generated parallel to $\dot{B}$ by induced supercurrents (y-axis) between 1-30 MA/cm^2 in a 1 μm thick sample as a function of normalised radius (x-axis); c) self-field parallel to $\dot{B}$ generated by circulating supercurrents (y-axis) of 30 MA/cm^2 in samples of varying diameter and thickness as a function of normalised radius (x-axis). Each region demarked with dotted black lines denotes a sample annulus that generates 10% of the total sample moment.

5.1.3 Irradiation Parameters

With the samples prepared and a method of measuring their superconducting properties defined, the methods of irradiating the samples with 2 MeV helium ions should be discussed. Given the results of chapter 4, the goal is to characterise my samples in stages up to a damage level of 4.5 mdpa and at a damage rate of 8.3x10^{-9} dpa/s.

The effects of 2 MeV helium irradiation on REBCO (RE=Y, Gd, (Gd,Y) and Eu) has been evaluated using SRIM using the REBCO properties in Table 2-3 and the experimental methods advised by Stoller, Weber and MacFarlane described in section 3.5.3 [231], [319], [345]. This showed that there is still some variation in the damage level of each layer of the REBCO volume even though the Bragg peak is well below the superconducting layer for all samples (i.e. in the substrate) (Figure 5.7a&b). As the superconducting property measurements described above are bulk measurements from the entire sample volume and as neutron damage is typically distributed uniformly throughout a material, it was decided that averaging the layer damage over the sample volume would give a sensible measure of the sample damage level. Given this volume averaged damage level for each sample (Figure 5.7c&d) and its dependence on sample thickness, and that all samples need to be irradiated together to make efficient use of the beam line, a fluence (Φ) of 4.2x10^{14} He/cm^2 was used as for most samples, except the thickest, STI17 CC, this resulted in a damage per irradiation step approaching 0.45 mdpa with minimal ion implantation (Table 5-1).

Equation 3-8 was used to determine what beam current density would lead to an appropriate damage rate. Delivering a damage rate of 8.3x10^{-9} dpa/s to these samples would require J_b ≈15 nA/cm^2 for ≈ 15.1 hours. Considering that several irradiations would be needed to reach 4.5 mdpa and given restricted access to the SIBC beam line, this time scale for the irradiations was deemed impractical. As a result, J_b =100 nA/cm^2 was used with each irradiation step taking ≈ 12 minutes, equivalent to a damage rate of ≈ 6.3x10^{-7} dpa/s for the Fujikura 2018 CC.

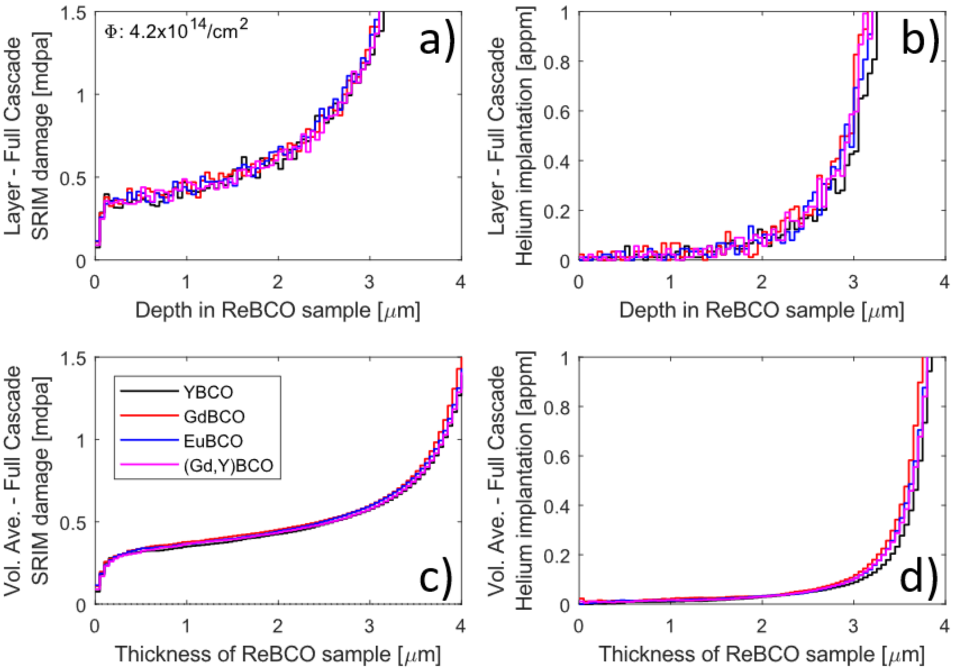

Figure 5.7: Results of full cascade SRIM calculation to determine the damage and implantation levels of each sample after 2MeV helium ion irradiation to 4.2x10^{14} He/cm^2. a&b) Layer damage (a) and implantation (b) (y-axis) versus depth into sample (x-axis) . c&d) volume averaged sample damage (c) and implantation (d) (y-axis) versus sample thickness (x-axis).

Table 5-1: SRIM calculations for available CC samples.

Designation	Rare Earth	Tech	REBCO Layer thickness [µm]	Damage per step* [Vol. Av. mdpa]	Implantation per step* [Vol. Av. appm]	Enhanced Pinning?
Br18	Y	PLD	2.0	0.4253	0.029	Yes
STI17	Gd	RCE-CDR	3.6	0.8621	0.529	No
Fu18	Gd	PLD	2.0	0.4522	0.033	No
Sh19_Gd	Gd	PLD	1.8	0.4176	0.025	No
Sh19_Eu	Eu	PLD	2.4	0.4861	0.042	Yes
SP11	(Gd,Y)	MOCVD	1.0	0.3645	0.016	Yes
SP17	(Gd,Y)	MOCVD	1.2	0.3838	0.024	Yes

* One irradiation step is 2 MeV helium ions delivered by a rastered beam at a J_b≈100nA/cm^2 over ≈ 12 minutes to a fluence of 4.2x10^{14}/cm^2.

5.2 Results

In this section, the results of the PPMS superconducting property measurements on ϕ3mm disk samples of the 7 types of CC described in Table 3-1 before and after sequential irradiations with 2 MeV helium ions are described. Details of the schedule of irradiations and a complete set of the plots referred to in this section can be found in appendix B.

Figure 5.8 shows how T_c and ΔT_c measured with B||c = 5 mT change with increasing damage from 2 MeV helium irradiation. These show that the "double-disordered" pinning enhancement process used to manufacture the Bruker CC significantly diminishes T_c compared to the other CCs which all have a pre-irradiation T_c between 91-93 K. For all CCs, the decline in T_c is systematic upon the application of irradiation at a rate of between 0.88 K/mdpa (STI17) and 1.7 K/mdpa (all others). The only exception is that the T_c of the Br18 CC is resilient to helium irradiation damage up to ≈ 1mdpa before it starts to drop at 1.7 K/mdpa. Figure 5.8b shows how ΔT_c increases with irradiation damage. These results suggest that the sample can be split into 2 groups: with the samples without pinning enhancements (i.e. Fu18, STI17, Sh19-Gd) showing a roughly linear increase in ΔT_c with damage whilst those with pinning enhancements (all the others) show a rate of increase in ΔT_c that accelerates with damage level.

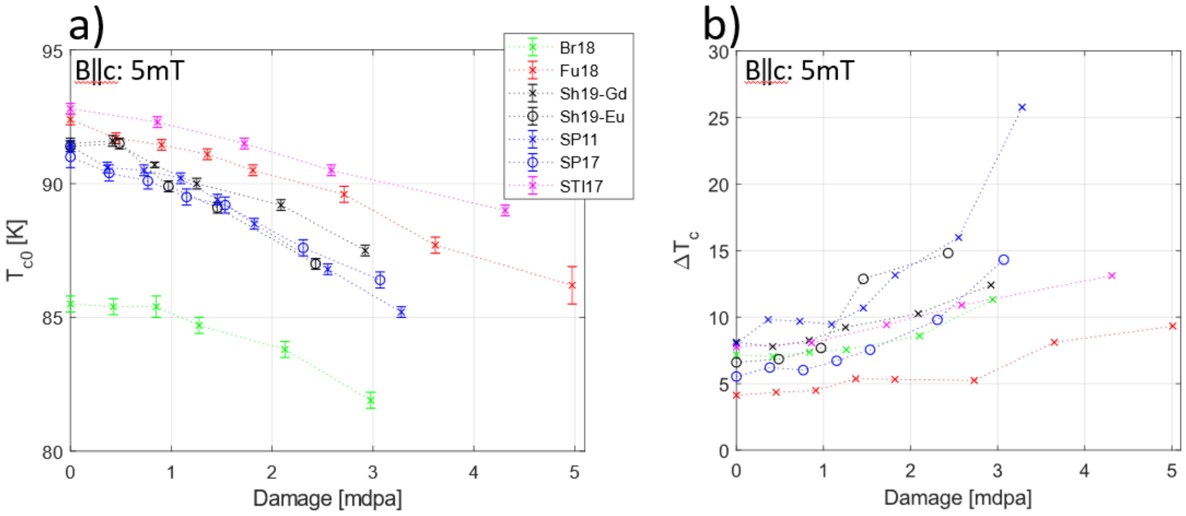

Figure 5.8: Change in (a) T_c and (b) ΔT_c measured at 5 mT (y-axis) due to lattice damage from 2 MeV helium ion irradiation (x-axis) for all CC samples tested.

By performing several m-T sweeps at varying field, the form of the irreversibility line can be determined for each sample, and changes tracked with increasing irradiation damage. Examples for the SP17, Fu18 and Br18 samples are shown in Figure 5.9, chosen as they are manufactured using different methods (Table 3-1), which are characteristic for all 7 samples measured. These show irreversibility lines for all 3 samples pre-irradiation that are similar to those found in the literature (e.g. [21]) with a negative dB_{irr}/dT at lower temperatures that tends towards zero gradient as $T \rightarrow$

T_{c0}. Although there is some variation in the shape of the irreversibility lines between samples, the shape of the irreversibility line of each sample does not change after ion irradiation, apart from it moving to lower temperatures.

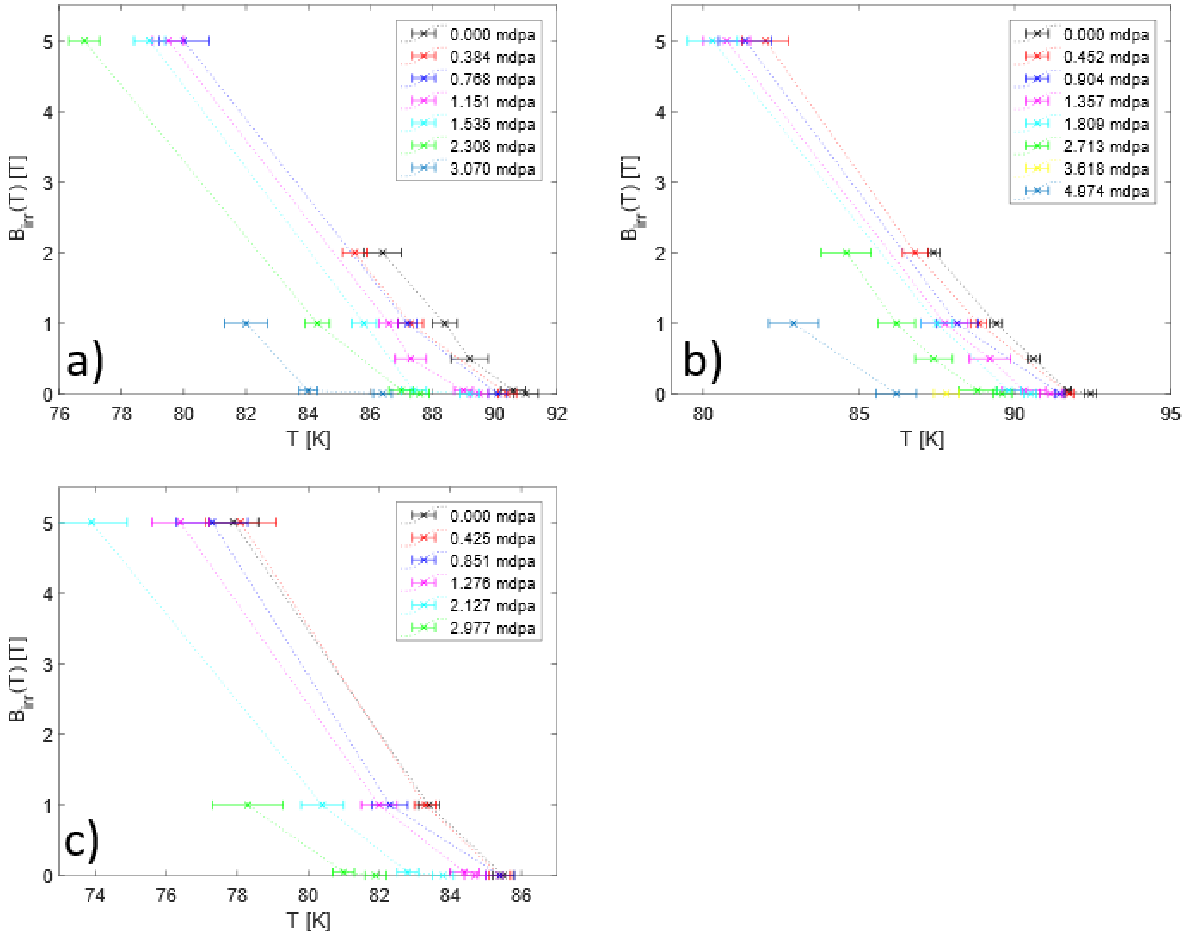

Figure 5.9: Movement of the irreversibility line of (a) SP17, (b) Fu18 and (c) Br18 samples due to irradiation damage. Each graph shows the irreversibility field (B_{irr}, y-axis) at a temperature (T, x-axis).

In Figure 5.10 the measured critical currents of each sample before irradiation are compared at 20 K, 50 K and 77 K. These show that across all temperatures and fields, the enhanced SP17 sample outperformed all other samples. This was not surprising given that the SP17 sample was doped with zirconium which has been shown to produce a mixture of nanocolumns parallel to the REBCO c-axis and nanoparticles that improve flux pinning, resulting in an enhancement of J_c at all temperatures and fields, regardless of field orientation [346], [347]. At 20 K, the Fu18 and Br18 samples also performed relatively well at high field, whilst these samples plus the SP11 and Br18 samples performed well at low field, achieving > 10 MA/cm^2. At 50 K and 77 K, the SP11, SP17 and Fu18 samples had superior I_c to other samples at fields up to 12 T or B_{irr}(T), whichever is lower. Another interesting feature of Figure 5.10 is that at different temperatures different CCs exhibit a range of fields over which the gradient of the loglog plot is constant, indicating that these ranges have a constant power law exponent (i.e. $J_c \propto B^{-\alpha}$), whilst others do not. These are summarised in Table 5-2 which implies that the samples with no advanced pinning centres are more likely to exhibit a range of fields over which the gradient of the loglog plot is constant.

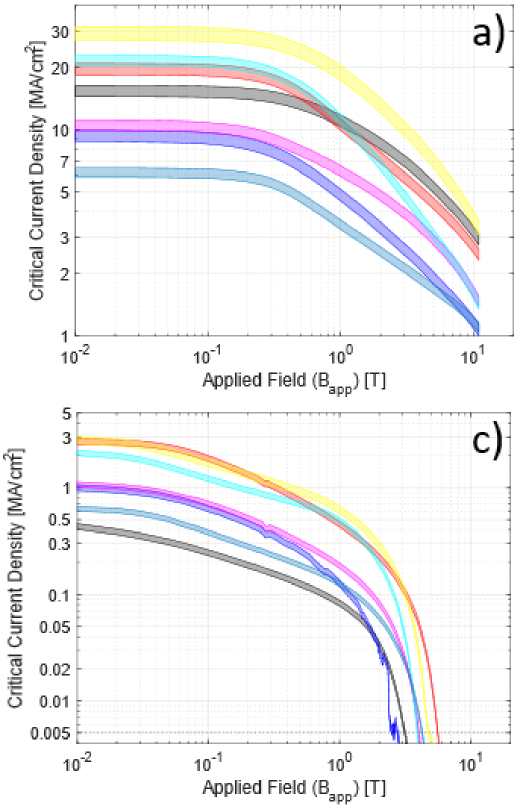

Figure 5.10: J_c (y-axis) versus B_{app} (x-axis) for all samples tested at (a) 20K, (b) 50K and (c) 77K before irradiation. The width of each line represents the error in the calculated J_c values based on the factors (e.g. sample radius) discussed in section 5.1.1 (in legend denotes pinning enhancement).*

Table 5-2: 'α' values (and magnetic field ranges in which they are constant) for the 7 CC samples.'-' indicates that 'α'is not constant at any field range.

Sample	20 K	50 K	77 K
Br18	-	0.23 (0.3-0.8)	-
STI17	0.44 (0.55-4.7)	0.34 (0.2-0.8)	0.45 (0.1-0.4)
Fu18	0.55 (0.75-3)	0.55 (0.45-1.5)	
Sh19_Gd	-	-	-
Sh19_Eu	-	-	-
SP11	-	-	0.35 (0.08-0.8)
SP17	-	-	0.40 (0.1-0.4)

Figure 5.11 shows how the absolute $J_c(B_{app})$ of samples SP17, Fu18 and Br18 CC change with increased irradiation damage and are representative of the trajectories of all 7 samples. These show that the J_c for all samples show a similar decline at self-field, reducing roughly systematically with increasing damage level at all temperatures. However, their responses differ at higher field, with the J_c values at 10 T of the Br18 sample showing a small initial improvement with irradiation damage at 20 K, whilst the Fu18 sample, which has no APCs, shows an initial improvement at both 20 K and 50 K and at fields as low as 0.5 T. All samples also show a decrease in the gradient of the power-law region of $J_c(B_{app})$ as the level of irradiation damage increases, which is consistent with findings reported in the literature (e.g. [21], [143], [263]). The trajectories of J_c with damage level are highlighted in Figure 5.12 where J_c relative to its initial value ($J_c/J_c(0)$) at self-field, 0.5 T and 10 T are shown. Figure 5.12 also highlights that $J_c/J_c(0)$ of the unenhanced CCs declines at a slower rate that the enhanced samples at all temperatures and fields, although only once $J_c/J_c(0)$ started to decline.

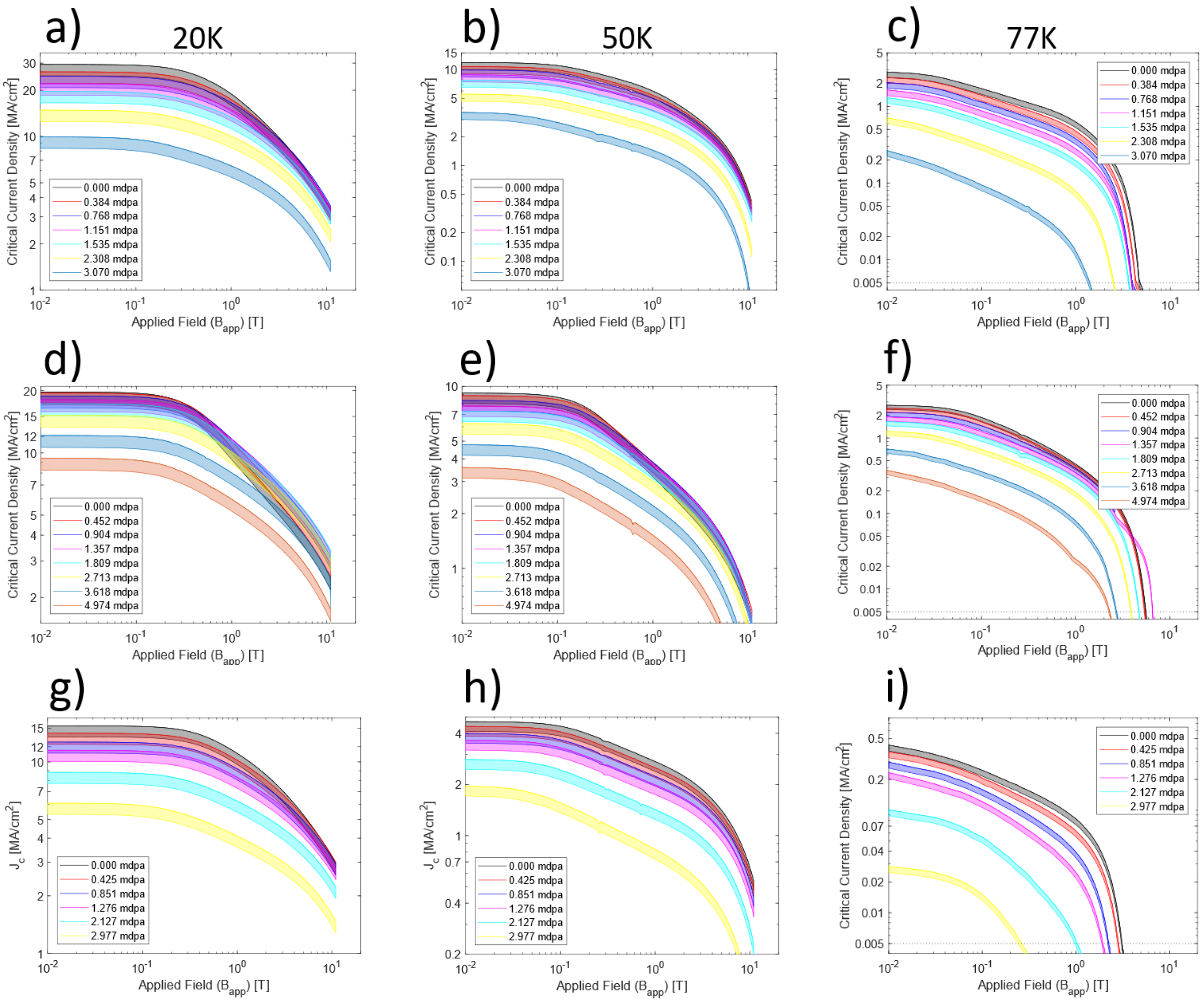

Figure 5.11: J_c (y-axis) versus B_{app} (x-axis) results for the SP17 (a-c), Fu18 (d-f) and Br18 (g-i) samples at 20K (a, d, g), 50K (b, e, h) and 77K (c, f, i).

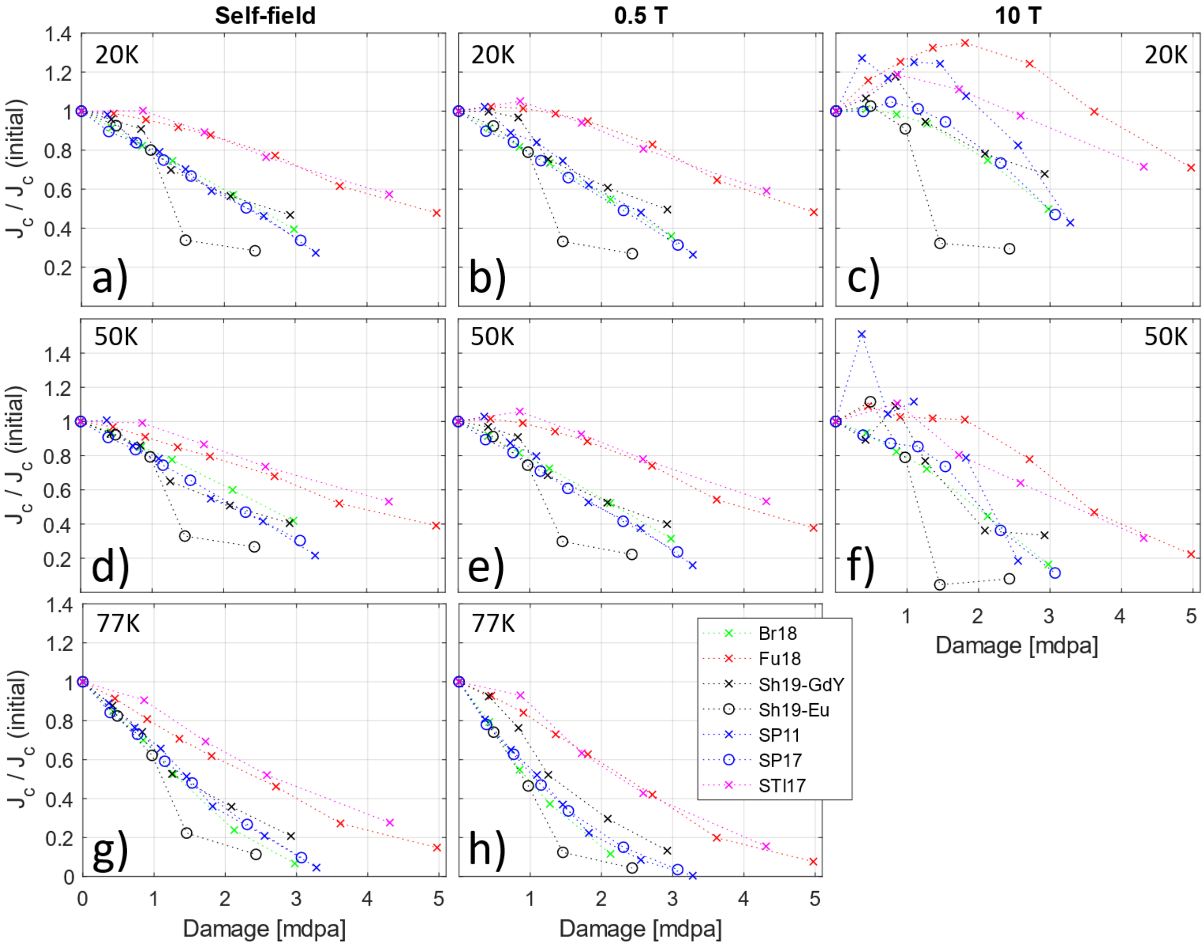

Figure 5.12: Change in J_c relative to its initial value with irradiation damage when B||c = self-field (a, d, g), 0.5 T (b, e, h) and 10T (c, f) for all samples at 20 K (a, b, c), 50 K (d, e, f) and 77 K (g, h).

5.3 Discussion

Based on the results presented in section 5.2, the ability of each CC sample to maintain a superconducting state at all the temperatures measured and at fields of 0-10 T reduces in response to 2 MeV helium irradiation. How each CC responds to irradiation, however, seems to be split into 2 groups depending on whether the sample has had its pinning landscape intentionally enhanced or not, regardless of its manufacturing process. An example of this difference is that the widening in ΔT_c at low field accelerates with increasing damage for the enhanced samples whereas it seems to progress roughly linearly for the unenhanced samples. In addition, the unenhanced samples were more likely to have a range of fields where the power law expression ($J_c \propto B^{-\alpha}$) can be fitted, whereas no such range exists for any of the enhanced samples, even after irradiation. Finally the J_c at all temperatures and fields of the unenhanced samples (although not Sh19Gd) seems to be less affected by irradiation than enhanced samples, characterised by a general lower rate of decline in $J_c/J_c(0)$ at all temperatures and fields than the enhanced samples. Whether $J_c/J_c(0)$ improved before this decline was, as expected from the literature, found to be maximised at low temperature and high field, likely due to the enhancement of flux pinning. That said, the decline in superconducting properties of all the samples did share some characteristics. These included that T_c declined at a similar rate with irradiation (except STI17[25]), that the irreversibility line simply shifts to a lower temperature with increasing damage without changing character and that, considered generally, irradiation led to a slower rate of decline in J_c with increasing B_{app}, regardless of whether $J_c \propto B^{-\alpha}$ can be fitted to a field region.

The above suggests that the methods used to enhance the flux pinning landscape of these samples to improve their superconducting properties make them less resilient to 2 MeV helium irradiation, regardless of manufacturing method used to create the REBCO layer, which is consistent of the findings of Fischer et al. [21] for fission neutron irradiation. Given the several mechanisms that affect T_c and $J_c(B,T)$ that are initiated by irradiation and that 2 MeV helium ions were chosen specifically to displace REBCO's oxygen atoms, the production of defects on the oxygen sublattice is expected to be the dominant cause of the effects presented here. However, the different microstructures in the 7 CC types will also have an important influence on the specific response to irradiation damage, and correlation of the data reported above with these microstructures (not all of which are available from the manufacturers) is an obvious topic for further research.

With the development of the Cold Irradiation Experiment, the primary focus of this investigation became to assess the radiation response of these CCs with a view to selecting one for cold irradiation experiments. The results above imply that unenhanced samples are more resilient to irradiation damage, hence either the Fu18, Sh19Gd or STI17 should be used going forward. Of these, the Fu18 CC was selected as it was thinner than the STI17 sample and therefore would have a more uniform damage profile through the sample thickness, it responded to irradiation with a similar trajectory to the most resilient CC studied by Fisher et al. using fission neutrons [21] and it was made by PLD which, according to a recent review [19], is a the most appropriate manufacturing method for fusion applications.

5.4 Conclusion

In this chapter, the superconducting properties of seven different CCs, subjected to 2 MeV helium ion irradiation, were tracked using magnetometry with the goal of choosing one CC to use during cold irradiation experiments. A valuable set of data was collected comparing the response of materials from different manufacturers. The results implied that samples whose superconducting properties had been artificially enhanced were, in general, less resilient to irradiation using 2MeV helium. Following advice from a recent review [19], and given that it was found to be the most

---

[25] This is suspected to be because the STI CC is thickest sample by a large margin and therefore subject to the largest variation in dpa rate through its thickness.

resilient CC when subject to irradiation by 2 MeV helium ions, the Fu18 CC was used going forward to cold irradiation experiments.

6 Development of the Cold Irradiation Experiment

With the room temperature baseline experiments reported in chapter 5 showing that 2MeV helium ions can produce a similar low temperature, high field J_c response in the Fujikura CC to that shown by Fischer et al. for TRIGA CIF spectrum neutrons [21], the next step to addressing my research questions is to perform experiments comparing samples irradiated at room temperature to samples irradiated and tested at their operating temperature, hereafter referred to as an 'in-situ' experiment. As no apparatus existed to perform this type of experiment, this chapter concerns the design and development of such apparatus, hereafter referred to as the cold irradiation experiment (CIE).

This chapter starts by reviewing the equipment made available by the Centre for Applied Superconductivity (CfAS) and the Surrey Ion Beam Centre (SIBC) before outlining the theoretical aspects of the design. These are split into 3 sections, focusing on the sample and sample stage design, electromechanical design and finally temperature sensing. Tests illustrating the performance of the CIE are then described before the in-situ experiments were started (chapter 7).

6.1 The Available Equipment

The basis of the CIE was a model C22 Cryodyne cryocooler (Figure 6.1, ❸) which can cool its second stage cold surface (Figure 6.1, ⓫) to below 20K using 250psi helium regulated by a model 8200 compressor (Figure 6.3, ❼) [348]. This cryocooler had been modified by the SIBC to allow assembly onto their 2 MeV beamline using ϕ10cm stainless steel vacuum spacers (Figure 6.3, ⓬) and a beam line mounting plate (Figure 6.1, ❺). This assembly allowed access for a ϕ5 mm diameter beam spot to the copper sample stage (Figure 6.1, ❶) via an aperture chamber (Figure 6.1, ❷) attached to the cryocooler's high temperature cold surface through a radiation shield and a low temperature radiation shield (Figure 6.1, ❻) attached to the sample stage. These radiation shields together greatly reduce the effect of radiative sample heating ($\propto \Delta T^4$). Attached to the sample stage, and in line with the beam path, was a copper angular offset (Figure 6.2, ⓬) which offsets the beam strike surface to the beam path by ≈ 20°. This was added as previous experimenters needed to avoid channelling in their textured substrates and was therefore retained for this work. This angular offset could also be moved parallel to the direction of the slope over a range of ≈4mm so that the beam strike location could be altered to account for the sample design. A silicon diode (SD) temperature sensor was also provided, attached via a spring clip to the cold side of the angular offset (Figure 6.2, ⓮). Electrical connections could be made through the vacuum vessel walls using two hermetically sealed electrical ports, both initially Fischer type 105A038 (Figure 6.1, ❼ and Figure 6.2, ❺).

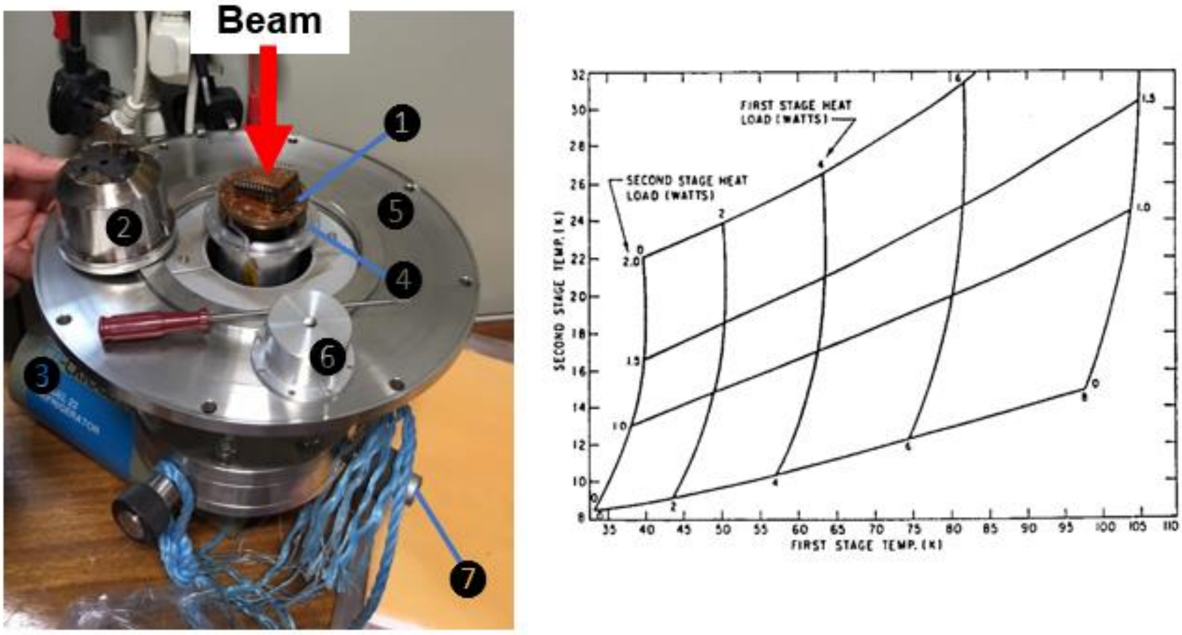

Figure 6.1: Equipment provided by SIBC for cold irradiation experiments. Figure shows (a) cold head demounted from the beam and dismantled to show internal components and (b) the typical refrigeration capacity of the Model 22 Cryodyne cryocooler, reprinted from [348]. *Labels are 1: Sample Stage; 2: Aperture Chamber; 3: Cryodyne C22 Cryocooler; 4: High Temperature Radiation Shield; 5: Beamline Mounting Plate; 6: Low Temperature Radiation Shield; 7: 2x 18-pin, hermetically sealed ports for electrical connections; 10: Spacer (φ10cm).*

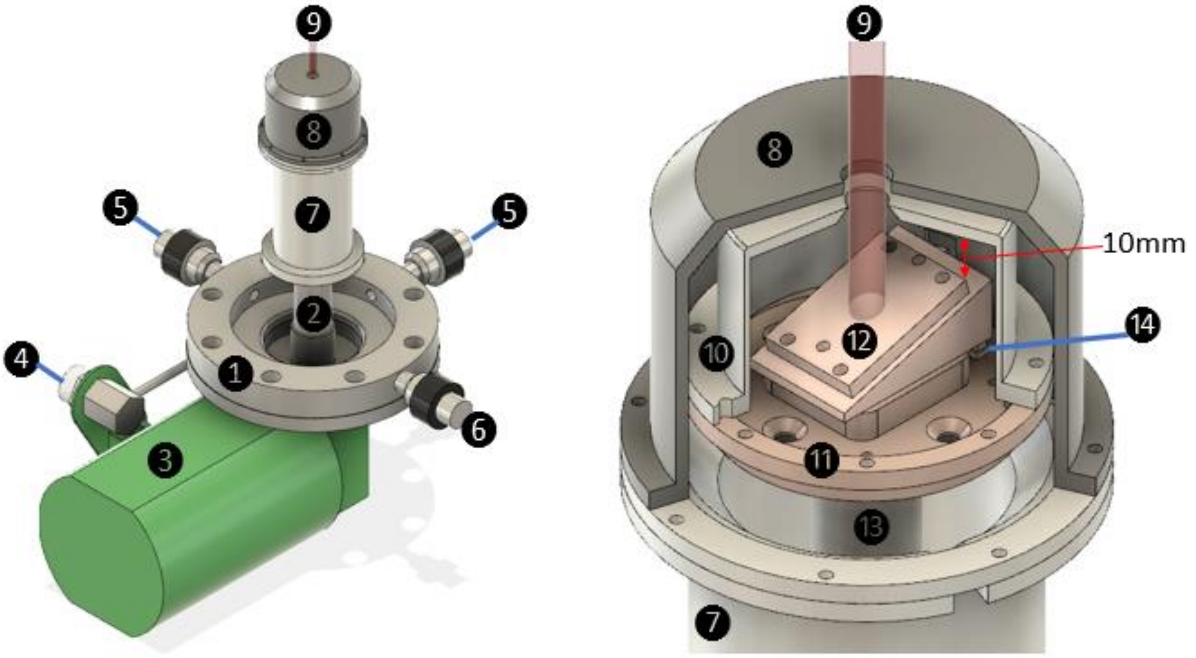

Figure 6.2: 3D CAD model of (a) the entire SIBC CH equipment and (b) a sectioned view of assembled sample stage. Labels are 1: Vacuum Chamber piece housing electrical ports ; 2: Cryocooler 1st Stage; 3: Cryodine C22 Cryocooler Body; 4: Ports for 250psi Helium lines; 5: Hermetically Sealed 16-pin Fischer connector (female); 6: Sealed Port; 7: High Temperature Radiation Shield (≈80K); 8: Aperture Chamber; 9: Expected Beam Path;10: Low Temperature Radiation Shield; 11: Sample Stage; 12: Angular Offset; 13: Cryocooler 2nd Stage; 14: Silicon Diode (SD) Temperature Sensor and its spring clamp. Important measurements include the interface area between 10 & 11: 486mm^2, the maximum interface area of 12 with the sample: 114mm^2 and the minimum distance between top of angular and Low Temperature Radiation Shield: 10mm.

Sample testing with the CIE required a plethora of additional equipment shown in and listed within the caption of Figure 6.3a. Most experiments were performed at CfAS and involved inserting a sample, cooling it for testing and then allowing it to warm back to room temperature. These will be referred to hereafter as “ex-situ” experiments, regardless of whether the sample was subsequently irradiated between tests. When moving to the SIBC beamline to perform “in-situ” experiments, the set-up of the additional equipment was identical with 2 exceptions; that the 8200 compressor was water cooled, as it and the beamline end station were in a cleanroom, and that the wiring between additional equipment and CIE had to be extended by ≈ 10m so that the additional equipment could be set-up outside the cleanroom.

One of my first tasks on getting the cryocooler to CfAS was testing its capabilities and comparing them with those stated in the manual (Figure 6.1b). The experiment set-up with an additional SD sensor attached to the top of the angular offset, before assembly of the low and high temperature radiation shields, is shown in Figure 6.4a. Figure 6.4b shows the resultant time trace of the temperature when the experiment is in vacuum and fully assembled with low and high temperature radiation shields. This implies that when subject only to radiative and sensor wiring heat loads, the sample stage can be cooled to 17-18K.

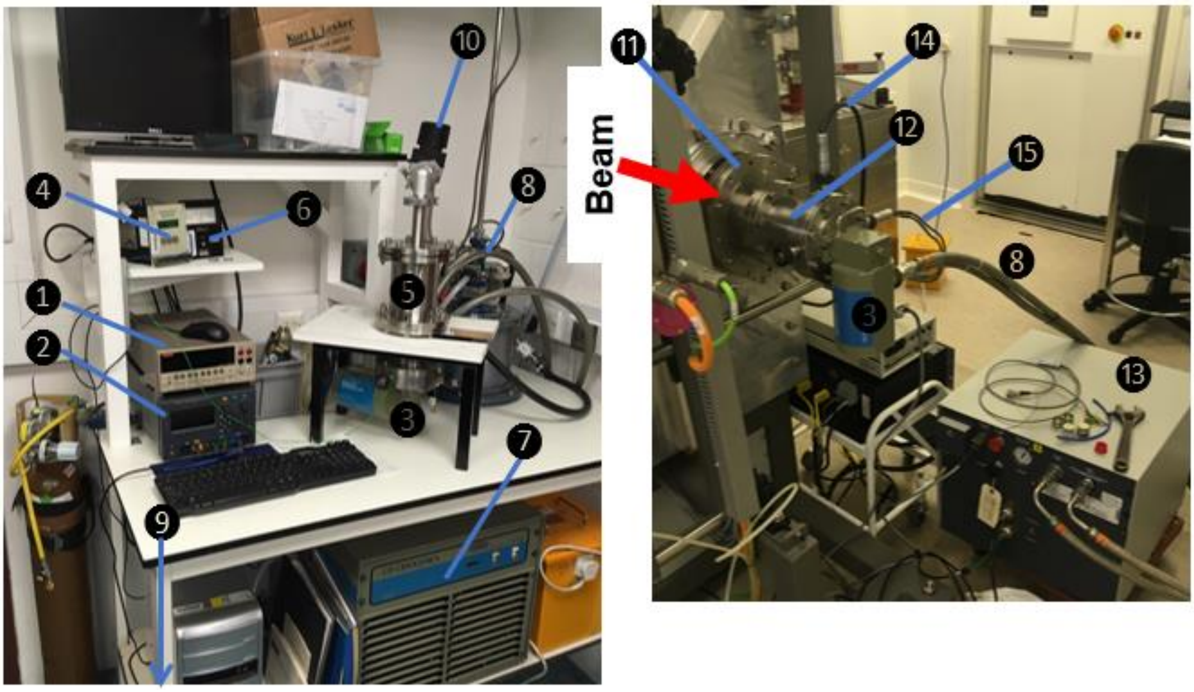

Figure 6.3: Experiment set-up at (a) CfAS and (b) SIBC for Cold Head experiments. Labels are 1: Keithley 2000 Voltmeter; 2: Keysight E36311A DC PSU; 3: Cryodyne C22 Cryocooler; 4: Temperature Indicator; 5: Vacuum Chamber (internal diameter: φ10cm); 6: Vacuum pressure gauge; 7: Air-cooled model 8650 Helium compressor; 8: 250psi helium lines; 9: Keysight N6971A DC Power Supply (20V / 100A) (received after February 2020); 10: Vacuum Pump Isolator Valve; 11: Beamline mounting plate; 12: Spacer (internal diameter: φ10cm); 13: Water-cooled model 8650 Helium compressor; 14: Voltage Tap, Temperature sensor & heater room temperature wiring; 15: Sample Current supply wiring.

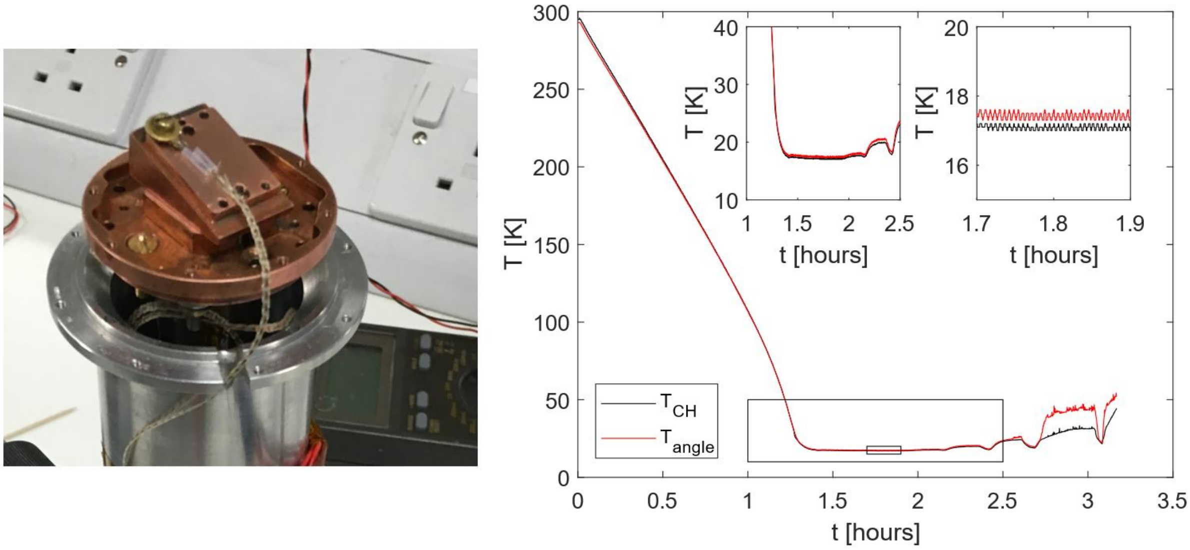

Figure 6.4: Preliminary experiment designed to assess the starting cooling capabilities of the cold irradiation experiment. a) the experiment set up showing the temperature sensor attached to the angular offset, b) the measure temperature (y-axis) vs experiment duration (x-axis) for the stripped down Cold Head experiment showing that the cold head cold surface can reach ≈17K.

6.2 The Cold Irradiation Experiment Design

In this section, the theoretical aspects of the sample and sample stage design, electromechanical design and requirements of temperature sensing and control are discussed with a view to performing in-situ critical current (I_c) measurements on REBCO CCs using the equipment described above.

6.2.1 Sample and Sample Plate Design

6.2.1.1 Superconductor Length and Width

In this experiment, transport current testing was used in the CIE with E_c =1μV/cm and t=2μm (Figure 6.6a), as introduced in chapter 3. One common feature of these experiments in the literature is that there is often a section of the J_c(B, T) that cannot be defined as the experiment is current supply limited (e.g. [84]). This issue persists here as the Keysight N6971A power supply unit (PSU) used for this work has a maximum DC current limit of 100A. This can be related to the maximum allowed width of the sample if it is assumed that the maximum J_c the CIE needs to be able to measure is 30MA/cm^2 – chosen with reference to the results of chapter 5. Given that determining J_c requires that an accurate voltage be measured across the sample, the maximum width of the sample therefore depends on L and the resolution of the voltmeter used. For this work, a Keithley 2000 voltmeter (K2000) was used whose resolution was measured at $\pm$1μV (Figure 6.5). To avoid systematic errors in L, it was decided that the entire length of each track should be irradiated, thus a practical limit on L is set to 4mm, 1mm less than the beam spot diameter. Given these values for E_c and L, regardless of sample width, the sample voltage at I_c is 0.4μV thus voltages generated by currents well in excess of I_c are required to define J_c. Leaving aside for the moment that excessive voltage in the superconductor leads to excessive heating (discussed in section 6.2.1.3), a voltage of 10µV was used to define the maximum sample width. Using this limit and equation 3-1, the maximum width (w_{max}) can be shown to be ≈ 142µm as a sample of this width and J_c = 30MA/cm^2 and n = 20 generates a voltage of ≈10 µV at 100 A, given its predicted I_c of 85.1 A. Given that the Fujikura CC being studied contains no artificial pinning centres, disruptions to the GdBCO layer typically nucleate at a small imperfection. These disruptions increase in lateral size as more layers of GdBCO are laid down on top of it. An example is shown in the inset of Figure 6.6a, implying that disruptions to the GdBCO layer manifest as surface imperfections (Figure 6.6b) and that the size of these surface imperfections is the maximum lateral extent of the defect. Based on Figure 6.6b, the lateral extent of these surface imperfections varies from 1-5 µm, much more than ξ_{ab} and the grain size of CC's pristine GdBCO (0.3-0.6 µm, Figure 6.6c&d). This means that tracks with a width > 40-50 µm, as a first estimate, should have a J_c that approaches the J_c of the entire tape, with some variation expected beyond that specified by the manufacturer (±2.6% measured at self-field and 77K [349]) as $w \ll$ 4 mm. This range of track widths (40-142 µm) means that processing the 4 mm CC to create tracks is required. This was achieved using photolithography and 0.7M H_3PO_4 etching, as discussed in chapter 3.

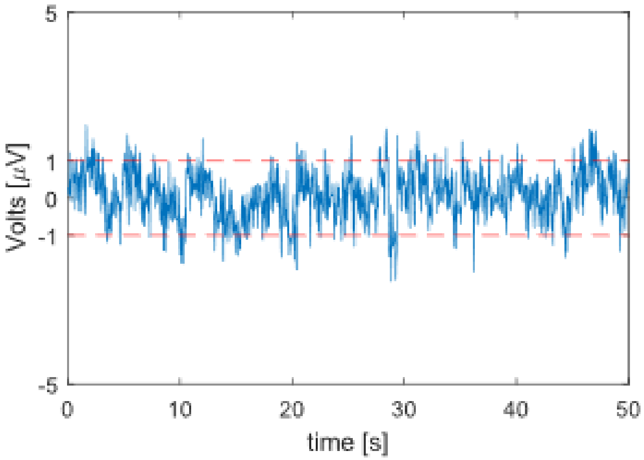

Figure 6.5: Variation over 50s (time on x-axis) in the Keithley 2000's DC voltage (y-axis) whilst voltage terminals were open circuit. (Medium acquisition mode, no sample filtering used).

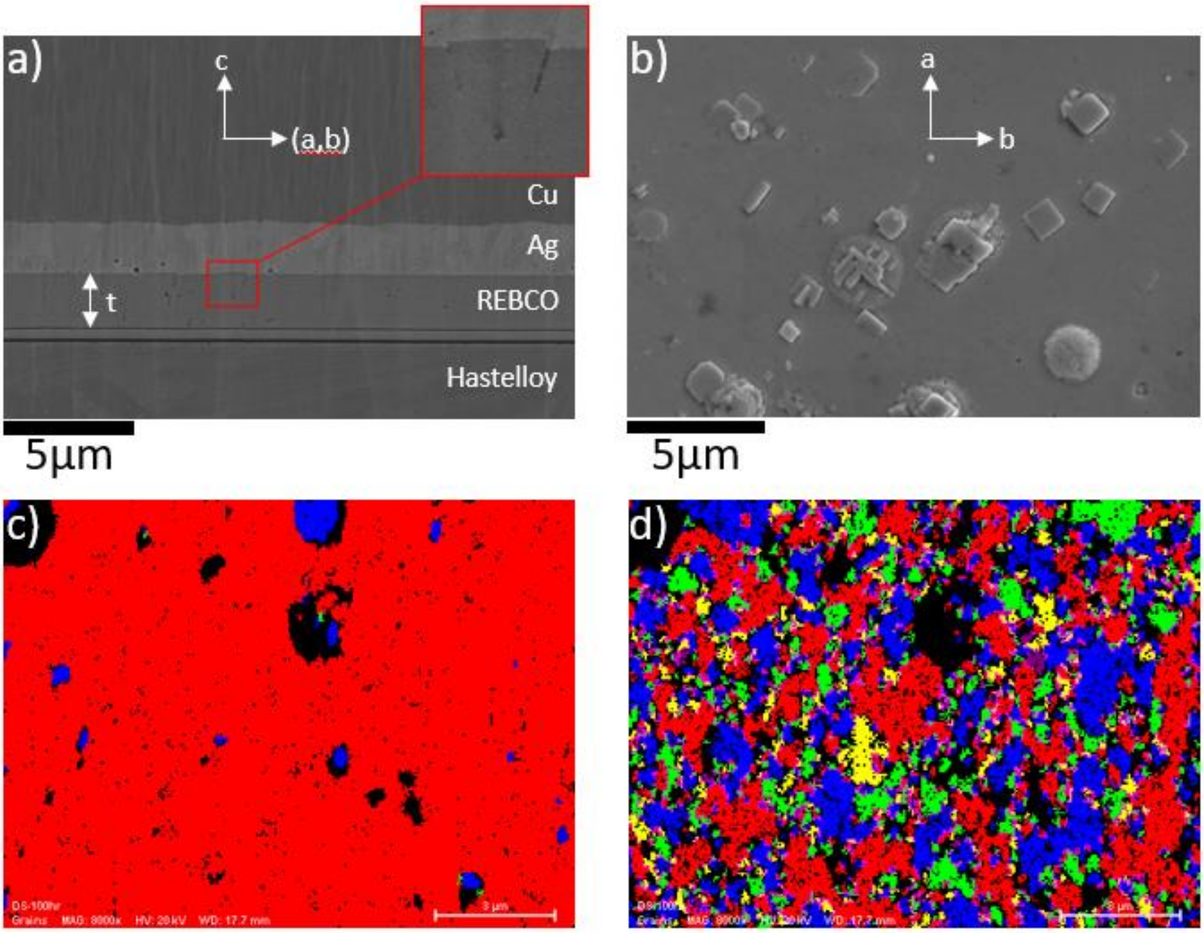

Figure 6.6: SEM and EBSD images of exposed GdBCO of the Fujikura 2018 CC. a) view parallel to the (a,b) plane after tape cross-sectioning in a Gatan Precision ion polishing system (PIPS); Inset: close-up of an imperfection in the GdBCO layer nucleated at a point and growing in lateral extent was more GdBCO is layered on top of it; b) View of Fujikura CC GdBCO layer surface parallel to GdBCO c-axis and CC normal direction; Grain orientation angle was determined using EBSD for a region of SEM image b). c) shows the data presented with a grain misalignment threshold of 0.6° and d) with a grain misalignment threshold of 0.3°. Images c&d courtesy of Sangeeta Santra and Josef Hazi.

6.2.1.2 Parallel Current Paths

In this section, the resistance of the current paths parallel to the SC layer – ie. the c276 Hastelloy substrate (c276) and surrounding copper and silver layers – are examined to evaluate whether their presence complicates the determination of I_c for the thin SC track. This would be the case if any or all of these layers have a similar resistance to the SC track during measurement of the transition to the normal state (ie. when $V_{sc} > 1\mu V$).

Given the SC track itself has current dependent properties due to its superconductivity and that the track's I_c is likely to diminish once it is irradiated, during a transition the track can be said to have an effective resistance $(R_{sc,eff}) = V_{sc}/I_{sc}$. Before irradiation, I_c should be relatively high and a measurable voltage should only appear when $I_{sc} > I_c$. Using the previously stated example of a track with L = 4mm and (I_c, n) ≈ (85.1A, 20), the potential drop along the track should only be V_{sc} = 10 µV at 100 A, thus the track's maximum $R_{sc,eff}$ = 0.1µΩ in the V_{sc} range of interest for determining

(I_c, n) (ie. V_{sc}=0-10 µV). After irradiation, however, I$_c$ has diminished: for example a track with (I_c, n) ≈ (1A, 20) will generate a V_{sc} = 10 µV at 1.175A, an effective resistance in the track of 8.51µΩ, rising to $R_{sc,eff}$ = 39.2 µΩ if V_{sc} was allowed to rise to 50 µV at I_{sc}=1.273A. Therefore, if the copper, silver and c276 Hastelloy (c276) substrate layers running in parallel with the current path in the track have a combined resistance, hereafter referred to as the non-track resistance ($R_{non-track}$), of the order of 10-100µΩ, current sharing between track and non-track current paths during each transition would be significant when I$_c$ is low and thus complicate the determination of (I_c, n). That said, if $R_{non-track}$ could be made to be $\gg$ 100µΩ then significant current sharing could be avoided in the sample voltage range V_{sc}=0 - 50 µV and the measured voltage along the sample would effectively equal V_{sc}.

Creating samples with $R_{non-track} \gg$ 100µΩ requires that the different current paths along a CC and their associated resistances be analysed and compared. In its normal state, the Fujikura CC being considered here is essentially a conductor with 2 copper layers, 2 silver layers, a GdBCO layer and the substrate layer in parallel, all electrical linked via the enveloping coper and silver layers[26]. Ideally, all these layers would remain unmodified in order to simplify the process of making samples. The width of the CC is 4mm, the layer thicknesses of the copper, silver and c276 substrate are 20µm, 2µm and 50µm (Figure 6.6b and [349]) respectively and the resistivity of the copper, silver and c276 substrate at 20K are 2x10^{-9}, 2x10^{-9} and 1.23x10^{-6} Ωm respectively [150], [350]. This results in the resistances per cm for each of the copper, silver and c276 layers of 250µΩ/cm, 2.5mΩ/cm and 60mΩ/cm respectively, therefore, assuming the REBCO layer is not superconducting at 20K, the unmodified CC would have a resistance ≈113µΩ/cm using the addition rules for resistors in parallel.

However, as shown by SRIM and the room temperature irradiation experiments described in chapter 5, the copper and silver layers must be removed from one side of the CC to expose the REBCO layer if 2MeV helium ions are to damage the REBCO layer without implanting. The first option therefore is to only remove the copper and silver from one side of the CC, resulting in a $R_{non-track}$ at 20K of ≈226µΩ/cm. Given the short lengths of the sample ($L \leq$ 4mm), this option was deemed to give an insufficient margin to $R_{sc,eff}$ to allow the measured voltage along the sample to equal V_{sc} in the range V_{sc}=0 – 50 µV, hence the option was taken to remove the copper and silver from both sides of the CC as this lead to a $R_{non-track}$ at 20K of ≈ 60 mΩ/cm, orders of magnitude higher than the 100 µΩ minimum required, even for these short track samples.

One of the drawbacks of removing copper and silver from both sides of the CC is that these metals are excellent thermal conductors, making them useful for extracting thermal energy from the REBCO

---

[26] despite some of buffer layers being excellent insulators

track during a superconducting-to-normal transition, discussed further in section 6.2.1.3. Further modification to the sample to tune $R_{non-track}$ to improve the thermal design of the sample were therefore considered but not implemented in this work[27], but would be important if quenches in higher I_c samples caused failures in future experiments.

6.2.1.3 Sample Heating

As alluded to above, a thin narrow track of REBCO carrying $I_{sc} > I_c$ will be subject to a flux flow resistance and, as $V_{sc} \neq 0$, will experience localised heating. As $V_{sc} \propto I_{sc}^n$, the magnitude of the ohmic heating builds up quickly as I_{sc} increases. At some higher current, however, the superconducting state breaks down, leading to significant current flow in the substrate (i.e. a quench) as, despite its much higher resistance, it will be the lowest resistance element of the sample. Hence the issue of sample heating occurs on 2 scales: if the sample quenches it could be damaged, partially or completely, due to localised heating[28], or, even if the sample remains superconducting, the shape of the I-V curve could be distorted, leading to errors in the fitting of equation 3-1. It is therefore especially important to avoid sample quenches due to the likelihood of damage and to minimise sample heating during a transition. That said, the experiment needs to measure I-V curves during a superconducting transition to determine I_c, therefore some sample heating is, by necessity, unavoidable. Given this sample heating, some time is therefore required between I-V curve measurements to allow the sample and its surrounds to return to their equilibrium temperatures. In this section, the issue of sample heating during the generation of I-V curves is examined to avoid sample damage and distortion of the I-V curve.

As a first approximation, the heating of the sample volume of interest is considered an adiabatic system, simply heated by the application of current with no heat dissipation to its surroundings. In this adiabatic approximation, the following expression can be applied to calculate the initial rate of temperature rise (dT/dt [K/s]):

$$\frac{dT}{dt} = \frac{V_{sc} I_{sc}}{D\, wLt\, C_p} \tag{6-1}$$

where D [kg/m^3] and C_p [J/kgK] are the density and specific heat of the volume subject to adiabatic heating respectively. Below I_{sc} the temperature will not change (as $V_{sc} \approx 0$), but the sample temperature will start to rise once $V_{sc} \neq 0$.

One key issue with equation 6-1 is to determine what is the appropriate sample volume to assume is inside the adiabatic volume, particularly relevant when considering the worst-case scenario in which

---

[27] I_c was reduced instead, as discussed in section 6.3.2

[28] in extreme cases even melting

only the track is included. In this worst-case, assuming $w = w_{max}$, D_{REBCO}=6.63g/cm^3 and $C_{p,REBCO}$=10.5 J/kgK [351], dT/dt is ≈1K/s at I/I_c= 75% rising to ≈12,700K/s at the voltage limit of 10µV (I/I_c: 117.5%). These temperature rises are extremely fast and imply that a constant current applied with I/I_c > 0.75 would result in a change in sample temperature that would affect the shape of the *I-V* curve. One solution would be to pulse current through the sample (t_{pulse}), although the worst-case scenario described above suggest t_{pulse} should be limited to less than 78µs to avoid a sample temperature rise of >1K as V_{sc} approached 10 µV.

Determining if the adiabatic volume can be enlarged in any direction requires an assessment of the rate of heat diffusion away from the track. The thermal property governing this is known as the Fourier Number (Fo) and equals 1 when the rate of heat diffusing away from a volume equals the rate at which it is being stored in that volume [352]:

$$Fo = \alpha\, s/d^2 \qquad \text{where} \qquad \alpha = \kappa/D\; C_p \tag{6-2}$$

where α [m^2/s] is the material's thermal diffusivity, s [s] is the time since a system's thermal shock began, d [m] is the length scale over which thermal conduction occurs away from the material and κ [W/mK] is the material's thermal conductivity [352].

As Fo depends on time (s), it implies that thermal energy generated in the track will initially lead to a temperature rise locally in the track which, over time, drives faster and faster thermal diffusion away from the volume of interest until only a small fraction of the energy is stored. Fo = 1 therefore can be used to determine the time scale over which a volume mostly stores energy (Fo<1) or transmits it to another volume (Fo>1). The relevant length scales for the track in this situation are the CC thickness, width and length, taken to be ≈ 50µm, 4mm and 1cm respectively for this analysis. Given these length scales and that $\alpha_{c276} \approx \alpha_{buffers} \approx \alpha_{REBCO} = 0.5$ cm^2/s at 20 K [150], [353], [354][29], thermal energy starts to dissipate away from the sample track faster than it is being stored after 50µs, 320ms and 2s parallel to the sample thickness, width and length respectively. These results imply that, even over the worst case t_{pulse} limit of 78µs, the Hastelloy volume directly below the track receives significant thermal energy and can be included in the adiabatic volume. Including this volume decreases dT/dt to ≈ 545 K/s at V_{sc}=10µV (I/I_c: 117.5%) and allows an increase in the maximum t_{pulse} to ≈2ms to avoid a sample temperature rise of >1K.

---

[29] No direct measurements of the thermal diffusivity of the buffer layers at 20K could be found but data from Hofmeister [382] and Suzuki et al. [383] suggest that the thermal diffusivity of 3 of the 4 the buffer layers (Al_2O_3, MgO and CeO_2) is > 0.15 cm^2/s at room temperature, the lowest temperature measured, and the character of each $d\alpha/dT$ curve suggests that the thermal diffusivity of each buffer layer should be of the order of 0.5 cm^2/s at 20 K.

Given these initial estimates, it is clear that direct sample heating due to flux flow during a transition is an issue that needed to be monitored. Although these estimates are conservative, given that the track and the c276 beneath it have relatively high thermal diffusivity and are not thermally insulated from the rest of the sample, t_{pulse} still needs to be minimised to avoid a significant temperature rise in the superconducting material being monitored. One alternative option is to increase the temperature of interest above 20K as this decreases sample J_c and the effective flux flow resistance for a given V_{sc}.

As a starting point, I considered that t_{pulse} lengths of the order of the sampling time of the K2000 (≈20ms in sub-µV range[355]) were required, with as fast as possible current rise and fall times, and therefore that some sample temperature increase should be expected during each current pulse where $V_{sc} \neq 0$. The length of time between pulses (t_{off}) should also be made sufficiently long to allow the sample temperature to return to its equilibrium value. For most current pulses, V_{sc} will be less than 1µV and indistinguishable from the noise and t_{off}= 0.5s was used in these cases. As the voltage increases very quickly with current during a transition, the magnitude of the current pulse was also raised at the smallest possible increment (≈0.02A for the N6971A) so that the low power sections of a transition can be identified and allow t_{pulse} and t_{off} to be adjusted, potentially on the fly. This should also have the benefit of maximising the number of points recorded during the transition, assuming voltages are recorded at the smallest possible time step without filtering, and thus reduce fitting errors in determining (I_c, n).

6.2.1.4 Sample Placement and Insulation

As shown in Figure 6.2, the beam strikes the angular offset roughly in line with the centreline of the sample stage. The angular offset has 4 tapped M2 holes to allow samples to be fixed to it. The sample also needs to be electrically isolated from the sample stage whilst being in good thermal contact. To achieve this, metal clad printed circuit board (MCPCB) was used as the sample plate. MCPCB consists of a thick aluminium sheet that has an insulating layer attached which is then overlaid with copper. The MCPCB used here[30] used 1.6mm thick aluminium and 70µm thick copper. Another benefit of this choice was that copper and aluminium are both compatible with REBCO CCs in terms of their thermal contraction during cooling from room temperature to 4.2 K[31], as shown by Barth [351].

---

[30] Provided by DK Thermal.

[31] integrated thermal contractions measured at $\varepsilon_{CC} = -0.27\%, \varepsilon_{Cu} = -0.32\%$ and $\varepsilon_{Al} = -0.41\%$ when dropping from RT to 4.2K.

6.2.1.5 Initial Design

The initial idea for the sample and sample plate is shown in Figure 6.7 and Figure 6.8. Both are prepared by first cutting a 4-5 cm long section of CC. The copper and silver envelopes are then removed, front & back, from the CC to expose the REBCO layer over a length of 8-10mm using a combination of $FeCl_3$ solution and $NH_4OH:H_2O_2$ solution etches, as described in section 3.4.2 (Figure 6.7).

The apparatus designed to perform this etch successfully whilst adhering to the required health and safety policy involved the use of 2 borosilicate glass slides and PTFE tape (both inert to attack from the $NH_4OH:H_2O_2$ etchant) to mask off sections of the CC where the copper and silver need to remain (Figure 6.7, ❷). Each glass slide has 10 wraps of PTFE tape around it with the adjacent edges 8-10mm apart, making sure the wraps are as neat and as flat as possible. The CC is then inserted between them, the assembly clamped together by hand and the pressure maintained using more PTFE tape. Etchant is then pipetted into the cavity created between the PTFE wraps and glass slides to begin etching. 10 wraps are used as this provided an optimum distance between each slide to allow etchant to access both sides of CC with surface tension keeping the etchant within the cavity.

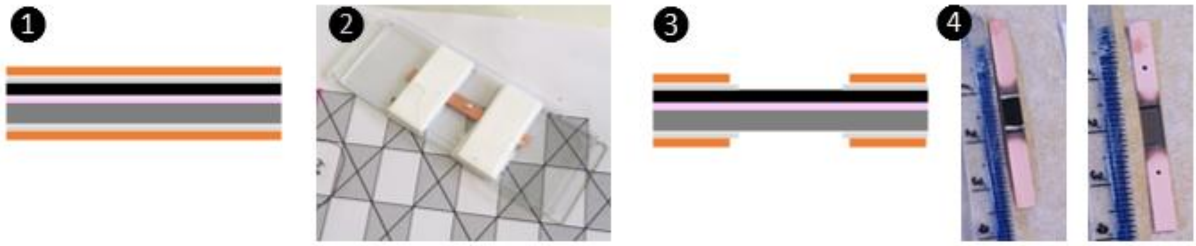

Figure 6.7: Stages 1 & 2 of the sample preparation process. Steps include 1: cutting a CC ≈ 4-5 cm long, 2: assembling the mask so that only a section of the CC 8-10mm long is contained in the cavity bounded by glass slides and PTFE tape, 3: Etching with $FeCl_3$ then $NH_4OH:H_2O_2$ solutions expose REBCO and Hastelloy substrate. 4: an example of an etched sample after removal from mask assembly (left: REBCO side up, right: Substrate side up).

Experimentation with this process showed that the $FeCl_3$ etch (60g $FeCl_3$: 100ml of water) worked best when the solution was replaced periodically and typically took 10-12 minutes. Overexposing the sample to the $FeCl_3$ etch, however, led to $FeCl_3$ build-up on the CC that prevented the $NH_4OH:H_2O_2$ etch from working correctly. The $NH_4OH:H_2O_2$ etchant consisted of a 1:1 mixture of each component, each a 30% water solution. Assuming no issues with the $FeCl_3$ etch, the REBCO exposure took 15-30s and required only 2ml of etchant.

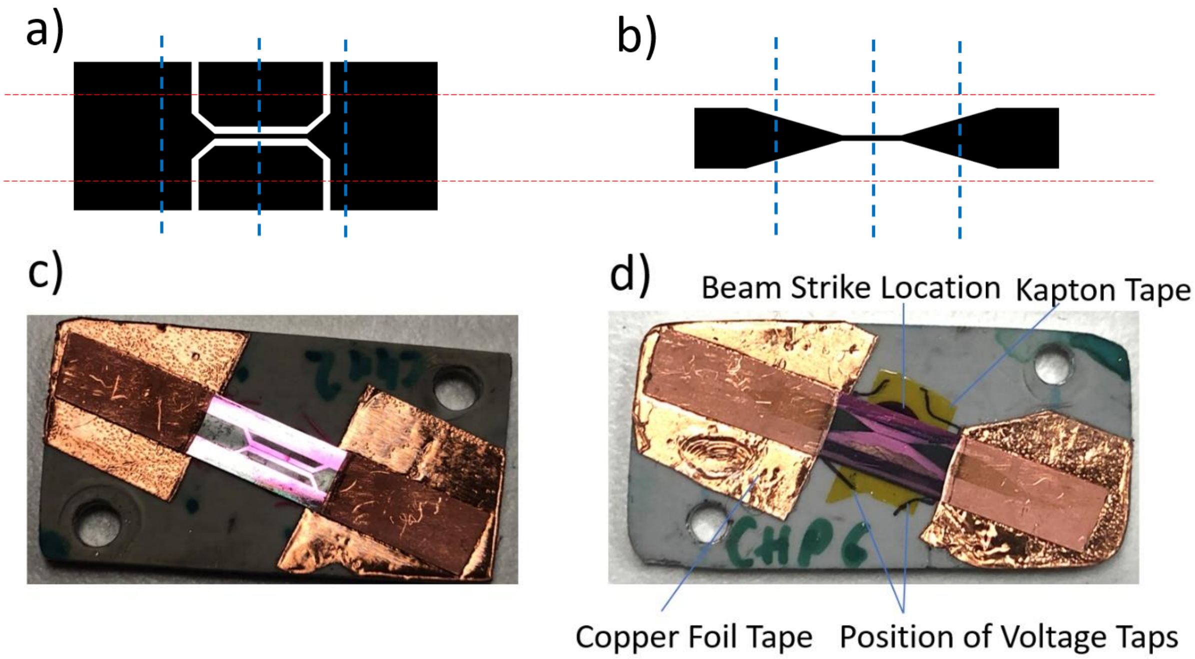

Figure 6.8: Example Photomasks designed to produce CIE samples with 200 µm wide tracks of length a) 4mm and b) 2mm. Red dashed lines denote position of CC and blue dashed line denote each end and the centreline of the exposed section of the CIE sample. Finished CIE samples of c) 4mm and d) 2mm in length assembled on sample plate ready for testing.

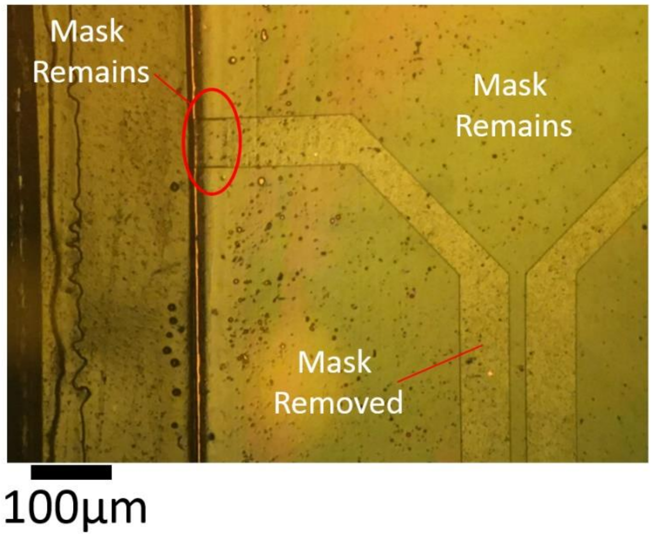

Figure 6.9: Light microscope image of a CIE sample with 4mm long track after being developed for 2 minutes. The photoresist remains on sections that needs to be etched due to a build-up of resist on that edge of the sample during spin coating..

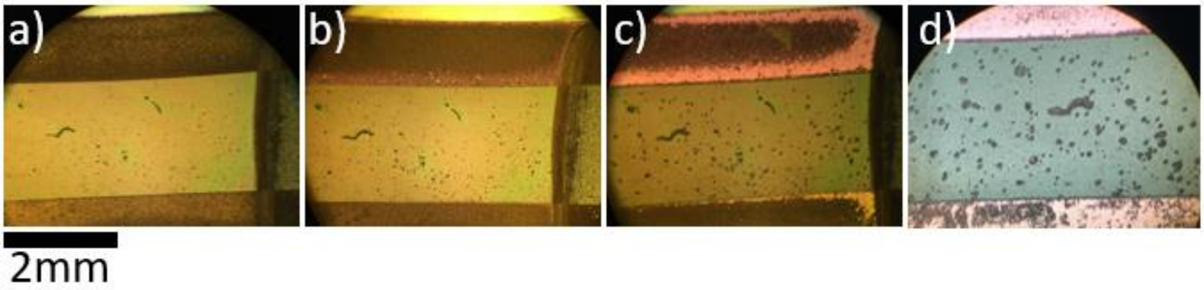

Figure 6.10: Etching test using a 1μm thickness photomask. Surface imperfection in the REBCO layer protruding through the photomask lead to significant undercutting the mask, an issue exacerbated as etching time increases. a) 10s; b) 90s; c) 140s and d) 200s with photomask removed.

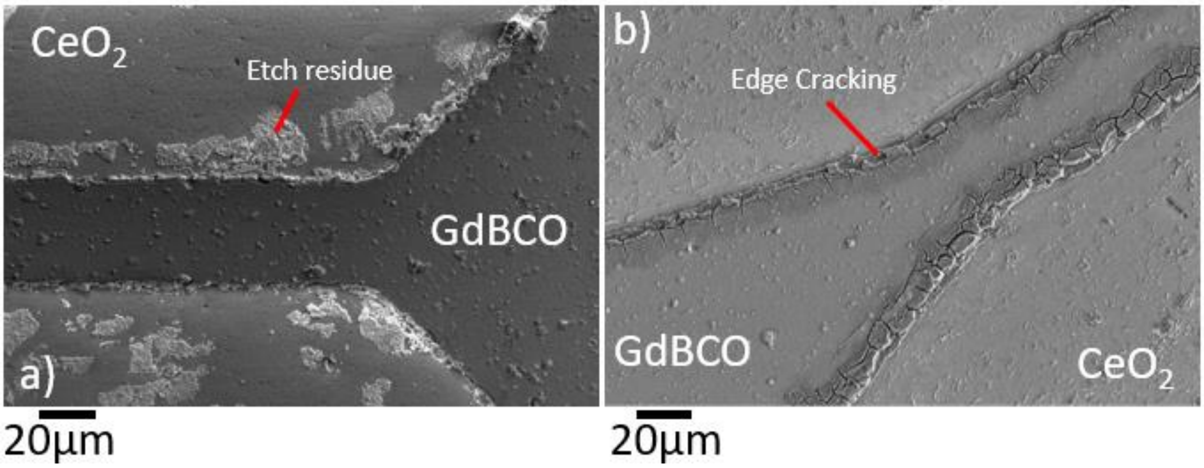

Figure 6.11: SEM images of a) sample RT2: a nominally 50μm wide, 4mm long track etched for 45s and b) sample RT3: a nominally 60μm wide, 2mm long track etched for 90s. Both images show that the average track widths are significantly reduced (a: 37 μm, b: 40 μm) and b) shows severe track edge damage due to cracking.

The next stage in the process was to create the narrow track in the REBCO layer. This is achieved using a combination of photolithography and etching with 0.7M H_3PO_4 solution. Applying the photomask was achieved by first attaching the sample to a silicon wafer using double sided Kapton tape. Shipley 1813A positive photoresist was then applied by pipetting 1 drop of resist on to the middle of the exposed REBCO and then spinning clockwise at 4000rpm for >30 seconds. The resist was then baked at 113°C for 1.5 minutes before being assembled into a mask aligner. 2 photomasks were designed for this work (Figure 6.8a&b) to produce 2mm or 4mm long tracks of widths between 20-500 µm and either removed thin trenches either side of the track (Figure 6.8a) or all excess REBCO (Figure 6.8b). Both were acquired from JD Photo Data [356] based on my designs.

Once aligned, the photoresist was exposed to UV light for 12-20 seconds (for both masks) and then removed using AZ726 developer solution for 2-4 minutes. A recurring issue during development was that the clockwise rotation of the spin coating often led to a thick build-up of photoresist on the anticlockwise edge of the CC which would then need significantly longer time in the developer to remove (Figure 6.9). 4 minutes was deemed the maximum allowable time for development as beyond 4 minutes the integrity of the unexposed photomask started to degrade.

After development, the position of the track was assessed using a light microscope to gauge whether the track should be etched. A common issue leading to the process needing to be restarted was that imperfections in the REBCO surface often protruded through the photomask. This issue is illustrated by the etching test shown in Figure 6.10 where even the smallest protrusions can lead to the REBCO beneath, which would otherwise be protected by the photomask, being removed over length scales of the order of 20µm over the course of a 200s etch.

Once a track with minimal imperfections has been successfully developed, etching with 0.7M H_3PO_4 solution was performed. A typical etch was performed in 10s intervals, monitoring the integrity of the track's mask between etches. Etch durations varied from 45-90s at which point the pink-purple colouring of the CeO_2 buffer layer beneath the REBCO was clearly visible. Even at this stage, etchant undercutting the mask was a typical issue which would significantly lower the average width of the track and, for longer etches, cause its edges to crack (Figure 6.11a&b). The performance of these tracks is discussed further in section 6.3 below.

With the sample finished and ready for testing, the sample plate was made by cutting a piece of MCPCB ≈ 4/5x the size required for a single sample plate from a larger sheet and etched in $FeCl_3$ solution to remove the Cu layer. As $FeCl_3$ also etches aluminium, a combination of Kapton tape, gaffer tape and sharpy pen were used to mask the aluminium. Post etching, the MCPCB was cut to $28x14mm^2$ and 2x ϕ2.2mm holes drilled to allow it to be fixed to the angular offset. Samples were cut to fit the MCPCB diagonal and affixed with double sided copper foil tape.

Sample placement with respect to the beam and the current contacts (described below) was ensured by assembling the MCPCB into the experiment without the sample attached and labelling it accordingly. Examples of finished samples on their plates are shown in Figure 6.8c&d. Figure 6.8d also includes a layer of Kapton tape beneath the sample so that the beam strike location could be confirmed.

6.2.2 Transport Current Equipment

In this section, the equipment, wiring and connections required to perform transport current experiments across a CIE sample are discussed, given the requirements described above. These include that the current through the sample should be pulsed with a flat top time of the order of 20ms, that the magnitude of current pulses should be stepped up slowly towards a maximum current of 100A, that the temperature of interest for cold irradiations is 20K but, if it must rise, this rise should be minimised given the operating temperature of compact fusion REBCO magnet are likely to be <25K [19], that the maximum voltage through the sample should be no less than 10 µV but not so high that the sample is damaged and that any new materials introduced should have a matched thermal contraction to the coated conductor (ε_{CC}≈-0.3%) on cooling to the base temperature.

This section is split into 4 sections, each based on their proximity to the sample: the sample current and voltage contacts, the wiring inside the vacuum vessel, heat sinking of the wiring inside the vacuum vessel and the wiring outside the vacuum vessel from the port(s) to the PSU.

6.2.2.1 Sample Current and Voltage Contacts

In this section, the design options for the current and voltage contacts required to perform a 4-point resistance measurement across the sample are discussed. Given the design of the sample and sample plate, it was necessary that any connections did not obscure the beam line from hitting the sample, that the voltage contacts be a precise distance apart and that any joints between wiring and sample be as low resistance as possible to minimise ohmic heating whilst retaining their electrical isolation from the bulk cold head.

Both soldering wires and making a plate to allow connections to be clamped to the sample were considered but the latter was used as soldering large wires to a flat sample was difficult and led to sample degradation due to the high temperatures involved. Although clamping the connections to the sample did have its drawbacks (e.g. additional joint resistances in the current circuit), it would work with the sample & plate solution described above and allow relatively quick sample changes.

The initial Connection Plate design (Figure 6.12a) was made from PCB with a ϕ1 cm hole through it to allow the beam access to the sample, making the distance between voltage taps ≈1 cm. Despite the PCB's copper layer being thin (≈ 70 µm), this had the advantage that it was mostly G10 which has a thermal expansion well matched to REBCO ($\varepsilon_{G10} = -0.24\%$) and that the whole copper surface of the PCB could be sanded flat to ensure low resistance jointing of both current and voltage contacts. The precise connections could be made by masking the required copper with Kapton tape or Sharpy pen and $FeCl_3$ etching. One disadvantage, however, was the flexibility of the G10, given that the clamping bolts pushing on the connection plate and the sample were offset. This was rectified using a brass plate to even out the pressure on the PCB. Minimising the joint resistance of the two pressed copper-to-copper joints required ensuring both surfaces were as clean as possible and fine adjustment of the clamping force on the pressure plate using Belleville washers. Peak performance was achieved when pressure was as high and evenly spread as possible, as recommended by Dhuley et al. [357] and Schoft [358]. Minimising electrical circuit resistance also had the bonus of minimising the thermal resistance across the joint. In the second design iteration, the 70µm copper layer on the PCB was completely removed and replaced by 2mm thick copper sections glued to the PCB using araldite (Figure 6.12b). This had the benefit of decreasing ohmic heating in the thin PCB copper whilst also increasing the thermal mass of the system in direct contact with the sample. A fine flat file was used to get the surfaces of each electrical connection as close to flat and parallel to each other as possible before assembly.

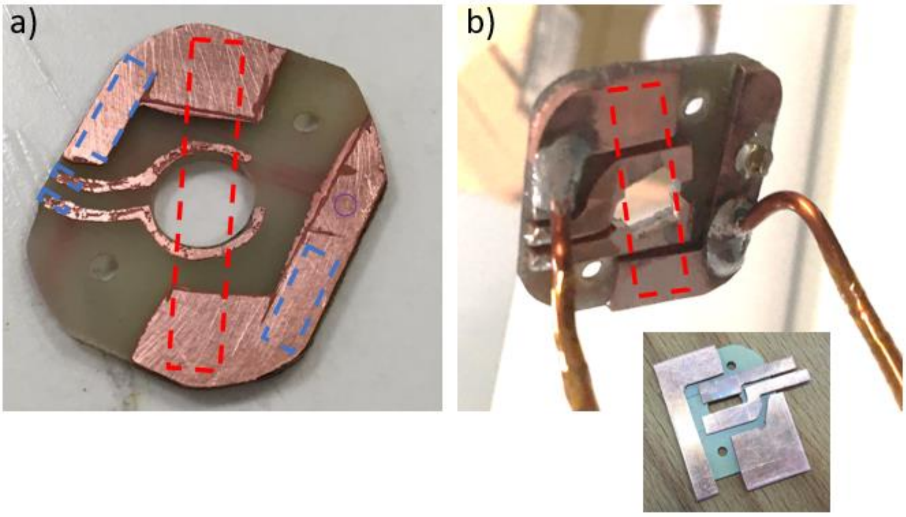

Figure 6.12: Current and Voltage Contacts. a) low current version made from etched PCB showing the rough relative position of sample (red dashed) and position of the soldered current and voltage contacts (blue dashed); b) high current version fully formed but pre-assembly onto CIE showing rough relative position of sample (red dashed). Inset: Roughs for copper contacts before soldering of wiring and filing to fit PCB.

6.2.2.2 Current Supply Wiring inside the vacuum chamber

This was potentially the most problematic aspect of the CIE design given that, due to the extra heating on the sample due to conduction down the current leads, it was likely that the achievable minimum temperature of sample stage (T_{min}) would increase above 17-18 K. The wires also had to carry current which, due to ohmic heating, could also affect the sample temperature, hence the design goal was to minimise excess sample heating whilst achieving the lowest possible T_{min}.

Minimising conductive heating down the current leads required the maximising of their thermal resistance (L/kA), suggesting the use of long, thin wires. Using thin wires, however, has the drawback that, for equal current, thinner wires heat up faster, with this excess thermal energy either leading to a rising sample temperature or, in extreme cases, causing the wire to fail, thus an optimum wire diameter needed to be determined. The CIE's layout also limited the diameter and length of any wiring, with the minimum length of the wiring from sample to port, via necessary deviations around other components, was ≈50 cm whilst the maximum was limited by assembly issues and the size of the CIE's vacuum chamber. The minimum diameter of the wiring was defined using the 1 s fusing current limit, as defined by Stauffacher [359], and the maximum diameter was limited to <ϕ2 mm as the wire needed to access the inside of the low temperature radiation shield.

Given these limits, a thermal analysis similar to that of McFee [360] was performed to optimise the wiring. Applying the thermal diffusivity equation to each wire [352], assuming steady state conditions, the total thermal power flowing through the low temperature end of each wire to the sample ($\dot{Q}_s$) can be calculated:

$$\dot{Q}_s = \dot{Q}_c + \dot{Q}_\Omega = \frac{\pi D_w^2}{4}\left[\frac{\overline{k_w}}{L_w}\Delta T + \frac{\overline{\rho_w}L_w}{2}J_w^2\right] \tag{6-3}$$

where $\dot{Q}_c$ [W] and $\dot{Q}_\Omega$ [W] are the thermal power flowing to the sample from the low temperature end of each wire due to conduction and ohmic heating of the wire respectively, D_w [m] and L_w [m] are the wire diameter and length respectively, J_w [A/m^2] is current density in the wire and $\overline{k_w}$ [W/mK] and $\overline{\rho_w}$ [Ωm] are temperature-integrated mean thermal conductivity and electrical resistivity of the wire respectively, determined using the following expression:

$$\bar{A} = \frac{1}{T_H - T_L}\int_{T_L}^{T_H} A(T)dT \tag{6-4}$$

where T_H [K] and T_L [K] are the temperatures of the high and low temperature ends of the wire respectively. Material properties for the copper wire was taken from Drexler et al. [350].

The analysis of McFee showed that, for a given T_H, T_L and constant current in the wire (I_w), there is a material dependent L/D ratio that minimised $\dot{Q}_s \approx 2\dot{Q}_c$, and that when moving away from this ratio in either direction $\dot{Q}_s$ rises steeply [360]. In this case, however, the current is pulsed, thus any solution should predominantly aim to minimise $\dot{Q}_c$ whilst secondarily minimising $\dot{Q}_s$. Three different analyses for different situations, covering a range of wire lengths and diameters, are shown in Figure 6.13a-c. Each contour marking the minimum achievable $\dot{Q}_s$ for each arrangement is labelled.

Figure 6.13a was used during initial experiments when the current was limited to 20 A, and the wires were attached directly from room temperature at one end to the sample at the other with no intermediate heats sinking. These experiments focused on assessing whether thin, short wires (Figure 6.13a, ✯A) with low $\dot{Q}_c$ and high $\dot{Q}_s$ would be sufficient to maintain sample temperature. These experiments found that, as expected, the cold head's T_{min} was not affected, but even short current pulses (20ms) could raise the sample's temperature[32] by several kelvin. This implied that the increased level of sample heating established itself quickly once the current was switched on and that $\dot{Q}_s \ll 19$ W is required.

---

[32] Details of temperature sensor locations are described in section 6.2.3.

Figure 6.13b&c show how the heat load on the sample ($\dot{Q}_\text{c}$ and $\dot{Q}_S$) varies for different wire lengths and diameters for the 100 A version. These high current experiments also made use of a heat sink (Figure 6.14b, discussed in section 6.2.2.3) at the cryocooler's first stage to reduce the heat load on the sample and to make the apparatus easier to assemble. ϕ2mm diameter wires were used for both 1st and 2nd stage as using this maximum permitted diameter minimised $\dot{Q}_\Omega$ for a given wire length. The effective diameter of the 1st stage wiring could be increased by having 2 wires in each direction, resulting in an effective diameter (D_{eff}) of 2.83mm.

Three combinations of wire lengths were tried to find a solution that led to the lowest $T_{\text{ch,min}}$ whilst minimising sample heating during current pulses (B-D, C-D and C-E, Figure 6.13b&c,☆). Table 6-1 shows the conductive and ohmic characteristics of each wiring solution tested and Table 6-2 shows the minimum temperatures achieve using the three combinations investigated. Solution C-E was eventually used as it allowed the cold head to reach a minimum temperature of 19.1 K (Figure 6.13d) whilst minimising the heat load, and therefore temperature difference, across the sample. Longer wiring would have been used but for lack of space inside the cold head vacuum chamber.

Table 6-1: Details of each Cold Head Wiring solution, as built. Columns are Temperature Range, Effective Wire Diameter ($D_{w,eff}$), Wire Length (L_w), Thermal energy leaving low temperature end of wire when I_{sc}=0 ($\dot{Q}_c$) and Thermal energy leaving low temperature end of wire when I_{sc}=maximum ($\dot{Q}_S$).

	T range [K]	**$D_{w,eff}$ [mm]**	**L_w [cm]**	**$\dot{Q}_c$ [W]**	**$\dot{Q}_s$ [W]***
A	300 → 20	0.26	60	0.015	19.2
B	300 → 80	2.828	60	0.97	5.9
D	80 → 20	2	60	0.39	1.2
C	300 → 80	2.828	180	0.32	15.7
E	80 → 20	2	180	0.13	2.5

* Calculated used the maximum current (i.e. Solution A: 20A, Solutions B-E: 100A)

Table 6-2: Cold Head Wiring combinations and the resultant measured temperature at the sample stage and I+ current contact with I_{sc} = 0 (ie. $\dot{Q}_\Omega$ = 0).

Combinations	**$T_{\text{CH,min}}$ [K]**	**$T_{\text{I+,min}}$ [K]**
A	16.5	23
B-D	22.3	38.4
C-D	21.9	29.3
C-E	19.1	24.4

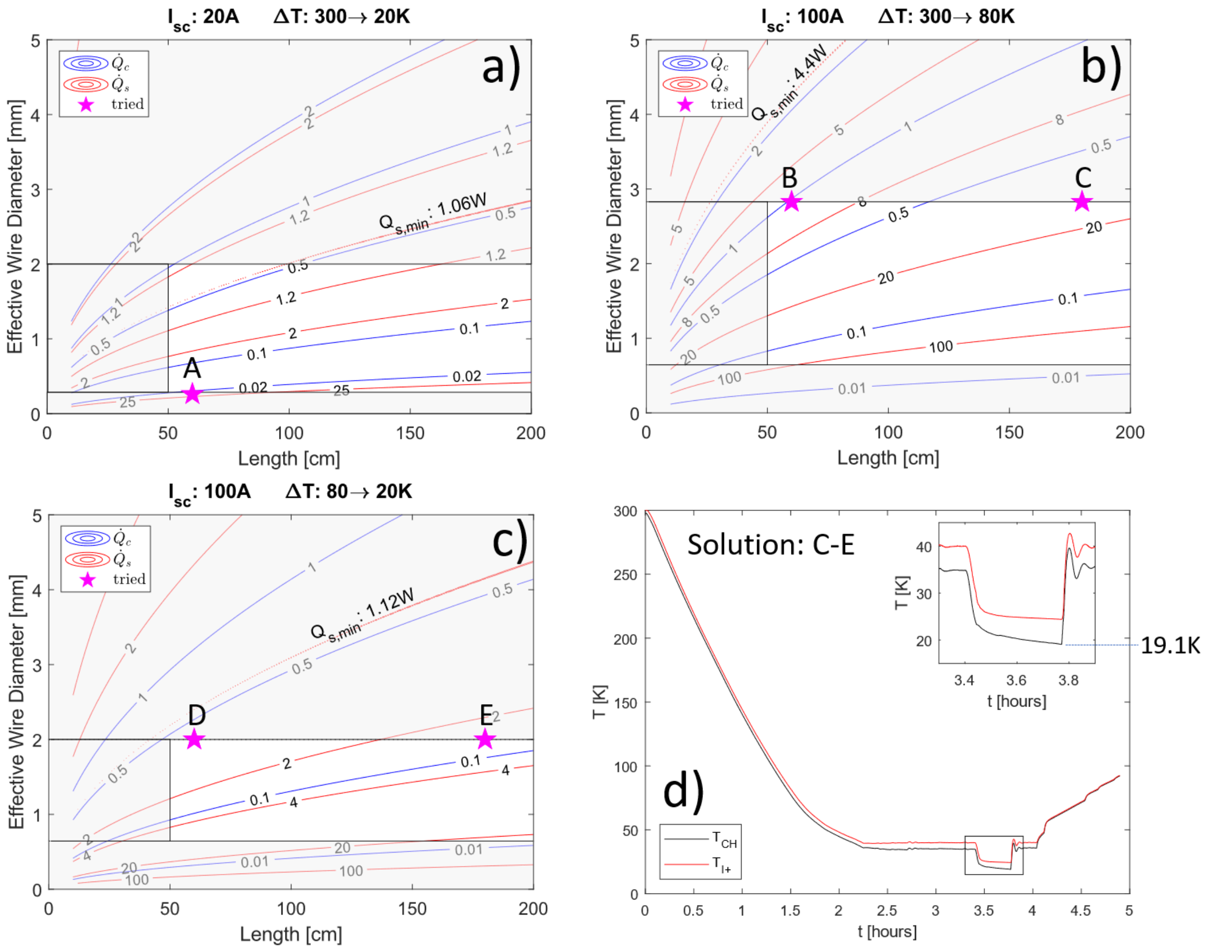

Figure 6.13: Wiring Analysis diagrams for a) 20 A version; b) 100 A version stage 1 wiring (300 to 80 K) and c) 100 A version stage 2 wiring (80 to 20 K). Each diagram (a-c) shows how changes in wire length (L_w x-axis) and effective diameter (D_w y-axis) affect the rate of thermal energy leaving the low temperature end of each wire when I_{sc} = 0 ($\dot{Q}_c$) or when I_{sc} equals the design maximum ($\dot{Q}_s$) calculated using equation 6-3. d) Temperature (y-axis) vs time (x-axis) trace for wiring combination C-E showing the achievement of $T_{ch,min}$=19.1 K.

To ensure fast current rise and fall times, the time constant (τ) of the current circuit needed to be checked. For a circuit without significant capacitance, τ is the product of the circuit resistance and inductance and, given the minimum t_{pulse} = 20 ms, $\tau < 2$ ms is required to ensure the circuit's inductance does not prevent the sample current reaching 99.9% of the required current within 20ms. Assuming the sample was optimally clamped to the current contacts, using internal wiring solution C-E and the room temperature wiring described below, the average whole circuit resistance was ≈200 mΩ. Given this circuit resistance, the required inductance to achieve $\tau < 2$ ms was $\leq 10\ mH$. A circuit inductance this high could likely be avoided if all current circuit wiring is assembled as twisted pairs.

Assembling the current wiring in twisted pairs also had the effect of cancelling out stray magnetic fields within the experiment. There was, however, a need for some untwisting at the wire terminals. Since this is in the general location of the sample and the temperature sensors, both of whose properties are affected by magnetic fields [84], [361], it is prudent to assess whether this field can have any effect on the measurements. In the worst-case scenario, 100A generates a field of 80 mT at 0.25 mm from the wire. This ruled out the sample being subjected to an external magnetic field that would affect its J_c during testing. The distance from the temperature sensor's packaging to the actual sensor inside it was 0.25 mm, thus the magnetic field at the sensor, even if the sensor is placed directly on a wire, was not sufficient to affect the measurement of the SD [361].

6.2.2.3 Heat sinking of Current Supply Wiring

The aim of heat sinking in the CIE was to ensure that any wiring attached to room temperature is bought as close as possible to the temperature of the sample stage before being attached to the sample [85]. If this can be achieved, thermal energy flow through the sample is minimised and the temperature difference between sample and stage is also minimised. On the sample stage, space for heat sinking is limited so the goal of modelling the heat sinking is to find out what level of sinking was available to a particular wiring solutions.

The model for effective heat sinking used here is that described by Hust [362]. The model assumes a circular wire of diameter D_w and length l_1 transverses a temperature gradient (T_1 to T_2) at which point it is attached using a contact agent to a surface at temperature T_s. The wire remains attached to this surface over a length l_2, at which point its temperature is T_3. Hust's model allows the determination of (l_2, T_2) given the material properties of the wire and contact agent, T_1, l_1, T_s, D_w, the width and thickness of the contact agent (w_{ca} & t_{ca} respectively) and the allowed deviation of T_3 from T_s (Θ_3= T_3 - T_s). The model was rebuild in MATLAB^{TM} and calibrated using data published by Hust [362]. One addition to Hust's model was to account for the ohmic heating in the wire during current pulses. As discussed in section 6.2.1.2, $\dot{Q}_s > \dot{Q}_c$ thus, given that Hust's model assumes only conductive heating, the extra thermal power delivered to the sample when $I_{sc} \neq 0$ has been compensated for by reducing the effective length of l_1 by the factor $\dot{Q}_s/\dot{Q}_c$.

For low current solution A (Figure 6.14a), heat sinking was only provided at the sample stage. The contact agent in this case was the 100 µm thick plastic insulation on the wire. Hust's model was used to calculate (l_2, T_2) using T_1, l_1, T_s, D_w, Θ_3, w_{ca} and t_{ca} equal to 300 K, 60 cm, 20 K, 0.26 mm, 1 K, 0.26 mm and 0.1 mm respectively, and the results are shown in Table 6-3. These show that effective heat sinking requires l_2=12.5 cm for conductive heating only and that, as current increases the optimal heat sinking solution stops being an effective barrier to thermal energy when $\dot{Q}_s/\dot{Q}_c$>12, equivalent to I>1.85 A (Table 6-3, I_{max}). Heat sinking for this solution therefore would only account for conduction heating and, given the limited space available, it was inevitable that the application of current would lead to sample heating (Figure 6.14a). To use heat sinking more effectively when going to the 100 A version, additional heat sinking was added at the cryocooler's 1st stage cold surface. This had the additional advantage that it allowed the wiring to be split into two, making the experiment easier to build. The cryocooler's 1st stage cold surface also has a higher cooling power (see Figure 6.1), meaning it could more readily absorb the thermal loads from the 1st stage wiring with the benefit of reducing the heat load on the sample. The required heat sink lengths for each wiring solution are shown in Table 6-3 as calculated using Hust's model. The contact agent in these cases was through a combination of 15 µm enamel insulation and a 70µm thick Kapton layer[33], with the relevant material properties for each taken from Ganesan [363] and Benford et al. [364] respectively. Inputs used besides the tabulated values in Table 6-3 were Θ_3 and t_{ca} equal to 1 K and 0.085 mm respectively. These results (Table 6-3) showed that effectively heat sinking stiff ϕ2mm diameter single core copper wires at the sample stage (solutions D and E) would not be possible without a significant redesign, hence there was no way to avoid the wire being heat sunk through the sample. This puts the onus on reducing the sample heat load on other areas of the design and meant experimentation was required to determine whether further modification to the sample stage was essential.

Table 6-3: Hust's model results for the built wiring stages. Columns are the Temperature Range, the Effective Wire Diameter ($D_{w,eff}$), the length of wire between the high and low temperature end (l_1), the ratio $\dot{Q}_S/\dot{Q}_c$ when I_{sc} is at the design maximum ($f_{\Omega,max}$), the heat-sunk length of wire required so that Θ_3<1 K when $I_{sc} = 0$ (l_2 ($I_{sc} = 0$)) and the heat-sunk length of wire (l_2) and the maximum current (I_{max}) allowable so that Θ_3<1 K when $I_{sc} = I_{max}$. This shows that solution A was not capable of effective heat-sinking up to its maximum current of 20 A.

	T range	$D_{w,eff}$ *	l_1	$f_{\Omega,max}$	l_2 ($I_{sc} = 0$)	$I_{sc} = I_{max}$	
	[K]	[mm]	[cm]		[cm]	l_2 [cm]	I_{max} [A]**
A	300 → 20	0.26	60	1295	12.6	15.9	1.85
B	300 → 80	2.83	60	6.2	5.3	7.8	100
D	80 → 20	2	60	3.1	14.7	16.7	100
C	300 → 80	2.83	180	47.4	3.3	8.5	100
E	80 → 20	2	180	19.6	9.0	15.3	100

Moving to the 1st stage heat sink, the aim was to design a solution that would be effective regardless of which 1st and 2nd stage wiring solution was implemented. The results in Table 6-3 show that, for cases B & C, >8.5 cm of heat sunk ϕ2 mm wiring was required to effectively heat sink each wire during current pulses of 100 A. The heat sinking clamp designed for the purpose is shown in Figure 6.14b-d and consisted of a semicircle of aluminium heat sink bolted to the 1st stage cold surface alongside the high temperature radiation shield. The 2 wiring stages each approach the clamp in twisted pairs spiralling around the cold head. Each pair is then untwisted so that each polarity can sit along the top or bottom of the aluminium heat sink. These wires are clamped to the aluminium heat

---

[33] added due to the tendency for the copper wire's enamel coating to crack when bent into shape and cause electrical shorting to the cryocooler body.

sink using nylon bolts so that the two 2nd stage wires are in the middle and the four 1st stage wires flank them. The 1st and 2nd stage wires are then electrically connected by scraping off the wire's insulation (Figure 6.14c) and using a clamp consisting of a copper sheet and aluminium sheet stuck together with double sided Kapton tape to provide adhesion and electrical insulation (shown schematically in Figure 6.14b). The clamping force is applied externally and maintained using nylon bolts. Thick indium foil is used within each clamp to ensure a good electrical connection between the copper sheet and each wire. Although the size of the clamp was limited by the available space, it manages to allow heat sinking to 12 cm of each wire, more than the 8.5cm required (Table 6-3).

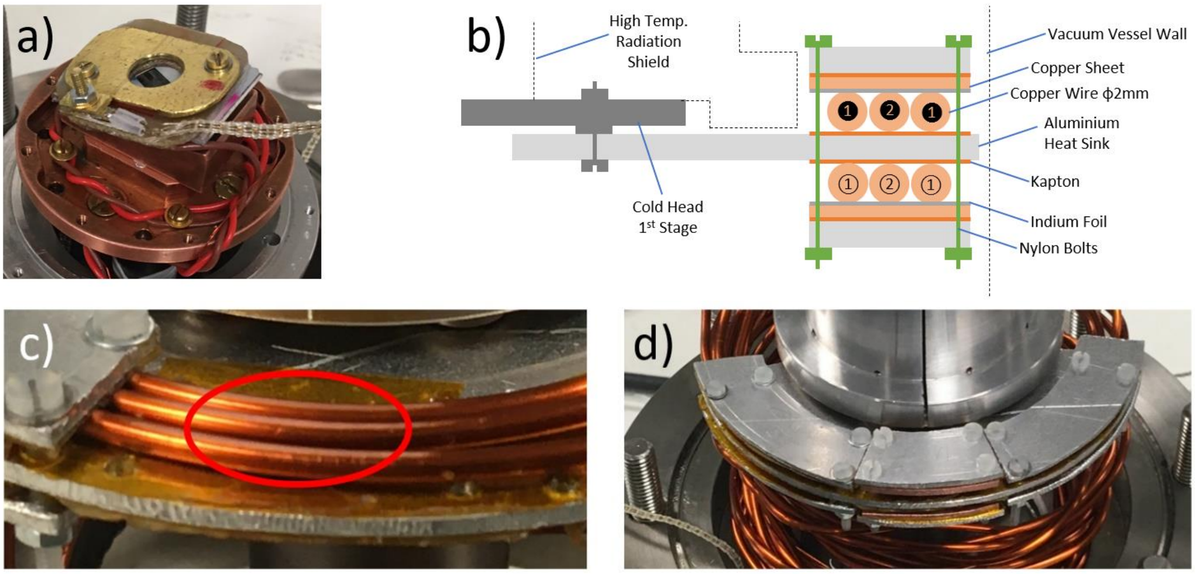

Figure 6.14: Heat Sinking of the CIE. a) 20 A version heat sinking solution at the sample stage using M2 bolts; b) schematic layout of 1st stage heat sink and position of kapton, indium and copper layers within the clamp; c) close up of copper wiring with enamel removed pre-assembly of clamp connecting them electrically; d) complete assembled 1st stage heat sink.]

6.2.2.4 Room Temperature Wiring and Data Acquisition

The circuit diagram for the wiring connecting the PSUs to the hermetically sealed ports on the cold head is shown in Figure 6.15 for the (a) 20 A and (b) 100 A circuits along with the connections of each component to the Data Acquisition (DAQ) equipment. All DAQ was implemented using LabView. The high current solution also needed to consider that the beam line end station at the SIBC was inside a clean room so all wiring was extended by ≈10 m so that the operator could run the experiment from outside the cleanroom. Lengthening the current wiring required the solution to be as low resistance and as low inductance as possible. Thus, extending the current circuit required the current wiring to be assembled as twisted pairs with total wire areas of > 6 mm^2 to avoid adding > 60 mΩ to the circuit. Given the 1st stage wiring solution had a total area > 6 mm^2, two ϕ2 mm diameter single core wires were also used for the room temperature wiring. The extra voltage tap resistance would not affect the sample voltage measurement but an extra resistance of > 10 Ω in the temperature sensor wiring would result in an error. To ensure this over 20 m, wires with area > 0.04

mm^2 were required. Given their availability, twisted pairs of larger cross sectional area wires were used.

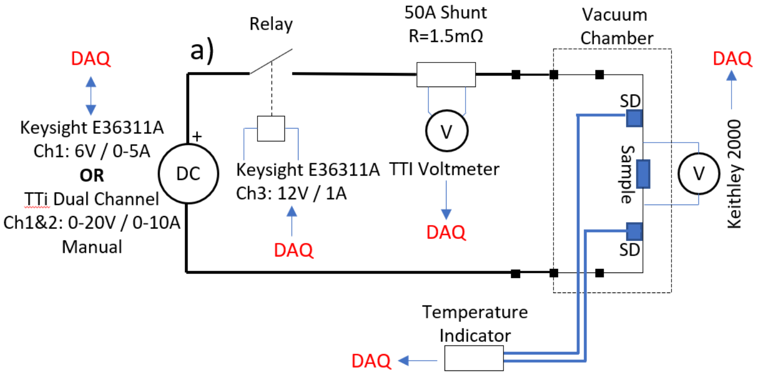

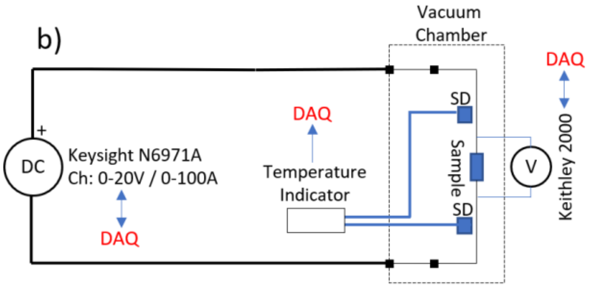

Figure 6.15: a) Circuit diagrams of the a) 20 A version of the external wiring which made use of a TTi Dual channel PSU and b) 100 A version of the external wiring which used the Keysight N6971A PSU. DAQ denotes a direct link to the experiment's Data Acquisition system for monitoring and control.

6.2.3 Sample Temperature Monitoring and Control

Measuring the sample temperature accurately is a necessary part of this experiment. Given the inevitability of a non-zero thermal power through the sample due to conduction down the current leads and that the joints between the sample and the cryocooler cold surface had a finite thermal resistance, there was likely to be a measurable difference between the sample temperature and that recorded by the SD temperature sensor provided with the cryocooler. Space being at a premium closer to the sample, an extra SD sensor was added to one of the current leads. This extra sensor would allow the range of possible sample temperatures to be determined, given they were on either side of the sample with respect to the thermal energy flow (Figure 6.16a). This range could be reduced as far as possible by assembling the sample into the CIE to reduce thermal resistance between the sensors. Given this, all exposed surfaces were cleaned as thoroughly as possible before assembly [358] with particular attention paid to the joint between sample and current contacts due to its low relative area (≈40 mm^2) compared to the angular offset mounting surface (≈115 mm^2).

SD sensors work by measuring the forward voltage across a diode whilst a small current is passing through it (10 µA). The resistance of the diode is temperature dependent and can vary from 50 kΩ at 300 K to 160 kΩ at 4.2 K. They are particularly useful at <25 K as their sensitivity increases roughly

10x [361]. The extra sensor used here was calibrated using the Electrical Transport Option of a QD PPMS [301] (Figure 6.16b) whilst calibration information was provided for the cryocooler sensor by the SIBC.

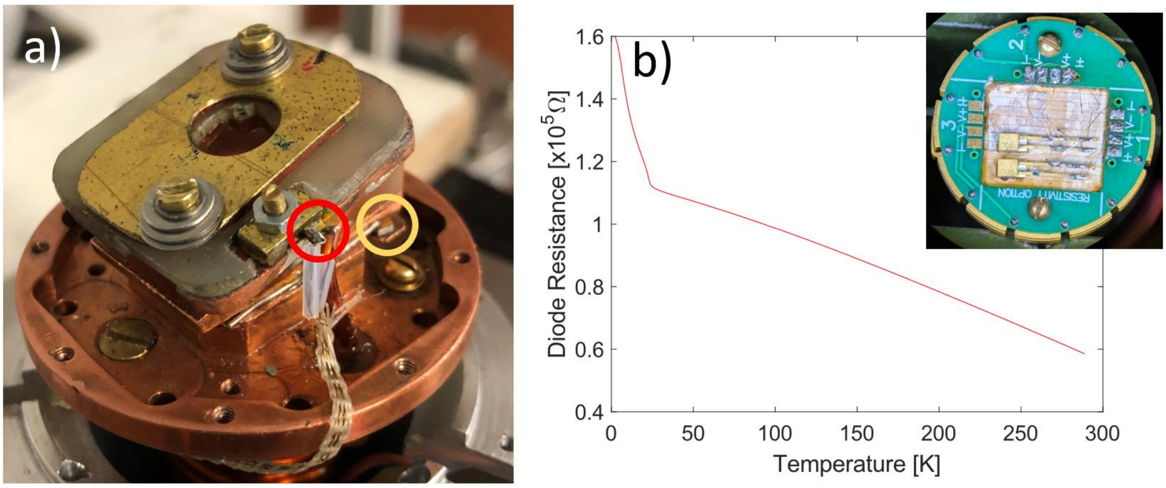

Figure 6.16: a) positions of the 2 SD sensors mounted in the CIE; b) resistance (y-axis) vs temperature (x-axis) curve recorded for the SD sensor that was added to the CIE (inset: 2 SD temperature sensors and the required electrical connections attached to the ETO's PUCK device before it was assembled into the PPMS).

Finally, the temperature sensors needed their own wiring solution inside the vacuum vessel. This involved 2 wires being connected to each diode terminal as this would allow the diode voltage to be measured directly, if required. ϕ110 µm Constantin loom was used due to its temperature independent electrical conductivity (66 Ω/m) [365] and low thermal conductivity compared to copper (≈0.02 $\bar{k}_{Cu\,(300\,-4.2\mathrm{K})}$ [85]). The loom length of 1 m was used to ensure conduction to the sample through the sensor was negligible (≈0.15 mW) whilst reducing its electrical resistance (132 Ω) to a small fraction of total sensor circuit resistance, adding ≈0.2% at room temperature. At the RT end of the Constantin loom, each wire was soldered directly to individual pins on the hermitically sealed ports.

Control of the sample temperature was achieved using a PID controlled 20 Ω NiCr heater attached to the low temperature radiation shield (Figure 6.17a). PID control of the heater, as well as temperature monitoring, data collection and formatting, were implemented in LabView. Subject to stable cooling from the cryocooler, this allowed the sample stage temperature to be stably controlled to within ±0.5 K for extended periods, as measured by the current lead SD (Figure 6.17b).

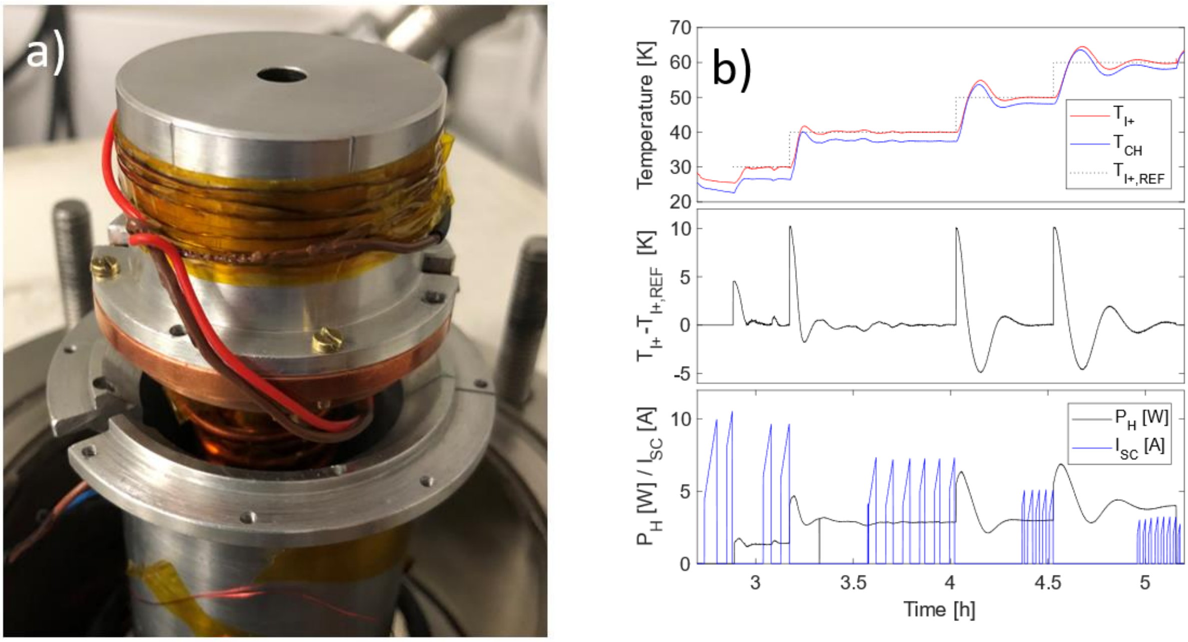

Figure 6.17: a) 20 Ω NiCr heater assembled onto low temperature radiation shield; b) time trace (x-axis) of the temperature sensor readings with respect to the set reference temperature (top y-axis), the temperature reading error (middle y-axis) and the heater power (P_h) and sample current (I_{sc}, bottom y-axis). This shows that a set temperature can be reached within 20-30 minutes and maintained there, subject to stable cryocooling, for extended periods.

6.3 Performance Testing

In this section, tests performed when the CIE was fully assembled are presented to illustrate its performance and discuss its accuracy.

6.3.1 Measuring T_c

Measuring T_c of CIE samples was achieved by cooling or warming the sample through its transition temperature whilst applying a constant current of 0.107 A. Even though the resistivity of REBCO above T_c is roughly equal to that of the c276 substrate, most current flows through the c276 when REBCO is in its normal state due to the much larger cross-sectional area of the substrate (≈ 2500x), thus $R_{sc} \approx R_{c276}$ just above T_c. As the sample temperature falls and the REBCO layer starts to superconduct, the proportion of the total current flowing through the REBCO layer rises, leading to a drop in the voltage across the sample until the effective resistivity of the REBCO becomes so low that there is no measurable voltage (Figure 6.18a&b). The definition of the T_c is complicated in this situation as the sample is 2 materials in parallel, both with different cross-sectional areas. After analysing the effect that the effective resistivity of the REBCO has on the sample resistance of Fujikura 2018 CC and how it varies from its value when $T > T_c$ (Figure 6.18c), a definition of T_c was defined based on the resistivity of copper at 20K ($\rho_{Cu,20K}$):

$$T_{ch} < T_c < T_{i+} \qquad \text{when} \qquad \rho_{REBCO} = \rho_{Cu,20K} \tag{6-5}$$

where T_{ch} and T_{i+} are the temperatures measured at the sample stage and current lead respectively. For example, once the resistivity of a 50 µm wide track of REBCO drops to $\rho_{Cu,20K}$, the resistance of a Fujikura CC-based sample, including the 4 mm wide, 50 µm thick Hastelloy substrate, would be 56.5% of its value when $T>T_c$, hence T_c is reached when $R_{sc} = 0.565\ R_{NON\text{-}SC}$. The transition width ($\Delta T_c$) was also defined in terms of $\rho_{Cu,20K}$, being the temperature range where the effective resistivity of the REBCO layer lies between 0.1-10 $\rho_{Cu,20K}$. An example of the calculation of T_c and ΔT_c for unirradiated sample RT5 is shown in Figure 6.18d where, assuming the sample temperature is the average of T_{ch} and T_{i+}, T_c=90.6K and ΔT_c=1.0K as measured on warming. Figure 6.18d illustrates that T_c and ΔT_c values measured on warming are more accurate due to the lower thermal energy flow through the sample, characterised by the small difference between the readings of the temperature sensors, and therefore warming data is used for determining T_c going forward. The results for all samples of sufficient quality to be used in irradiation experiments are shown in Table 6-4.

Another point illustrated by Figure 6.18d concerns the determination of the sample's track temperature from T_{ch} and T_{i+} when the cold head is on (ie. either during sample cooling or whilst the sample temperature is being controlled). Assuming that the sample's T_c is independent of how it is determined, the sample's track temperature, and thus its R_{sc}, should be equal at T_c and this should, therefore, be reflected in each experiment's calculated T_c. Comparing cooling and warming experiments in Figure 6.18d shows that T_c calculated on warming is subject to a smaller range of possible temperatures and therefore can be assumed to be closer to the actual T_c. Moving to the cooling experiment, the data implies that neither solely using T_{ch}, T_{i+} or their arithmetic average exactly predicts the same sample T_c as that calculated during the warming experiment. This therefore implies that neither solely using T_{ch}, T_{i+} or their arithmetic average exactly predicts the sample's track temperature near T_c and likely cannot be used to predict the sample's track temperature at other temperatures. A review of the experiments to determine T_c while cooling and warming for all samples used during irradiation experiments before they were unirradiated (Figure 6.18e) shows that the difference in measured T_c is consistent across all samples, with the arithmetic average of T_{ch} and T_{i+} during cooling experiments consistently being a better indicator of sample T_c than T_{ch} or T_{i+} alone, though be it a consistent 1-2 K higher than that measured during warming experiments. Figure 6.18e also shows that, despite my best efforts to reduce it, the difference between T_{ch} and T_{i+} varies between experiments, typically falling into the range 4-8 K on cooling and 0.5-1.5 K on warming (ie. with the cold head and heater turned off). This approximate range is also effected when the sample is controlled at 40 K, becoming 2-5 K, and also varies with sample temperature (see Figure 6.19 a, b, c), being generally constant down to ≈ 100 K and then increasing as $T_{ch} \rightarrow T_{min}$. This is likely due to subtle differences in the thermal resistance between T_{i+} and the sample relative to that between the sample and T_{ch}, that the thermal energy flow through the sample increases as $T_{ch} \rightarrow T_{min}$, that both thermal resistances have temperature dependent properties and that each thermal resistance has a different temperature. The practical result of these considerations is that, although the sample's track temperature definitely falls into the range T_{ch} to T_{i+}, it is hard to predict more precisely without further experimentation. The range T_{ch} to T_{i+} was therefore recorded as the sample temperature going forward and any future work should actively investigate methods of reducing the size of this range.

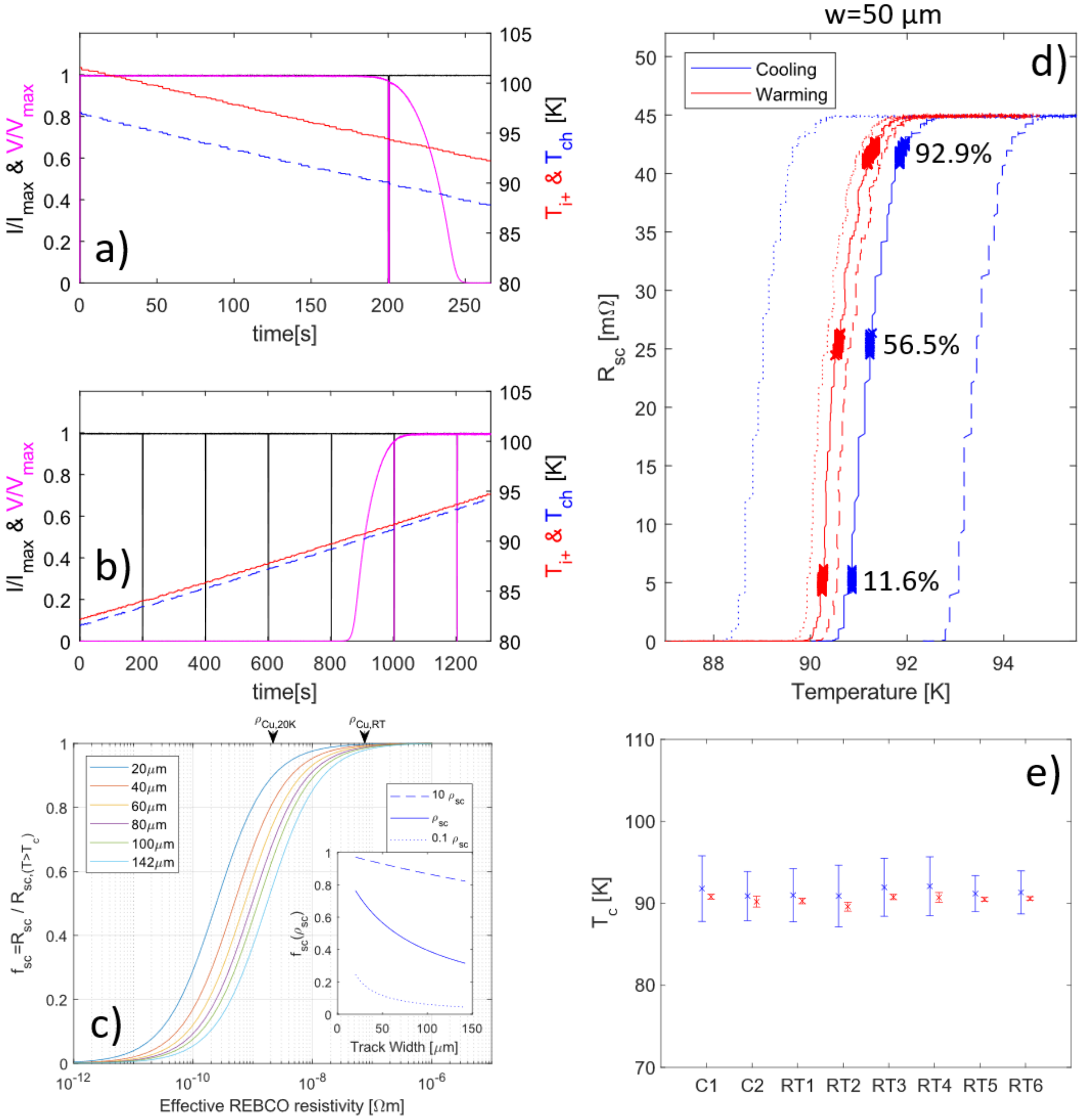

Figure 6.18: Error in T_c measurement when cooling versus warming. a & b) time trace for sample voltage (V), current lead temperature (T_{i+}) and cryocooler temperature (T_{ch}) for the constant current experiment (I_{sc}=0.107A) to determine T_c whilst a) cooling and b) warming. c) exploring how the effective REBCO resistivity of 2 μm thick tracks of varying widths effects the total resistivity of the sample (i.e. REBCO and substrate), normalised to its value above T_c (f_{sc}). Inset: graph showing the f_{sc} at which REBCO tracks of different widths have an effective resistivity equivalent to 0.1, 1 and 10 times that of copper at 20

K ($\rho_{Cu,20K}$). d) Temperature (x-axis) versus sample resistance (R_{sc}, y-axis) during low current transition illustrating difference between T_c and error in T_c calculated whilst cooling versus warming. The sample was unirradiated RT5 with w=50 µm, thus the effective resistivity of the superconductor was 0.1, 1 and 10 $\rho_{Cu,20K}$ when R_{sc}=11.6%, 56.5% and 92.9% of $R_{NON\text{-}SC}$ (≈45 mΩ) respectively, making T_c=90.6K and ΔT_c=1.0K. e) Comparison of T_c (y-axis) measured during cooling (blue) and warming (red) experiments. In each case, 'x' marks the average T_c calculated using the average of T_{ch} and T_{i+} when R_{sc} goes through the appropriate resistance. Error bars show the difference between T_{ch} and T_{i+}. In all cases, the T_c measured on warming is in a narrower range of temperatures and the calculated T_c is slightly less than that calculated during the experiment on cooling.

6.3.2 Measuring I_c

Measurement of the critical current (I_c) required that several current pulses, with slowly increasing magnitude, be applied to the sample and V_{sc} measured until the V_{sc} was > 10µV. Control of this process was implemented in LabView using a separate code running in parallel to that used for temperature monitoring and control. This LabView control system was designed so the user defines the start (I_{start}) and end current (I_{end}), the size of the current step between pulses (ΔI), the pulse flat top duration (t_{pulse}), the time between pulses (t_{off}) and the sample voltage at which the experiment should be stopped (V_{OVP} >10µV). To protect the sample, experiments are stopped if 1 data point was recorded with $V_{sc} > V_{OVP}$, even if this is a measurement error. With the parameters set, the experiment can be initiated and runs automatically whilst the data on the experiment time (t), set (I_s) and measured (I_{sc}) sample current, sample voltage (V_{sc}) and sample temperature[34] (T_{ch} and T_{i+}) is recorded until either $I = I_{end}$ or $V_{sc} > V_{OVP}$ is reached.

While optimising this process, 10s of samples were created but only a few will be described here. This is because many samples, especially the early ones, were damaged (e.g. they did not exhibit superconductivity) or did not yield good quality data, for example because they were under-etched, having an I_c too high to measure at 20-50 K. Once samples of sufficient quality with a measurable I_c had been created, the first experiments undertaken were to tune the appropriate values of t_{pulse}, t_{off} and V_{OVP} (with ΔI=0.02 A) so that the resultant *I-V* curves contained enough points before and during the superconducting transition to allow good quality and accurate fits to the data of equation 3-1 whilst avoiding sample damage and/or minimising sample temperature rises. These experiments revealed that, at the lowest temperature achievable (T_{ch} : 19.1K and T_{i+}:23.8K), even t_{pulse}=50 ms resulted in a measurable but small temperature rise in both T_{ch} and T_{i+} (Figure 6.19,☆), but this did not significantly grow when t_{pulse} was increased to 75 ms (Figure 6.19a,☆). In both cases, the magnitude of the temperature rise could be reduced by increasing t_{off} from 0.5 to 2 s. Regardless of t_{pulse} and t_{off}, however, most of the pulses shown in Figure 6.19a, using V_{OVP}=30 µV, ended in a sample quench (denoted 'Q'), some of which resulted in sample damage (denoted 'D') characterised by a small decrease in I_c, and it was only when V_{OVP} was reduced to 10 µV that

---

[34] Supplied by the temperature monitoring and control LabView code.

quenches could consistently be avoided (Figure 6.19a, ★). Similarly, the V_{OVP} needed to be reduced to 20 µV to prevent sample quenches when the sample temperature was controlled at T_{i+}=30 K (Figure 6.19b), and the sample temperature tended to become unstable, likely due to the temperature control system not being able to compensate for the changes in heat load during and between each I-V experiment (Figure 6.19b, time 345-375 mins). This issue with temperature instability during and between each I-V experiment was not present when the sample temperature was controlled at T_{i+} = 40K (Figure 6.19c), even with t_{off}=0.5 s and t_{pulse}=200 ms, and quenches were not forthcoming even when V_{sc} > 40 µV. This ability to consistently test samples up to 40 µV came in particularly useful when fitting equation 3-1 to the I-V curve as, due to the noise of the K2000, the resultant fit became more representative of the entire dataset as V_{OVP} was increased (Figure 6.19d). Given these results, it was decided that 40 K was a good benchmark temperature to perform experiments with samples that were to be irradiated.

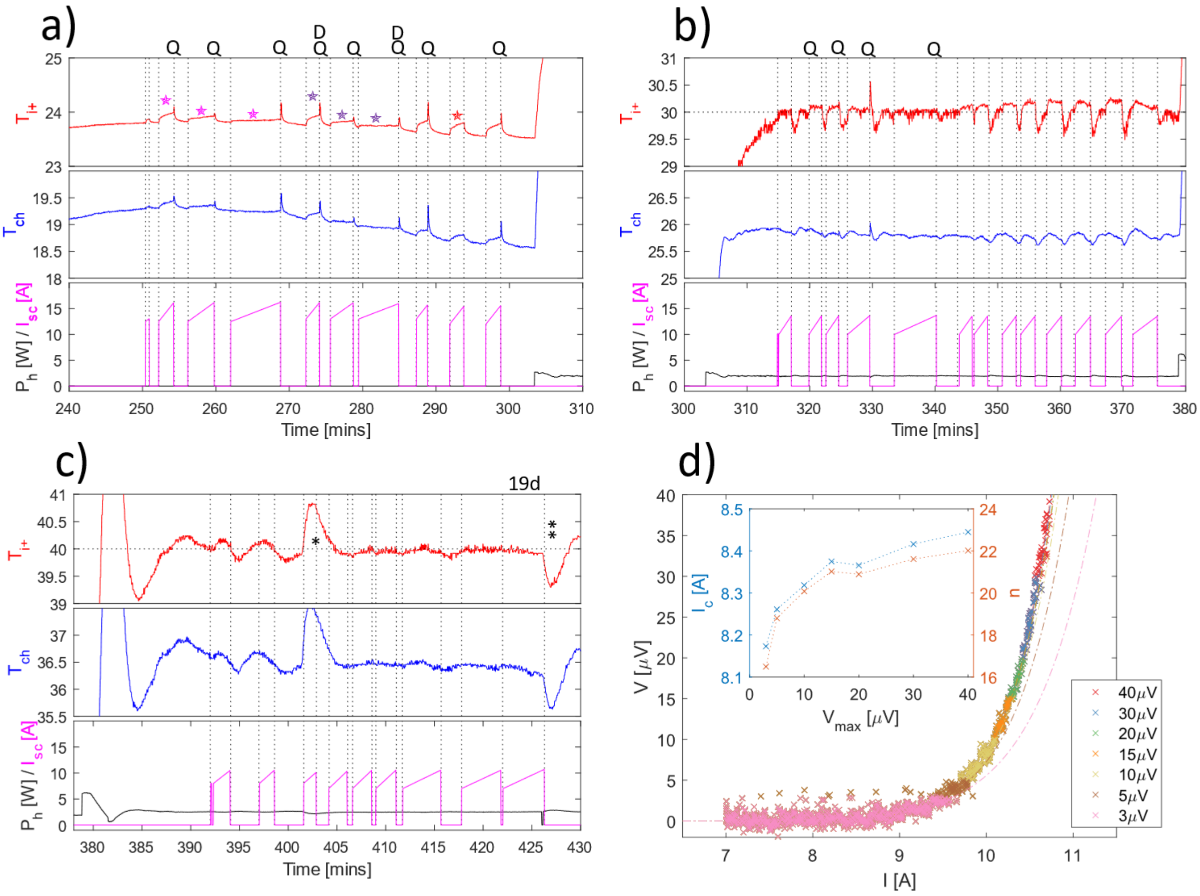

*Figure 6.19: Time traces (x-axis) of temperature (T_{i+} & T_{ch}), sample current (I_{sc}) and heater power (P_h) for sample RT6 during I-V experiments conducted at a) minimum temperature, b) T_{i+} controlled at 30 K and c) T_{i+} controlled at 40 K showing sample temperature rises due to an applied current when $T_{i+} \leq 30$ K. Annotations include Q – sample quench; D – sample sustained damage (I_c reduced); *: Cryocooler malfunction lead to loss of cooling; **: Heater malfunction lead to loss of heating; '19d': Experiment that led to I-V curve shown in figure 'd'. d) I-V curve for experiment conducted at T_{i+}=40 K which was not subject to temperature instability. Data point colouration used to illustrate the data that would have been available if V_{OVP} was set at the given value lower than 40 µV. Inset: the effect that changing V_{OVP} would have had on the fit in terms of calculated (I_c, n), illustrating that I_c measured approached actual I_c as V_{OVP} rises.*

To study whether sample heating was due to thermal energy dissipation in the REBCO track or generated externally to the track, an under-etched sample with I_c>100 A was tested at T_{min} up to 100 A using 100 ms pulses (Figure 6.20a). In this case, the sample temperature was 23.2<T<32.6 K and no measurable temperature increase was recorded. Although this does not reveal anything concrete about the sample, it did allow the CIE to be successfully tested at high current using a 100 ms pulse. As V_{sc} ≈ 0, this implied that a 100 ms pulse of 100 A did not lead to significant heating in the current supply wiring and that this source of sample heating has effectively been minimised.

Since the I_c of this sample was too high to be quenched to determine a starting J_c value, ruling it out for irradiation experiments, it was intentionally tested to failure to judge the limits of its resilience and determine the failure mode. Figure 6.20b shows the I-V experiment that finally destroyed the sample where, with 61<T<72 K[35], successive pulses at 44, 44.25 and 44.5 A led to jumps in V_{sc} from ≈30 µV to 50 mV to 3.5 V respectively. A closer look at the voltage response for these last 3 pulses (Figure 6.20c) shows that it was the pulse to 50 mV that initially damaged the superconducting layer, characterised by the voltage not returning to zero when the current was removed. The presence of this damage was confirmed by the final pulse that immediately went fully resistive (R_{sc}≈77 mΩ) with a larger sample resistance than that measured at room temperature ($R_{sc,RT}$ ≈65 mΩ) before the c276 substrate melted (Figure 6.20d). These results highlighted the importance of taking the extra time to allow the current pulse height to increase at its lowest possible rate – i.e. ΔI = 0.02 A versus the ΔI=0.25 A used here – and setting V_{OVP} appropriately. This can be compared to the tests depicted in Figure 6.21a,d,g where a 42 µm wide Fujikura sample of sufficient quality to be used in an irradiation experiment (RT5), measured in a similar temperature range, remained undamaged after a ≈7 A pulse to 50 µV, similar to all samples listed in Table 6-4. This implied that narrower tracks were more resilient than wider tracks as similar voltage responses were achieved at lower currents. Going forward, therefore, tracks of the order of 50 µm wide were used to minimise the likelihood of failure.

The I_c vs temperature curve (I_c-T) for all the samples listed in Table 6-4 were tested using the CIE before these samples were used in irradiation experiments. A wider survey of the results is left to chapter 7, given their context in the experiment to test the response of REBCO to irradiation whilst cold versus room temperature, but 3 examples of *I-V* curves measured for unirradiated sample RT6 are shown in Figure 6.21. These I-V tests were performed whilst the sample was being cooled (Figure 6.21a, d, g), whilst the sample temperature was being controlled at 40 K (Figure 6.21b, e, h) and

---

[35] Note this sample used double sided Kapton tape, not coil foil tape, hence the large difference between the temperature sensors.

whilst the sample was warming up with the cryocooler off and without external heating (Figure 6.21c, f, i). In each case, the power law was fit with a coefficient of determination $R^2 > 0.95$ [366].

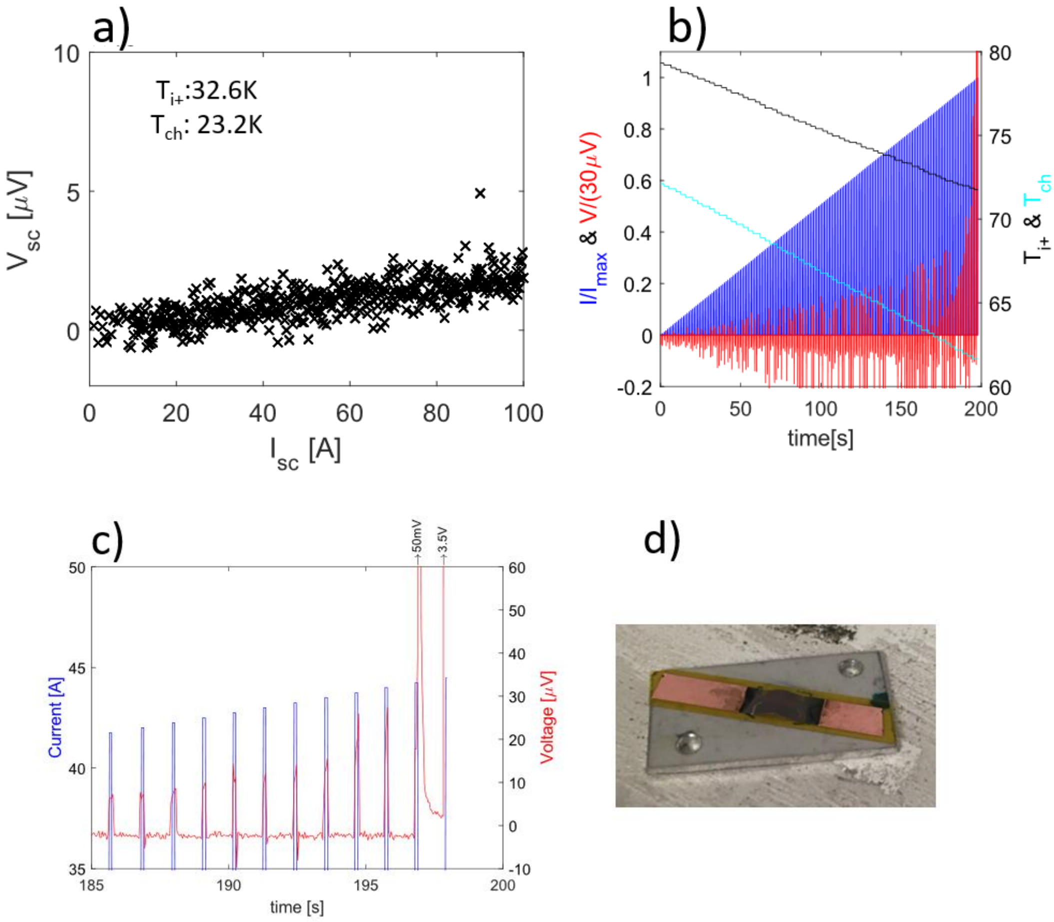

Figure 6.20: Stress testing of the CIE using an under-etched 4 mm long, nominally 100 μm wide track made from a Fujikura EuBCO-based CC, circa 2020. a) I-V curve as recorded at $T_{ch,min}$ showing no transition at 100 A. Slope in graph can be attributed to migration of the voltage reference during >2.5 h test and/or a thin damage or non-superconducting volume of the track spanning its entire width. b&c) same tape tested at 60-80 K up to I_{max}=44.5 A. Sufficient I-V data was recorded to calculate I_c but resistive transition at I > 44.25 A led to irreversible sample damage (c, inset).

To assess the CIE's accuracy, various aspects of the graphs shown in Figure 6.21 are discussed. Firstly, Figure 6.21a&c show that if the temperature is not controlled during a I-V test, the change in the sample temperature during the whole test can be large, especially if the test takes a long time. That said, for much of each test, current pulses lead to no voltage response as the sample is not transitioning, hence T_{ch} and T_{i+} at the beginning of a transition needed to be defined. Given that only sample voltages > 1 μV are measurable and that transitions in the CIE need to be judged based on measurable voltages, the start time of the transition was defined based on the last voltage of < 1μV measured during a current pulse (i.e. whilst $I_s \approx I_{sc}$). This time is marked on Figure 6.21a-c using a black dashed line, and allows the temperature range containing the sample temperature to be defined during each transition ($T_{ch,min}$ and $T_{i+,max}$). Secondly, even though the temperature change during a transition is not large (e.g. ≈ 0.5 K for Figure 6.21a&c), its effect on the shape of the

I-V curve, and therefore the measured n-value, is significant. This implies that there is a significant systematic error in the calculated n-values when I-V curves are generated whilst the temperature is not being controlled (Figure 6.21g&i), given that $dJ/dT < 0$ for REBCO. The extent of this difference is shown Figure 6.22a where the n-values calculated on cooling are consistently lower than those measured on warming (e.g. at 59 K, n_{cool} ≈19 whilst n_{warm}≈27). This systematic error in the n-values suggests that comparing them between experiments would be misleading and that their associated I_c values are also subject to an error when temperature is not controlled. The exact size of this error in I_c was difficult to determine but, given that measured I_c values on warming and cooling tended to be consistent with each other across many experiments (Figure 7.5), it was estimated to be small enough to assume its negligible going forward, especially when compared to the range in the sample temperature. Thirdly, Figure 6.21d-f shows that, close to V_{OVP}, the voltage across the sample increases slightly over the course of a pulse. This is likely due to a small temperature difference between the beginning and end of the pulse and suggests that the first voltage measured when $I_S = I_{SC}$ is the only voltage representative the actual sample response. Given the small relative change in voltage over a pulse, the inherent noise of the K2000 voltmeter and the steep-sloped nature of the power law transition, this change is neglected below. Finally, the measured and expected n-values for all tracks where the temperature was controlled at 40 K is shown in Table 6-4. Given the sources of error described above, each is reasonably close to the expected value of 23-26, based on data provided by the manufacturer.

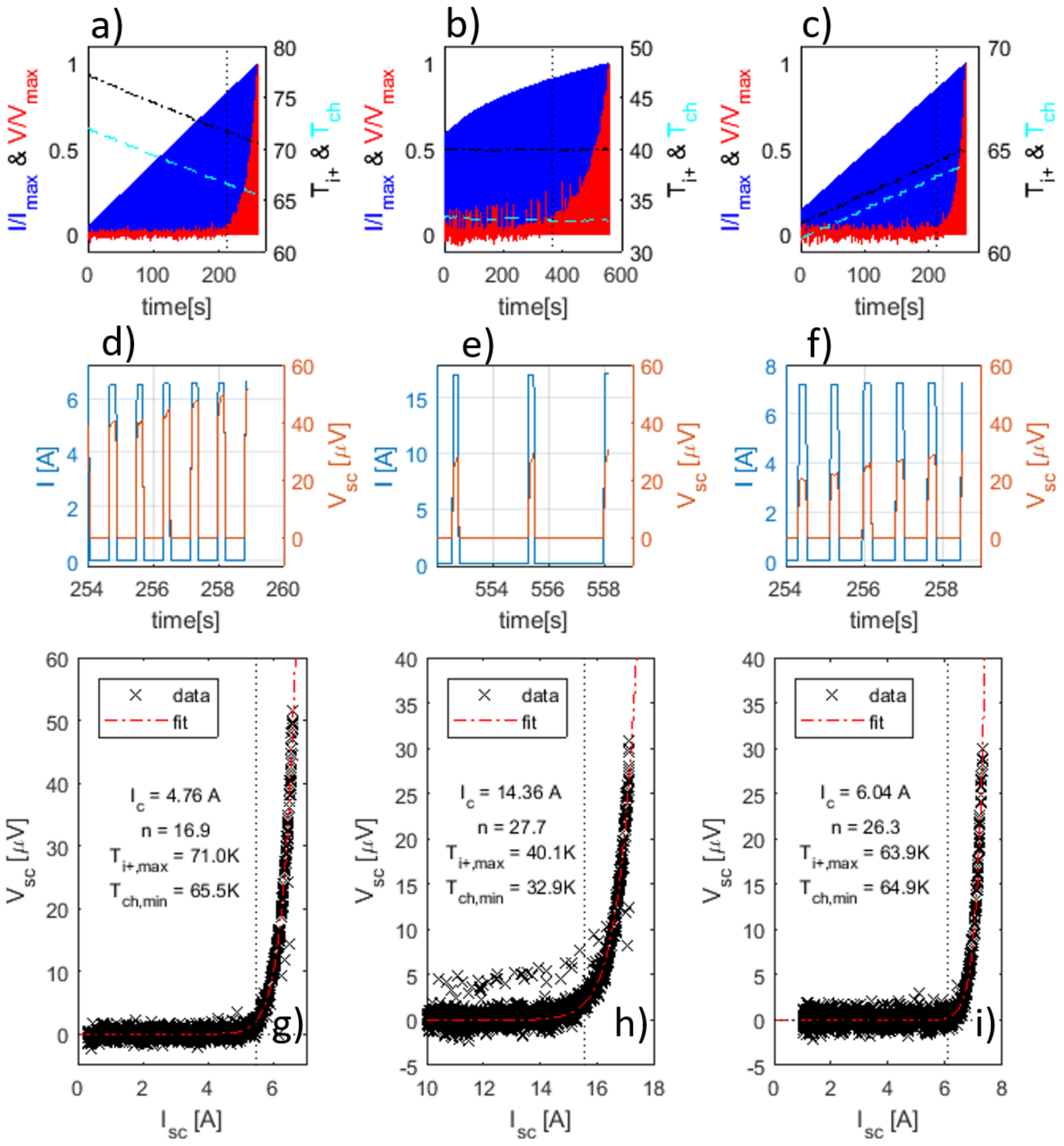

Figure 6.21: Experiments to determine single I-V curve for unirradiated RT6 sample recorded whilst experiment was cooling (a,d,g), whilst the sample temperature was being controlled at 40 K (b, e, h) and whilst the sample was warming up with the cryocooler off and no other heat sources (c, f, i). For each I-V test, a-c) shows the time trace (x-axis) for the experiment, illustrating how I_{sc} increased from I_{start} to the current where V_{OVP} was reached (y-axis). A dashed black line is added to define the start of the transition. d-f) show close-ups of individual current pulses leading to a voltage response over V_{OVP}. g-i) shows the resulting I-V curve constructed from the voltage responses of each pulse and the fit and parameters of the power law.

The resultant I_c-T curve and associated reference data provided by Fujikura for unirradiated sample RT6 are shown in Figure 6.22 and this shape of curve is representative for all the Fujikura 2018 samples tested during this work. The general shape of the I_c-T curve is very similar to the reference data, but with slightly higher I_c values for the track with a measured width of 42 µm. The track was examined by SEM and found to be of high quality with no edge cracking (Figure 6.22b&c). The high I_c values might be either because some of the REBCO on the etched section of the sample might not have been completely removed and thus provides a path for a small excess supercurrent (arrowed, Figure 6.22b), or that this section of track is of higher quality than the average properties of the full 4 mm width of the CC.

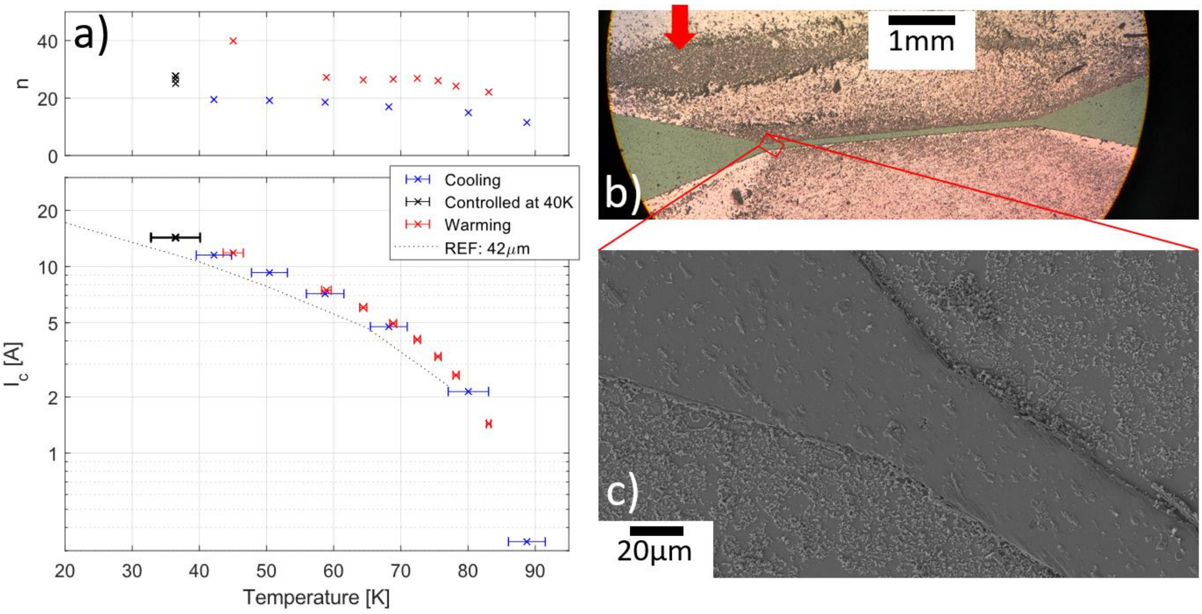

Figure 6.22: a) I_c *(bottom y-axis) and n (top y-axis) versus temperature (x-axis) for unirradiated sample RT6. Points are coloured depending on whether the sample was being cooled (blue), controlled at* T_{i+}*= 40 K (black) or warmed (red) and compared to the expected curve for a 42 µm wide track sample scaled from data provided by the manufacturer (REF)* [140], [293]. *b) light microscope image of RT6 showing entire track and area of possible under-etching (arrowed) and region of SEM image (red box). c) SEM image of small section of RT6 used for track width measurement.*

6.3.3 Track Edge Cracking

Cracking of the edges of the tracks has the potential to significantly decrease the effective track width of the superconducting layer. Cracking was found to be affecting tracks RT1 (Figure 6.23a), RT3 (Figure 6.11b), RT4 (Figure 6.23b) and RT5 but not samples C1, C2, RT2 (Figure 6.11a) or RT6 (Figure 6.22c). That said, the measured I_c (40 K) value before irradiation for RT1 was 9.2 A implying a J_c(40 K, self-field)=13.5 MA/cm^2 using the whole track width of 34 µm (Figure 6.23a, dimension A) and ≈ 25 MA/cm^2 using the reduced track width (Figure 6.23a, dimension B). Given the expected J_c(40 K, self-field) supplied by the manufacturer is 14 MA/cm^2 [349], this implies that track edge cracking does not have a significant effect on J_c(40 K, self-field). The track width measurements, ignoring edge cracking, and resulting superconducting properties for all samples before irradiation are shown in Table 6-4. These show that J_c(40 K, self-field) values for all samples lie between 7.4-17.1 MA/cm^2, also close to the expected value. Although the variation in J_c values is larger than that published for this tape (±2.6% measured at self-field and 77 K [349]) we would expect that measurements taken over the whole conductor width (4 mm) would average out the more local variations in superconducting properties that I detect in these narrow tracks. T_c values for the Fujikura 2018 sample determined using magnetometry[36] showed $T_c \approx 91$ K, similar to the values in Table 6-4 and close to that measured for similar samples by the RRI [17]. These measurements demonstrate that the patterning and etching process, even if it leads to track edge cracking, does not significantly effect T_c or J_c values of the remaining REBCO layer.

Table 6-4: Measurements of superconducting performance of un-irradiated samples

CC	Track	Measured* / Design Width [µm]	*H_3PO_4 aq. Etching Time[s]*	*T_c* [K]	*ΔT_c* [K]	*I_c (40 K)* [A]	*n (40 K)*	*J_c (40 K)* [MA/cm^2]
Fujikura 2018	C1	36 / 50	45	90.8	0.71	5.11-5.15	20.7-21.8	7.1
	C2	38 / 50	55	90.2	1.32	12.4-12.5	21.5-23.5	16.2
	RT1	34 / 50	70	90.3	0.90	9.2	23.0-24.0	13.5
	RT2	37 / 50	90	89.6	1.57	7.2	21.0-22.0	9.7
	RT3	40 / 60	90	90.8	1.21	8.7-8.9	28.4-32.6	11.0
	RT4	49 / 60	90	90.7	1.67	12.3-12.5	25.5-26.6	12.7
	RT5	54 / 60	90	90.5	0.93	15.2	27.3-29.4	14.1
	RT6	42 / 50	80**	90.6	1.18	14.2-14.4	25.0-27.7	17.1

*: Average of several measurements recorded along track length and accounting for mask undercutting but not edge cracking; ** 2.1M H_3PO_4 solution used.

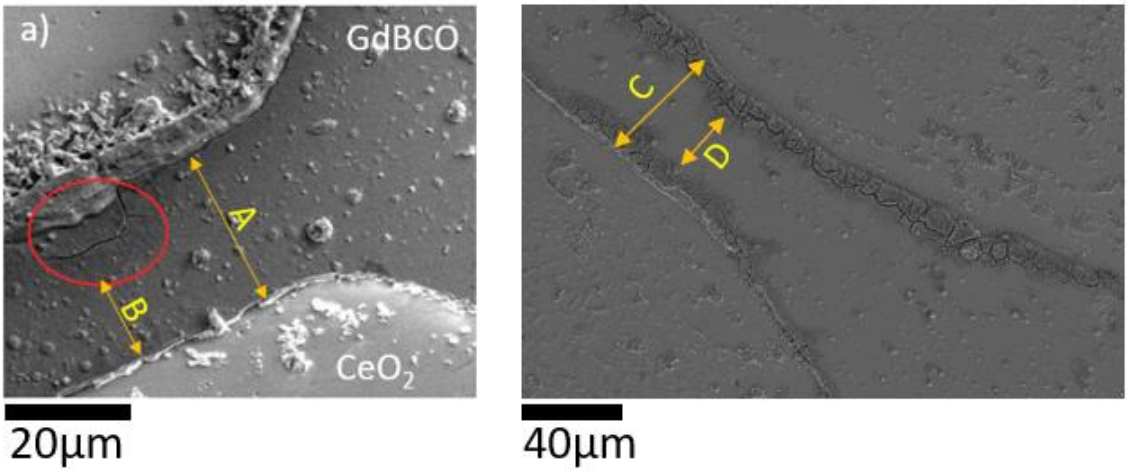

Figure 6.23: SEM investigation of track edge cracking. a) sample RT1: a 4 mm long, 34 µm wide track showing signs of etch undercutting the mask and edge crack (circled), potentially reducing the thinnest point of the track from 34 µm (dimension A) to ≈18 µm (dimension B); b) sample RT4: a 2 mm long, 49 µm wide track with edge cracking down the track's entire length, potentially reducing the thinnest point of the track from 49 µm (dimension C) to ≈23 µm (dimension D).

6.4 Summary and Conclusions

In this chapter, the equipment forming the basis of the CIE was described and the subsequent theoretical design discussed. Areas of the apparatus covered included the design of the sample and its plate, the current supply circuit wiring and connections, the method of determining the sample temperature and how LabView was used to control the sample temperature and perform

---

[36] Used $B_{app}||c$ = 5mT.

experiments designed to determine T_c and I_c at varying and constant temperature. Testing the CIE showed that it could successfully determine a track sample's T_c and (I_c, n) at self-field whilst stably maintaining a set sample temperature above T_{i+}=30 K, given the discussed sources of error. For the samples tested so far, recorded (I_c, n) values at 40K agree within the margin of error with the manufacturer's data and the $I_c(B_{self}, T)$ curve can be fit well with data supplied by the manufacturer, given the track widths measured using SEM imagery. Given these results, it can be concluded that the CIE performs sufficiently well to be used in both ex-situ and in-situ irradiation experiments, which form the subject of chapter 7.

7 Irradiation of a cold REBCO Coated Conductor

Based on the work described in chapters 4-6, the experiment described in this chapter has the goal of comparing the effects of room temperature versus cryogenic temperature 2 MeV helium ion irradiation on the T_c and J_c of CCs in self-field. This has been done using the CIE to compare samples irradiated at room temperature and then cooled for testing at 40 K (ex-situ) with samples maintained at 40 K whilst being put though cycles of ion irradiation and transport current testing (in-situ). As room temperature annealing of REBCO irradiated at low temperature has been reported to lead to partial recovery of the superconducting properties [262], similar experiments were also carried out on the two in-situ samples and four of the six ex-situ samples. Aspects of the experimental design are described before the results are presented and their implications discussed.

7.1 Experimental Set-up

Based on the CIE performance described in chapter 6, out of the 10s of tracks manufactured only 8 were of sufficient quality to be used in either in- or ex-situ irradiation experiments. Pre-irradiation details of each of these successful tracks are shown in Table 6-4.

Based on CIE performance testing described in section 6.3, the temperature of interest for this experiment was set to 40 K, the current pulse duration (t_{pulse}) used was 200 ms and the time between pulses (t_{off}) was set to 0.5 s. The aim was to observe the dependence on irradiation temperature of the superconducting performance of the Fujikura 2018 CC – $J_c(B_{self}, 40\text{ K})$ – as a function of dose. Although testing showed no measurable temperature change in the sample during a superconducting transition up to V_{OVP} = 40 µV, occasionally quenches occurred, therefore the minimum time between I-V curve generation was set to 30 s for tests that ended at I_{end} or V_{OVP} and this gap rose to 180 s for tests that ended in a quench, determined based my cumulative experience of using the CIE for many experiments instead of being formally defined during an experiment. That said, adding these short time intervals did not add a burdensome amount of extra time to each experiment, and allowed sufficient time for the sample to re-establish its temperature equilibrium before the next test.

7.1.1 Ex-situ Experiments

In these experiments, samples were irradiated at room temperature and then cooled to measure $J_c(B_{self}, T)$. During each experiment, particular attention was paid to ensure multiple measurements were performed while the CIE was controlled at T_{i+}=40 K.

The irradiation plate designed and built to secure and mask the samples during room temperature irradiation is shown in Figure 7.1. It was designed out of thin brass sheet to resemble the ϕ10cm silicon wafers used during CC disk irradiation (Figure 5.1c) so that it could similarly be mounted on one of the end stations of the SIBC 2MeV beamline (Figure 7.3b). Samples were secured using 4xM2 brass bolts through ϕ2.5 mm holes cut in the same pattern as MCPCB in both plate and mask. A ϕ5 mm hole was cut equidistant between each set of ϕ2.5 mm holes to allow the beam access to the sample. Kapton tape was used to confirm the beam strike location (Figure 7.1). Brass washers were used to ensure there was a gap between masking plate and sample, minimising the possibility that the two pieces touched. These washers also ensured that the sample was electrically connected to the irradiation plate, removing the possibility that charge build-up on the sample, which would otherwise have been isolated, would affect the trajectory of incoming ions.

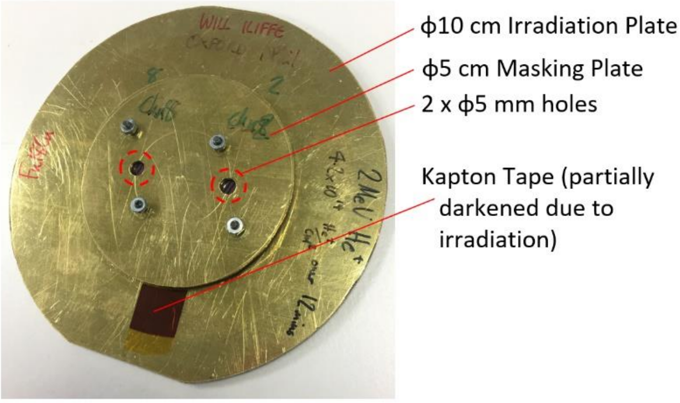

Figure 7.1: The φ10 cm brass irradiation plates used to conduct ex-situ irradiations of 2 samples at a time at the SIBC.

Light microscope images showing the areas of the sample that were accessible by the ion beam are shown in Figure 7.2. These show that the 4 mm long samples (Figure 7.2a&b), though ideally placed on the MCPCB to allow I-V testing, were not ideally centred with respect to the ϕ5 mm opening in the mask. This resulted in part of the track not being subjected to ion beam irradiation, although the whole width of the track was irradiated over a significant length. This led to the acquisition of a new mask allowing the creation of 2 mm long tracks. A similar analysis of the 2 mm long tracks (Figure 7.2c-f) showed that, even if they were not centred with respect to the mask opening, they were subjected to ion irradiation over their entire length.

Given that parts of the 4 mm long tracks RT1&2 would remain unirradiated, this means that the sample voltage (V_{sc}) for the pristine sample needed to be fitted with $L = L_{track}$= 4 mm, but once irradiated V_{sc} would consist of 2 voltages in series, one for the irradiated section of track ($V_{sc,irr}$) and one for the unirradiated section of track ($V_{sc,unirr}$), each of which would have its own power law with different (I_c, n):

$$V_{sc} = V_{sc,unirr} + V_{sc,irr} \tag{7-1}$$

$$V_{sc} = E_c\left(L_{unirr}\left(\frac{I_{sc}}{I_{c,unirr}}\right)^{n_{unirr}} + L_{irr}\left(\frac{I_{sc}}{I_{c,irr}}\right)^{n_{irr}}\right) \tag{7-2}$$

The length of the irradiated section of track (L_{irr}) was determined for RT1 and RT2 using the reference dimension marked on Figure 7.2a&b. This dimension was 0.65 mm, based on the mask being designed to have 0.3 mm wide channels on either side of the design track width, which for RT1 and RT2 were both 50 µm. Based on this, L_{irr} for RT1 and RT2 were determined to be ≈3.75 mm and ≈2.40 mm respectively. Although this correction was applied to each I-V curve generated for RT1&2, it did not result in a significant change in $I_{c,irr}$ when using $L = L_{irr}$, as for $V_{sc,unirr}$ to make up a significant fraction of V_{sc} the change in I_c due to irradiation had to be small, whilst the deterioration of the power law exponent has to be large; a situation which rarely occurred.

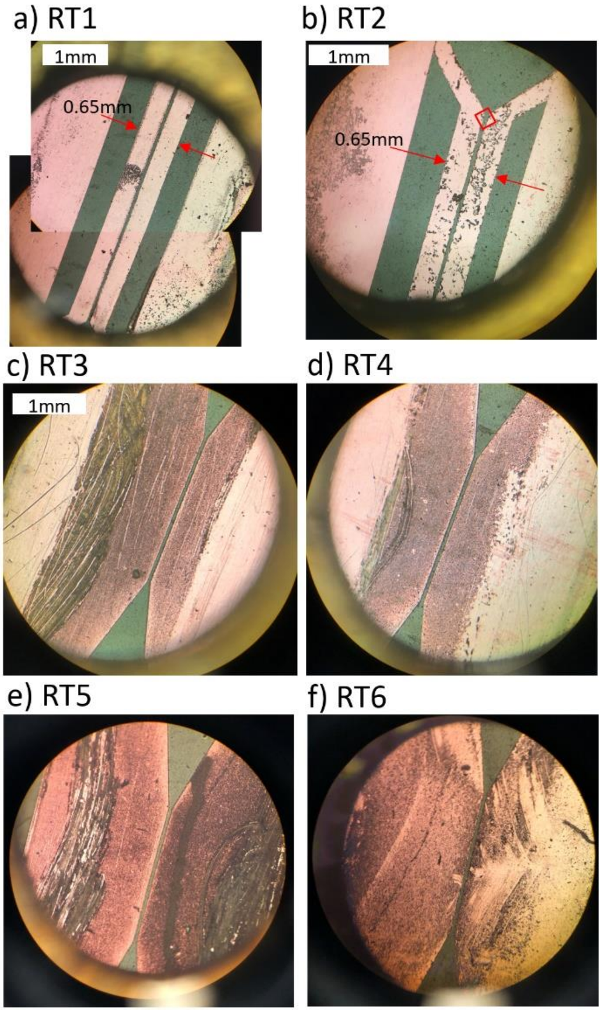

Figure 7.2: Light microscope images of the ex-situ samples RT1-6 (figures a-f) as seen through the φ5 mm hole in the brass irradiation masking plate. These show that the full length of the track of samples RT3-6 was exposed to the beam, but the tracks of RT1-2 were only partially exposed over lengths of 3.75 and 2.4 mm respectively. The red box in b) denotes the area magnified in Figure 7.12a.

7.1.2 In-situ Experiments at the Surrey Ion Beam Centre

Samples C1 and C2 were irradiated in-situ at the SIBC on their 2 MeV beamline (described in section 3.6) during the 7th and 8th December 2020 using the set-up shown in Figure 7.3. These samples had previously been tested ex-situ to confirm they were of sufficient quality to undergo in-situ experiments. 2 of the 2 MeV beamline's stages were used during the in-situ experiments; the charge collection stage (Figure 7.3, ❹) used in conjunction with 4 faraday cups further upstream (Figure 7.3, ❼) to measure the characteristics of the rastering beam and allow it to be manipulated to the required conditions before the beam is applied to the sample, and the opening in the sample mounting stage (Figure 7.3, ❺) which allowed the beam access to back loaded experiments. The CIE was assembled on to the back loading position of the SIBC 2 MeV beamline end station[37] (Figure 7.3, ❸), attached to its compressor and, via the associated wiring (Figure 7.3, ❿), to the required auxiliary equipment which was set up outside the clean room.

Once the CIE had cooled the sample down to a stably controlled T_{i+}=40 K and 3-5 I-V curves had been recorded as a reference, the beam was initiated and manipulated into the required conditions (2MeV helium at a beam current density (J_b) = 100 nA/cm^2 – the same as for the room temperature experiments described in chapter 5.1.3. The sample mounting section was then actuated to expose the sample to the beam for periods of 12 minutes each, delivering a dose equivalent to 0.455 mdpa with negligible helium implantation to the superconducting layer. The sample mounting section was then actuated to the charge collection position, protecting the sample for the beam, whilst 3-5 I-V curves were recorded using the CIE. This process of irradiation and testing was repeated until the allotted time for the experiment elapsed (≈8 h for C1, ≈12 h for C2).

As both cold irradiated samples were 4 mm long, it was not trivial to determine whether the whole track was under the beam before irradiation. Kapton tape was therefore added behind the sample on the MCPCB so that the beam strike location could be determined post-mortem.

---

[37] replacing the Faraday cup assembly which usually sits there.

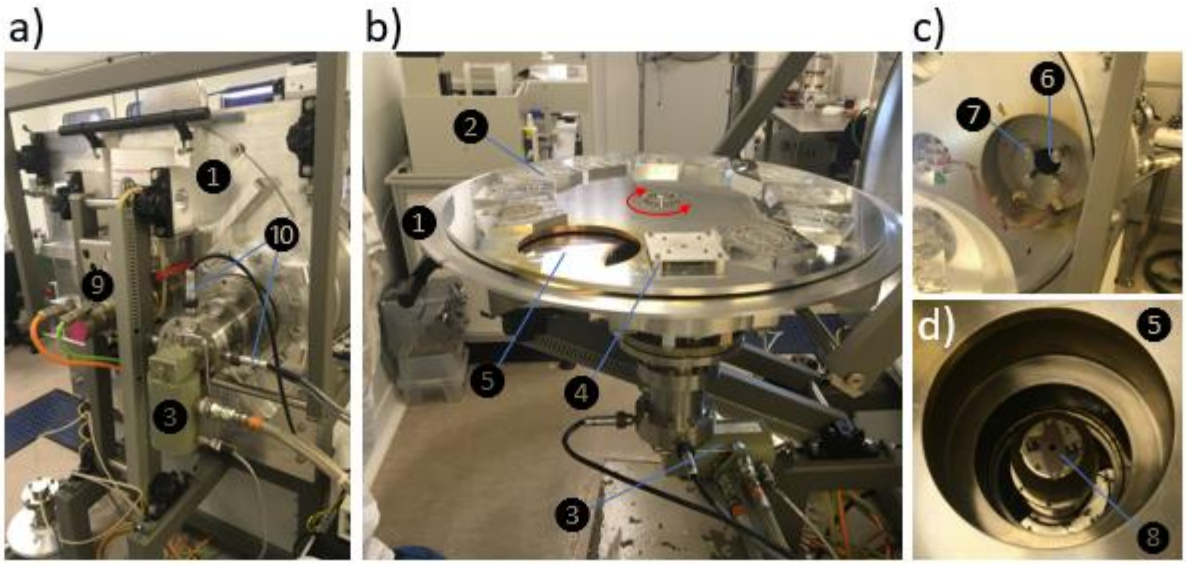

Figure 7.3: The set-up of in-situ experiments on the end station of the 2MeV beamline. Labels indicate: 1: beam line support structure and part of its vessel wall; 2: actuated sample mounting stage for up to 10 samples; 3: CIE cryocooler assembled on to 1; 4: charge collector; 5: opening in the sample mounting stage allowing the beam access to back loaded experiments; 6: opening where the beam comes out; 7: 4x Faraday cups (each 0.6 cm^2), 8: assembled CIE as viewed through 5; 9: actuating equipment for 2; 10: CIE room temperature wiring.

7.2 Results

In this section, the results of retesting samples C1&2 in-situ and RT1-6 ex-situ between 12-minute irradiations of 2 MeV helium ions at 100 nA/cm^2 are described. T_c and ΔT_c are calculated using the method based on the resistivity of copper at 20 K described in section 6.3.1 and I_c is determined by fitting the power law (equation 3-1) to the I-V curve unless the track length was found to be not equal to the irradiated track length (RT1&2) when equation 7-2 is used.

7.2.1 Ex-situ Experiments

During the period of November 2020 to June 2021, RT1-6 were irradiated in stages (for details, see Appendix Table S7-1 and S7-2). The changes in T_c, and ΔT_c are shown in Figure 7.4, $J_c(B_{self}, T)$ in Figure 7.5 and the evolution of $J_c(B_{self}, 40\text{ K})$ is shown in Figure 7.6.

The initial samples (RT1&2), both of which have tracks which are not irradiated along their full length, were irradiated up to 4.1 mdpa to assess the full $J_c(B_{self}, T)$ versus damage trajectory over the damage range suggested in chapter 4. These 2 samples showed a very different responses to irradiation, with the T_c of both dropping similarly up to ≈ 1.2 mdpa, but the T_c of RT1 continued to drop along the same trend line (≈ 5.5 K/mdpa) whilst the T_c of RT2 drops less quickly. There is also a marked difference between the samples in terms of how $J_c(B_{self}, T)$ changes with damage, with sample RT1 having no measurable $J_c(B_{self}, 40\text{ K})$ at 4.1 mdpa whilst RT2 could still maintain $J_c(B_{self}, 40\text{ K}) \approx 6$ MA/cm^2 at 4.1 mdpa, ≈60% of its initial J_c.

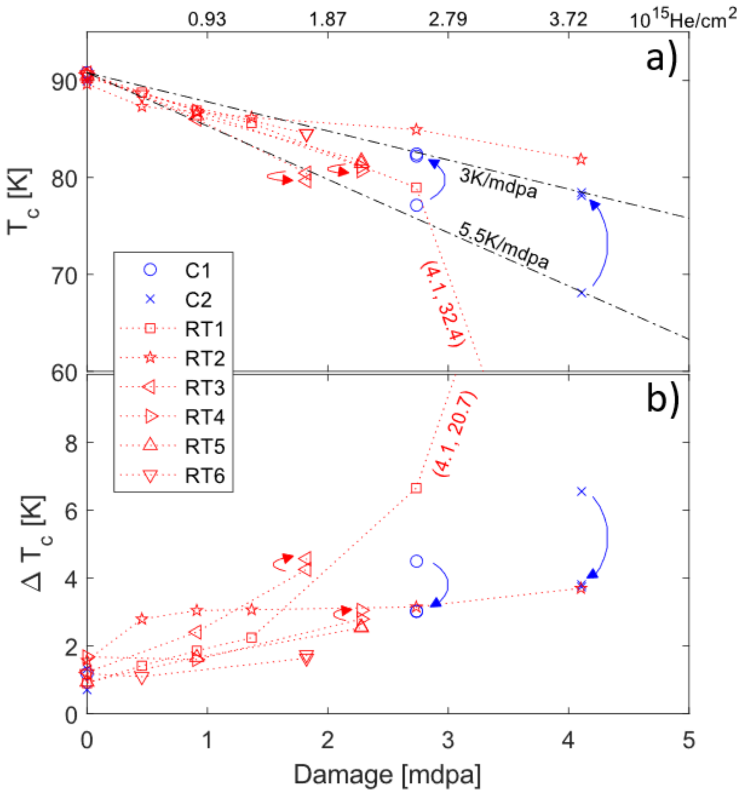

Figure 7.4: Critical temperature response to irradiation damage (x-axis). a) T_c (top y-axis) and b) ΔT_c (bottom y-axis) for the 2 in-situ samples (blue) and the 6 ex-situ samples (red). Top x-axis shows 2 MeV helium ion fluence.

The second set of samples (RT3-6) were created in response to the in-situ annealing experiments (described below), aiming to test what effect room temperature annealing had on the samples irradiated at room temperature whilst also trying to determine which of the irradiation responses of RT1 or RT2 was anomalous. As shown in Figure 7.4, the change in T_c and ΔT_c shown by samples RT3-6 mirrors that of RT1, and the $J_c(B_{self}, T)$ and $J_c(B_{self}, 40\ K)$ responses to irradiation (Figure 7.5 and Figure 7.6 respectively) are also more similar to RT1, with each sample showing a roughly systematic decline in $J_c(B_{self}, T)$ at a rate of ≈3.5-4 MA/cm^2/mdpa, or, in relative terms, ≈30 %/mdpa for $J_c(B_{self}, 40\ K)$.

Samples RT3-6 were also retested after a period of ≈30 days to see if time spent at room temperature after room temperature irradiation affected their superconducting properties. As shown in Figure 7.5 and Figure 7.6, time at room temperature led to a small drop in T_c and $J_c(B_{self}, T)$ and a slight widening of ΔT_c for all these samples, implying that there is no self-healing effect observed in samples irradiated at RT.

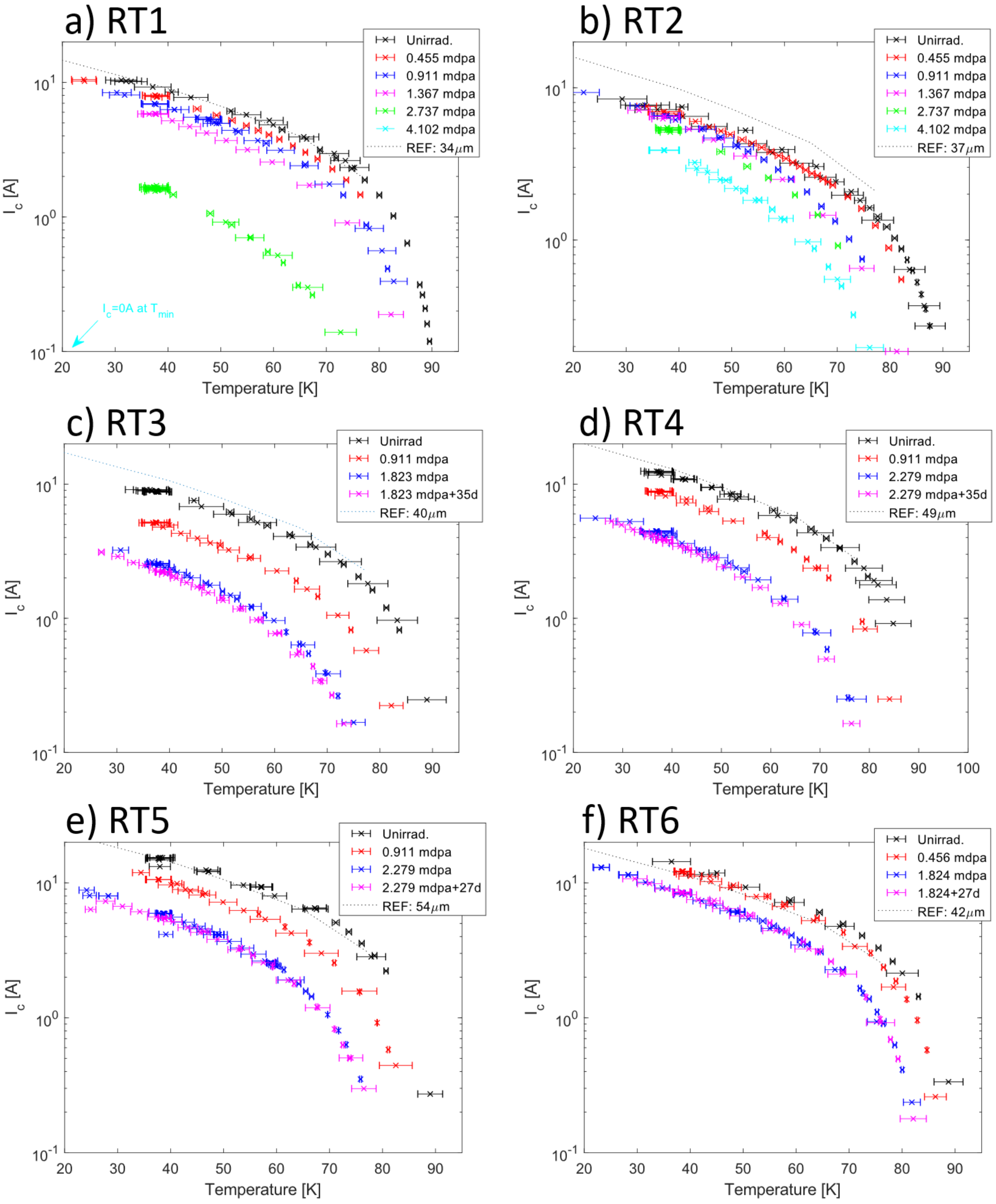

Figure 7.5: Full critical current (I_c, y-axis, log scale) versus temperature (T, x-axis, linear scale) plots for samples a) RT1; b) RT2; c) RT3; d) RT4; e) RT5 and f) RT6 showing the results of lattice damage due to helium irradiation. In each figure 'REF' refers to the expected I_c of the sample based on data from the manufacturer given its measured track width and '+…d' refers to the duration of the room temperature annealing between tests (eg. '+35d' = 35 days between initial test and post annealing test).

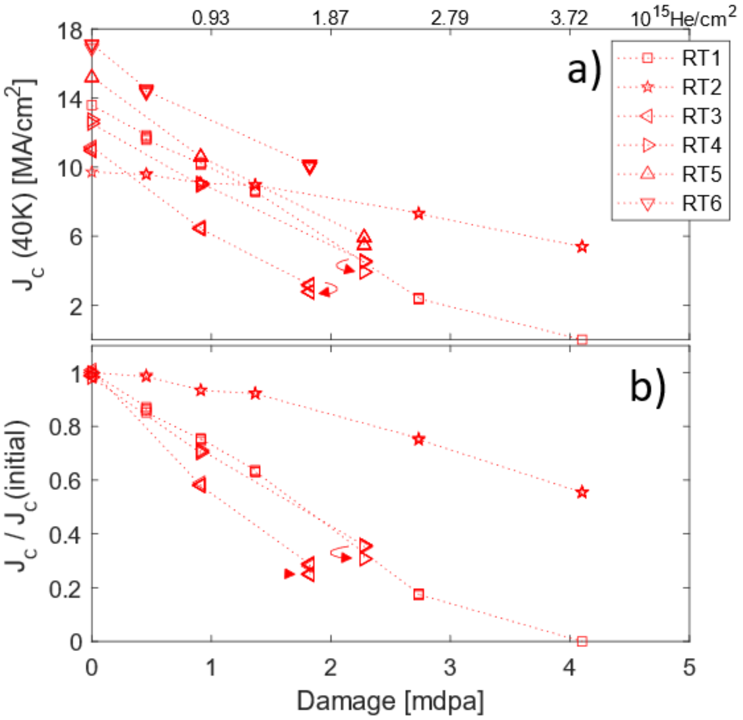

Figure 7.6: J_c (B_{self}, 40 K) versus irradiation damage level for samples RT1-6. Arrows indicate the change in J_c (B_{self}, 40 K) after room temperature annealing for ≈ 30 days.

7.2.2 In-situ Experiments

During the in-situ experiments on samples C1 and C2, temperature data was recorded throughout and (I_c, n) calculations were performed as they happened (Figure 7.7). The raw (I_c, n) data calculated by fitting the power law to the I-V curves, and the resulting temperature deviation during the transition, are shown in Figure 7.7a&b for C1 and C2 respectively. These show that (I_c, n) values for each sample before irradiation were consistent with those recorded during earlier ex-situ testing (circled points on Figure 7.7a&b), implying that sample integrity had been maintained between the ex-situ and the in-situ irradiation. During in-situ testing, the 4-6 I-V curves recorded between each irradiation were consistent with each other, implying that the sample was not being damaged during transport current testing, and that I_c dropped systematically with increasing fluence. They also show that T_{i+} was kept close to 40 K during every test and the temperature range across the sample was measured to have a constant value. The power law exponent of both samples dropped from 20-22 to 17-18 over the course of the experiments.

Figure 7.7c&d show that T_{i+} = 40 K could be maintained by the CIE heater for >450 mins, sufficient time to perform 10 cycles of testing with the associated 9 irradiation steps. The sample temperature did however fluctuate slightly when the beam was turned on, but T_{i+} = 40±1 K could be maintained. The beam heating was estimated to supply ≈0.5 W of thermal energy to the sample, signified by a drop of ≈0.5 W by the heater whilst the beam was on. The only unforeseen elements of the temperature traces shown in Figure 7.7c were the spikes in temperature shown by both sensors periodically during the experiment. The reason for these sudden changes in temperature became apparent when the CIE was re-examined after the experiment on C1. This revealed that much of the CIE's internal wiring had been subject to direct ion beam irradiation, characterised by the blackening of the enamel coating of the wires (Figure 7.7e). As the temperature sensor wiring also showed blackening, and that the spikes in temperature coincided with the beam being applied to the sample, it was hypothesised that the ion beam interacting with the wires was the cause of the sudden temperature changes. Moving forward to the testing of sample C2, steps were taken to cover the extremities of the opening to the CIE (Figure 7.3d) with silicon wafers to prevent the beam from directly interacting with the CIE wiring. When tested, this solution showed no signs of sudden temperature changes during irradiation (Figure 7.7d).

Figure 7.8 shows the results of the beam strike location test. These show that the beam interacted with the entire length of the track on C2 but not for C1. Using the full track length as the scaling dimension of 4 mm, L_{irr}= 3.9 mm was determined for sample C1 from Figure 7.8a. This new L_{irr} was used in conjunction with equation 7-2 to recalculate $I_{c,irr}$ for sample C1, resulting in a I_c correction of the order of 0.02 A for all I-V curves.

Figure 7.9a&b shows the absolute and relative trajectories of the $J_c(B_{self}$, 40 K) values for samples C1 and C2 as the damage level is increased. These show that, although the $J_c(B_{self}$, 40 K) of each sample does not deteriorate at the same rate in absolute terms, in relative terms $I_c(B_{self}$, 40K) decreases at roughly the same rate. The relative drop is characterised by a roughly linear drop down to 40-50% at ≈30 %/mdpa, followed by a tailing off in the rate of decline at damage levels > 2.5 mdpa.

Figure 7.9a&b also show one of the more unexpected results of this experiment; that the $J_c(B_{self}$, 40 K) of both cold irradiated samples shows a significant improvement after a period of 76 days of annealing at room temperature, with the I_c values recovering to values representative of those recorded at half the damage level. This improvement in the sample's properties was also characterised by a significant increase in T_c and narrowing of ΔT_c, as shown in Figure 7.4a&b. To see if this improvement continued, these samples were tested again after a further 40 days at room temperature and showed negligible improvement, suggesting that the recovery processes at room temperature do not carry on indefinitely.

The in- and ex-situ results are compared in Figure 7.9c, showing $J_c(B_{self}$, 40 K), and Figure 7.9d, showing the change in $J_c(B_{self}$, 40 K) relative to its value before irradiation and Figure 7.9e showing the associated power law exponents. Although there is some variation, Figure 7.9e shows that for all samples, the n-values decline due to irradiation. This decline is smallest for the in-situ irradiated samples (≈4-5) and more scattered for the ex-situ samples.

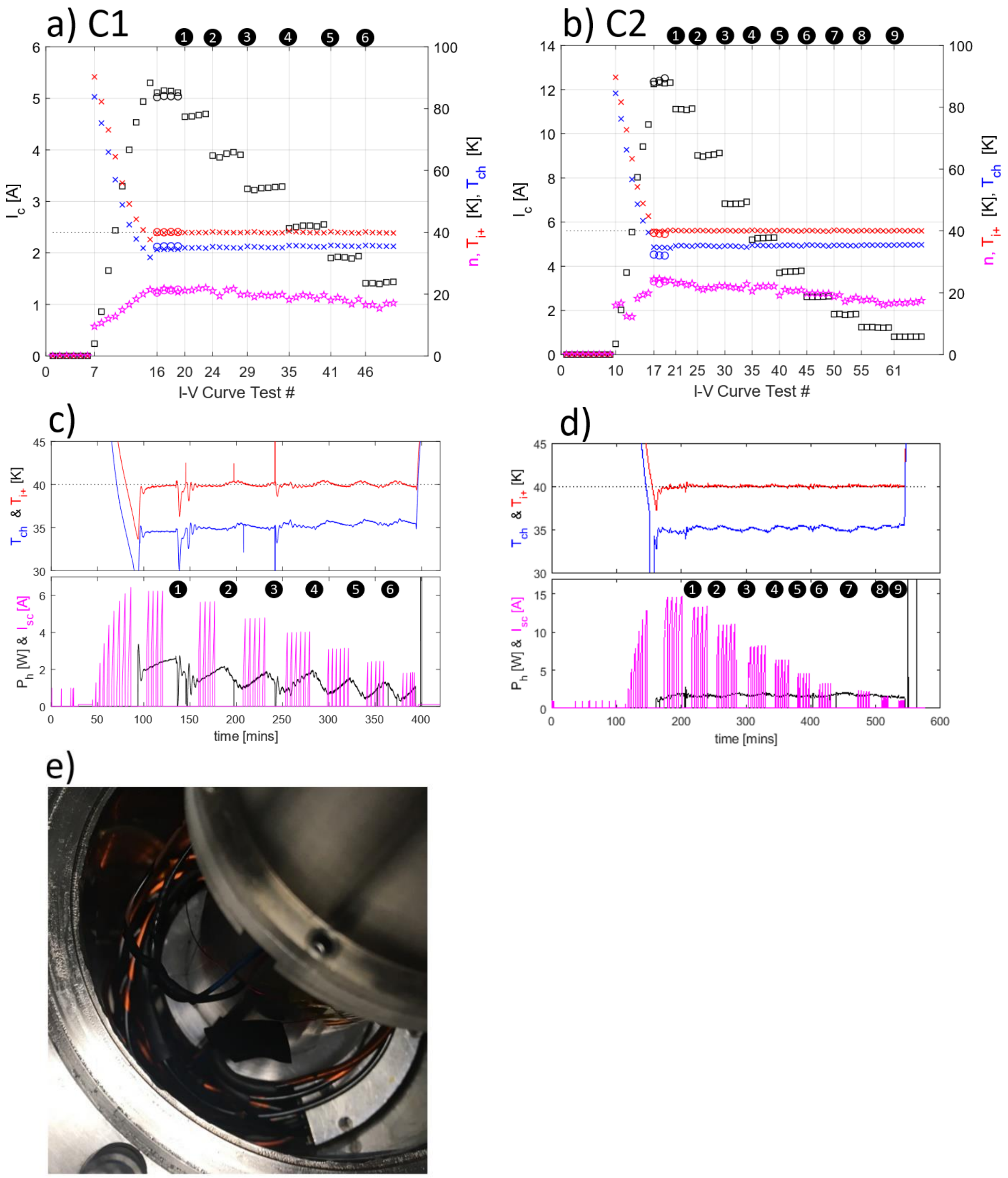

Figure 7.7: Plots from cold irradiation days at the SIBC. a&b) I_c (left y-axis), n, T_{ch}, T_{i+} (right y-axis) calculated from each I-V curve recorded during each pulse (x-axis) for samples C1 (a) and C2 (b), showing intervals (circled number along top x-axis) where the irradiation doses were applied. Circled data points are for the ex-situ test of each sample performed to test it properties before going to the SIBC. c&d) T_{ch}, T_{i+} (top y-axis), P_h and I_{sc} (bottom y-axis) versus time (x-axis) recorded during the entire experiment on sample C1 (c) and C2 (d) showing intervals where irradiation doses were applied. e) Inspection of CIE wiring after testing sample C1 shows blackening of the enamel coatings due to ion beam bombardment.

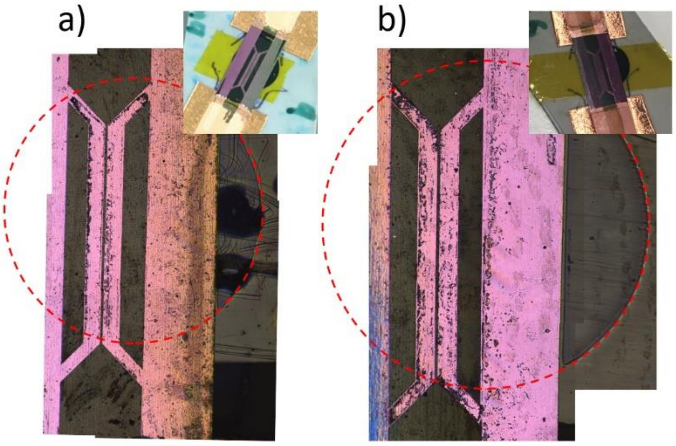

Figure 7.8: Post-mortem beam spot location analysis for in-situ samples C1 (a) and C2 (b) showing that C2 is irradiated along entire length of track whilst L_{irr} of C1 was reduced to 3.9 mm.

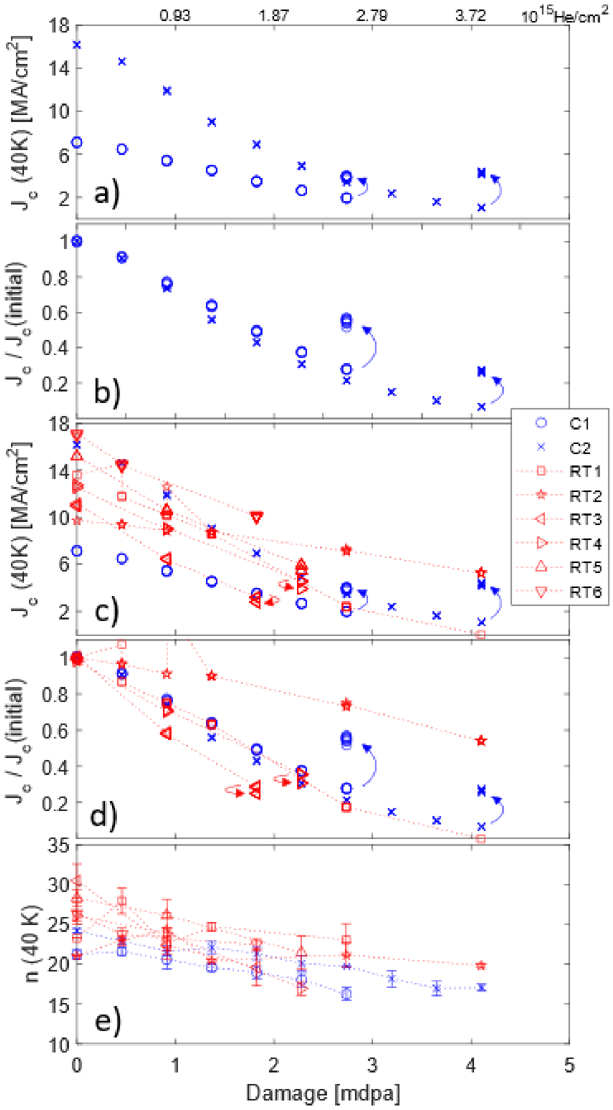

Figure 7.9: a&b) absolute (a) and relative (b) J_c (B_{self}, 40 K) versus irradiation damage (x-axis) for samples C1 and C2. Arrowed points indicate the change in that property due to a room temperature annealing step. c&d) absolute (c) and relative (d) J_c (B_{self}, 40 K) versus irradiation damage level for all in- and ex- situ samples. Relative graphs are all normalised to J_c (B_{self}, 40 K) before irradiation. e) the calculated power law exponents related to the J_c (B_{self}, 40 K) measurements.

7.3 Discussion

The results described above imply that there are differences between the response of REBCO to irradiation with 2 MeV helium ions that are dependent on the sample temperature, and that these differences manifest during the room temperature annealing of samples irradiated whilst cold. In this section, the results of the ex-situ irradiations are discussed and then compared to the results for the in-situ experiments.

7.3.1 Effect of ex-situ 2 MeV helium irradiation

The above results show that irradiating Fujikura GdBCO with 2 MeV helium ions leads to a drop of T_c at ≈5.5 K/mdpa (Figure 7.4) and a systematic drop in J_c v T (Figure 7.5), equivalent to a relative drop in $J_c(B_{self}, 40\text{ K})$ of 30 %/mdpa compared to the initial value (Figure 7.6), except for the anomalous RT2 sample. Given the ion-energy combination used during this experiment was specifically chosen to displace REBCO's oxygen atoms whilst avoiding ion implantation, the displacement of oxygen within the GdBCO lattice is expected to have caused the drop in T_c and the widening of ΔT_c. The suspected mechanism leading to this change, given that 1) the energy transferred to GdBCO's oxygen ions during each collision is essentially stochastic, that 2) the PKA generated interacts with a volume of GdBCO and that 3) the level of deoxygenation of this volume is likely directly proportional to the amount of energy transferred to the PKA, is that irradiation leads to the track becoming a GdBCO volume with varying levels of deoxygenation. Each of these different volumes would have its own T_c value with the net effect being that, when the track is subject to constant current, different volumes of GdBCO would become superconducting at different temperatures, widening ΔT_c and leading to T_c (now essentially a volume weighted average of the track's range of critical temperatures) moving to lower temperature.

The stochastic nature of the energy transferred from the bombarding ions to atoms in the GdBCO's lattice during irradiation means that a small fraction of the total collisions will be high angle, generating highly energetic PKAs. Though low angle collisions will be far more numerous, generating a plethora of additional weak pinning sites (point defects), high energy PKAs will likely generate a disproportionate number of defects in close proximity, leading to a change in the strong pinning landscape. This has been analysed with reference to the work of Nelson et al. and Blatter et al. [191], [192], introduced in section 2.2.2.6 which suggests that equation 2-10 for strong pins should be a good fit for the data recorded by my CIE ex-situ experiments. An example of fitting equation 2-10 to the data collected for sample RT3 is shown in Figure 7.10, which is characteristic of the graphs for all samples (except RT2). Figure 7.10 shows no deviation of the experimental data from the fit to equation 2-10 at the low temperature end, implying that lower temperature measurements would be required to assess the contribution of weak pins in this sample, and a deviation at the high temperature end that shifts to lower temperatures as damage increases, suggesting that the irreversibility line of the sample shifts to lower temperatures with increasing lattice damage, similar to the results presented in chapter 5.

Figure 7.11 shows how the fit parameters of equation 2-10 varied with damage level for samples RT1-6. In Figure 7.11a $J_c^{str}(0)$ drops linearly for samples RT1 and RT3-6 at ≈ 4-5 MA/cm^2/mdpa, implying that the contribution of strong pinning to J_c at 0K decreased linearly with damage level, whereas $J_c^{str}(0)$ for sample RT2 remains close to 15 MA/cm^2 up to 2.7 mdpa and only starts to show significant deterioration when the damage level approaches 4.1 mdpa. This anomalous behaviour of RT2 is mirrored in the progression of T^+ with damage level (Figure 7.11b), with the other samples all showing a linear decline in T^+ with damage level at ≈8 K/mdpa and the T^+ of RT2 declining erratically with damage. The decline in $J_c^{str}(0)$ and T^+ with damage for samples RT1&3-6 implies that the effectiveness of each strong pinning site has decreased relative to its initial value. This further implies that the potential well holding each traversing fluxon has decreased in absolute depth. This would result in a higher rate of fluxon movement for a given current density and sample temperature, lead to a lower J_c and is consistent with the apparent shift in the irreversibility line to lower temperatures with increasing lattice damage.

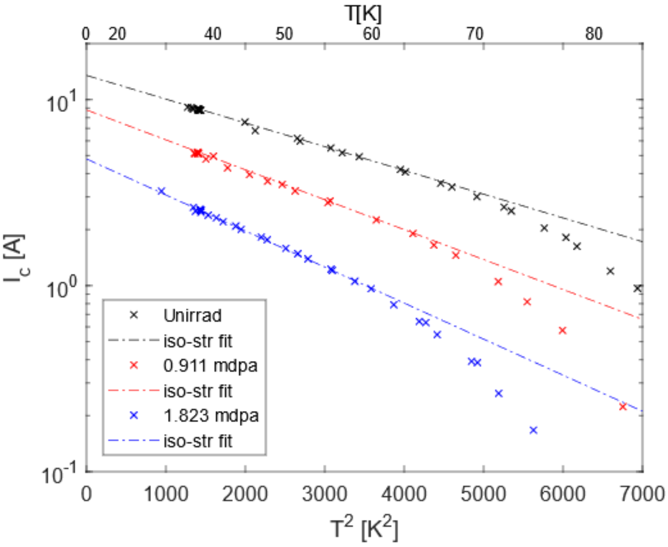

Figure 7.10: Fitting of strong pinning equation 2-10 to data for sample RT6 showing how I_c (y-axis) varies with T^2 (x-axis). These axes scales were used to allow the square exponential fit of equation 2-10 as a straight line

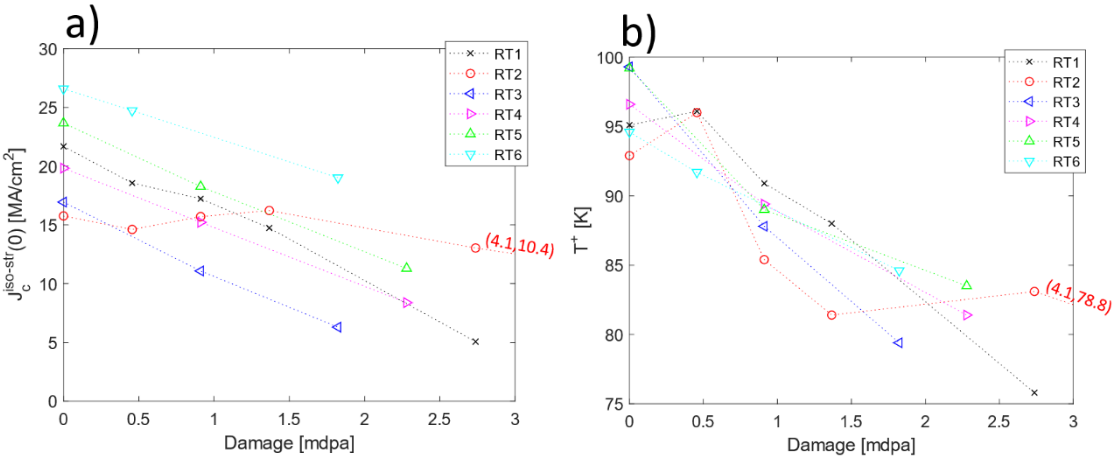

Figure 7.11: How the fitting parameters in the strong pinning equation 2-10 (y-axes) vary for increasing damage (x-axis) in samples RT1-6.

The behaviour of sample RT2 seems anomalous, and to investigate why this might be, SEM images of each end of the sample were examined for any obvious structural differences, given that one end of the sample was irradiated and the other was not. These images are shown in Figure 7.12a&b and suggest that the outward appearance of a track does not change markedly due to helium ion irradiation. This finding was checked by comparing the appearance and width of the track in sample RT5 after irradiation to 0.911mdpa and 2.28mdpa in Figure 7.12c&d respectively. This showed that many of the features present after the 1st irradiation stage are still present after the second, and that the track width after irradiation agreed within the margin of error (±1 µm) with the track width measured before irradiation.

The nature of the differences in microstructure and performance of RT2 versus the other ex-situ samples is now discussed. The diminished initial T_c and $J_c(B_{self,}\ 40\ K)$ versus the other room temperature samples (Table 6-4) indicates that the unirradiated superconducting matrix of sample RT2 is somehow degraded either due to a non-optimum oxygen stoichiometry [103], that the sample is strained [151], or perhaps as a result of disruption to the current path from the growth defects that create the protuberances visible on the REBCO surface. That the initial ΔT_c value was similar to the other room temperature samples indicated that this degradation is present throughout the superconducting volume. Of these possible causes, non-optimum oxygen stoichiometry is perhaps the most likely cause, given that although CC manufacturers take care to accurately control the stoichiometry of the REBCO layer, this sample went through several processing steps during the creation of the track after the REBCO layer was exposed to air, including processes that apply heat and strain to the sample. Although these processes are at much lower temperatures than those used during manufacture, and were applied to all samples, the possibility that some variation in the procedure could have adversely affected RT2's GdBCO layer, but not those of the other samples, cannot be ruled out. The sample being subject to a strain field also cannot be ruled out as, despite my best efforts, the thermal contraction of the sample to the surrounding materials was not perfectly matched, and both positive and negative strain of a CC has been shown to degrade T_c and J_c [367]. Given their similarities, the degradation in T_c and $J_c(B_{self,}\ 40\ K)$ due to strain applied by thermal contraction should affect all samples similarly, as the comparison of the ex-situ and initial in-situ testing of samples C1 and C2 suggests given that $J_c(B_{self,}\ 40\ K)$ did not change between the pre-in-situ irradiation test and the initial zero fluence test at the start of the in-situ irradiation experiment. If the microstructure of RT2 was somehow different to the other tracks, this difference could have manifested in its response to ion irradiation, whether or not it was also subject to an applied strain. In conclusion, the reason for the anomalous behaviour of RT2 has not been determined but given its increased resilience to helium ion damage compared to the other samples, should be investigated further. A detailed comparison of the microstructure of the tracks (perhaps by 3D FIB sectioning) could be a promising avenue for further work.

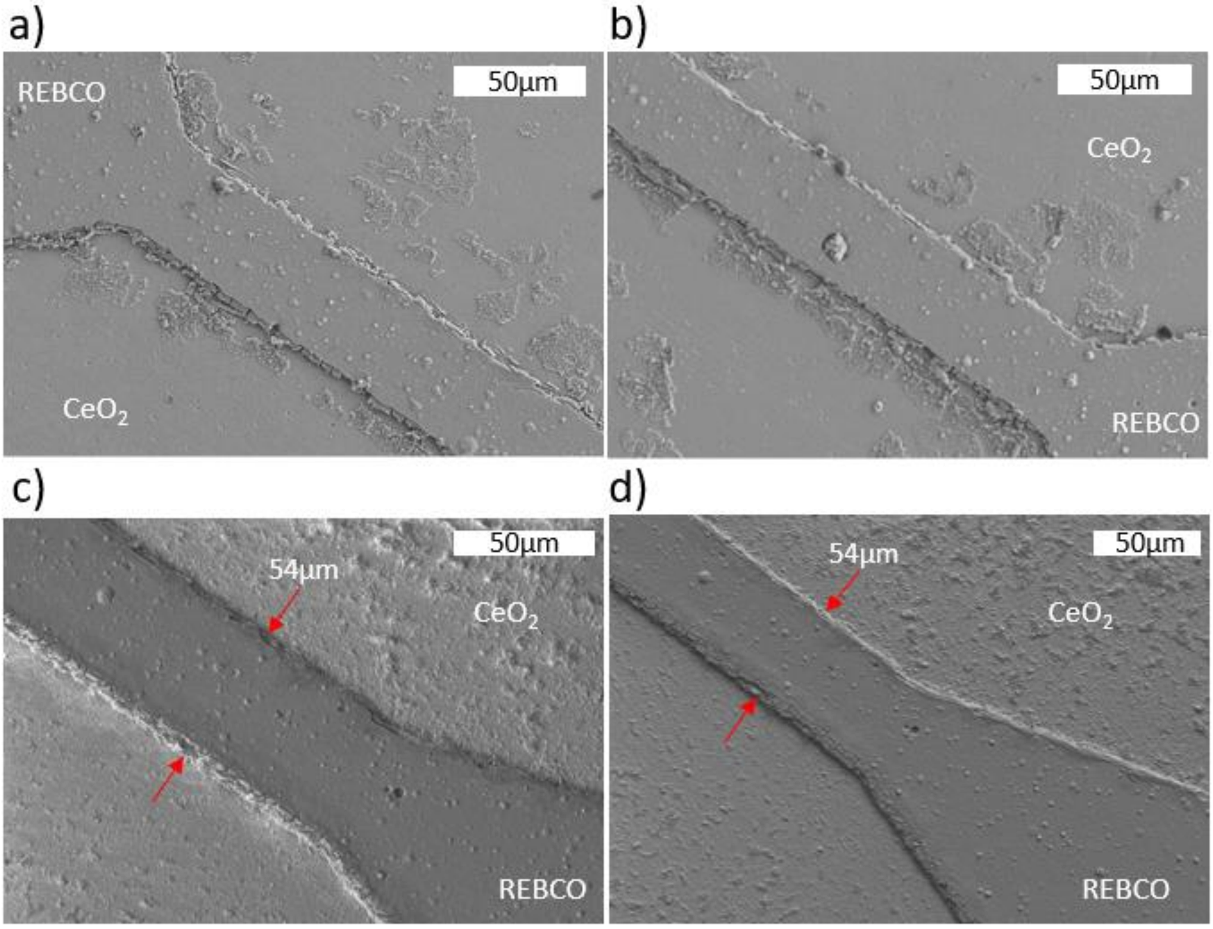

Figure 7.12: SEM images of RT2, a) the irradiated end and b) the unirradiated end, showing no discernible difference in their general appearance. c&d) A section of sample RT5 after irradiation to (c) 0.911 mdpa and (d) 2.28mdpa. Many of the features shown remain unchanged between irradiation steps, including the measured width of the track (54 µm)]

7.3.2 In-situ versus Ex-situ Irradiation

Finally, the similarities and differences in the response in T_c, ΔT_c and $J_c(B_{self}, 40\ K)$ of the in- and ex-situ samples to helium irradiation and subsequent room temperature annealing should be discussed (Figure 7.4a&b and Figure 7.9c-e), and compared to similar experiments performed by Sorbom [277] and recent results from Fischer et al. [368]. My key results were that the properties of both in-situ and ex-situ samples degrade at approximately the same rate, in relative terms, after 2 MeV helium ion irradiation, and while the properties of the ex-situ samples decline slightly on room temperature annealing, the in-situ irradiated samples show significant improvements in T_c, ΔT_c and $J_c(B_{self}, 40\ K)$ when allowed to anneal at room temperature, returning to values equivalent to those recorded at roughly half their damage level. Sorbom's key conclusions were that irradiating REBCO at a lower temperature led to a slower decline in REBCO J_c with increasing fluence, a higher proportion of the total defects being point defects (inferred with reference to MD simulations) and a decrease in the number of defects migrating to grain boundaries [277]. Fischer et al. showed that proton irradiation of a REBCO sample at 77 K led to defects that were stable up to 110 K, above which even short exposures to temperatures between 110-200 K improved the I_c and T_c values compared to post-irradiation levels [368].

My pre-annealing results were significant because they imply that the bulk structure of REBCO's responds to 2 MeV helium ion irradiation is the same, whether irradiated at 40 K or at room temperature. This is likely due to the energy deposited in the sample during each collision being much larger than the available thermal energy of the system, even at room temperature, meaning there is ample energy to create lattice defects of all shapes and sizes at the point the PKA is generated in both in- and ex-situ samples. It also implies that the same processes that affect the T_c, ΔT_c and $J_c(B_{self}, 40\ K)$ of the ex-situ samples, discussed above, also occur in the in-situ samples.

The difference in the post-annealing behaviour, however, implies that there are differences in REBCO's response to irradiation at room versus cold temperatures which, whatever their character in terms of number, distribution and type of defects, leads to different trajectories for T_c and $J_c(B_{self}, 40\ K)$ once the samples are allowed to anneal. My results show that T_c and $J_c(B_{self}, 40\ K)$ increase and ΔT_c narrows upon room temperature annealing, returning to values equivalent to those recorded at roughly half their damage level after 76 days. This sits well with the conclusion of Sorbom that irradiating REBCO at lower temperature leads to a slower decline in REBCO J_c with increasing fluence as, presumably[38], his samples were returned to room temperature for significant periods for the purposes of shipping before their properties were measured.

Given the several mechanisms that effect T_c and $J_c(B_{self}, 40\ K)$, this improvement could represent results from a number of processes during annealing. One likely example is if oxygen displacement within the GdBCO layer during irradiation is the cause of the diminished T_c. If this is the case then the subsequent improvement on annealing would be consistent with displaced oxygens recovering their original positions, most likely via diffusive processes. It is important to note that this improvement is not total – i.e. the initial levels of T_c and $J_c(B_{self}, 40\ K)$ are not re-established post annealing – which would be consistent with some oxygen being permanently lost from the GdBCO volume due to irradiation, or the creation of stable defect clusters that cannot be annealed out. It could then be argued that proportionally more oxygen is lost from the GdBCO layer, either to stable defects or from the sample altogether, during room temperature versus 40 K irradiation. If this is the reason for the improvement in T_c and $J_c(B_{self}, 40\ K)$ then the results of Fischer et al. that suggest that diffusive processes are halted in REBCO when maintained below 110K [368] would imply that defects created during in-situ irradiation were immobile during the entire irradiation phase whereas defect diffusion could occur during the irradiation of my ex-situ samples. It could then be argued that it is the action of defect diffusion during irradiation that accelerates the loss of oxygen from the GdBCO lattice, and that by halting diffusion by lowering sample temperature, more of the total oxygen in the system is retained near its original lattice site, facilitating its return to a vacant oxygen site once the sample temperature is increased. This sits well with Sorbom's conclusion that low temperature irradiation leads to a decrease in the rate of defect migration to grain boundaries as this would lead to the net retention of oxygen within the GdBCO lattice and a decrease in the rate that grain boundary widths increase with damage level.

Although the above explanation sits well with my experimental results and the results of 2 similar experiments, it by no means rules out other mechanisms affecting T_c and $J_c(B_{self}, 40\ K)$ as there is no way to deconvolute their effects from those reported. For example, the volume of superconducting material is likely changing due to the creation of additional defects in the GdBCO lattice. The pinning landscape could also be being affected by the a-axis grains being subject to irradiation, changing the local strain fields so that previously pristine GdBCO is now subject to strain and vice versa. The anomalous RT2 sample also suggests that certain volumes of GdBCO on a CC can be more resilient to

---

[38] Whether his samples are kept at their irradiation temperature or not until their properties are measured is not explicitly mentioned in the Sorbom thesis. This has been assumed since the sample irradiation and superconducting property measurement occurred in distance locations; North America and New Zealand respectively.

irradiation damage than the bulk. Deconvoluting these effects from those due to oxygen movement require dedicated microstructural analysis, preferably involving the use of TEM.

7.4 Conclusions

In this chapter an experiment to determine the differences in response to 2 MeV helium ion irradiation of Fujikura's 2018 GdBCO CC at room versus cold temperatures using the CIE was presented and results discussed. The CIE was used to test 6 samples that were irradiated at room temperature and the transport current tested at 40 K (ex-situ), and 2 samples irradiated and tested whilst being continuously maintained at 40 K (in-situ).

Analysis of the CIE data for the ex-situ samples showed that 2 MeV helium ion irradiation led to a systematic lowering of T_c, increase in ΔT_c and decline in $J_c(B_{self}, T)$. Analysis of the ex-situ J_c vs T plots implies that the decline in the CC's superconducting properties due to irradiation could be a result of the displacement of oxygen ions characterised by a diminishing T_c and a decrease in the effectiveness of strong pinning defects. This manifested in the linear decline of T_c and $J_c(B_{self}, T)$ in all samples except for RT2, which has been deemed anomalous, perhaps as a result of having a different local microstructure, which should be investigated during future work given its increased resilience to irradiation damage.

Comparing the T_c, ΔT_c and $J_c(B_{self}, 40\ K)$ results of in- versus ex-situ samples showed that although the properties of both sets of samples degraded similarly with irradiation fluence, the properties of the in-situ samples improved significantly when allowed to anneal at room temperature. Analysis of the data, in conjunction with the conclusions from two similar experiments, suggests a likely explanation for the different responses is that diffusion processes are frozen out during irradiation at 40 K, thus reducing the loss of oxygen from the cold irradiated samples to stable defects or from the GdBCO volume. That said, the effects of other processes cannot conclusively be ruled out without an analysis of the local microstructure, suggesting an investigation using TEM should be part of the suggested further work.

8 Summary and Conclusions

Superconducting wires are a key enabling technology for generating electricity from DT fusion reactions as they can carry high current densities in high magnetic fields, allowing them to make better use of the limited space available in a tokamak. Of the several superconductors available, REBCO was the focus of this thesis as it is the superconductor of choice for several TPP concepts due to REBCO-based CCs becoming increasingly commercially available, despite its documented degradation when neutron irradiated. This thesis has therefore presented a fundamental study of superconductivity in REBCO, the manufacturing and resultant properties of REBCO CCs and how their reaction to various types of irradiation has allowed the superconducting state of REBCO to be studied. This informed my own experimental work which included, in chapter 4, determining that, given the samples available to me (Table 3-1), 2 MeV helium ions should be used to emulate fusion neutron spectra irradiation of CCs, and that neutron fluences equivalent to ≈ $4.5\text{x}10^{-3}$ dpa were sufficient to decrease the low temperature, high field J_c of all CC samples so that even if they were of the type that initially showed an improvement in performance on irradiation (section 2.4), J_c would have declined below its initial value. In chapter 5, a variety of different coated conductor samples were subjected to 2 MeV helium ion irradiation at room temperature. The high field J_c of the Fujikura 2018 CC was found to be the most resilient to radiation damage, responding to helium ion irradiation with a similar J_c/dose trajectory to the most resilient fission neutron irradiated CC reported by Fisher et al. [21]. The Fujikura CC was therefore used going forward to the in-situ irradiation experiments. In chapter 6, the key design elements of an experiment to perform irradiation and electrical testing of a REBCO CC maintained below its T_c (but not subject to external magnetic fields) was described. This informed the build phase of the Cold Irradiation Experiment (CIE) which performed sufficiently well during testing to be used in a cold irradiation experiment at the Surrey Ion Beam Centre. Finally, in chapter 7, the CIE was used to perform concurrent 2 MeV helium irradiation and electrical testing of 2 Fujikura CC samples (in-situ) for comparison with 6 similar samples irradiated at room temperature and cooled for electrical testing. This comparison showed that the superconducting properties T_c and $J_c(B_{self}, 40\text{ K})$ decline at the same rate regardless of sample temperature. The key difference, however, was in the in-situ sample's response to room temperature annealing after irradiation, where the T_c and $J_c(B_{self}, 40\text{ K})$ of the samples irradiated cold recovered significantly if left to anneal at room temperature for 76 days whilst the room temperature irradiated sample properties remained relatively unchanged. Although the effects of other processes could not conclusively be ruled out, analysis of the data in conjunction with the results of two similar (and contemporary) experiments from other groups suggested that diffusion processes being halted during irradiation at 40 K being the likely cause for the different responses.

8.1 Further Work

The results reported in this thesis have suggested several areas of further work. These include:

Calibrating the ARC-NRT model for REBCO

Given the known limitations of the NRT model, it is suggested that Nordlund's ARC-NRT model [213] (section 2.3.1) be calibrated for REBCO. This would require REBCO to be studied using a properly calibrated MD model but would allow the calculated number of displacements for a given projectile and damage energy to be more accurately calculated. This calibrated model could then be incorporated into the SPECTRA-PKA model presented in chapter 4 to improve its accuracy.

Use TRIGA CIF to irradiate EuBCO

Given that impurity build-up due to transmutation of the rare-earth in EuBCO is orders of magnitude higher than in GdBCO, one potential experiment could be to use the TRIGA CIF to irradiate EuBCO and GdBCO CCs, preferably prepared without artificial pinning centres, and measure their superconducting properties periodically. If their response to TRIGA neutrons is at all effected by impurity accumulation, this may show up as differences in the character of their changing superconducting properties.

Improving the quality of the magnetometry experiment (chapter 5)

Although the magnetometry experiment (chapter 5) was sufficient to allow a decision to be made about which CC to use during the cold irradiation experiments, several improvements could have allowed it to also be a thorough examination of each CC's superconducting properties. These include:

- reducing the error in the sample diameter by removing the damaged outer circumference of REBCO using the photolithography techniques described in section 6.2.1.5
- increasing the number of m-T and m-H loop to > 10 to allow accurate fits of the irreversibility line [21], [369]–[371], equations 2-9 and 2-10 and the δT_c and δl pinning characteristics of each sample to be assessed with reference to the Thompson et al. model [372], [373]
- including relaxation experiments [86], [374]

Investigate samples using Raman Spectroscopy and / or TEM

Raman spectroscopy [375] and TEM (e.g. [269]) have been used to investigate the composition and microstructure of REBCO respectively. Given the presented differences in the responses of cold versus room temperature irradiated sample and the anomalous behaviour of sample RT2, it would be enlightening to subject these samples to either/both types of further analysis. It would also be valuable to use the same techniques to study the microstructure of the samples studied in Chapter 5 to help explain the differences in response to irradiation that were measured and predict how the next generation of CC could be designed to minimise their degradation behaviour under irradiation by fusion spectrum neutrons.

Appendices

A. Chapter 4 Supplementary Information

a. SPECTRA-PKA Example Code

Code sets SPECTRA-PKA up to analysis the irradiation of YBCO with ST135 TF neutrons

“2_ST135_spectrapka.dat”

(Note: [pwd] is shorthand for the path to the directory containing the recoil energy cross-sections)

```
flux_filename="spectra/2_ST135_spectrapka.dat"
results_stub="Z_OP_1A_25"
num_columns=6
columns= pka_filename pka_ratios parent_ele parent_num ngamma_parent_mass ngamma_daughter_mass
[pwd]/O016s.asc  0.537153 O  16 15.994914 16.999131
[pwd]/O017s.asc  0.000205 O  17 16.999131 17.999159
[pwd]/O018s.asc  0.001104 O  18 17.999159 19.003577
[pwd]/Cu063s.asc 0.159577 Cu 63 62.929597 63.929763
[pwd]/Cu065s.asc 0.071192 Cu 65 64.927789 65.928868
[pwd]/Y089s.asc  0.076923 Y  89 88.905841 89.907144
[pwd]/Ba130s.asc 0.000163 Ba 130 129.906320 130.906941
[pwd]/Ba132s.asc 0.000155 Ba 132 131.905061 132.906007
[pwd]/Ba134s.asc 0.003718 Ba 134 133.904508 134.905688
[pwd]/Ba135s.asc 0.010142 Ba 135 134.905688 135.904578
[pwd]/Ba136s.asc 0.012083 Ba 136 135.904578 136.905827
[pwd]/Ba137s.asc 0.017280 Ba 137 136.905827 137.905247
[pwd]/Ba138s.asc 0.110305 Ba 138 137.905247 138.908841
flux_norm_type=2
pka_filetype=2
do_mtd_sums=.false.
do_ngamma_estimate=.t.
do_global_sums=.t.
do_exclude_light_from_total=.t.
number_pka_files=13
flux_rescale_value=1
max_global_recoils=400
energies_once_perfile=.t.
do_tdam=.t.
assumed_ed=25.0
```

b. FISPACT-II Example Codes

FISPACT-II uses a combination of 5 files to run its simulations (files, collapse.i, condense.i, print_lib.i, inventoryYBCO.i). Following codes sets FISPACT-II up to analysis the irradiation of YBCO (defined in inventoryYBCO.i) with ST135 TF neutrons “2_ST135_TF_709_709” based on the TENDL 2017 nuclear data file.

files

```
ind_nuc       [pwd]/nuclear_data/decay/decay_2012_index_2012
xs_endf        [pwd]/nuclear_data/TENDL2017data/tal2017-n/gxs-709
prob_tab      [pwd]/nuclear_data/TENDL2017data/tal2017-n/tp-709-294
fy_endf       [pwd]/nuclear_data/GEFY61data/gefy61_nfy
sf_endf       [pwd]/nuclear_data/GEFY61data/gefy61_sfy
dk_endf       [pwd]/nuclear_data/decay/decay_2012
hazards        [pwd]/nuclear_data/decay/hazards_2012
clear          [pwd]/nuclear_data/decay/clear_2012
a2data         [pwd]/nuclear_data/decay/a2_2012
absorp        [pwd]/nuclear_data/decay/abs_2012
fluxes        2_ST135_TF_709_709 << file containing the neutron spectra in 709-format >>
collapxi      COLLAPX
collapxo       COLLAPX
arrayx        ARRAYX
```

collapse.i

```
CLOBBER
GETXS 1 709
FISPACT
* COLLAPSE tal2017-n/gxs-709 decay12 index
PRINTLIB 4
END << End of file >>
```

condense.i

```
CLOBBER
SPEK
GETDECAY 1
FISPACT
* CONDENSE dec_2012, tal2017-n/GEF61-nFY
END << End of file >>
```

print_lib.i

```
CLOBBER
GETXS 0 << read condensed data from binary ARRAYX file>>
GETDECAY 0 << End of control phase >>
FISPACT
* PRINTLIB for tal2014-n/gxs-709 dec2012/gef42 << Do a large printlib - writes decay data, collapse XS data and more!
>>
PRINTLIB  0
END << End of input >>
```

inventoryYBCO.i

```
CLOBBER << Overwrite existing inventory.log and inventory.out files >>
JSON << Enable JSON file format output for inventory data >>
GETXS 0 << Read COLLAPX files >>
GETDECAY 0 << Read ARRAYX files >>
<< End of control >>

FISPACT
* YBCO in ST135 Central Column at 0.2m radius after 1 FPY

<< Material definition - start of initialisation phase >>
DENSITY 6.376 << Density is in units of g/cm3 >>
<< Elemental definition of material >>
MASS 1.0E-3 4 << total mass = 1g, with 4 elements>>
Y   13.35 << Yttrium at 13.35wt%>>
BA 41.23 << Barium at 41.23wt%>>
CU 28.62 << Copper at 28.62wt%>>
O   16.81<< Oxygen at 16.81wt%>>

MIND 1E3 << Set the minimum number of atoms to track - 1000 atom threshold>>
GRAPH 7 2 1 1 2 3 4 5 6 7 << Produce all graph files for GNU plot for post processing >>
UNCERTAINTY 2 << Output estimates of both uncertainty and pathway analysis >>
HALF << Output half-lives to output inventory information >>
HAZARDS << Output ingestion and inhalation doses to output >>

<< -----irradiation phase----- >>
<< ATOMS= tells FISPACT-II to solve rate equations and dump output to file >>
FLUX 3.15E+13 << sets neutron flux and adjusts spectrum according>>
ATOMS
TIME 1 SECS ATOMS << progresses time 1 secs then solves rate equation >>
TIME 618 SECS ATOMS << progresses time 618s (10^-5 dpa) then solves rate equation >>
PULSE 8 << starts loop solves rate equation 8 times, 619s apart (each step 10^-5 dpa) >>
    TIME 619 SECS ATOMS
ENDPULSE
PULSE 9 << starts loop solves rate equation 9 times, 6188s apart (each step 10^-4 dpa)>>
    TIME 6188 SECS ATOMS
ENDPULSE
PULSE 9 << starts loop solves rate equation 9 times, 61878s apart (each step 10^-3 dpa)>>
    TIME 61878 SECS ATOMS
ENDPULSE
PULSE 9<< starts loop solves rate equation 9 times, 618776s apart (each step 10^-2 dpa)>>
    TIME 618776 SECS ATOMS
ENDPULSE
<< -----cooling phase----- >>
FLUX 0. << Set flux to 0 to tell F-II that no irradiation is occuring and it is decay only >>
ZERO << sets time back to zero at start of cooling phase >>
TIME    1 ATOMS << advances 1s then solves rate equation >>
TIME    9 ATOMS << advances 9s then solves rate equation >>
TIME    90 ATOMS << advances 90s then solves rate equation >>
TIME    900 ATOMS <<…>>
TIME    9000 ATOMS <<…>>
TIME    90000 ATOMS <<…>>
TIME    900000 ATOMS <<…>>
TIME    9000000 ATOMS <<…>>
TIME    90000000 ATOMS <<…>>
TIME    900000000 ATOMS <<…>>
TIME    9000000000 ATOMS <<…>>
TIME    90000000000 ATOMS <<…>>
TIME    900000000000 ATOMS <<…>>
END << End of file >>
```

c. All SPECTRA-PKA Output

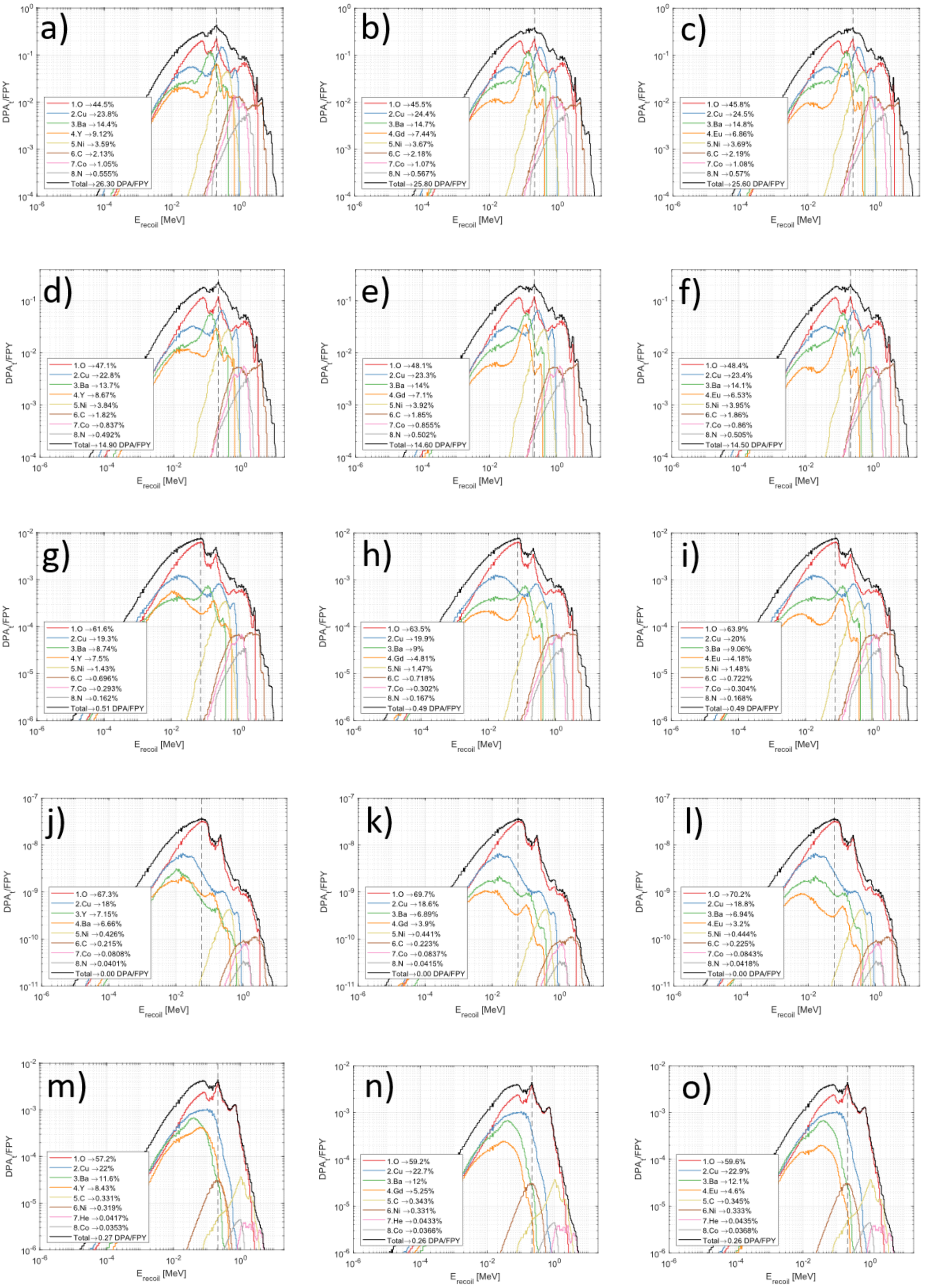

Figure S4-1: SPECTRA-PKA output for YBCO (a, d, g, j, m), GdBCO (b, e, h, k, n) and EuBCO (c, f, i, l, o) due to neutrons from ST135 FW (a, b, c), DEMO FW(d, e, f), ST135 TF (g, h, i), DEMO TF (j, k, l) and TRIGA CIF (m, n, o)

d. All FISPACT-II Output

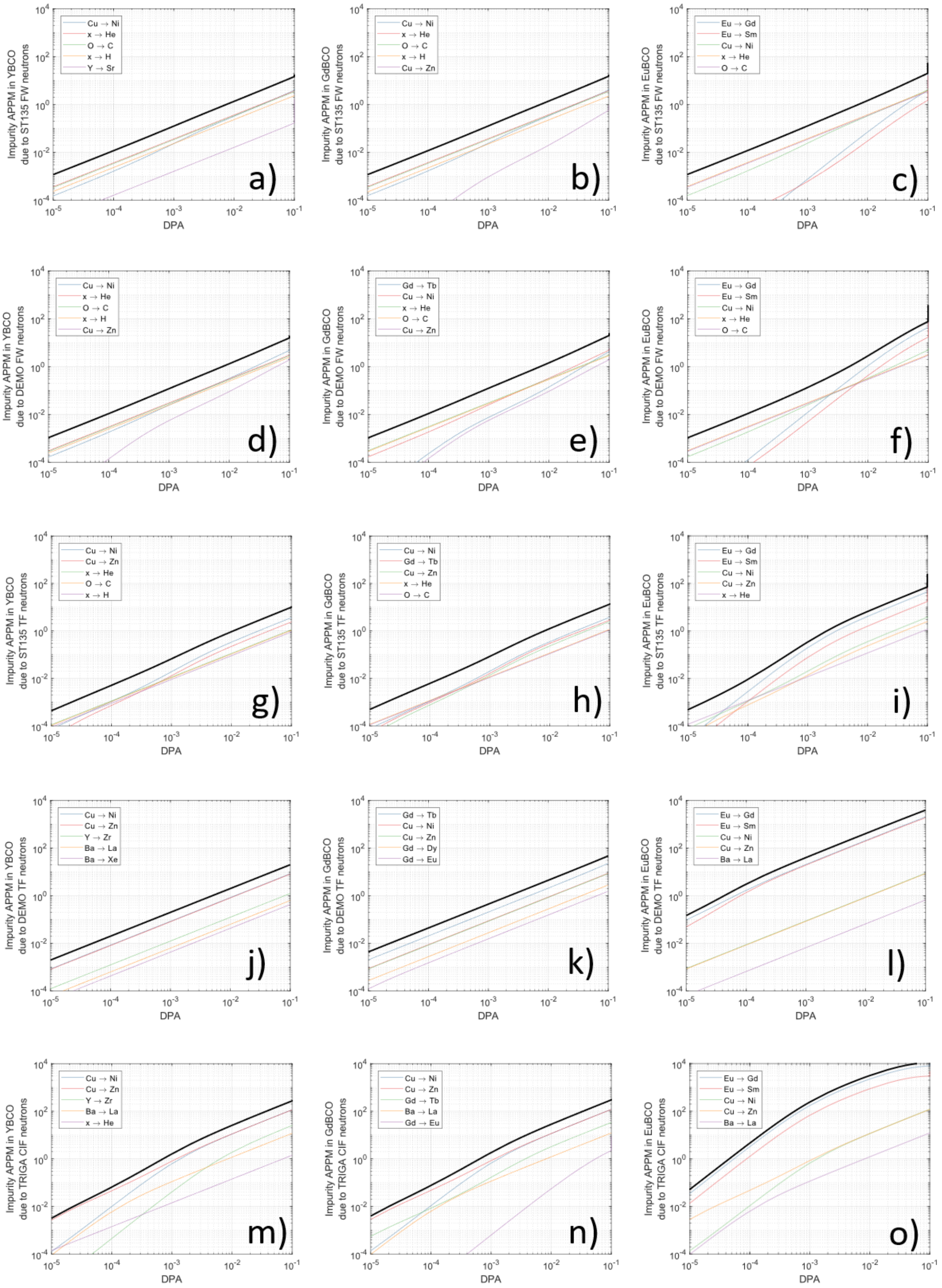

Figure S4-2: FISPACT-II output for YBCO (a, d, g, j, m), GdBCO (b, e, h, k, n) and EuBCO (c, f, i, l, o) due to neutrons from ST135 FW (a, b, c), DEMO FW(d, e, f), ST135 TF (g, h, i), DEMO TF (j, k, l) and TRIGA CIF (m, n, o)

B. Chapter 5 Supplementary Information

a. Bruker 2018

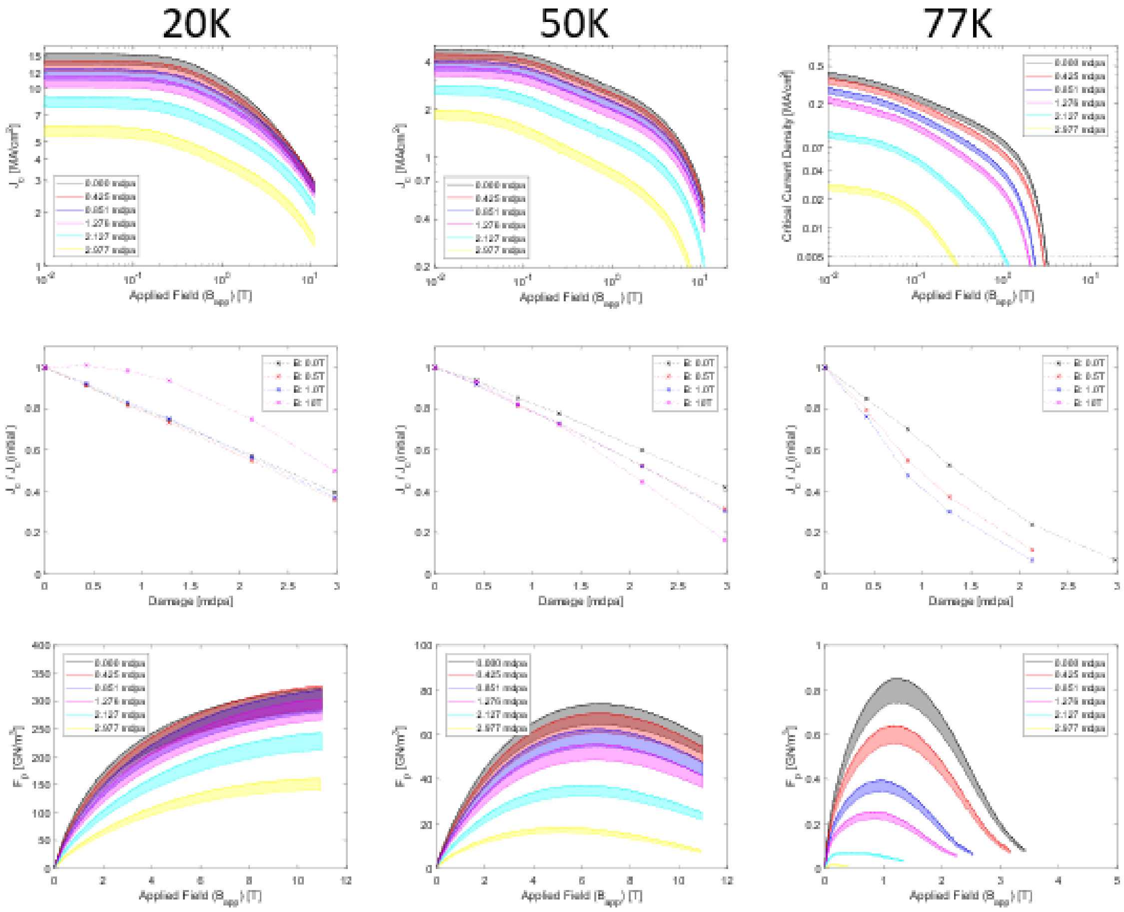

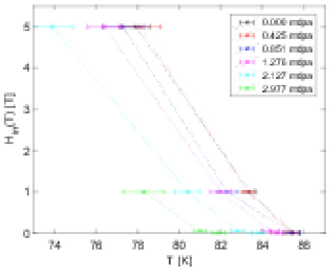

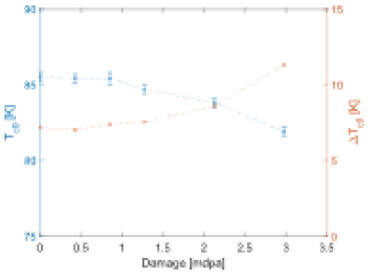

b. STI 2017

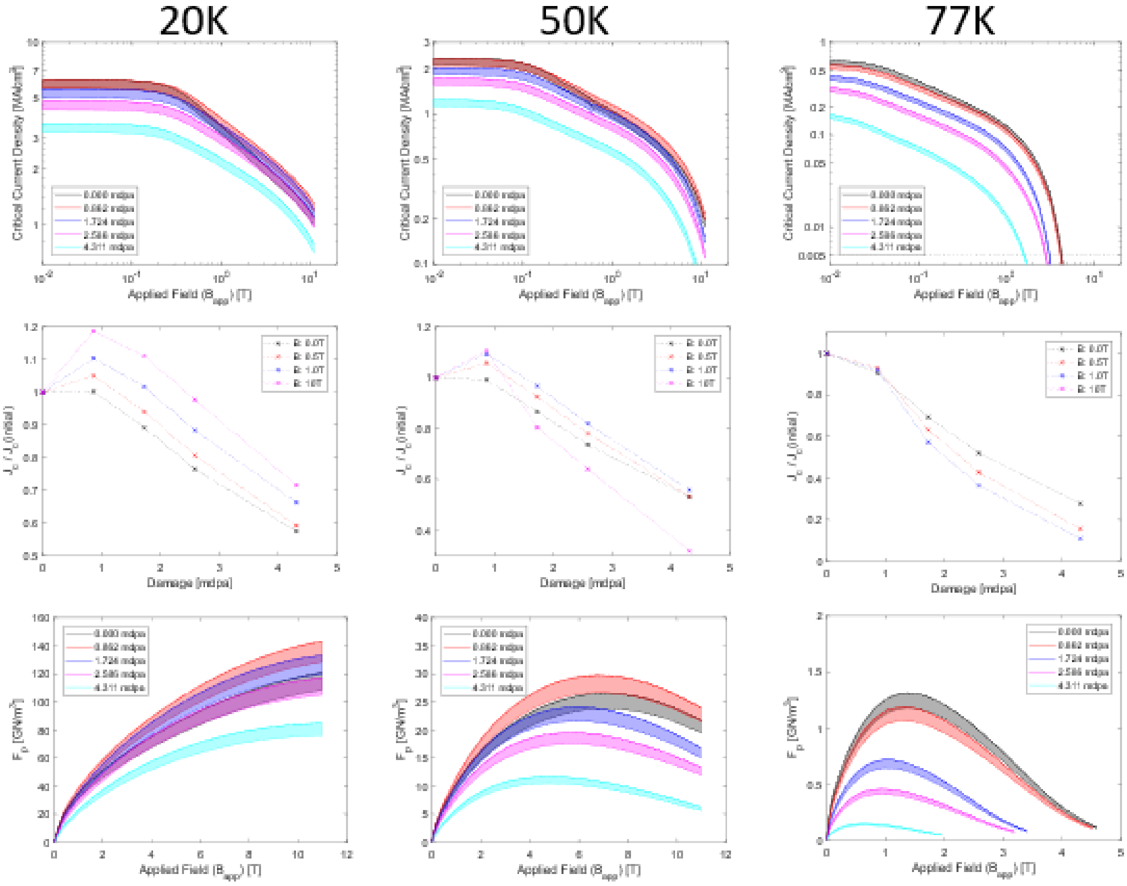
20K
50K
77K
Critical Current Density [MA/m²]
Applied Field (B_app) [T]
0.000 mdpa
0.862 mdpa
1.724 mdpa
2.586 mdpa
4.311 mdpa
J_c / J_c(initial)
Damage [mdpa]
B: 0.0T
B: 0.5T
B: 1.0T
B: 10T
F_p [GN/m³]
Applied Field (B_app) [T]

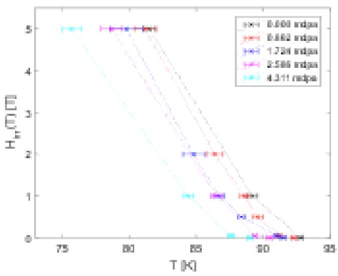
H_irr(T) [T]
T [K]
0.000 mdpa
0.862 mdpa
1.724 mdpa
2.586 mdpa
4.311 mdpa

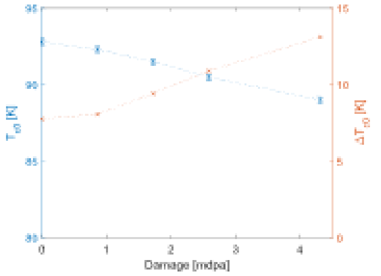
T_c0 [K]
ΔT_c0 [K]
Damage [mdpa]

c. Fujikura 2018

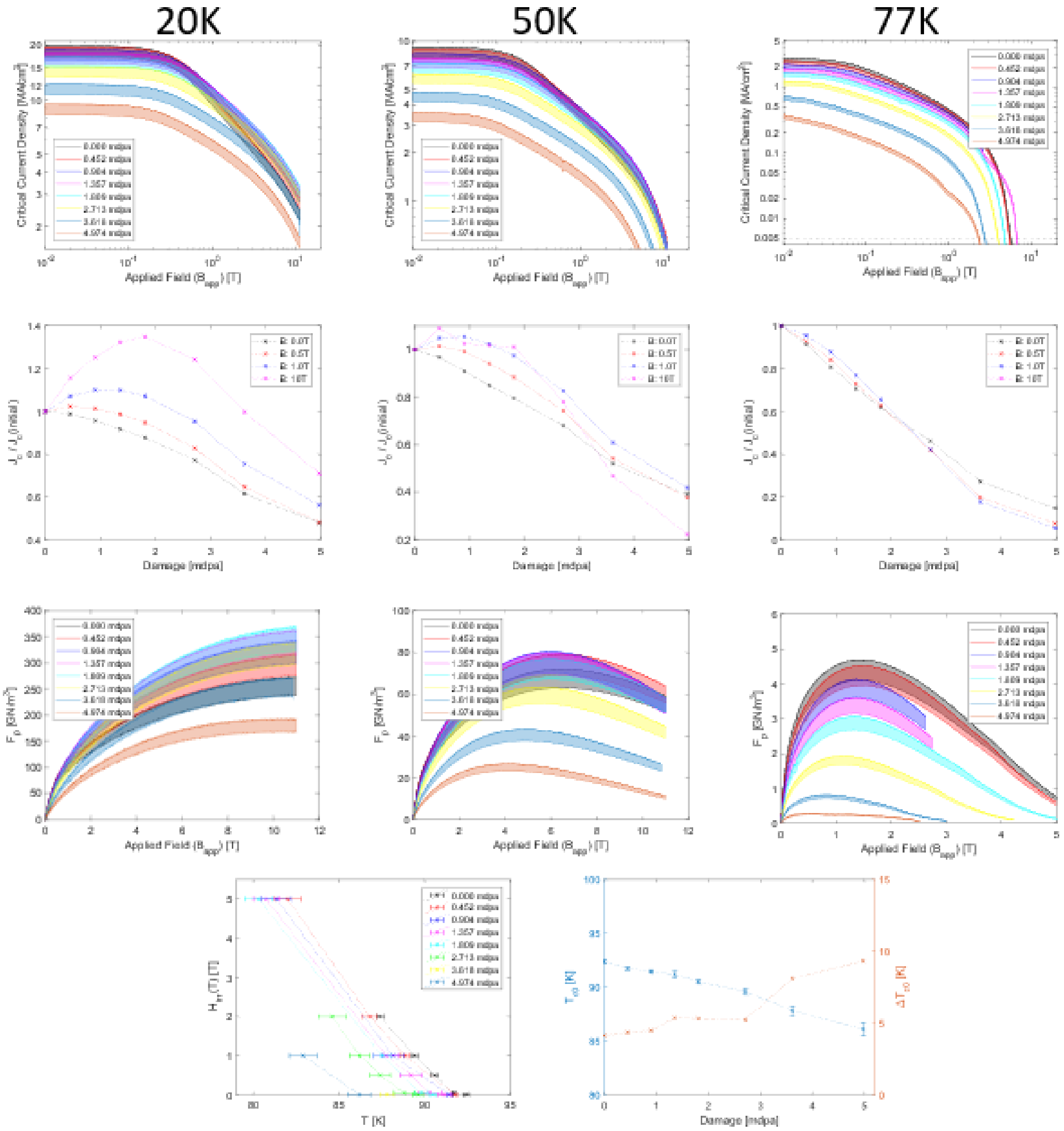

d. Shanghai Superconductor 2019 GdBCO

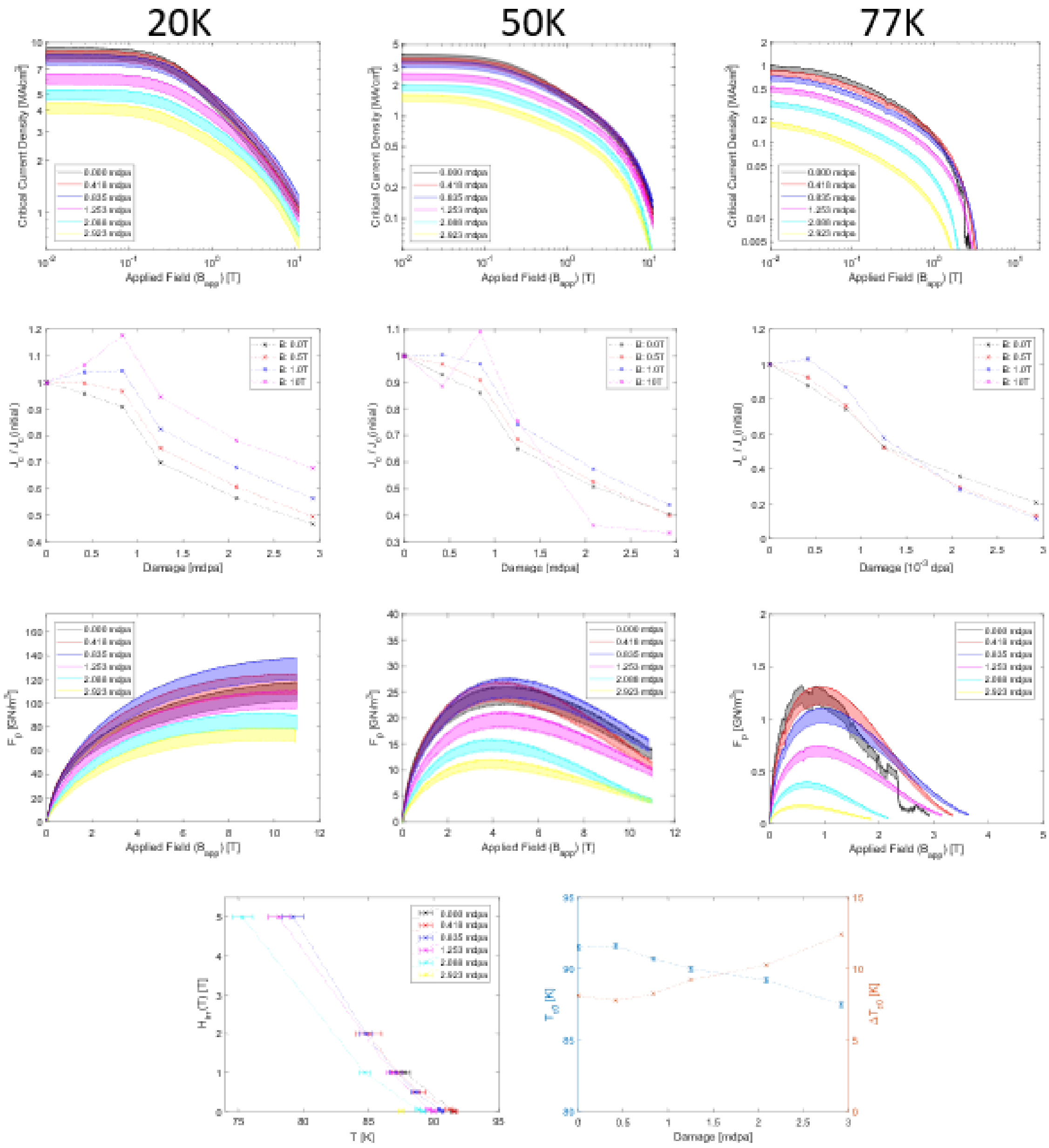

e. Shanghai Superconductor 2019 EuBCO

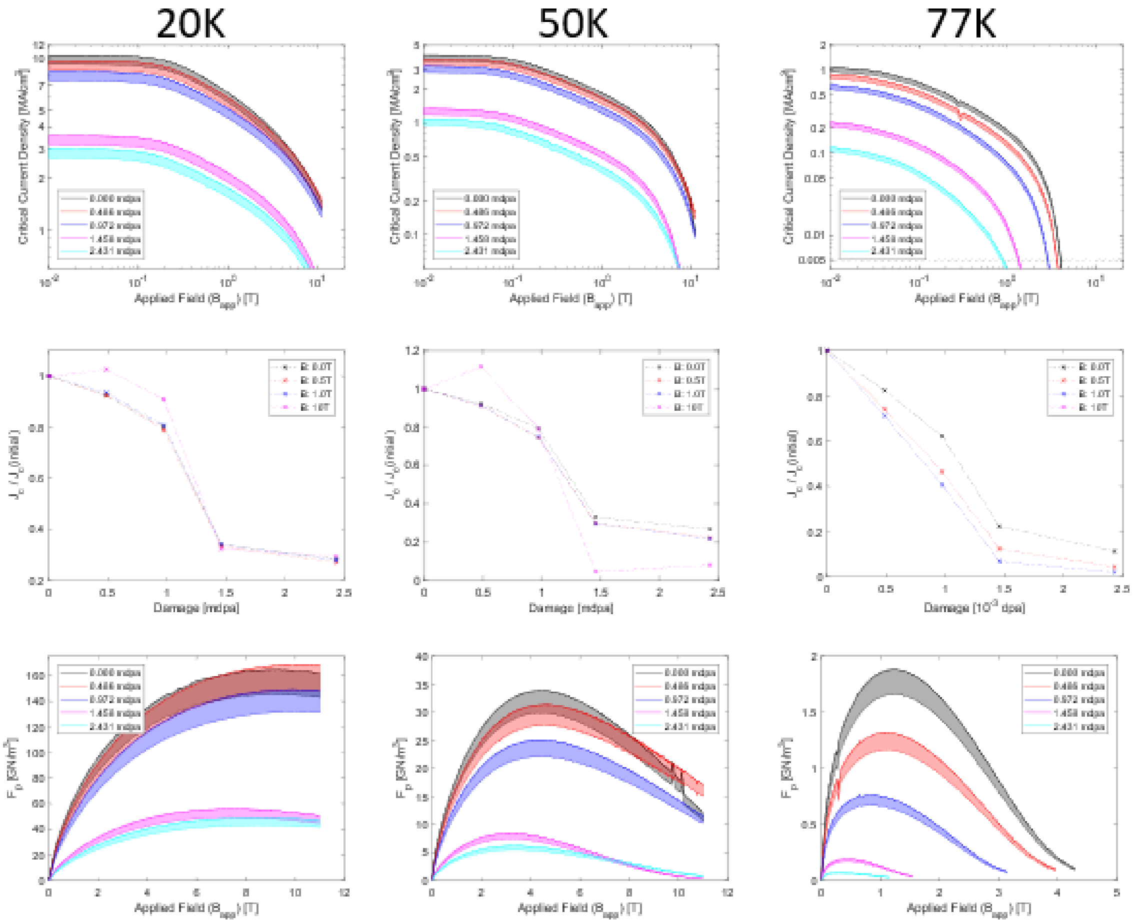

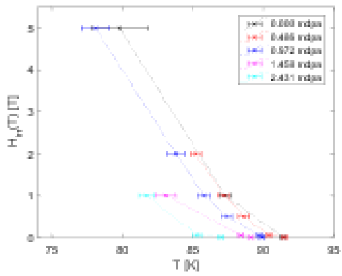

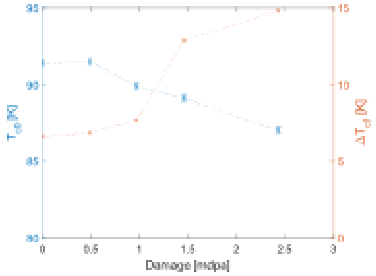

f. SuperPower 2011

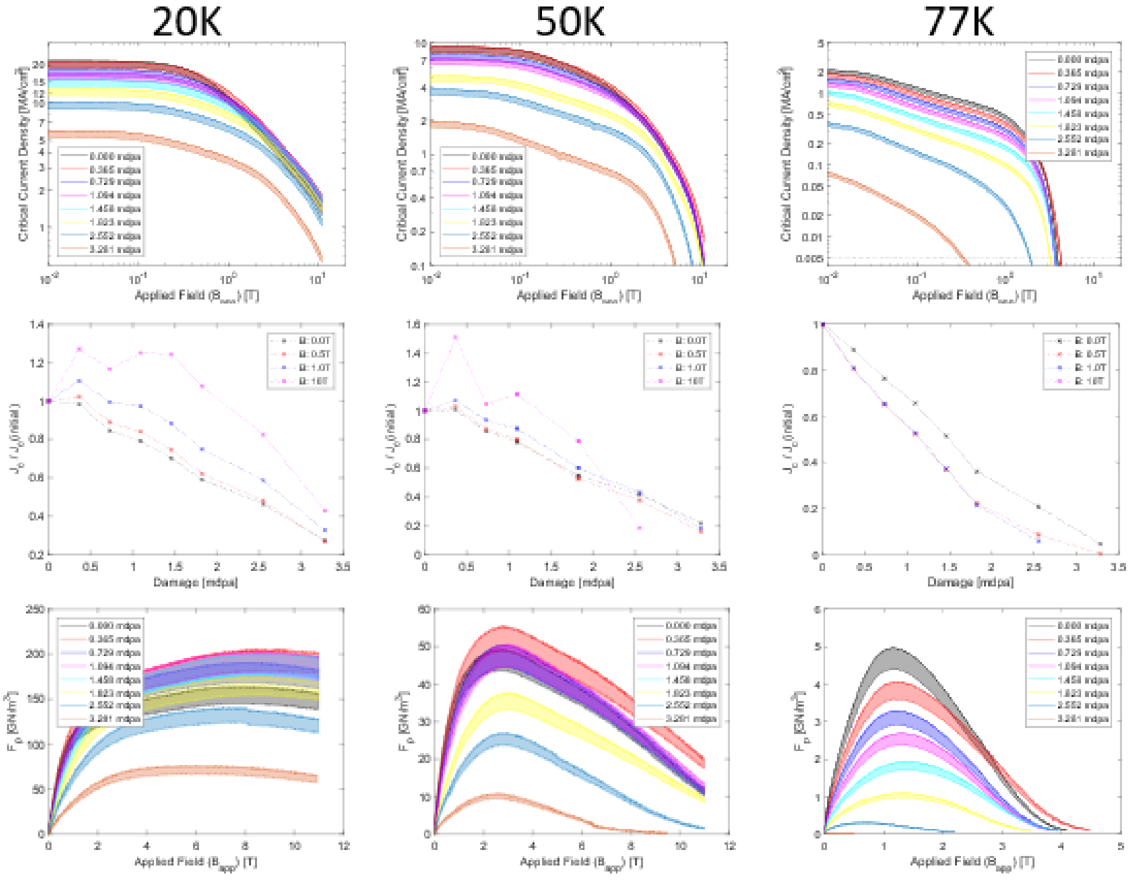

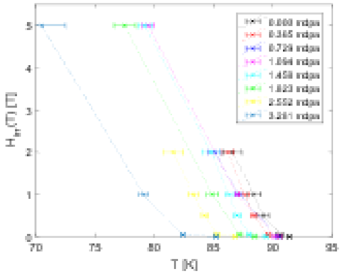

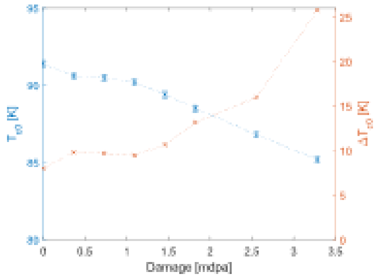

g. SuperPower 2017

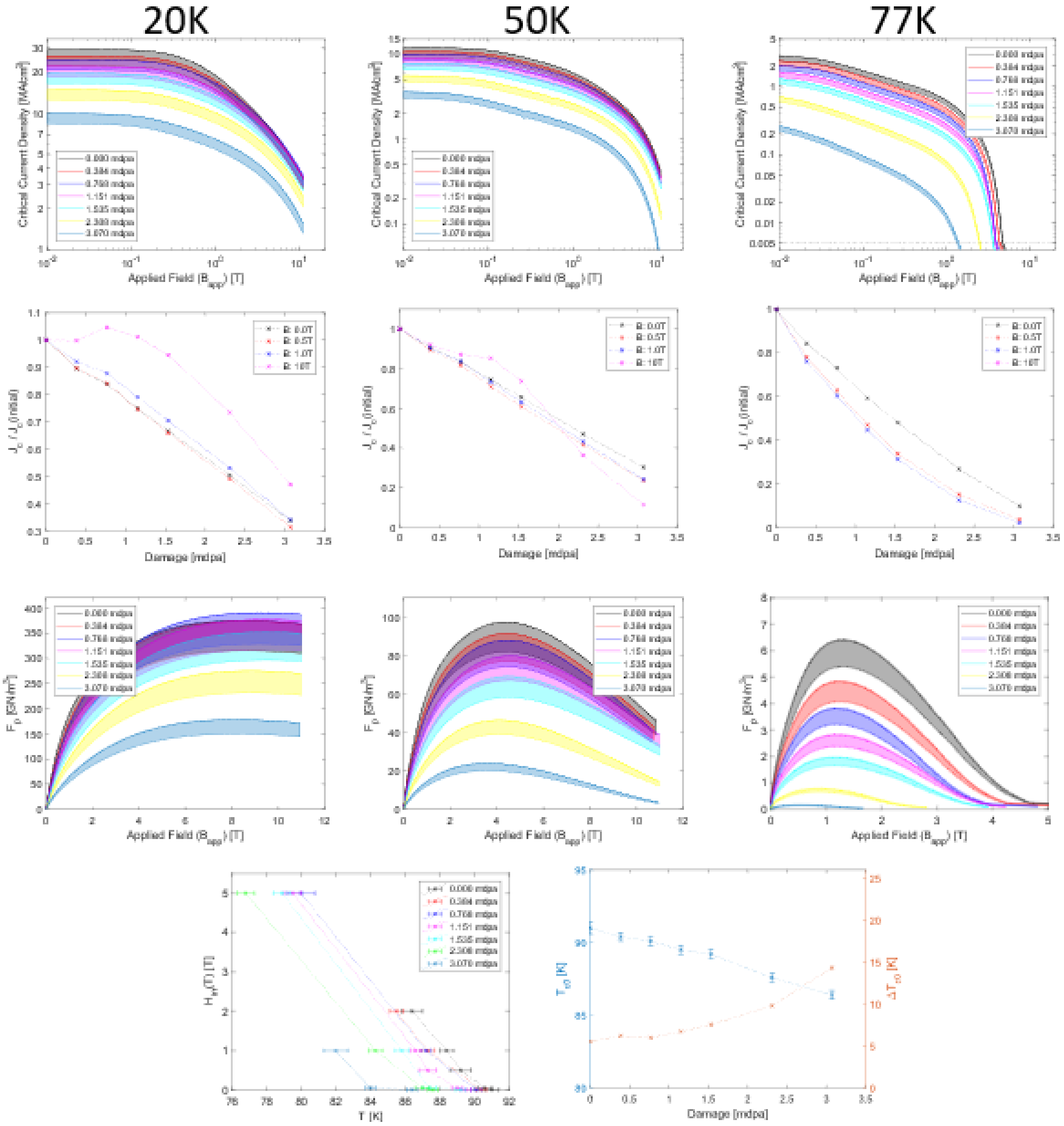

h. Coated Conductor Cross Sections

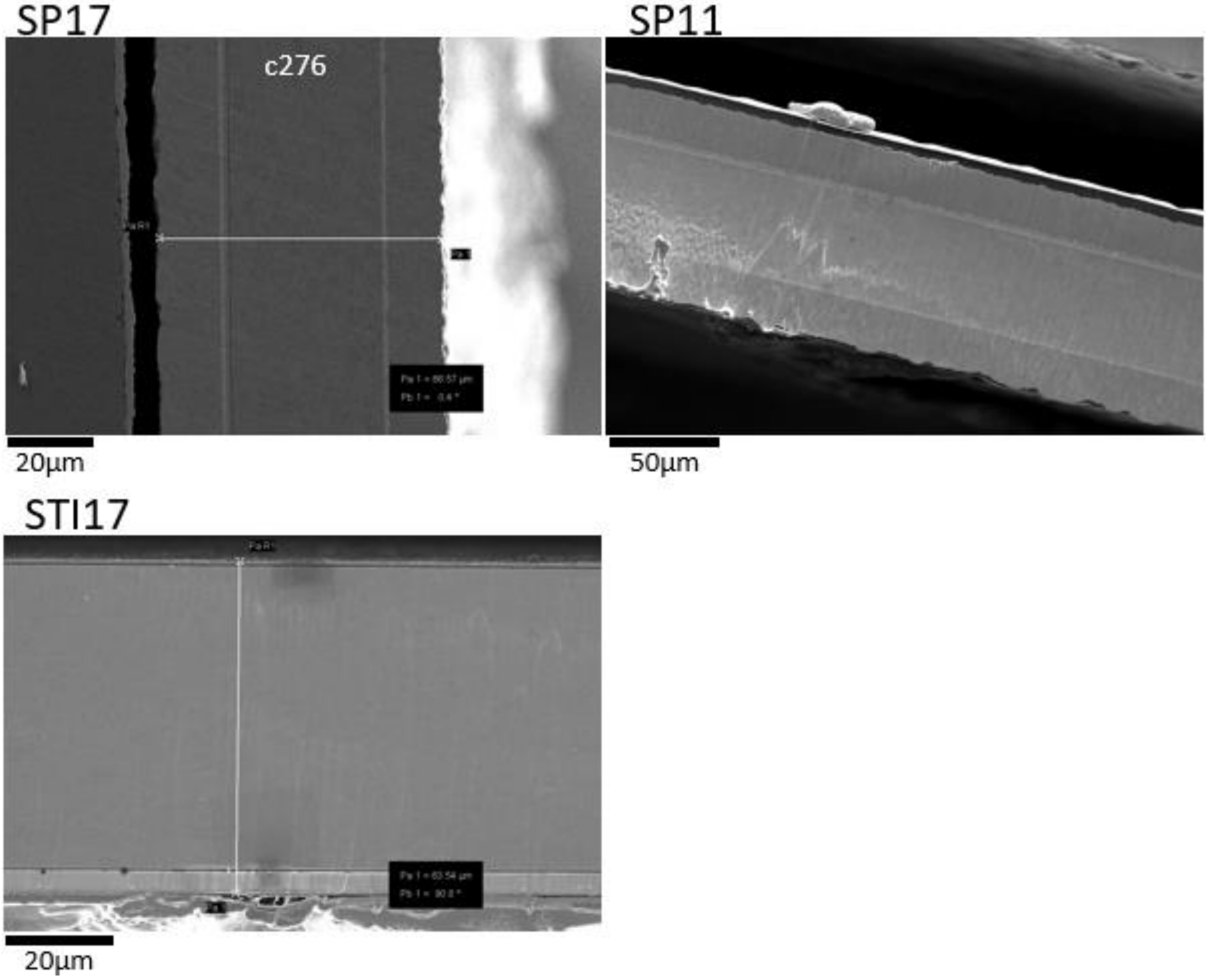

Figure S5-1: Cross Sections of 3 different CC

C. Chapter 6 Supplementary Information

Table S6-1: Copper Integrated Material Properties [350]

Temperature Range [K]	$\overline{\rho}$ [nΩm]	$\overline{k}$ [W/mK]	$\overline{c_p}$ [J/gK]
300K	16.8	397.0	0.3636
300 → 80K	10.5	422.2	0.3267
300 → 20K	8.47	597.0	0.2766
300 → 4K	8.02	655.8	0.2617
80 → 20K	0.84	1238.2	0.09267
80 → 4K	0.71	1332.3	0.07365

Temperature Integrated parameter calculated using: $\overline{A} = \frac{1}{T_H - T_L}\int_{T_L}^{T_H} A(T)dT$

D. Chapter 7 Supplementary Information

Table S7-1: Irradiation Schedule for Room Temperature samples. Circle numbers denote the irradiation detailed in Table S7-2

Sample	Irradiation Number					Total Doses
	1st	2nd	3rd	4th	5th	
RT1	①	②	③	④	⑤	9
RT2						
RT3	⑥	⑦	Ⓐ			4
RT4		⑦⑧	Ⓐ			5
RT5	⑨⑩	⑪	Ⓐ			5
RT6	⑨		Ⓐ			4

Ⓐ: Room Temperature Anneal

Table S7-2: Details of each irradiation applied to the ex-situ samples (for sample specific information).

Irradiation No.	Date	Dose[1]	Time [s]	Dose Rate Error[2]
①	22/11/20	1	705	+2.13%
②	28/11/20	1	704	+2.27%
③	06/12/20	1	737	-2.31%
④	22/01/21	3	2154	+0.28%
⑤	08/03/21	3	2148	+0.56%
⑥	15/03/21	2	1429	+0.77%
⑦	20/04/21	2	1444	-0.28%
⑧		1	725	-0.69%
⑨	30/04/21	1	730	-1.37%
⑩		1	712	+1.12%
⑪	14/06/21	3	2114	+2.13%

1: Fluence = Dose x $4.2\text{x}10^{14}$ He/cm^2 and dpa = Dose x 0.455mdpa

2: Compared to $4.2\text{x}10^{14}$ He/cm^2 in 12 minutes ($5.83\text{x}10^{11}$ He/cm^2/s)

Bibliography

[1] A. Grübler, M. Jefferson, and Nakicenovic, "Global energy perspectives: A summary of the joint study by IIASA and World Energy Council," *Technol. Forecast. Soc. Chang.*, vol. 51, no. 3, pp. 237–264, 1996.

[2] "Kyoto Protocol to the United Nations Framework Convention on Climate Change." [Online]. Available: http://unfccc.int/resource/docs/convkp/kpeng.pdf. [Accessed: 28-Jan-2021].

[3] McKinsey Energy Insights, "Global Energy Perspective 2019 : Reference Case," *Energy Insights by McKinsey & Company*, 2019. [Online]. Available: https://www.mckinsey.com/industries/oil-and-gas/our-insights/global-energy-perspective-2019. [Accessed: 28-Jan-2021].

[4] Masson-Delmotte and I. Team, "Summary for Policymakers. In: Global Warming of 1.5°C. An IPCC Special Report on the impacts of global warming of 1.5°C above pre-industrial levels and related global greenhouse gas emission pathways, in the context of strengthening the global response to," 2018. [Online]. Available: https://www.ipcc.ch/site/assets/uploads/sites/2/2019/05/SR15_SPM_version_report_LR.pdf . [Accessed: 28-Jan-2021].

[5] J. P. Freidberg, *Plasma Physics and Fusion Energy*, 1st ed. Cambridge University Press, 2007.

[6] J. P. Freidberg, F. J. Mangiarotti, and J. Minervini, "Designing a tokamak fusion reactor - How does plasma physics fit in?," *Phys. Plasmas*, 2015.

[7] "EFDA EUROfusion Website." [Online]. Available: www.euro-fusion.org. [Accessed: 08-May-2018].

[8] J. Barber, J. Brisson, and J. Minervini, "Forced flow cooling of high field, REBCO-based, fusion magnets using supercritical hydrogen, helium, and neon," *Cryogenics (Guildf).*, vol. 96, no. February, pp. 34–43, 2018.

[9] M. Soell and M. Van Der Klein, "The influence of low temperature neutron irradiation on superconducting magnet systems for fusion reactors," *IEEE Trans. Magn.*, vol. MAG-11, no. 2, pp. 178–181, 1975.

[10] A. Umezawa *et al.*, "Enhanced critical magnetization currents due to fast neutron irradiation in single-crystal YBa2Cu3O7-," *Phys. Rev. B*, vol. 36, no. 13, pp. 7151–7154, 1987.

[11] A. E. Costley, J. Hugill, and P. F. Buxton, "On the power and size of tokamak fusion power plants and reactors," *Nucl. Fusion*, vol. 033001, p. 33001, 2015.

[12] M. Kovari, R. Kemp, H. Lux, P. Knight, J. Morris, and D. J. Ward, "PROCESS: A systems code for fusion power plants - Part 1: Physics," *Fusion Eng. Des.*, vol. 89, no. 12, pp. 3054–3069, 2014.

[13] M. Kovari *et al.*, "PROCESS: A systems code for fusion power plants - Part 2: Engineering," *Fusion Eng. Des.*, vol. 104, pp. 9–20, 2016.

[14] Z. Dragojlovic *et al.*, "An advanced computational algorithm for systems analysis of tokamak power plants," *Fusion Eng. Des.*, vol. 85, no. 2, pp. 243–265, 2010.

[15] M. Coleman and S. McIntosh, "BLUEPRINT: A novel approach to fusion reactor design," *Fusion Eng. Des.*, vol. 139, no. December 2018, pp. 26–38, 2019.

[16] M. R. Gilbert, S. Zheng, R. Kemp, L. W. Packer, S. L. Dudarev, and J. C. H. Sublet, "Comparative assessment of material performance in demo fusion reactors," *Fusion Sci. Technol.*, vol. 66, no. 1, pp. 9–17, 2014.

[17] "Robinson Research Institute: High Temperature superconducting wire critical current database," 2019. [Online]. Available: http://htsdb.wimbush.eu/. [Accessed: 12-Oct-2020].

[18] Y. Zhang, M. W. Rupich, V. Solovyov, Q. Li, and A. Goyal, "Dynamic behavior of reversible oxygen migration in irradiated-annealed high temperature superconducting wires," *Sci. Rep.*, vol. 10, no. 1, pp. 1–8, 2020.

[19] J. L. MacManus-Driscoll and S. C. Wimbush, "Processing and application of high-temperature superconducting coated conductors," *Nat. Rev. Mater.*, vol. 6, no. 7, pp. 587–604, 2021.

[20] K. Nordlund and F. Djurabekova, "Multiscale modelling of irradiation in nanostructures," *J. Comput. Electron.*, vol. 13, no. 1, pp. 122–141, 2014.

[21] D. X. Fischer, R. Prokopec, J. Emhofer, and M. Eisterer, "The effect of fast neutron irradiation on the superconducting properties of REBCO coated conductors with and without artificial pinning centers," *Supercond. Sci. Technol.*, vol. 31, no. 4, p. 44006, 2018.

[22] M. L. E. Oliphant, E. S. Shire, and B. M. Crowther, "Separation of the Isotopes of Lithium and Some Nuclear Transformations Observed with them," *Proc. R. Soc. London A.*, vol. 146, no. 859, pp. 922–929, 1934.

[23] P. E. Stott, "The feasibility of using D-3He and D-D fusion fuels," *Plasma Phys. Control. Fusion*, vol. 47, no. 8, pp. 1305–1338, 2005.

[24] E. A. Azizov, "Tokamaks: from A D Sakharov to the present (the 60-year history of tokamaks)," *Physics-Uspekhi*, vol. 55, no. 2, pp. 190–203, 2012.

[25] J. D. Lawson, "Some Criteria for a Power Producing Thermonuclear Reactor," *Proc. Phys. Soc.*, vol. B70, pp. 5–10, 1957.

[26] X. Z. Li, Q. M. Wei, and B. Liu, "A new simple formula for fusion cross-sections of light nuclei," *Nucl. Fusion*, vol. 125003, p. 5, 2008.

[27] B. N. Sorbom *et al.*, "ARC: A compact, high-field, fusion nuclear science facility and demonstration power plant with demountable magnets," *Fusion Eng. Des.*, vol. 100, pp. 378–405, 2015.

[28] G. Federici *et al.*, "Overview of EU DEMO design and R&D activities," *Fusion Eng. Des.*, vol. 89, no. 7–8, pp. 882–889, 2014.

[29] J. E. Menard, T. Brown, and M. Boyer, "Fusion Nuclear Science Facilities and Pilot Plants Based on the Spherical Tokamak," *Nucl. Fusion*, vol. 56, pp. 1–97, 2016.

[30] R. Betti *et al.*, "Thermonuclear ignition in inertial confinement fusion and comparison with magnetic confinement," *Phys. Plasmas*, vol. 17, no. 5, 2010.

[31] "Royal Society Conference: Fusion energy using tokamaks: can development be accelerated?" [Online]. Available: www.royalsociety.org/science-events-and-lectures. [Accessed: 08-May-2018].

[32] D. Jassby, "ITER is a showcase... for the drawbacks of fusion energy," *Bulletin of the Atomic Scientistis*, 2018. [Online]. Available: https://thebulletin.org/2018/02/iter-is-a-showcase-for-the-drawbacks-of-fusion-energy/. [Accessed: 15-Dec-2020].

[33] D. Jassby, "Fusion reactors: Not what they're cracked up to be," *Bulletin of the Atomic Scientistis*, 2017. [Online]. Available: https://thebulletin.org/2017/04/fusion-reactors-not-what-theyre-cracked-up-to-be/. [Accessed: 15-Dec-2020].

[34] C. C. Petty, J. C. Deboo, R. J. La Haye, T. C. Luce, P. A. Politzer, and C. P. C. Wong, “Feasibility study of a compact ignition tokamak based upon gyroBohm scaling physics,” *Fusion Sci. Technol.*, vol. 43, no. 1, pp. 1–17, 2002.

[35] M. Shimada *et al.*, “Chapter 1 : Overview and summary,” *Nucl. Fusion*, vol. 47, pp. S1–S17, 2007.

[36] J. Trefil, *Encyclopedia of Physical Science and TEchnology*, 3rd ed. Routledge, 2001.

[37] W. Biel, M. Beckers, R. Kemp, R. Wenninger, and H. Zohm, “Systems code studies on the optimization of design parameters for a pulsed DEMO tokamak reactor,” *Fusion Eng. Des.*, vol. 123, pp. 206–211, 2017.

[38] A. Sykes *et al.*, “Compact fusion energy based on the spherical tokamak,” *Nucl. Fusion*, vol. 58, no. 1, 2018.

[39] C. G. Windsor and G. Morgan, “Private Communication.” 2019.

[40] R. Prokopec, D. X. Fischer, H. W. Weber, and M. Eisterer, “Suitability of coated conductors for fusion magnets in view of their radiation response,” *Supercond. Sci. Technol.*, vol. 28, no. 1, p. 014005, 2015.

[41] L. Ballabio, “Calculation and Measuremnt of the neutron emission spectrum due to thermonuclear and higher order reactions in tokamak plasmas,” Uppsala, Sweden, 2003.

[42] J. T. Goorley *et al.*, “Initial MCNP6 Release Overview - MCNP6 version 1.0,” 2013.

[43] H. W. Weber, H. Böck, E. Unfried, and L. R. Greenwood, “Neutron dosimetry and damage calculations for the TRIGA MARK-II reactor in Vienna,” *J. Nucl. Mater.*, vol. 137, no. 3, pp. 236–240, 1986.

[44] M. R. Gilbert, T. Eade, C. Bachmann, U. Fischer, and N. P. Taylor, “Activation, decay heat, and waste classification studies of the European DEMO concept,” *Nucl. Fusion*, vol. 57, no. 4, 2017.

[45] J. G. Bednorz and K. A. Müller, “Possible High T c Superconductivity in the Ba — La — Cu — O System,” *Zeitschrift fur Phys. B - Condens. Matter*, vol. 64, pp. 189–193, 1986.

[46] J. Muller, “A15-type superconductors,” *Reports Prog. Phys.*, vol. 43, p. 641, 1980.

[47] C. W. Chu, P. H. Hor, R. L. Meng, L. Gao, Z. J. Huang, and Y. Q. Wang, “Evidence for Superconductivity above 40K in La-Ba-Cu-O Compound Sytem,” *Phys. Rev. Lett.*, vol. 58, no. 4, p. 405, 1987.

[48] M. K. Wu *et al.*, “Superconductivity at 93 K in a new mixed-phase Y-Ba-Cu-O compound system at ambient pressure,” *Phys. Rev. Lett.*, vol. 58, no. 9, pp. 908–910, 1987.

[49] D. G. Hinks *et al.*, “Phase diagram and superconductivity in the Y-Ba-Cu-O system,” *Appl. Phys. Lett.*, vol. 50, no. 23, pp. 1688–1690, 1987.

[50] A. I. Golovashkin *et al.*, “Low temperature measurements of Hc2 in HTSC using megagauss magnetic fields,” *Phys. B Phys. Condens. Matter*, vol. 177, no. 1–4, pp. 105–108, 1992.

[51] S. I. Bondarenko, V. P. Koverya, A. V. Krevsun, and S. I. Link, “High-temperature superconductors of the family (RE)Ba2Cu3O7-δ and their application (Review Article),” *Low Temp. Phys.*, vol. 43, no. 10, pp. 1125–1151, 2017.

[52] H. Maeda, Y. Tanaka, M. Fukutomi, and T. Asano, “A New High-T c Oxide Superconductor without a Rare Earth Element,” *Jpn. J. Appl. Phys.*, vol. 27, p. L209, 1988.

[53] J. Nagamatsu, N. Nakagawa, T. Muranaka, Y. Zenitani, and J. Akimitsu, “Superconductivity at 39 K in magnesium diboride,” *Nature*, vol. 410, no. 6824, pp. 63–64, 2001.

[54] V. Braccini *et al.*, “High-field superconductivity in alloyed MgB 2 thin films,” *Phys. Rev. B - Condens. Matter Mater. Phys.*, vol. 71, no. 1, pp. 24–27, 2005.

[55] G. Biswal and K. L. Mohanta, “A recent review on iron-based superconductor,” *Mater. Today Proc.*, vol. 35, pp. 207–215, 2021.

[56] “Tokamak Energy,” 2021. [Online]. Available: https://www.tokamakenergy.co.uk/. [Accessed: 08-Mar-2021].

[57] W. Meissner and R. Ochsenfeld, “Ein neuer Effekt bei Eintritt der Supraleitfahigkeit,” *Naturwissenschaften*, vol. 21, no. 44, pp. 787–788, 1933.

[58] Onnes, “No Title,” *Commun. Phys Lab. Univ Leden Suppl.*, vol. 29, 1911.

[59] D. Van Delft and P. Kes, “The discovery of superconductivity,” *Physics Today*, pp. 38–43, Sep-2010.

[60] H. Ibach and H. Luth, *Solid-State Physics: An Introduction to Principles of Materials Science*, 4th ed. Springer, 2009.

[61] C. P. Poole, H. A. Farach, R. J. Creswick, and R. Prozorov, *Superconductivity*, 2nd ed. Elsevier Ltd, 2007.

[62] N. Phillips, “Heat Capacity of Aluminum between 0.1K and 4K,” *Phys. Rev.*, vol. 114, pp. 676–685, 1959.

[63] P. J. Hoffman, “Superconductivity in Cuprates,” 2010. [Online]. Available: http://hoffman.physics.harvard.edu/materials/SCintro.php. [Accessed: 10-May-2018].

[64] F. London and H. London, “Electrodynamics of Macroscopic Fields in Supraconductors,” *Nature*, vol. 137, pp. 991–992, 1936.

[65] V. L. Ginzburg, “On the theory of superconductivity,” *Nuovo Cim. Ser. 10*, vol. 2, no. 6, pp. 1234–1250, 1955.

[66] A. A. Abrikosov, “On the Magnetic Properties of Superconductors of the Second Group,” *Sov. Phys. JETP*, vol. 5, no. 6, pp. 1174–1182, 1957.

[67] A. A. Abrikosov, “Nobel Lecture: Type-II superconductors and the vortex lattice,” *Rev. Mod. Phys.*, vol. 76, no. 3 I, pp. 975–979, 2004.

[68] J. Bardeen, L. Cooper, and J. Schrieffer, “Theory of superconductivity,” *Phys. Rev.*, vol. 108, no. 5, 1956.

[69] P. Townsend and J. Sutton, “Investigation by Electron tunneling of the Superconducting Energy Gaps in Nb, Ta, Sn and Pb,” *Phys. Rev.*, vol. 128, no. 2, pp. 591–595, 1962.

[70] B. S. Deaver and W. M. Fairbank, “Experimental evidence for quantized flux in superconducting cyclinders,” *Phys. Rev. Lett.*, vol. 7, no. 2, pp. 43–46, 1961.

[71] A. K. Jha and K. Matsumoto, “Superconductive REBCO thin films and their nanocomposites: The role of rare-earth oxides in promoting sustainable energy,” *Front. Phys.*, vol. 7, no. JUN, pp. 1–21, 2019.

[72] D. Dew-Hughes, “Flux pinning mechanisms in type II superconductors,” *Philos. Mag.*, vol. 30, no. 2, pp. 293–305, 1974.

[73] D. R. Strachan, M. C. Sullivan, and C. J. Lobb, “Probing the limits of superconductivity,” in *International Society of Optical Engineering*, 2002, no. July.

[74] D. S. Fisher, B. Laboratories, and D. A. Huse, “Thermal Qcutuations, quenched disorder, phase transitions, and transport in type-II superconductors,” *Phys. Rev. B*, vol. 43, no. 1, p. 130, 1991.

[75] V. M. Vinokur, M. V. Feigelman, V. B. Geshkenbein, and A. I. Larkin, “Resistivity of High-Tc Superconductors in a Vortex-Liquid State,” *Phys. Rev. Lett.*, vol. 65, no. 2, pp. 259–262, 1990.

[76] P. L. Gammel, L. F. Schneemeyer, J. V. Wasczak, and D. J. Bishop, “Evidence from mechanical measurements for flux-lattice melting in single-crystal YBa2Cu3O7 and Bi2.2Sr2Ca0.8Cu2O8,” *Phys. Rev. Lett.*, vol. 61, no. 14, pp. 1666–1669, 1988.

[77] A. B. Pippard, “An experimental and theoretical study of the relation between magnetic field and current in a superconductor,” *Proc. R. Soc. London. Ser. A. Math. Phys. Sci.*, vol. 216, no. 1127, pp. 547–568, 1953.

[78] D. Dew-Hughes, “The critical current of superconductors: An historical review,” *Low Temp. Phys.*, vol. 27, no. 9–10, pp. 713–722, 2001.

[79] G. Zerweck, “On pinning of superconducting flux lines by grain boundaries,” *J. Low Temp. Phys.*, vol. 42, no. 1–2, pp. 1–9, 1981.

[80] A. I. Larkin and Y. N. Ovchinnikov, “Pinning in type II superconductors,” *J. Low Temp. Phys.*, vol. 34, no. 3–4, pp. 409–428, 1979.

[81] P. Berghuis *et al.*, “Current-Voltage measurements sa a probe of the activation barriers for flux creep in thin films of YBCO,” *Phys. C*, vol. 256, pp. 13–32, 1996.

[82] E. F. Talantsev, “On the fundamental definition of critical current in superconductors.” [Online]. Available: https://arxiv.org/abs/1707.07395. [Accessed: 23-Aug-2021].

[83] N. M. Strickland, C. Hoffmann, and S. C. Wimbush, “A 1 kA-class cryogen-free critical current characterization system for superconducting coated conductors,” *Rev. Sci. Instrum.*, vol. 85, no. 11, 2014.

[84] S. C. Wimbush and N. M. Strickland, “A Public Database of High-Temperature Superconductor Critical Current Data,” *IEEE Trans. Appl. Supercond.*, vol. 27, no. 4, pp. 10–14, 2017.

[85] J. W. Ekin, *Heat Transfer at Cryogenic Temperatures*. Oxford: Oxford University Press, 2006.

[86] Y. Yeshurun, a. Malozemoff, and a. Shaulov, “Magnetic relaxation in high-temperature superconductors,” *Rev. Mod. Phys.*, vol. 68, no. 3, pp. 911–949, 1996.

[87] R. G. Mints and A. L. Rakhmanov, “Critical state stability in type-II superconductors and superconducting-normal-metal composites,” *Rev. Mod. Phys.*, vol. 53, no. 3, pp. 551–592, 1981.

[88] J. Mannhart, R. Gross, R. P. Huebener, P. Chaudhari, D. Dlmos, and C. C. Tsuel, “Spatially resolved observation of charge transfer across single grain boundaries in YBaCuO films,” *Cryogenics (Guildf).*, vol. 30, no. 5, pp. 397–400, 1990.

[89] B. D. Josephson, “The Discovery of Tunnelling Supercurrents - Nobel Lecture,” *Proc. IEEE*, vol. 62, no. 6, pp. 838–841, 1974.

[90] G. H. Lee and H. J. Lee, “Proximity coupling in superconductor-graphene heterostructures,” *Reports Prog. Phys.*, vol. 81, no. 5, 2018.

[91] R. L. Fagaly, “Superconducting quantum interference device instruments and applications,” *Rev. Sci. Instrum.*, vol. 77, no. 10, 2006.

[92] J. G. Noudem *et al.*, “Infiltration and top seed growth-textured YBCO bulks with multiple holes,” *J. Am. Ceram. Soc.*, vol. 90, no. 9, pp. 2784–2790, 2007.

[93] Y. Iijima, N. Tanabe, O. Kohno, and Y. Ikeno, “In-plane aligned YBa2Cu3O7-x thin films deposited on polycrystalline metallic substrates,” *Appl. Phys. Lett.*, vol. 60, no. 6, pp. 769–771, 1992.

[94] J. D. Jorgensen *et al.*, “Oxygen ordering and the orthorhombic-to-tetragonal phase transition in YBA2Cu3O7-x,” *Phys. Rev. B*, vol. 36, no. 7, pp. 3608–3616, 1987.

[95] J. J. Capponi *et al.*, “Structure of the 100 K Superconductor $Ba_2YCu_3O_7$ between (5 ÷ 300) K by Neutron Powder Diffraction,” *Europhys. Lett.*, vol. 3, no. 12, pp. 1301–1307, Jun. 1987.

[96] P. M. Grant *et al.*, “Superconductivity above 90K in compound YBCO: Structural, Transport and magnetic properties,” *Phys. Rev. B*, vol. 35, no. 13, pp. 7242–7244, 1987.

[97] M. Takata *et al.*, “The nuclear density of YBCO by the maximum entropy method using neutron powder data,” *Phys. C Supercond. its Appl.*, vol. 263, no. 1–4, pp. 176–179, 1996.

[98] J. D. Jorgensen *et al.*, “Structural properties of oxygen-deficient YBa2Cu3O7-d,” *Phys. Rev. B*, vol. 41, no. 4, pp. 1863–1877, 1990.

[99] R. J. Cava *et al.*, “Structural anomalies, oxygen ordering and superconductivity in oxygen deficient Ba2YCu3Ox,” *Phys. C Supercond.*, vol. 165, no. 5–6, pp. 419–433, 1990.

[100] M. A. Beno *et al.*, “Structure of the single-phase high- temperature superconductor YBa2Cu3O7−δ Cite,” *Appl. Phys. Lett.*, vol. 51, no. 1, p. 57, 1987.

[101] R. J. Cava, B. Batlogg, C. H. Chen, E. A. Rietman, S. M. Zahurak, and D. Werder, “Oxygen stoichiometry, superconductivity and normal-state properties of YBa2 Cu307-d,” *Nature*, vol. 329, pp. 423–425, 1987.

[102] E. Dagotto, “Correlated electrons in high-temperature superconductors,” *Rev. Mod. Phys.*, vol. 66, no. 3, pp. 763–840, 1994.

[103] J. L. Routbort and S. J. Rothman, “Oxygen diffusion in cuprate superconductors,” *J. Appl. Phys.*, vol. 76, no. 10, pp. 5615–5628, 1994.

[104] I. K. Schuller, D. G. Hinks, M. A. Beno, D. W. Capone, and L. Soderholm, “Structural Phase Transition of YBCO: The Role of Dimensionality for high temperature superconductivity,” *Solid State Commun.*, vol. 63, no. 5, pp. 385–388, 1987.

[105] J. Ayache, “Grain boundaries in high temperature superconducting ceramics,” *Philos. Mag.*, vol. 86, no. 15, pp. 2193–2239, 2006.

[106] C. B. Eom *et al.*, “Growth mechanisms and properties of 90’ grain boundaries in YBCO thin films,” *Phys. Rev. B*, vol. 46, no. 18, pp. 902–913, 1992.

[107] W. K. Kwok, U. Welp, G. W. Crabtree, K. G. Vandervoort, R. Hulscher, and J. Z. Liu, “Direct observation of dissipative flux motion and pinning by twin boundaries in YBa2Cu3O7-single crystals,” *Phys. Rev. Lett.*, vol. 64, no. 8, pp. 966–969, 1990.

[108] D. R. Harshman *et al.*, “Magnetic penetration depth in singel-crystal YBCO,” *Phys. Rev. B*, vol. 39, no. 1, pp. 851–854, 1989.

[109] L. Krusin-Elbaum, A. P. Malozemoff, Y. Yeshurun, D. C. Cronemeyer, and F. Holtzberg,

"Temperature dependence of lower critical fields in Y-Ba-Cu-O crystals," *Phys. Rev. B*, vol. 39, no. 4, pp. 2936–2939, 1989.

[110] T. Pereg-Barnea *et al.*, "Absolute values of the London penetration depth in YBa2Cu 3O6+y measured by zero field ESR spectroscopy on Gd doped single crystals," *Phys. Rev. B - Condens. Matter Mater. Phys.*, vol. 69, no. 18, pp. 1–13, 2004.

[111] A. Gauzzi, B. Johan Jönsson-Åkerman, A. Clerc-Dubois, and D. Pavuna, "Scaling between superconducting critical temperature and structural coherence length in YBa2Cu3O6.9 films," *Europhys. Lett.*, vol. 51, no. 6, pp. 667–673, 2000.

[112] T. Terashima, K. Shimura, Y. Bando, Y. Matsuda, A. Fujiyama, and S. Komiyama, "Superconductivity of one-unit-cell thick YBa2Cu3O7 thin film," *Phys. Rev. Lett.*, vol. 67, no. 10, pp. 1362–1365, 1991.

[113] G. Krabbes, G. Fuch, W.-R. Canders, H. May, and R. Palka, *High Temperature Supercondcutor Bulk Materials*. WILEY -VCH, 2006.

[114] B. Oh *et al.*, "Upper critical field, fluctuation conductivity, and dimensionality of YBa2Cu3O7-x," *Phys. Rev. B*, vol. 37, no. 13, pp. 7861–7864, 1988.

[115] R. Hott, "Materials Aspects of High-Temperature Superconductors for Applications," no. July 2003, 2003.

[116] E. M. Gyorgy, R. B. van Dover, K. A. Jackson, L. F. Schneemeyer, and J. V. Waszczak, "Anisotropic critical currents in Ba2YCu3O7 analyzed using an extended Bean model," *Appl. Phys. Lett.*, vol. 55, p. 283, 1989.

[117] A. Mogro-Campero, L. G. Turner, and E. L. Hall, "Large differences of critical current density in thin films of superconducting YBa2Cu3O7-x," *J. Appl. Phys.*, vol. 65, no. 12, pp. 4951–4954, 1989.

[118] L. Luo *et al.*, "a-axis oriented YBa2Cu3O7−x thin films on Si with CeO2 buffer layers," *Appl. Phys. Lett.*, vol. 59, no. June, p. 2043, 1991.

[119] T. E. Mitchell, T. Roy, R. B. Schwartz, J. F. Smith, and D. Wohlleben, "Electron Microscopy Study of Twin Behavior in GdBCO and YBCO," *J. Electron Microsc. Tech.*, vol. 8, no. 3, pp. 317–323, 1988.

[120] H. Hilgenkamp, "Grain boundaries in high- T c superconductors," *Rev. Mod. Phys.*, vol. 74, no. April, pp. 485–549, 2002.

[121] B. D. Josephson, "Supercurrents Through Barriers," *Adv. Phys.*, vol. 14, no. 56, pp. 419–451, 1965.

[122] J. Halbritter, "Pair weakening and tunnel channels at cuprate interfaces," *Phys. Rev. B*, vol. 46, no. 22, pp. 14861–14871, 1992.

[123] X. M. Xie and T. G. Chen, "Investigation of substitution for copper in YBCO in internal friction measurement," *Supercond. Sci. Technol.*, vol. 5, no. 5, pp. 290–294, 1992.

[124] R. V. Vovk, M. A. Obolenskii, A. A. Zavgorodniy, D. A. Lotnyk, and K. A. Kotvitskaya, "Temperature dependence of the pseudogap in aluminum and praseodymium-doped YBa2 Cu3 O7 - δ single crystals," *Phys. B Condens. Matter*, vol. 404, no. 20, pp. 3516–3518, 2009.

[125] D. Varshney, A. Yogi, N. Dodiya, and I. Mansuri, "Alkaline Earth (Ca) and Transition Metal (Ni) Doping on The Transport Properties Of YBCO Superconductors," *J. Mod. Phys.*, vol. 02, no. 08, pp. 922–927, 2011.

[126] C. Y. Yang *et al.*, “X-ray absorption near-edge studies of substitution for Cu in YBCO with Fe, Co, Ni and Zn,” *Phys. Rev. B*, vol. 42, no. 4, pp. 2231–2241, 1990.

[127] R. K. Singhal, “How the substitution of Zn for Cu destroys superconductivity in YBCO system?,” *J. Alloys Compd.*, vol. 495, no. 1, pp. 1–6, 2010.

[128] M. Ionescu *et al.*, “Properties of yttrium barium copper oxide (YBCO) containing vanadium,” *Electr. Power Syst. Res.*, vol. 36, no. 3, pp. 139–143, 1996.

[129] L. Hanlon, C. Bradshaw, C. Crowley, D. Melody, G. O’Sullivan, and B. McBreen, “Silver substitution for Copper in Y1Ba2Cu307-y,” *Appl. Supercond.*, vol. 1, no. 10–12, pp. 1939–1948, 1993.

[130] S. A. Syed Asif, P. Somasundaram, A. M. Umarji, and S. K. Biswas, “Effect of Lanthanum substitution at the Barium site on the mechanical behaviour in YBCO superconductor,” *Mater. Res. Bull.*, vol. 28, pp. 73–80, 1993.

[131] A. W. Norazidah, H. Azhan, K. Azman, H. N. Hidayah, and J. . Hawa, “Superconducting Properties of Calcium Substitution in Barium Site of Porous YBCO Ceramics,” *Adv. Mater. Res.*, vol. 501, pp. 294–298, 2012.

[132] N. Ahmad and S. H. Naqib, “Estimation of Cooper pair density and its relation to the critical current density in Y(Ca)BCO high-Tc cuprate superconductors,” *Results Phys.*, vol. 17, no. January, 2020.

[133] S. Zhang *et al.*, “Broad temperature study of RE-substitution effects on the in-field critical current behavior of REBCO superconducting tapes,” *Supercond. Sci. Technol.*, vol. 31, no. 12, 2018.

[134] J. G. Lin, C. Y. Huang, Y. Y. Xue, C. W. Chu, X. W. Cao, and J. C. Ho, “Origin of the R-ion effect on Tc in REBCO,” *Phys. Rev. B*, vol. 51, no. 18, pp. 900–903, 1995.

[135] “Micron & Nacropowders - SkySpring Nanomaterials.” [Online]. Available: https://ssnano.com/nanopowders---micron-powders. [Accessed: 20-Aug-2020].

[136] J. Hykawy and T. Chudnovsky, “Rare earths,” 2021.

[137] A. Usoskin, U. Betz, J. Gnilsen, S. Noll-Baumann, and K. Schlenga, “Long-length YBCO coated conductors for ultra-high field applications: Gaining engineering current density via pulsed laser deposition/alternating beam-assisted deposition route,” *Supercond. Sci. Technol.*, vol. 32, no. 9, 2019.

[138] K. Kakimoto *et al.*, “Long RE123 coated conductors with high critical current over 500 A/cm by IBAD/PLD technique,” *Phys. C Supercond. its Appl.*, vol. 471, no. 21–22, pp. 929–931, 2011.

[139] Y. Chen *et al.*, “Enhanced flux pinning by BaZrO3 and (Gd,Y)2 O 3 nanostructures in metal organic chemical vapor deposited GdYBCO high tempe rature superconductor tapes,” *Appl. Phys. Lett.*, vol. 94, no. 6, pp. 1–4, 2009.

[140] S. Fujita *et al.*, “Flux-pinning properties of BaHfO3 -Doped EuBCO-Coated Conductors Fabricated by Hot-Wall PLD,” *IEEE Trans. Appl. Supercond.*, vol. 29, no. 5, p. 8001505, 2019.

[141] F. Prado, A. Caneiro, and A. Serquis, “High temperature thermodynamic properties, orthorhombic/tetragonal transition and phase stability of GdBa2Cu3Oy and related R123 compounds,” *Phys. C Supercond. its Appl.*, vol. 295, no. 3–4, pp. 235–246, 1998.

[142] A. Sedky and M. I. Youssif, “Low-field AC susceptibility study of critical current density in Eu:123 and Bi:2223 superconductors,” *J. Magn. Magn. Mater.*, vol. 237, no. 1, pp. 22–26,

2001.

[143] S. Eley *et al.*, “Decoupling and tuning competing effects of different types of defects on flux creep in irradiated YBCO coated conductors,” *Supercond. Sci. Technol.*, vol. 30, p. 015010, 2017.

[144] M. D. Vazquez-Navarro, “A thermogravimetric study of oxygen diffusion in YBa2Cu3O7-δ,” University of Cambridge, 1998.

[145] S. J. Rothman, J. L. Routbort, U. Welp, and J. E. Baker, “Anisotropy of oxygen tracer diffusion in single-crystal YBa2Cu3O7,” *Phys. Rev. B*, vol. 44, no. 5, pp. 2326–2333, 1991.

[146] M. Ronay and P. Nordlander, “Anisotrphy of Oxygen Transport in YBCO: The role of the [1/2, b, 0] tunnels,” *Phys. C*, vol. 153–5, pp. 834–835, 1988.

[147] A. P. Mozhaev and S. V Chernyaev, “Oxygen Diffusion in YBa2Cu306+x Ceramics,” *J. Mater. Chem.*, vol. 4, no. 7, pp. 1107–1110, 1994.

[148] T. Umemura, K. Egawa, W. Mitsunobu, and K. Yoshizaki, “Absorption and Desorption of Oxygen in YBCO,” *Jpn. J. Appl. Phys.*, vol. 28, no. 11, pp. L1945–L1947, 1989.

[149] M. W. Rupich *et al.*, “Second generation wire development at AMSC,” *IEEE Trans. Appl. Supercond.*, vol. 23, no. 3, pp. 3–7, 2013.

[150] J. Lu, E. S. Choi, and H. D. Zhou, “Physical properties of Hastelloy® C-276™ at cryogenic temperatures,” *J. Appl. Phys.*, vol. 103, no. 6, pp. 1–7, 2008.

[151] K. Osamura *et al.*, “Inverted-parabolic and weak strain dependencies on the critical current in practical <110> and <100> oriented REBCO tapes,” *AIP Adv.*, vol. 9, no. 7, 2019.

[152] X. Obradors and T. Puig, “Coated conductors for power applications: Materials challenges,” *Supercond. Sci. Technol.*, vol. 27, no. 4, 2014.

[153] K. Radcliff, “Mechanical properties of SuperPower and SuNam REBCO coated conductors,” Florida State Uinversity, 2018.

[154] A. Sundaram *et al.*, “2G HTS wires made on 30 μm thick Hastelloy substrate,” *Supercond. Sci. Technol.*, vol. 29, no. 10, 2016.

[155] Y. Xia *et al.*, “Reel-to-reel deposition of epitaxial double-sided Y2O3 buffer layers for coated conductors,” *Phys. C Supercond. its Appl.*, vol. 476, pp. 48–53, 2012.

[156] M. G. Norton, L. A. Tietz, S. R. Summerfelt, and C. B. Carter, “Observation of the early stages of growth of superconducting thin films by transmission electron microscopy,” *Appl. Phys. Lett.*, vol. 55, no. 22, pp. 2348–2350, 1989.

[157] S. R. Foltyn *et al.*, “Strongly coupled critical current density values achieved in Y1Ba2Cu3O7-δ coated conductors with near-single-crystal texture,” *Appl. Phys. Lett.*, vol. 82, no. 25, pp. 4519–4521, 2003.

[158] R. P. Reade, P. Berdahl, R. E. Russo, and S. M. Garrison, “Laser deposition of biaxially textured yttria-stabilized zirconia buffer layers on polycrystalline metallic alloys for high critical current Y-Ba-Cu-O thin films,” *Appl. Phys. Lett.*, vol. 61, no. 18, pp. 2231–2233, 1992.

[159] V. Selvamanickam, G. B. Galinski, G. Carota, J. Defrank, and C. Trautwein, “High-current Y – Ba – Cu – O superconducting films by metal organic chemical vapor deposition on flexible metal substrates,” pp. 155–162, 2000.

[160] M. W. Rupich *et al.*, “Advances in second generation high temperature superconducting wire

manufacturing and R&D at American Superconductor Corporation," *Supercond. Sci. Technol.*, vol. 23, no. 1, 2010.

[161] F. K. Shokoohi *et al.*, "Wet chemical etching of high-temperature superconducting Y-Ba-Cu-O films in ethylenediaminetetraacetic acid," *Appl. Phys. Lett.*, vol. 55, no. 25, pp. 2661–2663, 1989.

[162] S. R. Foltyn, P. Tiwari, R. C. Dye, M. Q. Le, and Wu X.D., "Pulsed laser deposition of thick YBCO films with Jc > 1MA/cm2," *Appl. Phys. Lett.*, vol. 63, no. May, p. 1848, 1993.

[163] H. Wang, S. R. Foltyn, P. N. Arendt, Q. X. Jia, and X. Zhang, "Identification of the misfit dislocations at YBa2Cu3O7-δ/SrTiO3 interface using moiré fringe contrast," *Phys. C Supercond. its Appl.*, vol. 444, no. 1–2, pp. 1–4, 2006.

[164] J. Xiong *et al.*, "MOCVD derived double-sided YBa2Cu3O 7-δ films on Y2O3/YSZ/CeO2 buffered textured metal substrates," *Sci. China Technol. Sci.*, vol. 57, no. 4, pp. 720–724, 2014.

[165] W. Prusseit *et al.*, "Evaporation - The way to commercial coated conductor fabrication," *Phys. C Supercond. its Appl.*, vol. 392–396, no. PART 2, pp. 801–805, 2003.

[166] S. R. Foltyn *et al.*, "Materials science challenges for high-temperature superconducting wire," *Nat. Mater.*, vol. 6, pp. 631–642, 2007.

[167] A. Ibi *et al.*, "Development of Long Coated Conductors with High In-field IcPerformance by PLD Method at High Production Rate," *Phys. Procedia*, vol. 81, pp. 97–100, 2016.

[168] J. D. Suh *et al.*, "Cubic Y-Ba-Cu-O thin films by high speed pulsed laser deposition," *Phys. C Supercond. its Appl.*, vol. 308, no. 3–4, pp. 251–256, 1998.

[169] D. Q. Shi *et al.*, "Effects of deposition rate and thickness on the properties of YBCO films deposited by pulsed laser deposition," *Supercond. Sci. Technol.*, vol. 17, no. 2, 2004.

[170] V. Matias *et al.*, "YBCO films grown by reactive co-evaporation on simplified IBAD-MgO coated conductor templates," *Supercond. Sci. Technol.*, vol. 23, no. 1, 2010.

[171] T. Puig *et al.*, "The influence of growth conditions on the microstructure and critical currents of TFA-MOD YBa2Cu3O7 films," *Supercond. Sci. Technol.*, vol. 18, no. 8, pp. 1141–1150, 2005.

[172] M. W. Rupich, X. Li, S. Sathyamurthy, C. Thieme, and S. Fleshler, "Advanced development of TFA-MOD coated conductors," *Phys. C Supercond. its Appl.*, vol. 471, no. 21–22, pp. 919–923, 2011.

[173] H. Matsui *et al.*, "Increase of achievable film thickness by UV-lamp irradiation in a fluorine-free metal-organic deposition process of YBa2Cu3O7," *Thin Solid Films*, vol. 519, no. 22, pp. 8063–8065, 2011.

[174] S. Rasi *et al.*, "Relevance of the Formation of Intermediate Non-Equilibrium Phases in YBa2Cu3O7-x Film Growth by Transient Liquid-Assisted Growth," *J. Phys. Chem. C*, vol. 124, no. 28, pp. 15574–15584, 2020.

[175] L. Soler *et al.*, "Ultrafast transient liquid assisted growth of high current density superconducting films," *Nat. Commun.*, vol. 11, no. 1, 2020.

[176] S. I. Shah, "Annealing studies of YBCO thin films," *Appl. Phys. Lett.*, vol. 53, no. August, pp. 612–614, 1988.

[177] A. Mogro-Campero, L. G. Turner, A. Bogorad, and R. Herschitz, "The effect of temperature

cycling on thin films of YBa2Cu 3O7," *Supercond. Sci. Technol.*, vol. 3, no. 11, pp. 537–539, 1990.

[178] R. L. Barns and R. A. Laudise, "Stability of superconducting YBa2Cu3O7 in the presence of water," *Appl. Phys. Lett.*, vol. 51, no. 17, pp. 1373–1375, 1987.

[179] M. M. Garland, "Degradation of Y-Ba-Cu-O in a high-humidity environment," *J. Mater. Res.*, vol. 3, pp. 830–831, 1988.

[180] A. Mogro-Campero, K. W. Paik, and L. G. Turner, "Degradation of thin films of YBa2Cu3O7 by annealing in air and in vacuum," *J. Supercond.*, vol. 8, no. 1, pp. 95–98, 1995.

[181] Y. Iwasa and M. W. Sinclair, "Protection of large superconducting magnets: maximum undetected quench voltage," *Cryogenics (Guildf).*, pp. 711–714, 1980.

[182] W. Eidelloth and R. L. Sandstrom, "Wet etching of gold films compatible with high Tc superconducting thin films," *Appl. Phys. Lett.*, vol. 59, no. 13, pp. 1632–1634, 1991.

[183] X. Xiong *et al.*, "Progress in High Throughput Processing of Long-Length, High Quality and Low Cost IBAD MgO Buffer Tapes at SuperPower," *IEEE Trans. Appl. Supercond.*, vol. 19, no. 3, pp. 3319–3322, 2009.

[184] K. Tsuchiya *et al.*, "Critical current measurement of commercial REBCO conductors at 4.2 K," *Cryogenics (Guildf).*, vol. 85, pp. 1–7, 2017.

[185] M. W. Rupich, "Second-generation (2G) coated high-temperature superconducting cables and wires for power grid applications," in *Superconductors in the Power Grid: Materials and Applications*, Elsevier, 2015, pp. 75–95.

[186] A. Usoskin *et al.*, "Double-Disordered HTS-Coated Conductors and Their Assemblies Aimed for Ultra-High Fields: Large Area Tapes," *IEEE Trans. Appl. Supercond.*, vol. 28, no. 4, pp. 1–6, 2018.

[187] Y. Zhao *et al.*, "Progress in fabrication of second generation high temperature superconducting tape at Shanghai Superconductor Technology," *Supercond. Sci. Technol.*, vol. 32, no. 4, 2019.

[188] W. Prusseit *et al.*, "Commercial coated conductor fabrication based on inclined substrate deposition," *IEEE Trans. Appl. Supercond.*, vol. 15, no. 2 PART III, pp. 2608–2610, 2005.

[189] J. H. Lee, H. Lee, J. W. Lee, S. M. Choi, S. I. Yoo, and S. H. Moon, "RCE-DR, a novel process for coated conductor fabrication with high performance," *Supercond. Sci. Technol.*, vol. 27, no. 4, 2014.

[190] S. Lee *et al.*, "Development and production of second generation high Tc superconducting tapes at SuperOx and first tests of model cables," *Supercond. Sci. Technol.*, vol. 27, no. 4, 2014.

[191] D. R. Nelson and V. M. Vinokur, "Boson localization and correlated pinning of superconducting vortex arrays," *Phys. Rev. B*, vol. 48, no. 17, pp. 13060–13097, 1993.

[192] G. Blatter, M. V. Feigelman, V. B. Geshkenbein, A. I. Larkin, and V. M. Vinokur, "Vortices in high temperature superconductors," *Rev. Mod. Phys.*, vol. 66, no. 4, p. 1125, 1994.

[193] A. Palau *et al.*, "Disentangling vortex pinning landscape in chemical solution deposition of YBa2Cu3O7-x coated conductors," *Supercond. Sci. Technol.*, vol. 31, no. 3, p. 034004, 2018.

[194] L. Civale *et al.*, "Understanding high critical currents in YBCO thin films and coated

conductors," *J. Low Temp. Phys.*, vol. 135, no. 1–2, pp. 87–98, 2004.

[195] G. Blatter, V. B. Geshkenbein, and A. I. Larkin, "From isotropic to anisotropic superconductors: A scaling approach," *Phys. Rev. Lett.*, vol. 68, no. 6, pp. 875–878, 1992.

[196] X. Obrados *et al.*, "Epitaxial YBa2Cu3O7−x nanocomposite films and coated conductors from BaMO3 (M = Zr, Hf) colloidal solutions," *Supercond. Sci. Technol.*, vol. 31, no. 4, p. 044001, 2018.

[197] C. J. van der Beek *et al.*, "Strong pinning in high-temperature superconducting films," *Phys. Rev. B - Condens. Matter Mater. Phys.*, vol. 66, no. 2, p. 024523, 2002.

[198] Y. N. Ovchinnikov and B. I. Ivlev, "Pinning in layered inhomogeneous superconductors," *Phys. Rev. B*, vol. 43, no. 10, pp. 8024–8029, 1991.

[199] V. Vinokur, B. Khaykovich, E. Zeldov, M. Konczykowski, R. A. Doyle, and P. H. Kes, "Lindemann criterion and vortex-matter phase transitions in high-temperature superconductors," *Phys. C Supercond. its Appl.*, vol. 295, no. 3–4, pp. 209–217, 1998.

[200] T. Puig *et al.*, "Vortex pinning in chemical solution nanostructured YBCO films," *Supercond. Sci. Technol.*, vol. 21, no. 3, p. 034008, 2008.

[201] J. P. F. Feighan, A. Kursumovic, and J. L. MacManus-Driscoll, "Materials design for artificial pinning centres in superconductor PLD coated conductors," *Supercond. Sci. Technol.*, vol. 30, no. 12, p. 123001, 2017.

[202] K. Nordlund *et al.*, "Primary radiation damage: A review of current understanding and models," *J. Nucl. Mater.*, vol. 512, no. October, pp. 450–479, 2018.

[203] K. R. Whittle, *Nuclear Materials Science*, 1st ed. Liverpool: IOP Publishing, 2016.

[204] A. J. Koning and D. Rochman, "Modern Nuclear Data Evaluation with the TALYS Code System," *Nucl. Data Sheets*, vol. 113, no. 12, pp. 2841–2934, 2012.

[205] W. Wesch and E. Wendler, *Ion Beam Modification of Solids*, 1st ed. Jena: Springer, 2016.

[206] G. S. Was, *Fundamentals of Radiation Materials Science - Metals and Alloys*. New York: Springer Berlin Heidelberg, 2007.

[207] K. Nordlund, "Historical review of computer simulation of radiation effects in materials," *J. Nucl. Mater.*, vol. 520, pp. 273–295, 2019.

[208] G. H. Kinchin and R. S. Pease, "Displacement of Atoms in Solid by Radiation," *Rep. Prog. Phys.*, vol. 18, 1955.

[209] J. Lindhard, H. E. Schiøtt, M. Scharff, and H. Schiott, "Range concepts and heavy ion ranges (Notes on atomic collisions, II)," *Mat. Meddelelser udgivet af Det K. Danske Vidensk. Selsk.*, vol. 33, no. 14, p. 42 p., 1963.

[210] M. J. Norgett, M. T. Robinson, and I. M. Torrens, "A proposed method of calculating displacement dose rates," *Nucl. Eng. Des.*, vol. 33, pp. 50–54, 1975.

[211] M. T. Robinson, "Basic physics of radiation damage production," *J. Nucl. Mater.*, vol. 216, no. C, pp. 1–28, 1994.

[212] M. R. Gilbert and J. C. Sublet, "Differential dpa calculations with SPECTRA-PKA," *J. Nucl. Mater.*, vol. 504, pp. 101–108, 2018.

[213] K. Nordlund *et al.*, "Improving atomic displacement and replacement calculations with

physically realistic damage models," *Nat. Commun.*, vol. 9, p. 1084, 2018.

[214] P. J. Hasnip, K. Refson, M. I. J. Probert, J. R. Yates, S. J. Clark, and C. J. Pickard, "Density functional theory in the solid state," *Phil. Trans. Roy. Soc. A*, vol. 372, p. 270, 2013.

[215] S. K. Nayak, W. A. Adeagbo, H. T. Langhammer, W. Hergert, T. Müller, and R. Böttcher, "Study of charged defects for substitutionally doped chromium in hexagonal barium titanate from first principles," *Phys. Status Solidi Rapid Reseach Lett.*, vol. 6, pp. 527–531, 2014.

[216] S. N. Basu, T. E. Mitchell, and M. Nastasi, "Electron-beam-irradiation effects in bulk YBCO," *J. Appl. Phys.*, vol. 69, p. 3167, 1991.

[217] S. Mohr *et al.*, "Accurate and efficient linear scaling DFT calculations with universal applicability," *Phys. Chem. Chem. Phys.*, vol. 17, p. 31360, 2015.

[218] S. Plimpton, "Computational limits of classical molecular dynamics simulations," *Comput. Mater. Sci.*, vol. 4, pp. 361–364, 1995.

[219] X. Zhou, M. E. Foster, J. A. Ronevich, and C. W. San Marchi, "Review and construction of interatomic potentials for molecular dynamics studies of hydrogen embrittlement in Fe – C based steels," *J. Comput. Chem.*, vol. 41, pp. 1299–1309, 2020.

[220] P. M. Derlet, M. R. Gilbert, and S. L. Dudarev, "Simulating dislocation loop internal dynamics and collective diffusion using stochastic differential equations," *Phys. Rev. B*, vol. 84, p. 134109, 2011.

[221] T. D. De Rubia, R. S. Averback, R. Benedek, and W. E. King, "Role of Thermal Spikes in Energetic Displacement Cascades," *Phys. Reivew Lett.*, vol. 59, no. 17, pp. 1930–1933, 1987.

[222] J. F. Briesmeister, "MCNPTM – A General Monte Carlo N-Particle Transport Code," *Los Alamos Natl. Lab.*, no. March, p. 790, 2000.

[223] J. C. Sublet, J. W. Eastwood, J. G. Morgan, M. R. Gilbert, M. Fleming, and W. Arter, "FISPACT-II: An Advanced Simulation System for Activation, Transmutation and Material Modelling," *Nucl. Data Sheets*, vol. 139, pp. 77–137, 2017.

[224] J.-C. C. Sublet, J. W. Eastwood, and J. G. Morgan, *The FISPACT -II User Manual*, no. CCFE-R(11)11 6. CCFE, 2014.

[225] M. T. Robinson and I. M. Torrens, "Computer simulation of atomic-displacement cascades in solids in the binary-collision approximation," *Phys. Rev. B*, vol. 9, no. 12, pp. 5008–5024, 1974.

[226] M. T. Robinson, "Computer simulation studies of high-energy collision cascades," *Nucl. Instruments Methods Phys. Res. B*, vol. 67, pp. 396–400, 1992.

[227] J. F. Ziegler, J. P. Biersack, and M. D. Ziegler, *SRIM - The Stopping and Range of Ions in Matter*, 5th ed. SRIM Company, 2015.

[228] D. Drouin, "CASINO: 'Monte Carlo simulation of Electron trajectory in Solids.'" [Online]. Available: http://www.gel.usherbrooke.ca/casino/index.html. [Accessed: 15-Oct-2018].

[229] D. Drouin, A. R. Couture, and R. Gauvin, "CASINO V2.0 : An advanced simulation tool for scanning electron microscopy users," *Microsc. Microanal.*, vol. 7, no. S2, p. 684, 2001.

[230] J. P. Biersack and L. G. Haggmark, "A Monte Carlo computer program for the transport of energetic ions in amorphous targets," *Nucl. Instruments Methods*, vol. 174, no. 1–2, pp. 257–269, 1980.

[231] W. J. Weber and Y. Zhang, “Predicting damage production in monoatomic and multi-elemental targets using stopping and range of ions in matter code: Challenges and recommendations,” *Curr. Opin. Solid State Mater. Sci.*, vol. 23, p. 100757, 2019.

[232] G. Demange, E. Antoshchenkova, M. Hayoun, L. Luneville, and D. Simeone, “A rational use of BCA code MARLOWE for ballistic effects of ion beam irradiation in the ion mixing formalism: comparison to Molecular Dynamics,” 2016. [Online]. Available: https://arxiv.org/pdf/1610.08659.pdf. [Accessed: 04-Sep-2020].

[233] V. V. Kirsanov, N. N. Musin, and H. J. Shamarina, “Displacement threshold energy in high-temperature superconductors. II. Thresholds for O, Ba and Y in YBa2Cu3O7,” *Phys. Lett. A*, vol. 171, no. 3–4, pp. 223–233, 1992.

[234] F. Z. Cui, J. Xie, and H. D. Li, “Preferential radiation damage of the oxygen sublattice in YBa2Cu307: A molecular-dynamics simulation,” *Phys. Rev. B*, vol. 46, no. 17, pp. 11182–11185, 1992.

[235] F. Z. Cui, H. D. Li, L. Jin, and Y. Y. Li, “Simulations on radiation damage initiated by O(1) PKA in YBa2Cu3O7,” *Nucl. Inst. Methods Phys. Res. B*, vol. 91, no. 1–4, pp. 374–377, 1994.

[236] J. F. Smith and D. Wohlleben, “Twin refinement below room temperature in the 1-2-3 high Tc superconductors,” *Zeitschrift für Phys. B Condens. Matter*, vol. 72, no. 3, pp. 323–334, 1988.

[237] J. Giapintzakis *et al.*, “Production and identification of flux-pinning defects by electron irradiation in YBCO,” *Phys. Rev. B*, vol. 45, no. 18, pp. 10677–10683, 1992.

[238] G. Wilson and J. R. Dennison, “Approximation of range in materials as a function of incident electron energy,” *IEEE Trans. Plasma Sci.*, vol. 40, no. 2 PART 1, pp. 291–297, 2012.

[239] H. W. Seo *et al.*, “Chain-oxygen ordering in twin-free Y Ba2 Cu3 O7-δ single crystals driven by 20-keV electron irradiation,” *Phys. Rev. B - Condens. Matter Mater. Phys.*, vol. 72, no. 5, pp. 1–4, 2005.

[240] S. K. Tolpygo, J. Y. Lin, M. Gurvitch, S. Y. Hou, and J. M. Phillips, “Tc enhancement by low energy electron irradiation and the influence of chain disorder on resistivity and Hall coefficient in YBa2Cu3O7 thin films,” *Phys. C Supercond. its Appl.*, vol. 269, no. 3–4, pp. 207–219, 1996.

[241] S. K. Tolpygo, J. Y. Lin, M. Gurvitch, S. Y. Hou, and J. M. Phillips, “Effect of oxygen defects on transport properties and Tc of YBa2Cu3O6x: Displacement energy for plane and chain oxygen and implications for irradiation-induced resistivity and Tc suppression.,” *Phys. Rev. B*, vol. 53, no. 18, pp. 12462–12474, 1996.

[242] A. Legris *et al.*, “Effects of electron irradiation on YBCO superconductor,” *J. Phys. I*, vol. 3, pp. 1605–1615, 1993.

[243] K. N. Tu, N. C. Yeh, S. I. Park, and C. C. Tsuei, “Diffusion of oxygen in superconducting YBa2Cu3O7-δ ceramic oxides,” *Phys. Rev. B*, vol. 39, no. 1, pp. 304–314, 1989.

[244] S. T. Murphy, “A point defect model for YBa2Cu3O7 from density functional theory,” *J. Phys. Commun.*, vol. 4, no. 11, pp. 1–14, 2020.

[245] R. Grey, “Private Communication.” 2021.

[246] J. R. Cost, J. O. Willis, J. D. Thompson, and D. E. Peterson, “Fast neutron irradiation of YBCO,” *Phys. Rev. B*, vol. 48, no. 7, pp. 4575–4585, 1988.

[247] J. -W. Lee *et al.*, “Observation of proposed flux pinning sites in neutron-irradiated

YBa2Cu3O7−x,” *Appl. Phys. Lett.*, vol. 57, no. 20, pp. 2150–2152, Nov. 1990.

[248] K. E. Sickafus *et al.*, “Neutron-radiation-induced flux pinning in Gd-doped YBa2Cu3O7-x and GdBa2Cu3O7-x,” *Phys. Rev. B*, vol. 46, no. 18, pp. 11862–11870, 1992.

[249] H. W. Sauerzopf, F M, Wiesinger, H P, Kritscha, W, Weber, “Neutron irradiation effects on critical current densities in sigle crystalline YBCO,” *Phys. Rev. B*, vol. 43, no. 4, 1991.

[250] M. Sauerzopf, W. Weber, H. P. Wiesinger, and G. W. Crabtree, “Analysis of pinning effects in YBCO single crystals after fast neutron irradiation,” *Phys. Rev. B*, vol. 51, no. 9, pp. 6002–6012, 1995.

[251] B. M. Vlcek *et al.*, “Flux pinning in YBCO single crystals: Neutron irrradiation and annealing,” *Phys. Rev. B*, vol. 46, no. 10, pp. 6441–6451, 1992.

[252] B. M. Vlcek *et al.*, “Role of point defects and their clusters for flux pinning as determined from irradiation and annealing experiments in YBCO single crystals,” *Phys. Rev. B*, vol. 48, no. 6, 1993.

[253] M. C. Frischherz, M. A. Kirk, J. Farmer, L. R. Greenwood, and H. W. Weber, “Defect Cascades Produced by Neutron-Irradiation in YBCO,” *Phys. C Supercond. its Appl.*, vol. 232, no. 3–4, pp. 309–327, 1994.

[254] M. A. Kirk, “Structure and flux pinning properties of irradiation defects in YBCO,” *Micron*, vol. 30, pp. 507–526, 1999.

[255] R. Fuger, M. Eisterer, F. Hengstberger, and H. W. Weber, “Influence of neutron irradiation on high temperature superconducting coated conductors,” *Phys. C Supercond.*, vol. 468, pp. 1647–1651, 2008.

[256] R. Fuger, M. Eisterer, and H. W. Weber, “YBCO coated conductors for fusion magnets,” *IEEE Trans. Appl. Supercond.*, vol. 19, no. 3, pp. 1532–1535, 2009.

[257] C. Paunoiu, D. Barbos, and M. Ciocanescu, “Triga 14 mw research reactor status and utilization,” pp. 1–89.

[258] M. Eisterer, R. Fuger, M. Chudy, F. Hengstberger, and H. W. Weber, “Neutron irradiation of coated conductors,” *Supercond. Sci. Technol.*, vol. 23, p. 014009, 2010.

[259] M. Chudy, M. Eisterer, H. W. Weber, J. Veterníková, S. Sojak, and V. Slugeň, “Point defects in YBa2Cu3O7− x studied using positron annihilation,” *Supercond. Sci. Technol.*, vol. 25, no. 7, p. 075017, 2012.

[260] G. S. Was *et al.*, “Emulation of reactor irradiation damage using ion beams,” *Scr. Mater.*, vol. 88, pp. 33–36, 2014.

[261] G. J. Clark, A. D. Marwick, R. H. Koch, and R. B. Laibowitz, “Effects of radiation damage in ion-implanted thin films of metal-oxide superconductors,” *Appl. Phys. Lett.*, vol. 51, no. 2, pp. 139–141, 1987.

[262] G. Xiong, H. Li, G. Linker, and O. Meyer, “Transport properties, phase transition, and recovery near 200 K of proton-irradiated YBCO thin films,” *Phys. Rev. B*, vol. 38, no. 1, pp. 240–243, 1988.

[263] H. Matsui *et al.*, “4-fold enhancement in the critical current density of YBa2Cu3O7 films by practical ion irradiation,” *Appl. Phys. Lett.*, vol. 101, no. 23, p. 232601, 2012.

[264] M. Toulemonde, S. Bouffard, and F. Studer, “Swift heavy ions in insulating and conducting

oxides: tracs and physical properties," *Nucl. Instruments Methods Phys. Res. B*, vol. 91, pp. 108–123, 1994.

[265] B. Roas, B. Hensel, G. Saemann-Ischenko, and L. Schultz, "Irradiation-induced enhancement of the critical current density of epitaxial YBCO thin films," *Appl. Phys. Lett.*, vol. 54, no. 11, pp. 1051–1053, 1989.

[266] V. Hardy, D. Groult, M. Hervieu, J. Provost, B. Raveau, and S. Bouffard, "Latent track formation induced by high energy heavy ions in superconductive copper oxides," *Nucl. Inst. Methods Phys. Res. B*, vol. 54, no. 4, pp. 472–481, 1991.

[267] G. Isobe, M. Kiuchi, E. S. Otabe, T. Matsushita, S. Okayasu, and W. Prusseit, "Effect of heavy ion irradiation on critical current property in DyBCO coated conductors," *Phys. C Supercond. its Appl.*, vol. 468, no. 15–20, pp. 1656–1660, 2008.

[268] L. Civale *et al.*, "Vortex confinement by columnar defects in YBa2Cu3O7 crystals: Enhanced pinning at high fields and temperatures," *Phys. Rev. Lett.*, vol. 67, no. 5, pp. 648–651, 1991.

[269] E. I. Suvorova *et al.*, "Energy dependent structure of Xe ion tracks in YBCO and the effect on the superconductive properties in magnetic fields," *J. Appl. Phys.*, vol. 126, p. 145106, 2019.

[270] R. W. Hamm and M. E. Hamm, "The beam business: Accelerators in industry," *Phys. Today*, vol. 64, no. 6, pp. 46–51, 2011.

[271] A. A. Gapud *et al.*, "Irradiation response of commercial, high-Tcsuperconducting tapes: Electromagnetic transport properties," *J. Nucl. Mater.*, vol. 462, pp. 108–113, 2015.

[272] H. Matsui *et al.*, "Enhancement of critical current density in YBa2Cu3O7 films using a semiconductor ion implanter," *J. Appl. Phys.*, vol. 117, no. 4, pp. 0–5, 2015.

[273] M. W. Rupich *et al.*, "Engineered Pinning Landscapes for Enhanced 2G Coil Wire," *IEEE Trans. Appl. Supercond.*, vol. 26, no. 3, pp. 16–19, 2016.

[274] M. LeRoux *et al.*, "Rapid doubling of the critical current of YBa2Cu3O7-δ coated conductors for viable high-speed industrial processing," *Appl. Phys. Lett.*, vol. 107, p. 192601, 2015.

[275] K. J. Kihlstrom *et al.*, "Large enhancement of the in-field critical current density of YBCO coated conductors due to composite pinning landscape," *Supercond. Sci. Technol.*, vol. 34, no. 1, p. 015011, 2021.

[276] H. Vichery *et al.*, "Effects of low temperature electron irradiation on single crystal and sintered YBa2Cu3O7-δ," *Phys. C Supercond. its Appl.*, vol. 159, no. 5, pp. 697–706, 1989.

[277] B. Sorbom, "The Effect of Irradiation Temperature on REBCO Jc Degradation and Implications for Fusion Magnets," Massachusetts Institute of Technology, 2017.

[278] G. A. Greene, R. C. Gupta, W. B. Sampson, and C. L. Snead, "The effect of proton irradiation on the critical current of commercially produced YBCO conductors," *IEEE Trans. Appl. Supercond.*, vol. 19, no. 3, pp. 3164–3167, 2009.

[279] H. Matsui *et al.*, "Influence of middle-energy ion-irradiation on the flux pinning properties of YBCO films: Comparison between different synthesis methods," *J. Phys. Conf. Ser.*, vol. 507, no. PART 2, pp. 3–7, 2014.

[280] Y. Jia *et al.*, "Doubling the critical current density of high temperature superconducting coated conductors through proton irradiation," *Appl. Phys. Lett.*, vol. 103, p. 122601, 2013.

[281] K. J. Leonard *et al.*, "Irradiation Response of Next Generation High Temperature

Superconducting Rare Earth and Nanoparticle-Doped YBa2Cu3O7-x Coated Conductors for Fusion Energy Applications," *FUSION Mater. Semiannu. Prog. Rep. PERIOD End. 31/12/2013*, vol. 55, pp. 54–62, 2013.

[282] K. J. Leonard *et al.*, "Irradiation Response of Next Generation High Temperature Superconducting Rare- Earth and Nanoparticle-Doped YBa2Cu3O7-x Coated Conductors for Fusion Energy Applications," *FUSION Mater. Semiannu. Prog. Rep. PERIOD End. 30/6/2013*, pp. 125–134, 2013.

[283] N. Haberkorn *et al.*, "High-temperature change of the creep rate in YBa 2Cu 3O 7-δ films with different pinning landscapes," *Phys. Rev. B - Condens. Matter Mater. Phys.*, vol. 85, no. 17, pp. 1–7, 2012.

[284] N. Haberkorn, J. Kim, S. Suárez, J. H. Lee, and S. H. Moon, "Influence of random point defects introduced by proton irradiation on the flux creep rates and magnetic field dependence of the critical current density J c of co-evaporated GdBa2Cu3O7-δ coated conductors," *Supercond. Sci. Technol.*, vol. 28, no. 12, 2015.

[285] N. Haberkorn *et al.*, "Effect of mixed pinning landscapes produced by 6 MeV oxygen irradiation on the resulting critical current densities J c in 1.3 μm thick GdBa 2 Cu 3 O 7- d coated conductors grown by co-evaporation," *Phys. C Supercond. its Appl.*, vol. 542, pp. 6–11, 2017.

[286] N. Haberkorn, J. Guimpel, S. Suárez, J. Lee, H. Lee, and S. H. Moon, "Competition between pinning produced by extrinsic random point disorder and superconducting thermal fluctuations in oxygen-deficient GdBa2Cu3Ox coated conductors," *Supercond. Sci. Technol.*, vol. 32, p. 125015, 2019.

[287] W. J. Choi, D. Ahmad, Y. I. Seo, R. K. Ko, and Y. S. Kwon, "Effect of the proton irradiation on the thermally activated flux flow in superconducting SmBCO coated conductors," *Sci. Rep.*, vol. 10, no. 1, pp. 1–12, 2020.

[288] A. V. Antonov *et al.*, "Critical-field slope reduction and upward curvature of the phase-transition lines of thin disordered superconducting YBa2Cu3O7−x films in strong magnetic fields," *Phys. C Supercond. its Appl.*, vol. 568, no. October 2019, 2020.

[289] Z. Xia, J. Bray-Ali, J. Zhang, W. R. Fink K.S., C. M. Gould, and H. M. Bozler, "Magnetization of materials used in cryostats," *J. Low Temp. Phys.*, vol. 126, no. 1–2, pp. 655–660, 2002.

[290] D. R. Lide, *CRC Handbook of Chemistry and Physics, Internet Version 2005*. Boca Raton, FL: CRC Press., 2005.

[291] V. Selvamanickam *et al.*, "Correlation between in-field critical currents in Zr-added (Gd, Y)Ba 2Cu3Ox superconducting tapes at 30 and 77 K," *Supercond. Sci. Technol.*, vol. 27, no. 5, 2014.

[292] D. Abraimov *et al.*, "Double disordered YBCO coated conductors of industrial scale: High currents in high magnetic field," *Supercond. Sci. Technol.*, vol. 28, no. 11, 2015.

[293] "Fujikura HTS home page." [Online]. Available: www.fujikura.co.uk. [Accessed: 22-Jan-2021].

[294] S. J. Singh *et al.*, "Ultrahigh critical current densities, the vortex phase diagram, and the effect of granularity of the stoichiometric high-Tc superconductor CaKFe4As4," *Phys. Rev. Mater.*, vol. 2, no. 7, pp. 1–13, 2018.

[295] C. P. Bean, "Magnetization of hard superconductors," *Phys. Rev. Lett.*, vol. 8, no. 6, pp. 250–253, 1962.

[296] H. P. Wiesinger, F. M. Sauerzopf, and H. W. Weber, "On the calculation of Jc from

magnetization measurements on superconductors," *Phys. C Supercond. its Appl.*, vol. 203, no. 1–2, pp. 121–128, 1992.

[297] H. Yamasaki and Y. Mawatari, "Electric-Field Criterion for the Magnetic Measurement of Critical Current Densities of Oxide Superconductors," *Adv. Supercond. XII*, vol. 1, no. M, pp. 473–475, 2000.

[298] Y. Mawatari, A. Sawa, H. Obara, M. Umeda, and H. Yamasaki, "Field-sweep rate dependence of magnetization and current-voltage characteristics in superconducting disks," *Appl. Phys. Lett.*, vol. 70, no. 17, pp. 2300–2302, 1997.

[299] A. M. Campbell and J. E. Evetts, "Flux vortices and transport currents in type II superconductors," *Adv. Phys.*, vol. 21, no. 90, pp. 199–428, 1972.

[300] E. H. Brandt, "Electric field in superconductors with rectangular cross section," *Phys. Rev. B*, vol. 52, no. 21, pp. 15442–15457, 1995.

[301] "Pharos Digital Library - Quantum Design." [Online]. Available: https://www.qdusa.com/pharos/browse.php. [Accessed: 28-Jan-2021].

[302] K. Tsuno, "Resolution limit of a transmission electron microscope with an uncorrected conventional magnetic objective lens," *Ultramicroscopy*, vol. 50, no. 3, pp. 245–253, 1993.

[303] D. B. Williams and C. B. Carter, *Transmission Electron Microscopy: A Textbook for Materials Science*, vol. 1–4. 2009.

[304] J. I. Goldstein *et al.*, *Scanning Electron Microscopy and X-ray Microanalysis*, 3rd ed. 2003.

[305] "David Cockayne Centre for Electron Microscopy - Instruments," 2021. [Online]. Available: https://www-em.materials.ox.ac.uk/instruments#/. [Accessed: 31-Aug-2021].

[306] P. Walker and W. H. Tarn, *Handbook of Metal Etchants*. CRC Press LLC, 1991.

[307] G. D. Brittles, T. Mousavi, C. R. M. Grovenor, C. Aksoy, and S. C. Speller, "Persistent current joints between technological superconductors," *Supercond. Sci. Technol.*, vol. 28, no. 9, p. 93001, 2015.

[308] M. Weigand, "Grain Boundaries in Coated Conductors," Cambrigde University, 2010.

[309] M. L. Chen, K. Viggiano, S. H. Hong, and Q. Y. Ma, "Chemical etching of pure and implanted superconducting oxide films," *Supercond. Sci. Technol.*, vol. 10, no. 2, pp. 106–108, 1997.

[310] C. Cobb *et al.*, "Hysteretic loss reduction in straited YBCO," *Phys. C Supercond. its Appl.*, vol. 382, no. 1, pp. 52–56, 2002.

[311] S. Terzieva *et al.*, "Investigation of the effect of striated strands on the AC losses of 2G Roebel cables," *Supercond. Sci. Technol.*, vol. 24, no. 4, 2011.

[312] D. S. Ginley, C. I. H. Ashby, T. A. Plut, D. Urea, M. P. Siegal, and J. S. Martens, "Di- and Tricarboxylic-acid-based etches for processing high temperature superconducting thin films," *Appl. Phys. Lett.*, vol. 63, no. 17, pp. 2429–2431, 1993.

[313] J. A. Beall *et al.*, "YBCO/insulator multi-layers for crossover fabrication," *IEEE Trans. Magn.*, vol. 27, no. 2, p. 1596, 1991.

[314] V. R. Gómez, "Controlling Vortex Pinning and Dynamics of Nanostructured YBCO Thin Films Grown by Chemical Solution Deposition Víctor Rouco Gómez," Universitat Autonoma de Barcelona, 2014.

[315] J. S. Martens, T. E. Zipperian, D. S. Ginley, V. M. Hietala, C. P. Tigges, and T. A. Plut, “The effects of processing sequences on the microwave surface resistance of TlCaBaCuO,” *J. Appl. Phys.*, vol. 69, no. 12, pp. 8268–8271, 1991.

[316] C. G. Windsor *et al.*, “Tungsten boride shields in a spherical tokamak fusion power plant,” *Nucl. Fusion*, vol. 61, no. 8, p. 86018, 2021.

[317] A. J. Koning, D. Rochman, and J. C. Sublet, “TENDL Nuclear Data File,” 2019. [Online]. Available: https://tendl.web.psi.ch/tendl_2019/tendl2019.html. [Accessed: 04-Sep-2020].

[318] A. J. Koning, D. Rochman, J. Sublet, N. Dzysiuk, M. Fleming, and S. Van Der Marck, “TENDL : Complete Nuclear Data Library for Innovative Nuclear Science and Technology,” *Nucl. Data Sheets*, vol. 155, pp. 1–55, 2019.

[319] R. E. MacFarlane and A. C. Kahler, “Methods for Processing ENDF/B-VII with NJOY,” *Nucl. Data Sheets*, vol. 111, no. 12, pp. 2739–2890, 2010.

[320] M. R. Gilbert, J. Marian, and J. C. Sublet, “Energy spectra of primary knock-on atoms under neutron irradiation - Supplementary Information,” *J. Nucl. Mater.*, vol. 467, no. 2, p. 121, 2015.

[321] J. F. Ziegler, “SRIM - The Stopping and Range of Ions in Matter,” 2013. [Online]. Available: http://www.srim.org/. [Accessed: 02-Sep-2021].

[322] M. N. Rosenbluth, “Genesis of the Monte Carlo Algorithm for Statistical Mechanics,” *AIP Conf. Proc.*, vol. 690, no. November 2003, pp. 22–30, 2003.

[323] O. S. Oen and M. T. Robinson, “Computer studies of the reflection of light ions from solids,” *Nucl. Instruments Methods*, vol. 132, pp. 647–653, 1976.

[324] R. E. Stoller, M. B. Toloczko, G. S. Was, A. G. Certain, S. Dwaraknath, and F. A. Garner, “On the use of SRIM for computing radiation damage exposure,” *Nucl. Instruments Methods Phys. Res. Sect. B Beam Interact. with Mater. Atoms*, vol. 310, pp. 75–80, 2013.

[325] K. Jin *et al.*, “Electronic stopping powers for heavy ions in SiC and SiO2,” *J. Appl. Phys.*, vol. 115, no. 4, pp. 1–11, 2014.

[326] C. D. Hardie, “Micro-Mechanics of Irradiated Fe-Cr Alloys for Fusion Reactors,” Oxford University, 2013.

[327] W. Iliffe *et al.*, “In-situ measurements of the effect of radiation damage on the superconducting properties of coated conductors . Authors,” *Supercond. Sci. Technol.*, vol. 34, p. 09LT01, 2021.

[328] G. Federici, W. Biel, M. R. Gilbert, R. Kemp, N. Taylor, and R. Wenninger, “European DEMO design strategy and consequences for materials,” *Nucl. Fusion*, vol. 57, no. 9, 2017.

[329] IAEA, “Live Chart of Nuclides,” 2021. [Online]. Available: https://www-nds.iaea.org/relnsd/vcharthtml/VChartHTML.html. [Accessed: 05-Feb-2021].

[330] M. T. Simnad, “Nuclear Reactors: Shielding Materials,” *Encycl. Mater. Sci. Technol.*, pp. 6377–6384, 2001.

[331] OECD-NEA, “JANIS Book,” 2020. [Online]. Available: https://www.oecd-nea.org/jcms/pl_44624/janis-books. [Accessed: 11-Mar-2021].

[332] C. Hardie, “Private Communications.” 2021.

[333] L. W. Packer, M. Gilbert, S. Hughes, S. Lilley, R. Pampin, and J. C. Sublet, “UK fusion

technology experimental activities at the ASP 14 MeV neutron irradiation facility," *Fusion Eng. Des.*, vol. 87, no. 5–6, pp. 662–666, 2012.

[334] Q. U. A. Sahi and Y. S. Kim, "Primary radiation damage characterization of α-iron under irradiation temperature for various PKA energies," *Mater. Res. Express*, vol. 5, no. 4, 2018.

[335] D. A. Terentyev *et al.*, "Displacement cascades in Fe-Cr: A molecular dynamics study," *J. Nucl. Mater.*, vol. 349, no. 1–2, pp. 119–132, 2006.

[336] K. Öztürk, Ş. Çelik, U. Çevik, and E. Yanmaz, "The effect of Gd diffusion-doped on structural and superconducting properties of YBa2Cu3O7-x superconductors," *J. Alloys Compd.*, vol. 433, no. 1–2, pp. 46–52, 2007.

[337] P. T. Wady *et al.*, "Accelerated radiation damage test facility using a 5 MV tandem ion accelerator," *Nucl. Instruments Methods Phys. Res. Sect. A Accel. Spectrometers, Detect. Assoc. Equip.*, vol. 806, pp. 109–116, 2015.

[338] "SPI Supplies - Disc Punch, Produces 3 mm Discs," *Structure Probe Inc.*, 2021. [Online]. Available: https://www.2spi.com/item/17001-ab/. [Accessed: 18-Aug-2021].

[339] R. Bowers, "Magnetic Susceptibility of Copper Metal at Low Temperatures," *Phys. Rev.*, vol. 102, no. 6, pp. 1486–1488, 1956.

[340] D. R. Smith and F. R. Fickett, "Low-Temperature Properties of Silver," *J. Res. Natl. Inst. Stand. Technol.*, vol. 100, no. 2, p. 119, 1995.

[341] M. A. Garcia *et al.*, "Sources of experimental errors in the observation of nanoscale magnetism," *J. Appl. Phys.*, vol. 105, no. 1, pp. 1–17, 2009.

[342] P. Das, C. V. Tomy, S. S. Banerjee, H. Takeya, S. Ramakrishnan, and A. K. Grover, "Surface superconductivity, positive field cooled magnetization, and peak-effect phenomenon observed in a spherical single crystal of niobium," *Phys. Rev. B - Condens. Matter Mater. Phys.*, vol. 78, no. 21, pp. 1–7, 2008.

[343] W. Braunisch *et al.*, "Paramagnetic Meissner Effect in Bi High-Temperature Superconductors," *Phys. Reivew Lett.*, vol. 68, no. 12, p. 1908, 1992.

[344] S. Reidling *et al.*, "Observation of the Wohlleben effect in YBCO single crystals," *Phys. Rev. B*, vol. 49, no. 18, p. 49, 1994.

[345] R. E. Stoller, M. B. Toloczko, G. S. Was, A. G. Certain, S. Dwaraknath, and F. A. Garner, "On the use of SRIM for computing radiation damage exposure," *Nucl. Instruments Methods Phys. Res. Sect. B Beam Interact. with Mater. Atoms*, vol. 310, 2013.

[346] V. Selvamanickam *et al.*, "Influence of Zr and Ce doping on electromagnetic properties of (Gd,Y)-Ba-Cu-O superconducting tapes fabricated by metal organic chemical vapor deposition," *Phys. C Supercond. its Appl.*, vol. 469, no. 23–24, pp. 2037–2043, 2009.

[347] E. Galstyan, M. H. Gharahcheshmeh, L. Delgado, A. Xu, G. Majkic, and V. Selvamanickam, "Microstructure characteristics of high lift factor MOCVD REBCO coated conductors with high Zr content," *IEEE Trans. Appl. Supercond.*, vol. 25, no. 3, pp. 1–5, 2015.

[348] Brooks, "Multiple Uses of Model 22 C / 350C Cryodyne ® Refrigerators Installation, Operation and Servicing Instructions," 2013. [Online]. Available: https://brooks.com/support/technical-support/documentation/cryochillers-cryocoolers/~/media/Files/Support/Documentation/Vacuum/WaterpumpChillers/Manual Cryocoolers/8040272.pdf. [Accessed: 22-May-2021].

[349] Fujikura, "Introduction of FUJIKURA RE-based HTS Wire," 2019. [Online]. Available: https://www.fujikura.co.jp/eng/products/newbusiness/superconductors/01/superconductor.pdf. [Accessed: 09-Apr-2021].

[350] E. S. Drexler, N. J. Simon, and R. P. Reed, "Properties of copper and copper alloys at cryogenic temperatures," *NIST monograph*, 1992. [Online]. Available: https://nvlpubs.nist.gov/nistpubs/Legacy/MONO/nistmonograph177.pdf. [Accessed: 22-May-2021].

[351] C. Barth, "High Temperature Superconductor Cable Concepts for Fusion Magnets," Karlsruhe Institute of Technology, 2013.

[352] J. H. Lienhard IV and J. H. Lienhard V, *A heat transfer textbook*, 4th ed. Boston, MA, USA: Phlogiston Press, 2015.

[353] R. Jha, P. Rani, and V. P. S. Awana, "Revisiting heat capacity of bulk polycrystalline YBa2Cu 3O7-δ," *J. Supercond. Nov. Magn.*, vol. 27, no. 2, pp. 287–291, 2014.

[354] B. M. Terzijska, R. Wawryk, D. A. Dimitrov, C. Marucha, V. T. Kovacheva, and J. Rafalowicz, "Thermal conductivity of YBCO and thermal conductance at YBCO/ruby boundary. Part 1: joint experimental set-up for simultaneous measuremend and experimental study in the temperature range 10-260K," *Cryogenics (Guildf).*, vol. 32, no. 1, pp. 53–59, 1992.

[355] Tektronix, "Keithley Model 2000 Multimeter User's Manual," 2010. [Online]. Available: https://download.tek.com/manual/2000-900_J-Aug2010_User.pdf. [Accessed: 11-Jun-2021].

[356] "JD Photo Data," 2021. [Online]. Available: https://www.jd-photodata.co.uk/. [Accessed: 02-Jul-2021].

[357] R. C. Dhuley, "Pressed copper and gold-plated copper contacts at low temperatures – A review of thermal contact resistance," *Cryogenics (Guildf).*, vol. 101, no. June, pp. 111–124, 2019.

[358] S. Schoft, "Joint resistance depending on joint force of high current aluminum joints," *Proc. 50th IEEE Holm Conf. Electr. Contacts 22nd Int. Conf. Electr. Contacts*, no. December, pp. 502–510, 2004.

[359] E. R. Stauffacher, "Short-time Current Carrying Capacity of Copper Wire," *General Electric Review*, vol. 31, no. 6. pp. 326–327, 1928.

[360] R. McFee, "Optimum input leads for cryogenic apparatus," *Rev. Sci. Instrum.*, vol. 30, no. 2, pp. 98–102, 1959.

[361] L. S. Cryogenics, "DT-670 Silicon Diode Specifications," 2019. [Online]. Available: https://www.lakeshore.com/. [Accessed: 25-May-2021].

[362] J. G. Hust, "Thermal anchoring of wires in cryogenic apparatus," *Rev. Sci. Instrum.*, vol. 41, no. 5, pp. 622–624, 1970.

[363] L. J. Ganesan, D. E. Selvaraj, and J. Ramathilagam, "Experimental Analysis of Thermal Conductivity of Enamel Filled With," *Int. Jour. Adv. Res. Elec. Elect. Instr. Eng.*, vol. 2, no. 7, p. 2907, 2013.

[364] D. J. Benford, T. J. Powers, and S. H. Moseley, "Thermal conductivity of Kapton tape," *Cryogenics (Guildf).*, vol. 39, no. 1, pp. 93–95, 1999.

[365] CMR-Direct, "Cryoloom (R) - Cryogenic Woven Loom," 2021. [Online]. Available: http://www.cmr-direct.com/en/woven-loom. [Accessed: 25-May-2021].

[366] W. P. Vogt and R. B. Johnston, *The SAGE Dictionary of Statistics & Methodology*, 5th ed. SAGE Publications, Inc;, 2015.

[367] D. C. Van Der Laan *et al.*, “Anisotropic in-plane reversible strain effect in Y0.5Gd0.5Ba2Cu3O7 - δcoated conductors,” *Supercond. Sci. Technol.*, vol. 24, no. 11, 2011.

[368] D. X. Fischer *et al.*, “Presentation: Degradation and annealing of coated conductors after cryogenic irradiation,” Moscow, Russia 5-9 September, 2021.

[369] R. Sultana, P. Rani, A. K. Hafiz, R. Goyal, and V. P. S. Awana, “An inter comparison of the upper critical fields (Hc2) of different superconductors - YBCO, MgB2, NdFeAsOF, FeSeTe and NbPdS,” *J. Supercond. Nov. Magn.*, vol. 29, pp. 1–10, 2016.

[370] N. R. Werthamer, E. Helfand, and P. C. Hohenberg, “Temperature and Purity Dependence of the Superconducting Critical Field Hc2. 3 Electron Spin and Spin-Orbit Effects,” *Physical*, vol. 147, no. 1, p. 295, 1966.

[371] V. P. S. Awana, A. Pal, A. Vajpayee, B. Gahtori, and H. Kishan, “Superconductivity and thermal properties of sulphur doped FeTe with effect of oxygen post annealing,” *Phys. C Supercond. its Appl.*, vol. 471, no. 3–4, pp. 77–82, 2011.

[372] S. R. Ghorbani, X. L. Wang, M. Shahbazi, S. X. Dou, and C. T. Lin, “Fluctuation of mean free path and transition temperature induced vortex pinning in (Ba,K)Fe 2As 2 superconductors,” *Appl. Phys. Lett.*, vol. 100, no. 21, pp. 0–4, 2012.

[373] J. R. Thompson *et al.*, “Effect of flux creep on the temperature dependence of the current density in Y-Ba-Cu-0 crystals,” *Phys. Rev. B*, vol. 47, no. 21, p. 14440, 1993.

[374] Y. Yeshurun and A. P. Malozemoff, “Giant flux creep and irreversibility in an Y-Ba-Cu-O crystal: An alternative to the superconducting-glass model,” *Phys. Rev. Lett.*, vol. 60, no. 21, pp. 2202–2205, 1988.

[375] D. J. Miller *et al.*, “Characterization of Long-Length , MOCVD-Derived REBCO Coated-Conductors,” *IEEE Trans. Appiled Supercond.*, vol. 19, no. 3, pp. 3176–3179, 2009.

[376] S. M. Lim, H. S. Kim, K. C. Chung, B. S. Lee, and D. Youm, “Comparative studies on the growth conditions of CeO2 and Y2O3 buffer layers on NiW tapes,” *Supercond. Sci. Technol.*, vol. 17, no. 1, pp. 148–154, 2004.

[377] J. Xiong, B. W. Tao, W. F. Qin, J. L. Tang, X. Han, and Y. R. Li, “Reel-to-reel continuous simultaneous double-sided deposition of highly textured CeO2 templates for YBa2Cu3O 7-δ coated conductors,” *Supercond. Sci. Technol.*, vol. 21, no. 2, 2008.

[378] M. B. Chadwick *et al.*, “ENDF / B-VII . 1 Nuclear Data for Science and Technology : Cross Sections , Covariances , Fission Product Yields and Decay Data,” *Nucl. Data Sheets*, vol. 112, pp. 2887–2996, 2011.

[379] D. A. Brown *et al.*, “ENDF / B-VIII . 0 : The 8th Major Release of the Nuclear Reaction Data Library with CIELO-project Cross Sections, New Standards and Thermal Scattering Data,” *Nucl. Data Sheets*, vol. 148, pp. 1–142, 2018.

[380] OECD, “Joint Evaluated Fusion and Fission file.” [Online]. Available: http://www.oecd-nea.org/dbdata/jeff-beta/JEFF33T2/neutrons/. [Accessed: 04-Sep-2020].

[381] K. Shibata *et al.*, “JENDL-4 . 0 : A New Library for Nuclear Science and Engineering,” *J. Nucl. Sci. Technol.*, vol. 48, no. 1, pp. 1–30, 2011.

[382] A. M. Hofmeister, “Thermal diffusivity and thermal conductivity of single-crystal MgO and

Al2O3and related compounds as a function of temperature," *Phys. Chem. Miner.*, vol. 41, no. 5, pp. 361–371, 2014.

[383] K. Suzuki *et al.*, "Thermal and mechanical properties of CeO2," *J. Am. Ceram. Soc.*, vol. 102, no. 4, pp. 1994–2008, 2019.